THÈSE DE DOCTORAT
DE L'UNIVERSITÉ PIERRE ET MARIE CURIE

Spécialité : Physique

École doctorale 107 : Physique en Ile-de-France

réalisée au

Service de Physique de l'État Condensé, CEA Saclay
Groupe Nanoelectronique

présentée par

Andrey MOSTOVOV

pour obtenir le grade de :

DOCTEUR DE L'UNIVERSITÉ PIERRE ET MARIE CURIE

Sujet de la thèse :

Quantum Shot Noise in Graphene

présentée et soutenue publiquement le 23 avril 2014

devant le jury composé de :

M. Dimitry RODITCHEV	Président
M. Massimo MACUCCI	Rapporteur
M. François LEFLOCH	Rapporteur
M. Romain DANNEAU	Examinateur
M. Denis Christian GLATTLI	Directeur de thèse
M. Preden ROULLEAU	Invité

Contents

Introduction **1**

I Overview of Graphene Physics and Mesoscopic Transport **7**

1 Physical Properties of Graphene **9**
1.1 Crystal Structure of Graphene 9
1.2 Graphene Band Structure 11
1.2.1 Basic Principles 11
1.2.2 Band Structure Calculations 13
1.2.3 Low-Energy Excitations 16
1.3 Properties of Dirac Fermions 18
1.3.1 Probabilty Current Density 19
1.3.2 Zitterbewegung, Chirality and Klein Tunneling 19

2 Transport in Mesoscopic Systems **23**
2.1 Mesoscopic Scale 24
2.1.1 Classical Discription of Transport 24
2.1.2 Quantum Phase Coherent Systems 26
2.1.3 Effects of the Coherence on Transport Properties 27
2.2 Scattering Approach 30
2.2.1 Framework, Hypotheses, Formulation 30
2.2.2 Scattering Approach at Work 32
2.3 Quantum Hall Effect 36
2.3.1 Landau Quantization 38
2.3.2 Integer Quantum Hall Effect 40

3 Mesoscopic Transport in Graphene **45**
3.1 Conducance and Shot Noise in Graphene 45
3.2 Quantum Hall Effect in Graphene 49

3.3 Experimental Results 52

II Experimental Setup and Device 59

4 Measurement System Principle 61
4.1 Experimental Requirements and Techniques 61
4.1.1 Typical Scales 61
4.1.2 Noise Measurement Techniques 63
4.2 Technical Realisation 65
4.2.1 Device Design 66
4.2.2 Measurement System 67
4.2.3 Cryogenic Amplification System 70

5 Device Fabrication 75
5.1 Methods 76
5.1.1 Obtaining Graphene 76
5.1.2 Making Graphene Visible 80
5.1.3 Raman Spectroscopy of Graphene 82
5.1.4 Graphene Oxygen Plasma Etch 85
5.2 Processes 85
5.2.1 Wafers Preparation 85
5.2.2 Graphite Deposition 87
5.2.3 Graphene Flakes Detection 89
5.2.4 Microcircuit Deposition 90
5.2.5 Nano-Constriction in Graphene 94
5.2.6 Device Test 95
5.2.7 Difficulties and Solutions 96

III Experimental Results 99

6 Measurement System Calibration 101
6.1 Low Frequency Calibration 103
6.1.1 Lines Tuning 103
6.1.2 Two-point Measurement 104
6.1.3 Calibration 105
6.2 High Frequency Calibration 108
6.2.1 Lines Tuning 108
6.2.2 Current Measurement 111

7 Conductance Measurements at Zero Magnetic Field 119
7.1 Conductance at Zero Bias . . . 119
7.1.1 Ballistic Regime Hypothesis . . . 120
7.1.2 Diffusive Regime Hypothesis . . . 122
7.1.3 Discussion . . . 125
7.1.4 Model for the "altered" Curves . . . 128
7.2 Conductance Spectroscopy . . . 130

8 Conductance in the Magnetic Field 139
8.1 Measurement Principle . . . 139
8.2 Results and Discussion . . . 142

9 Shot Noise in Graphene 149
9.1 Measurement Principle . . . 149
9.2 Shot Noise in Presence of Joule Heating . . . 152
9.2.1 Cooling by Electron Diffusion . . . 153
9.2.2 Data Fit . . . 154
9.2.3 Cooling by Phonon Emission . . . 155
9.3 Noise Power Fluctuations . . . 159
9.4 Results and Discussion . . . 161

Conclusion 169

Appendices 173

A Device Fabrication 173
A.1 Recipes . . . 173
A.2 Introduction to Raman scattering . . . 173
A.3 Common Nano-fabrication Techniques . . . 175
A.3.1 Microlithography Principle . . . 175
A.3.2 Optical and E-Beam lithography . . . 176
A.3.3 Thin Films Deposition . . . 177

B Measurement System 179
B.1 Cryogenic Inset . . . 179
B.2 Data Acquisition Module . . . 179
B.3 RLC-Filter Pass-Band Calculation . . . 182

Bibliography 185

Résumé en français

Résumé de la thèse

Dix ans après sa découverte, le graphène demeure une thématique très en vogue en physique de la matière condensée et en sciences des matériaux. Cet unique matériaux, un cristal véritablement bidimensionnel, qui a couté à ses inventeurs A. Geim and K. Novoselov un Prix Nobel[?], est considéré comme très prometteur aussi bien de point de vue fondamental que pratique. La raison pour cela est la physique des électrons dans le graphène, qui sous certains conditions peuvent être vu comme des particules relativistes sans masse, décrites par l'équation de Dirac. Par conséquent, le graphène pourrait servir comme un banc d'essai à état solid pour des expériences en Électrodynamique Quantique. Des effets mésoscopiques spécifiques comme l'Effet Hall Quantique non-conventionnel (relativiste) ou anti-localisation faible sont observés dans le graphène. D'autre part, ce matériaux devrait permettre la fabrication des transistors extrêmement rapides et des électrodes transparents, ainsi que trouver son application en photovoltaïque. Plusieurs autres applications sont envisagées.

Physique du Graphène

Le graphène est plus connu sous forme de graphite, qui est tout simplement un tas des plans de graphène, tenus par les forces de van der Waals. Les atomes de carbone dans le graphène sont placés sur un réseau hexagonal (ou en nid d'abeilles). Ce réseau ne constitue pas un réseau de Bravais, faute de sa symétrie et la maille élémentaire contient deux atomes. Par conséquent, il est d'usage de distinguer deux sous-réseaux d'atomes **A** et **B** (voir fig. 1.a). Le réseau de Bravais dans ce cas est de type triangulaire avec des vecteurs de base

$$\mathbf{a}_1 = \sqrt{3}a\mathbf{e}_x \qquad \text{and} \qquad \mathbf{a}_2 = \frac{\sqrt{3}a}{2}\left(\mathbf{e}_x + \sqrt{3}\mathbf{e}_y\right). \tag{1}$$

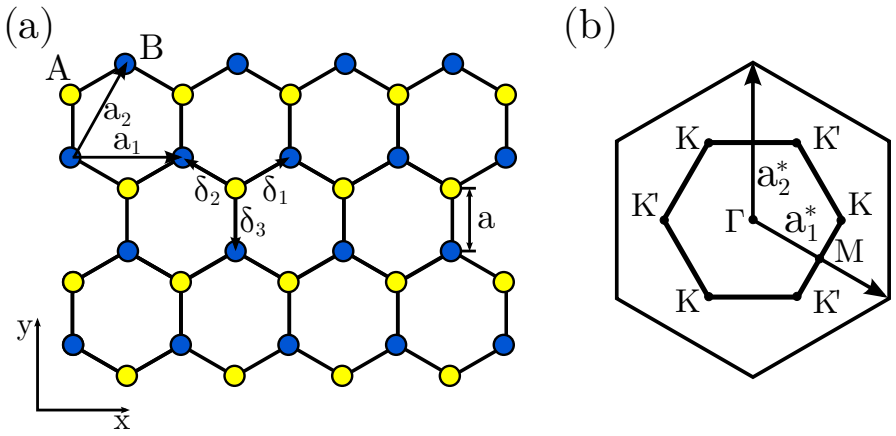

Figure 1: (a) Réseau hexagonal (ou en nid d'abeilles) du graphène avec deux sous-réseaux en couleurs différentes, distance interatomique $a = 0.142\,\text{nm}$. (b) La première zone de Brillouin et les points K et K' (deux seulement sont inéquivalents).

Le réseau réciproque est engendré par les vecteurs suivants

$$\mathbf{a}_1^* = \frac{2\pi}{\sqrt{3}a}\left(\mathbf{e}_x - \frac{\mathbf{e}_y}{\sqrt{3}}\right) \qquad \text{and} \qquad \mathbf{a}_2^* = \frac{4\pi}{3a}\mathbf{e}_y, \tag{2}$$

et la première zone de Brillouin est représenté sur fig. 1.b. Deux points particuliers situés sur les coins de la première zone de Brillouin seront importants dans la suite. Nous les notons K et K', ils sont donnés par les vecteurs

$$\pm\mathbf{K} = \pm\frac{4\pi}{3\sqrt{3}a}\mathbf{e}_x. \tag{3}$$

Dans l'approximation de liaisons fortes on peut chercher les fonctions d'ondes propres du système sous forme de combinaison linéaire des fonctions de Bloch de deux sous-réseaux A et B:

$$\psi_{\mathbf{k}}(\mathbf{r}) = a_{\mathbf{k}}\varphi_{\mathbf{k}}^A(\mathbf{r}) + b_{\mathbf{k}}\varphi_{\mathbf{k}}^B(\mathbf{r}) \tag{4}$$

Les valeurs propres de l'équation de Schrödinger $H\psi_{\mathbf{k}} = \epsilon_{\mathbf{k}}\psi_{\mathbf{k}}$ seront données par l'équation séculaire[1]

$$\det\begin{bmatrix} -\varepsilon_{\mathbf{k}} & t\cdot\gamma_{\mathbf{k}} \\ t\cdot\gamma_{\mathbf{k}}^\dagger & -\varepsilon_{\mathbf{k}} \end{bmatrix} = 0 \tag{5}$$

[1]Ici nous somme dans une approximation qui consiste à restreindre le couplage aux premiers voisins uniquement et négliger le recouvrement entre les orbitaux atomiques.

t étant l'intégrale de transfert ($t \approx -3\,\mathrm{eV}$) et $\gamma_{\mathbf{k}} \equiv 1 + e^{-\imath \mathbf{k}\cdot\mathbf{a}_2} + e^{-\imath \mathbf{k}\cdot(\mathbf{a}_2 - \mathbf{a}_1)}$ est un préfacteur de phases des premier voisins, venant du fait que chaque atome a trois premiers voisins, dont deux n'appartiennent pas au même nœuds du réseau de Bravais que lui-même. Cela donne deux solutions:

$$\varepsilon^{\pm}_{\mathbf{k}} = \pm t|\gamma_{\mathbf{k}}| = \pm t\sqrt{3 + 2\sum_{i=1}^{3}\cos\left(\mathbf{k}\cdot\mathbf{a}_i\right)} \tag{6}$$

Les solutions positives et négatives correspondent aux bandes de Conduction et de Valence respectivement. Les deux bandes se touchent en deux points de la première zone de Brillouin déjà mentionné: K et K'. En particulier, la relation de dispersion est linéarisables au voisinage de ses deux points. On utilise la notation suivante: $\mathbf{k} = \pm\mathbf{K} + \mathbf{q}$ où le vecteur $\mathbf{q}$ est tel que $|\mathbf{q}| \ll |\mathbf{K}|$. Cela résulte en Hamiltonien effectif linéarisé autour du point K (pour K' il faut inverser le signe):

$$\widetilde{\mathcal{H}}_{\mathbf{q}} = \hbar v_{\mathrm{F}} \mathbf{q}\boldsymbol{\sigma} \tag{7}$$

avec $v_{\mathrm{F}} \equiv -\frac{3ta}{2\hbar} \approx 1 \times 10^6\,\mathrm{m\,s^{-1}}$ — *vitesse de Fermi* and $\boldsymbol{\sigma} \equiv (\sigma^x, \sigma^y)$ — vecteur de matrices de Pauli matrices. Mis sous cette forme, ce Hamiltonien est souvent appelé *le Hamiltonien de Dirac* par analogie avec la physique des particules. La relation de dispersion linéarisée est finalement donnée par:

$$\varepsilon^{\pm}_{\mathbf{q}} = \pm\hbar v_{\mathrm{F}}|\mathbf{q}|, \tag{8}$$

aussi bien pour la linéarisation autour du point K, que autour du point K', ce qui résulte en dégénérescence supplémentaire dite de vallée. Il est courant, en vue de la forme du Hamiltonien (7), d'employer la notation vectorielle ou d'un spinor (également par similitude avec la notation en physique des particules) pour décrire les états du système:

$$\Psi^{\pm}_{\mathbf{k}} = \begin{pmatrix} a^{\pm}_{\mathbf{k}} \\ b^{\pm}_{\mathbf{k}} \end{pmatrix} \tag{9}$$

où les composantes de ce vecteur sont les facteurs de phase avec lesquelles les deux sous réseaux contribuent à l'état donné. En particulier, les vecteurs propres du nouveau Hamiltonien s'écrivent

$$\Psi^{\pm}_{\mathbf{k}} = \frac{1}{\sqrt{2}}\begin{pmatrix} 1 \\ \pm e^{\imath\phi_{\mathbf{k}}} \end{pmatrix}, \quad \text{avec} \quad \phi_{\mathbf{k}} = \arctan\left(\frac{\mathbf{Im}\gamma_{\mathbf{k}}}{\mathbf{Re}\gamma_{\mathbf{k}}}\right) \tag{10}$$

Cela n'est pas superflu de souligner ici que les caractéristiques extraordinaires de ce matériau sont surtout déterminées par ces propriétés physiques singulières.

Transport Mésoscopique dans le Graphène

Dans ce travail, le graphène est examiné du point de vu de la physique mésoscopique, en particulier le mesures de la conductance et du bruit sont réalisées. Ce champ de physique de la matière condensée s'intéresse aux systèmes dont la taille caractéristique appartient à l'échelle"intermédiaire" entre l'échelle microscopique et l'échelle macroscopique. La limite inférieure de cette échelle peut être donnée par la taille d'un atome, alors que la limité supérieur est déterminée par la longueur de cohérence de phase l_ϕ, la distance maximale sur laquelle la cohérence quantique de phase des états est préservée. Sous ces conditions les effets quantiques tels que les fluctuations quantiques, les interférences quantiques et parfois également les interactions commencent a jouer un rôle important. Afin de briser la cohérence de phase une diffusion inélastique est nécessaire et à basse température, où le couplage électron-phonon est faible, celle-ci est due aux interactions électron-électron. En dessous de l_ϕ on peut également distinguer deux régimes différents. Si en traversant l'échantillon, les électrons subissent un grand nombre de collisions élastiques, c'est un régime dit *diffusif*. Alors que, si en traversant l'échantillon ils ne subissent aucun choc, c'est un régime dit *balistique*. La longueur caractéristique de transition entre ces deux régimes s'appelle le *libre parcours moyen*, l_e.

L'approche le plus rependu de traiter les problèmes à l'échelle mésoscopique est celle de la théorie de la diffusion proposé par R. Landauer[91, 93, 94, 19, 92] et développée ensuite par M. Büttiker[19, 20, 92, 16, 17, 18], Y. Imry[72, 19, 20, 73, 141, 74] et d'autres personnalités. L'idée de cette théorie consiste a relier les propriétés de transport du système étudié (e.g. conductance, les fluctuations du courant) à ses propriétés de diffusion, considérées d'être connues à partir des calculs de la mécanique quantique. Par exemple analysons le cas d'un conducteur à deux terminaux (le gauche et le droit), connecté à deux réservoirs d'électrons (voir fig. 2). On peut distinguer deux types d'états aussi bien à gauche qu'à droite: les états incidents sur le conducteur et les états quittant le conducteur vers l'un ou l'autre réservoir. Le bilan de tous ses états va déterminer les propriétés de transport du système étudié. La théorie de la diffusion propose donc de calculer la matrice dite de la diffusion reliant les états incidents aux états quittant le conducteur à gauche et à droite. Les éléments de cette matrice permettent de parvenir jusqu'aux coefficients de la transmission ou de la diffusion de chaque mode de propagation, D_n et $R_n = 1 - D_n$, n étant l'indice de mode (évidemment $D_n \leq 1$).

Mentionnons deux principaux résultats de cette théorie. Tout d'abord la conductance d'un conducteur cohérent est donnée par la formule

$$G = \frac{2e^2}{h} \sum_n D_n \tag{11}$$

la quantité $\frac{2e^2}{h}$, appelée le quantum de conductance, définit la conductance maxi-

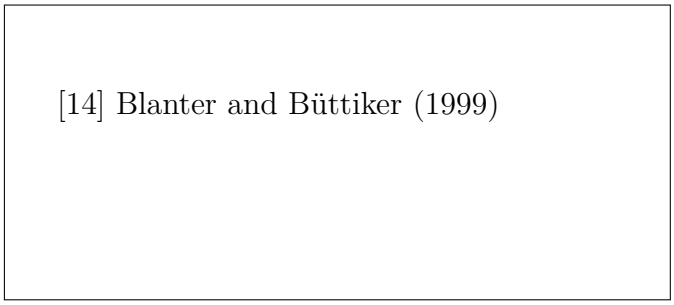

Figure 2: Exemple du problème d'un conducteur à deux terminaux dans la théorie de la diffusion. Adopté de [14].

male que peux avoir un mode de transmission. Ce résultat est d'une très grande portée, car il montre que même en absence de toute diffusion la conductance n'est pas infini, ce qu'un modèle classique n'est pas capable de prédire. En effet, ce fait est une conséquence à la fois du principe de Pauli et du prince d'incertitude d'Heisenberg. Le premier limite le nombre d'électrons par état à deux (spin up et spin down), alors que le dernier défini l'espacement sur l'axe temporel des paquets d'ondes d'une tranche d'énergie donnée (égale à $\mu_{\mathrm{L}} - \mu_{\mathrm{R}}$) et ainsi limite la fréquence d'injection des paquets dans le conducteur.

Le deuxième résultat concerne le bruit de partition. La densité spectrale de "pur" bruit de partition (i.e. à température nul) s'écrit

$$S_{\mathrm{I}} = 2eI \frac{\sum_n D_n(1 - D_n)}{\sum_n D_n} \tag{12}$$

et si le bruit thermique est pris en compte, on obtient

$$S_{\mathrm{I}} = 4\frac{2e^2}{h} \sum_n D_n^2 k_{\mathrm{B}} T + 2e\frac{2e^2}{h} \sum_n D_n(1 - D_n) V \coth\left(\frac{eV}{2k_{\mathrm{B}}T}\right) \tag{13}$$

On introduit alors une quantité qu'on appel le facteur de Fano:

$$\mathfrak{F} = \frac{\sum_n D_n(1 - D_n)}{\sum_n D_n} \tag{14}$$

La conductance et le facteur de Fano sont les caractéristiques principales d'un conducteur mésoscopique. Prenons quelques exemples type. Le facteur de Fano d'un conducteur balistique est évidemment nul, tandis que pour une jonction tunnel où tous les coefficients de transmission sont extrêmement faibles, il vaut un. Le cas d'un conducteur diffusif est plus compliqué, car il n'y est pas possible de calculer précisément les coefficients de transmission D_n. Seulement la distribution de probabilités pour ces coefficients de prendre une valeur est calculable. Avec ce résultat le facteur de Fano égal à 1/3 a été déduit.

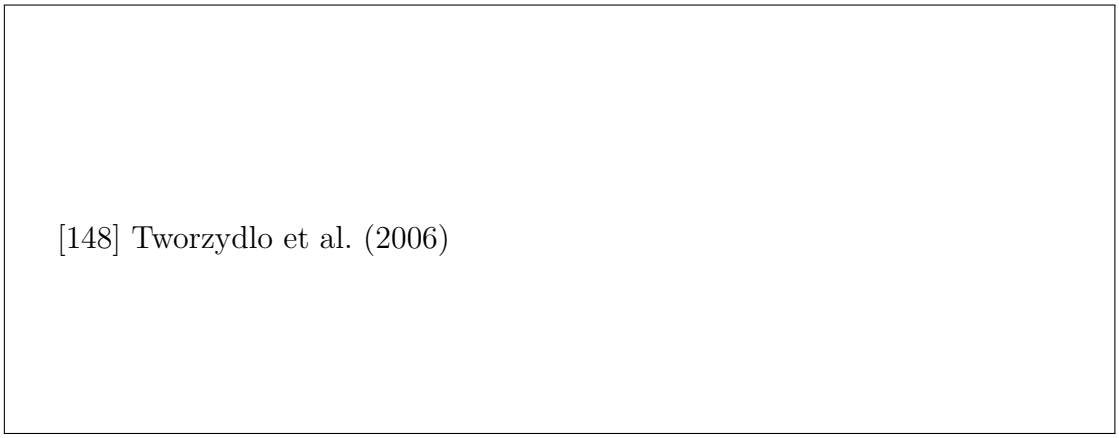

Figure 3: Dépendance en énergie de la conductivité σ (a) et du facteur de Fano $\mathfrak{F}$ (b) pour un rapport d'aspects $W/L = 5$. Le minimum de la conductivité au point de Dirac correspond au maximum du facteur de Fano. Adopté de [148].

Revenons à présent au graphène. Les propriété du transport cohérent d'un ruban de graphene idéal ont été calculées par Tworzydlo et al. de façon analytique. Les coefficients de la transmission sont donnés par la formule suivante

$$D_n = \left| \frac{k_n}{k_n \cos(k_n L) + \imath(\mu/\hbar v_{\mathrm{F}}) \sin(k_n L)} \right|^2, \tag{15}$$

où μ est le potentiel électrochimique du conducteur, q_n — le moment transversal du mode n et $k_n = \sqrt{(\mu/\hbar v_{\mathrm{F}})^2 - q_n^2}$. À l'aide de cette formule, la conductance (ou la conductivité $\sigma \equiv G \times L/W$) et le facteur de Fano sont calculés. Dans la limite $W/L \to \infty$ (déjà satisfaite pour $W/L \gtrsim 4$) on conclue, que ses quantités au point de neutralité prennent des valeur universelles:

$$\sigma \to \frac{4e^2}{\pi h}, \qquad \mathfrak{F} \to 1/3, \qquad \text{lors que} \quad \mu = 0 \tag{16}$$

Les résultats plus complets son présentés sur fig. 3. La conductivité atteint donc son minimum au même temps que le facteur de Fano atteint son maximum et cela au point de neutralité (aussi appelé le point de Dirac).

Il est remarquable que dans un ruban de graphène idéal et donc balistique le facteur de Fano prenne au point de neutralité la valeur 1/3, qui est celle d'un conducteur diffusif. Ce fait a suscité beaucoup d'intérêt.

D'autre part, pour le graphène diffusif il n'existe pas de modèle analytique et il n'y pas d'unanimité sur la valeur exacte du facteur de Fano ainsi que de sa dépendance en potentiel électrochimique et en degré de désordre. Citons quelque résultats numériques. San-Jose et al. examinent le problème dans le cadre du

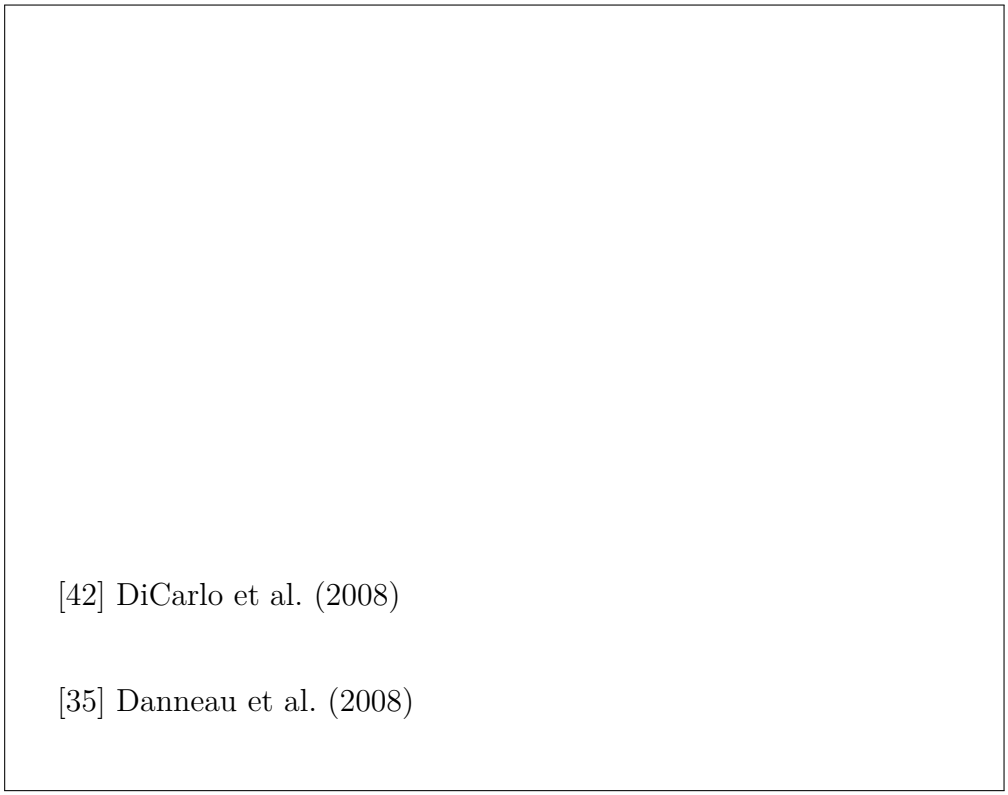

Figure 4: Résultats précédents. Mesure par DiCarlo et al. de la résistance (a) et du facteur de Fano (b). Adopté de [42]. (c) et (d) — mesures des mêmes quantités par Danneau et al., adopté de [35]

formalisme des matrices de transfert en considérant un potentiel de désordre lisse uni- et bi-dimensionnel. Ils obtiennent le valeurs $F_{1D} = 0.243$ et $F_{2D} = 0.295$ dans ces deux cas respectifs. Lewenkopf et al. ont utilisé la méthode des fonctions de Green récursives pour le désordre à longue portée. Ils concluent pour un niveau de désordre modéré, que le facteur de Fano est situé autour de $0.25-0.29$ (en fonction du degré de désordre), mais également prédisent l'apparition d'un pic au point de neutralité. Logoteta et al. étudie le facteur de Fano en fonction du potentiel électrochimique en résolvant l'équation de Dirac par la méthode des fonctions enveloppes et de Fourier[103]. Pour les rapports d'aspects et les concentrations d'impuretés qui nous intéresseront, ils trouvent que $\mathfrak{F}$ oscille autour de 0.25 et atteint au point de neutralité 0.35.

Finalement, regardons des travaux d'expérimentateurs à ce sujet, présentés en partie sur la fig. 4. Seulement deux études du bruit dans le graphène ont été menées précédemment. La première, a été réalisée à l'Université de Harvard par DiCarlo et al. Leurs échantillons se sont montrés diffusifs et ils ont observé

le facteur de Fano situé près de 0.35 et pratiquement indépendant du potentiel électrochimique. Quant à la conductivité au point de neutralité, celle-ci à largement dépassé la valeur $\frac{4e^2}{\pi h}$. La deuxième étude réalisée par Danneau et al. à l'Université de Helsinki montre sur un échantillon que les valeurs universelles de la conductivité et du facteur de Fano sont atteint, alors que leurs mesures sur les autres échantillons sont moins concluantes. Il reste donc bien des questions ouvertes atour de ce sujet.

Présentation de l'approche expérimentale

Nous présentons ici une troisième expérience de bruit quantique dans le graphène, complétant les deux travaux ci-dessus. Dans notre expérience nous avons eu recours à un nombre de techniques de mesures de bruit pour ainsi obtenir des conditions expérimentales les plus favorables et dépasser certaines limitations des travaux précédents. Notamment dans notre expérience nous appliquons la méthode de corrélations croisées qui, au prix d'un doublement du nombre des lignes de détection, permet de réduire significativement l'impacte du système de détection sur le bruit détecté. De plus, nous faisons une mesure quatre points, qui a des avantages évidents pour une mesure de conductance mais également pour celle du bruit, car elle exclut la source parasite de bruit thermique que sont les résistances de contacte. Utilisation des amplificateurs cryogéniques bas bruit (faits maison) placés à proximité de l'échantillon et couplés aux circuits résonants (fréquence de résonance $\simeq 3.3\,\mathrm{MHz}$) rendent la détection plus efficace et rapide et la contribution du bruit en $1/f$ négligeable. Finalement la chute du potentiel est retrouvée grâce à deux amplificateurs différentiels (situés à température ambiante), les signaux sont numérisés par une carte rapide d'acquisition (échantillonnage à 10 MHz) et la puissance spectrale est calculé par l'ordinateur à l'aide d'un module de transformé de Fourier rapide. Le principe de notre système expérimental est décrit dans la sec. 4.2.

Notre échantillon comporte également des avantages (voir subsec. 4.2.1). Premièrement, il a une géométrie spéciale: nous étudions le transport non pas à travers toute la couche de graphène, mais seulement à travers une étroite constriction que possède la couche. La constrictions étant beaucoup plus étroite que le reste de la couche, ces propriétés vont dominer le transport à travers l'échantillon. Les problèmes de mauvais contacts entre les réservoirs d'électrons et le conducteur (i.e. la région étudiée) seront ainsi évités, car les trois font partie de la même couche de graphène. Finalement, afin d'échapper aux capacités parasites par l'intermédiaire du substrat nous avons déposé le graphène sur un substrat de silicium non-dopé et utilisons des grilles latérales à la place de la grille arrière. Toutes les étapes de fabrication de l'échantillon ont été effectué par l'auteur et uniquement dans le laboratoire d'origine, elles sont exposées dans le Chapitre 5. ¡Schéma du cir-

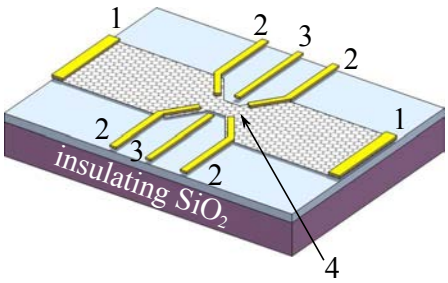

Figure 5: Dessin du dispositif à base de graphène utilisé dans nos expériences: 1 — deux électrodes d'injection du courant, 2 — quatre sondes de tension, 3 — grilles latérales (déconnectées électriquement du graphène), 4 — nano-constriction, jouant le rôle d'un conducteur cohérent (proportions ne sont pas conservées pour meilleure visibilité). L'ensemble est situé sur un substrat de silicium isolant (en violet), contenant une couche de SiO_2 (in bleu claire).

cuit de mesure avec un dessin de l'échantillon au centre: six contacts ohmiques sont colorés en jaune et les grilles latérales en vert, la constriction est montrée explicitement et notée R_s. Quatre lignes de mesure de tension identiques sont connectées à l'échantillon, chacune contient un circuit résonant et un amplificateur cryogénique. A température ambiante elles sont connectées à deux amplificateurs différentiels *NF SA-420F5*, ce qui résulte au final en deux canaux de sortie (ch0 et ch1), qui à leur tour sont branchés sur les entrées des différents instruments de mesure, y compris la carte rapide acquisition (aussi dessinée). Une grande partie du circuit (délimitée sur le schéma par une ligne de tirets) est située dans une canne frigorifique, les températures expérimentales possibles sont indiquées.

En revanche, le prix à payer pour les bénéfices remarquables que représente l'architecture de notre système expérimental est une fabrication des échantillons extrêmement laborieuse (voir Chapitre 5), mais aussi une calibration du système expérimental difficile et très subtile, due au fait que les amplificateurs cryogéniques employés ont un gain ajustable et apriori inconnu. Par conséquent, nous devions nous assurer d'abord que les quatre lignes de mesure de tension, que nous utilisons pour la détection du bruit, ont précisément le même gain chacune et ensuite déterminer ce gain. À la procédure de calibration est consacré le Chapitre 6 de ce manuscrit.

Présentation des résultats

Avant de passer à la mesure du bruit nous avons mené quelques mesures préliminaires. La conductance de notre échantillon en fonction de la tension de grille a été déterminée (voir Chapitre 7). A la base, notre échantillon est dopé en

trous, mais grâce aux grilles latérales nous pouvons largement dépasser le point de neutralité et doper notre échantillon en électrons. La comparaison des résultats de cette mesure avec les prédictions théoriques pour le régime balistique et celui diffusif nous permet de confirmer le caractère diffusif de notre échantillon (voir subsec. 7.1.1 et subsec. 7.1.2). Nous avons pu également estimer la mobilité, le libre parcours moyen, la densité d'impuretés, la longueur de cohérence et certains autres caractéristiques de notre échantillon, ce que nous décrivons dans la subsec. 7.1.3.

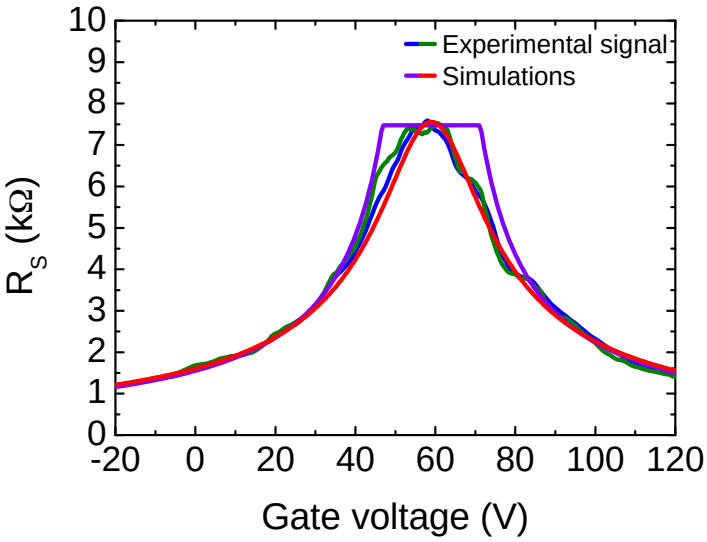

Figure 7: La résistance de la constriction en fonction de la tension de grille (vert et bleu). Les résultats d'ajustement des paramètres en considérant le modèle de transport diffusif décrit dans le texte (en violet) et une amélioration de ce modèle (en rouge).

En outre, nous avons sondé les propriété non-linéaires de notre échantillon par une mesure de conductance différentiel en fonction de la tension DC appliquée (voir sec. 7.2). Cela nous sert entre autre à relier lors de la mesure du bruit le courant DC que nous injectons dans l'échantillon et la tension qui se forme au bord de la constriction.

Une mesure dans le régime d'Effet Hall Quantique a été aussi effectuée, ce que nous décrivons dans le Chapitre 8. Celle-ci nous a notamment permis de connaître la densité de porteurs de charge en fonction de la tension de grille appliquée.

Finalement, nous avons procédé aux mesures du bruit. Les expériences précédentes nous ont servi de correctement interpréter nos mesures (voir sec. 9.1). A partir des résultats de celles-ci nous avons conclu, que la température des électrons dans la constriction dépasse la température du bain d'hélium. Nous avons tenté

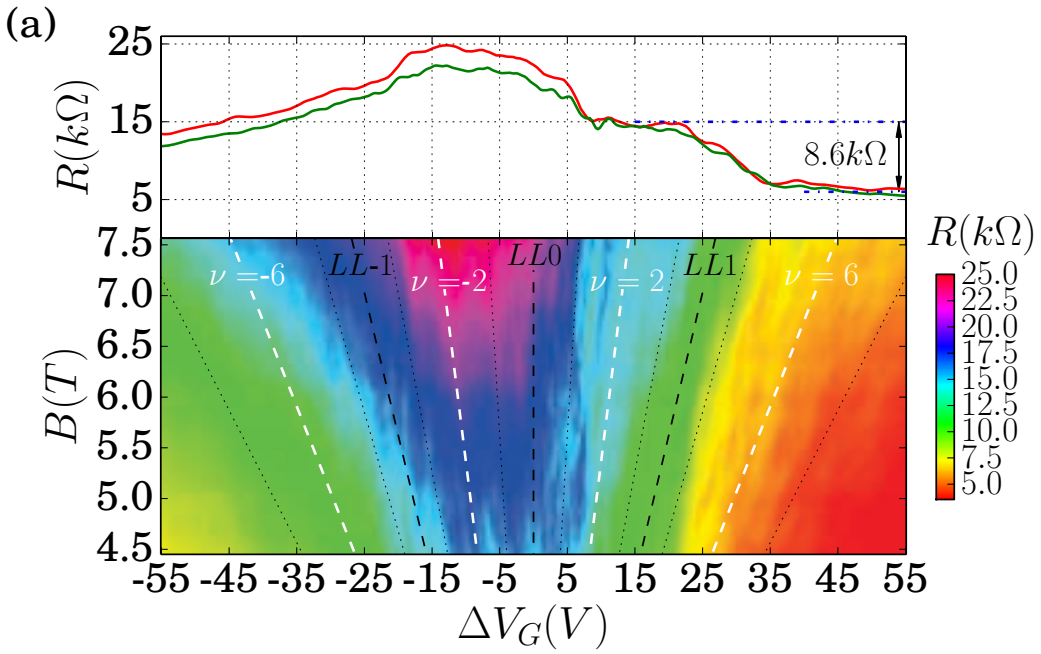

Figure 8: Un graphique couleur de la résistance mesurée avec la combinaison croisée des sondes de tension (voir le texte) en fonction de $\Delta V_{\mathrm{G}} = V_{\mathrm{G}} - V_{\mathrm{D}}$ et du champ magnétique B. Les courbes du haut montre la variation de la résistance au champ magnétique maximal $B = 7.565\,\mathrm{T}$ (courbe rouge) et de la résistance moyennée sur les lignes (radiales) de facteur de remplissage constant (courbe verte).

d'expliquer ce fait par la dissipation dans un des contacts d'injection du courant, qui s'est avéré de très haute résistance. Initialement le modèle de propagation de la chaleur par la diffusion électronique seule a été envisagé (conductance thermique donnée par la loi Wiedemann-Franz, voir subsec. 9.2.1). En utilisant ce modèle la dépendance de la température électronique du courant injecté a été déterminée pour l'utiliser dans le modèle du bruit (représenté à température constante par l'équation (13), voir subsec. 9.2.2). De là nous avons extrait le facteur de Fano et une raisonnable température (proche de celle du bain d'hélium) de l'étage où l'échantillon est thermiquement ancré. En revanche, le troisième paramètre ajustable extrait correspondait a une résistance du graphène plus faible que ce que nous avons estimé. Par conséquent, nous avons évoqué le mécanisme de refroidissement d'électrons par le couplage aux phonons décrit dans la subsec. 9.2.3. Nous avons calculé la distance après laquelle la température électronique sera peu différente de la température du réseau cristallin. Cette distance caractéristique est comparable à la distance entre la source de chaleur et la constriction, ce qui confirme l'efficacité de ce deuxième mécanisme.

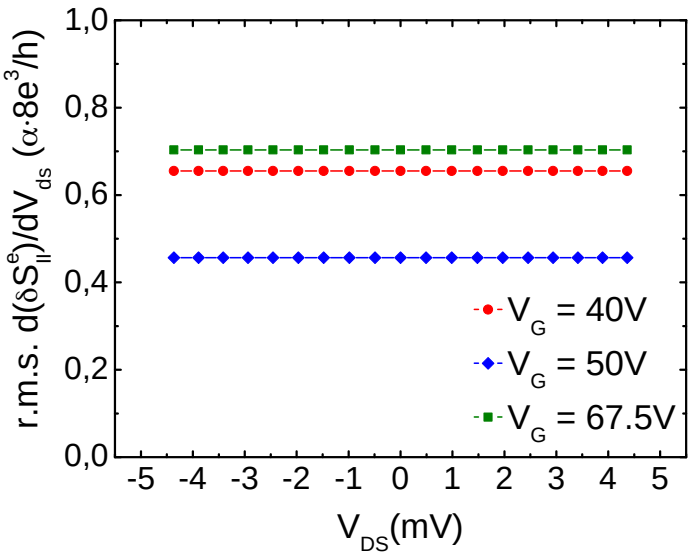

Figure 9: Étude des fluctuations de la puissance spectrale du bruit d'après la rélation (17). La valeur théorique correspond à 1 dans ces unités, $\alpha = \sqrt{\frac{46}{2835}}$.

Dans la sec. 9.3 nous nous sommes également intéressé aux irrégularités des courbes de bruit obtenues. Ces irrégularités sont les fluctuations de la puissance spectrale du bruit, qui ont le même origine que les fluctuations universelles de la conductance à savoir les interférences complexes entre les différents chemins de propagation dans un conducteur diffusif, qui dépendent de l'énergie de la particule injectée et vont ainsi impacter les coefficients de la transmission. Ce phénomène a été examiné de façon théorique dans des gazes bidimensionnels d'électrons conventionnels par de Jong and Beenakker, qui ont proposé l'expression suivante pour les fluctuations de la densité spectrale:

$$\text{r.m.s. } \delta S_{\text{II}} = 2e|V_{\text{ds}}|\frac{2e^2}{h}\sqrt{\frac{46}{2835}} \tag{17}$$

Applicabilité de cette formule dans le cas du graphène a été vérifiée. Nos résultats sont montés sur la fig. 9 et exposés de façon plus détallée dans la sec. 9.3. Nous concluons que (17) est en effet applicable à un coefficient numérique près.

Nos mesures nous fournissent la dépendance du facteur de Fano de la tension de grille représentée sur la fig. 10. La variation avec la tension de grille est faible, le facteur de Fano reste proche de ≈ 0.25. En revanche, les fluctuations du facteur de Fano sont bien prononcées.

Comme il a déjà été noté, notre échantillon est diffusif, le comportement du facteur de Fano n'est pas décrit par le modèle proposé par Tworzydlo et al. pour

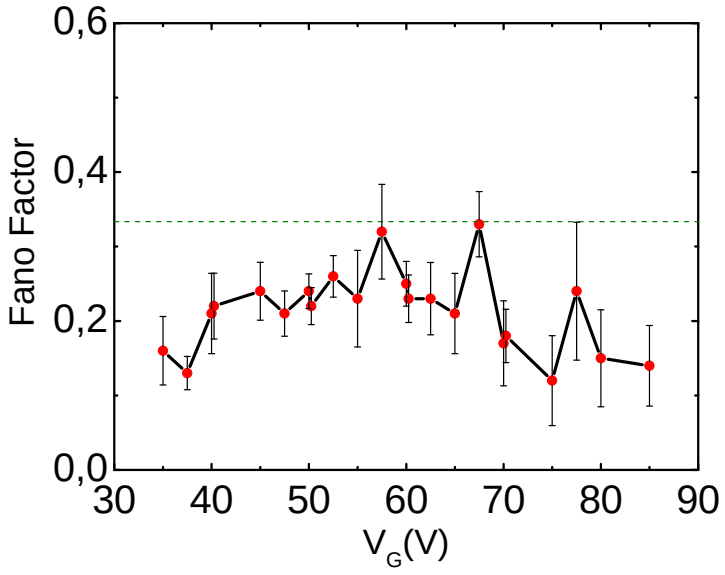

Figure 10: Facteur de Fano en fonction de la tension de grille, extrait des données expérimentales par l'ajustement des trois paramètres, la ligne horizontale en pointillés correspond à la valeur 1/3. Le point de Dirac se trouve entre 58 et 61 V.

un ruban idéal (balistique) de graphène. En revanche, nos résultats présentent une forte similitude avec ceux de Danneau et al. pour leur échantillon diffusif (échantillon E). Quant à DiCarlo et al., il ont mesuré des valeurs ≈ 0.35, de 45% supérieur par rapport aux nôtres et le facteur de Fano dans leur mesure ne varie pas du tout avec la tension de grille. Nous attribuons cette disparité entre les deux résultats aux différences dans le degré du désordre entre deux échantillons. L'accord avec les résultats théoriques, présentés au début de ce résumé (voir les travaux de San-Jose et al., Lewenkopf et al., Logoteta et al.) est également bon. Notamment, le pic au point de neutralité, prédit par Lewenkopf et al. et par Logoteta et al. est clairement visible sur la fig. 10. Une analyse plus conséquent de nos résultat se trouve dans la sec. 9.4.

Introduction

Ten years after its discovery, graphene remains the hottest topic of the condensed matter physics and the materials science. This unique, truly two-dimensional carbon based crystal "costed" their inventors A. Geim and K. Novoselov a Nobel Prize[?]. Today, new, more "industrializable" deposition techniques are ready to replace the *micromechanical cleavage*, once allowed to isolate the first graphene layer[114]. These technique (CVD, SiC sublimation, MBE), already employed in the laboratories, can in a not so far future bring graphene into the everyday life devices.

So, let us see, what graphene is exactly about. The carbon atoms in graphene are arranged in a *hexagonal* or *honeycomb* lattice as shown in fig. 11.a. Particular symmetries of this lattice together with the confinement in two-dimensions result in what became the hallmark of graphene: to some extent, electrons in graphene are considered to have *zero effective mass* and obey *Dirac Equation*, described by matrix Hamiltonian

$$\mathcal{H}_{\mathbf{q}} = \hbar v_{\mathrm{F}} \begin{pmatrix} 0 & q_x - \imath q_y \\ q_x - \imath q_y & 0 \end{pmatrix} \tag{18}$$

where $\mathbf{q}$ is the wave vector with respect to one of two very singular points of graphene Brillouin Zone, called *Dirac points* and denoted K and K'. This equation leads to a linear dispersion relation around each of these two points, known as *Dirac cones* or *valleys*, shown in fig. 11.a, yielding additional two-fold valley degeneracy. The above-mentioned facts determine most of the singular physical properties of this unique material. But, why exactly is this material so fascinating?

For the fundamental scientists, graphene appeared attractive promptly after revealing its potential to turn into a solid-state test bed for the *Quantum Electrodynamics* (QED). Low-energy electronic excitations in graphene, being massless chiral Dirac fermions with an effective speed of light $\approx c/300$[115], hence mimic their QED counterparts (like neutrino for instance) and could probably allow to observe in an nanometre-size 2D crystal certain High Energy Physics phenomena, for which usually atom-smasher-scale facilities are required. In particular, some relativistic effects, theoretically predicted, but experimentally not yet confirmed, such as Klein paradox[86] (transmission of particles through a classically forbidden

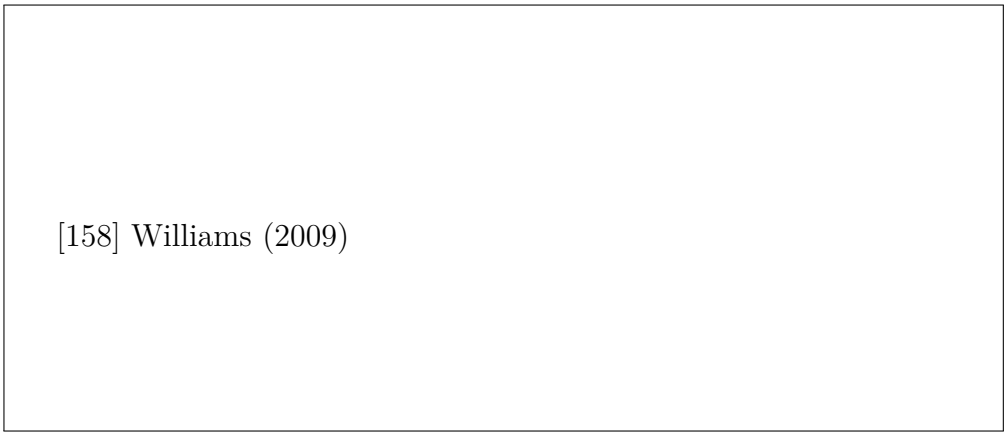

Figure 11: (a) Graphene honeycomb lattice with two sublattices A and B highlighted with different colours. Interatomic distance $a = 0.142\,\mathrm{nm}$. (b) Dirac cone. From [158]

region with probability close to one) or Zitterbewegung[133] (jittery motion of a particle, due to interference between components of its wavefunction belonging to positive (electron) and negative (positron) energy states), are likely to manifest themselves in graphene[82, 81].

On the other hand, several singularities of graphene physics present an interest for a condensed matter physicists, regardless of any QED considerations. To name only few, unconventional Quantum Hall Effect, observed even at room temperature thanks to the the large cyclotron energies of electrons in graphene[116], Quantum Hall Isospin Ferromagnetism, due to its fourfold spin–valley degeneracy and the strong Coulomb interactions[166] or 2π Berry phase-related weak anti-localization effect enhancing the classical Drude conductivity[161]. In addition, pronounced ambipolar electric field effect and predicted high room-temperature mobilities even up to $200\,000\,\mathrm{cm^2\,V^{-1}\,s^{-1}}$[27] (such mobilities, but at 5 K and in suspended samples were reported by Bolotin et al.) make of graphene a very appealing material for experimentalist, but also for microelectronics engineers. Graphene-based high-speed electronics is among the most promising applications of this material: implementation of a room-temperature ballistic transistor, operating at THz frequencies would be a ground breaking achievement of the microelectronics. Recently reported 427 GHz graphene transistor[31] and new graphene-adapted logic circuits architecture[98] together with latest numerical results[174], make believe that the idea of large-scale manufacturing of such devices is not just hypothetical. Another, more trivial application of graphene in the field of microelectronics are flexible transparent electrodes.

Microelectronics is not the only sphere of graphene application. Other poten-



Figure 12: Fermi energy dependence of the conductivity σ (a) and the Fano factor $\mathfrak{F}$ (b) at fixed aspect ratio $W/L = 5$. The conductivity minimum at the Dirac point corresponds to maximal Fano factor. From [148].

tial application is the photovoltaics. According to the recent study by Tielrooij et al., in graphene the internal quantum efficiency is enhanced through "hot-carrier multiplication" cascade-type process. In a nutshell, photoexcited carriers transfer their excess energy to other charge carriers, creating additional electron-hole pairs, instead of heating the lattice as it is often the case in other materials. In addition, by placing an appropriate plasmonic nanostructures near graphene p-n junction, the efficiency can be further enhanced by order of magnitude[46]. Besides, graphene is a very hopeful candidate for the development of Terahertz domain detectors[79, 154], which is a challenging task of today's photonics. Finally, it is also worth citing several other applications as chemical and bio sensors[134], nanoelectromechanical devices[69], data storage devices[77], supercapacitors[168, 118] and very efficient membranes[113], the list is not exhaustive.

In the present work we approach graphene from the position of the mesoscopic physics. This field of condensed matter physics, emerged in early 80s, study low-dimensional systems of micrometer size in which quantum effects such as fluctuations and interferences are observable (very low temperatures are also generally required). It is obvious, that graphene, being a standalone two-dimensional system, presents an extraordinary opportunity for mesoscopic physicists. Most of emblematic mesoscopic physics phenomena (e.g. Integer and Fractional Quantum Hall effects, Shubnikov–de Haas and Aharonov-Bohm effects and many others, see refs. [173, 41, 166, 164, 145, 160, 45, 147, 29, 10, 122, 162, 89]) were tested in this system.

More specific to graphene problem of minimal conductivity and Fano factor[2] at Dirac point was addressed by Tworzydlo et al. in the case of short and large ideal (ballistic) graphene nano-ribbons. Minimal conductivity is an interesting problem, since on one hand graphene is a gapless semi-metal and isolator state is not attainable in it. On the other hand, precisely at the Dirac point the carrier density is zero, so one would expect the conductivity going to zero as well. The conclusions of Tworzydlo et al. were that minimum of conductivity is indeed reached at the Dirac point, yet its value is not zero but rather $\frac{4e^2}{\pi h}$. As for the Fano factor, it was shown that in contrast to what happens in conventional ballistic systems, at the Dirac point this quantity is not zero but equals 1/3 (same value is observed in diffusive systems), tending to zero only far from it. Both results are shown in fig. 12.

Two experimentalists groups tried to challenge these theoretical predictions. First group from Harvard University measured shot noise in graphene samples of several aspect ratios and lengths as well as in a graphene p-n junction, see ref. [42]. However, these samples turned out to be diffusive, i.e. having mean free path ($\approx 40\,\mathrm{nm}$) much shorter than their length. As a consequence, the observed behaviour of Fano factor with injection energy was found to be the usual one for diffusive systems: it took energy independent value, close to 1/3 (≈ 0.35). While minimum of conductivity was found to significantly overcome the theoretical $\frac{4e^2}{\pi h}$. Second group from Helsinki University (see ref. [35]) have also conducted their study over an important set of samples and succeeded to measure in one of these samples the minimal conductivity close to $\frac{4e^2}{\pi h}$ as well as the predicted Fano factor variation (although, the quantitative agreement was not reached). As for the other samples they measured, the results are less obvious to interpret. Hence, based on these two works (some of the results are shown in fig. 13), no indisputable conclusion about the validity of the theory in ref. [148] can be drawn and a third study in this direction could shine light on this question.

In the Nanoelectronics group of SPEC (CEA Saclay) where my PhD work took place under direction of professor D. C. Glattli, all type of noise measurements is the key skill. Furthermore, a project of Terahertz detector based on the measurement of Photon-Assisted shot noise in a graphene sample, placed in an antenna is taking off and an experience in noise measurements in graphene was necessary. Accordingly, a real necessity of an extra experiment to once again test the above-mentioned theoretical result together with the availability in the group of the recognized competences to realize such an experiment and finally interest in this topic in view of applications for Terahertz detection are motivated the present work.

On the other hand, for this same reason, i.e. because the midterm goal of this

[2] quantity characterizing current fluctuations

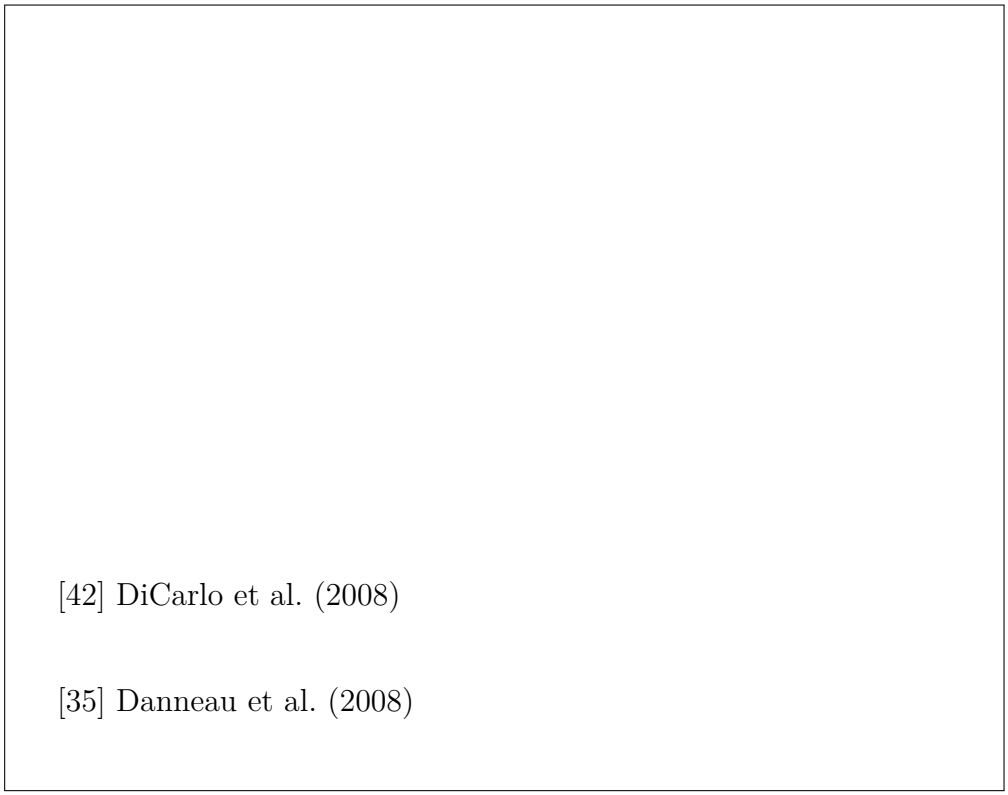

Figure 13: Previous Results. Measurement by DiCarlo et al. of resistance (a) and Fano factor (b). From [42]. (c) and (d) — measurement of the same quantities by Danneau et al., from [35]

project is precisely to attempt to settle up the disagreement between two already performed experiments, the project is particularly challenging. Namely, this meant that it was necessary to conceive the samples and the system for noise measurements, taking into account all limitations of above-mentioned studies and, above all, manage to attain better experimental conditions and thus obtain sufficiently reliable data to conclude about the results of these studies.

The realization of this project thus dictated the following tasks to be accomplished:

- Design and fabricate graphene-based devices for the experiment
- Build up the experimental setup
- Tune, calibrate and test the measurement system
- Investigate the conductance and Fano factor in graphene

To fulfil the above-mentioned requirements it was decided to use pristine exfoliated graphene samples and fabricate an experimental device without the back-gate (to avoid the capacitive shunt), replacing it by the side-gates. It would also be perfect to suspend the graphene layer (since it is the best way to reach high mobilities), but this was not accomplished due to the technical difficulties. Measurement approach was also carefully thought over: four-point and cross-correlation techniques were employed, cryogenic low-noise amplifiers together with band-pass filters were used for noise detection.

Hence, conductance and Fano factor were successfully investigated in a graphene sample being in the diffusive regime. Technical difficulties together with time constraints prevented us from realizing the same measurements in a ballistic sample, but the obtained results proved the attainability of the ballistic limit in our samples as well as the conformity of the characteristics of our experimental setup to the requirements of the prospected goals.

The results of my work are described in the present manuscript. It is organised in the following way: the first part provides the brief insight into both graphene and mesoscopic physics. As for the second part, the details concerning our experimental approach are clarified in one chapter, while another one is devoted to the device fabrication. In the last part our own results are presented.

Part I

Overview of Graphene Physics and Mesoscopic Transport

Chapter 1

Physical Properties of Graphene

1.1 Crystal Structure of Graphene

Graphene is best known under its graphite form which is simply a stack of graphene planes, held by van der Waals forces and is the most widespread of all carbon allotropes. A single carbon atom has a following electronic structure: $1s^2 2s^2 2p^2$. However, it turns out that, while forming a covalent bonds with other atoms, it is often energetically favourable to promote one electron from $2s$ orbital to $2p$ orbital, as a resulting bond energy will be lower in that case. Moreover, one $2s$ and two $2p$ orbitals (p_x and p_y for example) can hybridize into three sp^2 orbitals with 120° angle between them (see: fig. 1.1.a) as it occurs in graphene. These hybridized orbitals will form strong covalent in-plane σ bonds between carbon atoms, that will therefore condense in a hexagonal (sometimes also called *honeycomb*) crystal lattice with interatomic distance a of 0.142 nm. The remaining p_z orbitals point out of plane, forming weaker π bonds. It is the π electrons, delocalized over the whole crystal, that give rise to the valence band states.

Crystalline solid is a type of solid in which atoms are arranged with certain periodicity in a way that will entail several translational and rotational symmetries. The common method of representing these symmetries is *Bravais lattice*, which is an infinite lattice generated by all such vectors, that will leave the crystal, if considered as infinite, invariant under translation by any of these vectors. It usually writes down (in two dimensions) as:

$$\mathbf{R}_{\boldsymbol{\ell}} = l_1 \mathbf{a}_1 + l_2 \mathbf{a}_2 \tag{1.1}$$

with $\boldsymbol{\ell}$ components l_1 and l_2 being integer, and $\mathbf{a}_1$ and $\mathbf{a}_2$ known as primitive vectors of Bravais lattice or basis vectors. These are the smallest possible translations which leave the crystal invariant. Crystal symmetries will play an important role in the band structure calculations, presented in the next section.

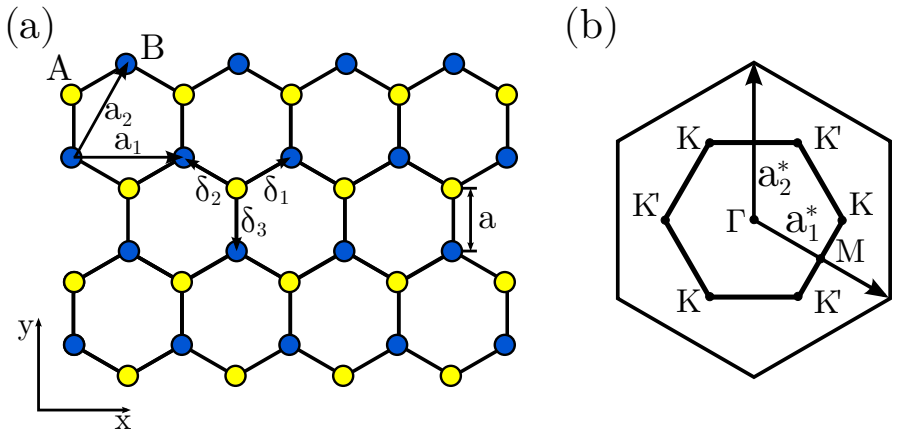

Figure 1.1: (a) Graphene honeycomb lattice with two sublattices highlighted with different colours. Interatomic distance $a = 0.142\,\text{nm}$. Also shown primitive vectors of Bravais lattice $\mathbf{a}_1$ and $\mathbf{a}_2$ as well as vectors $\boldsymbol{\delta}_1$, $\boldsymbol{\delta}_2$ and $\boldsymbol{\delta}_3$ linking any atom from A sublattice to its three next neighbours. (b) First Brillouin zone (inner hexagon) centred at the point noted Γ, while its corners are noted K and K' (only two are inequivalent). Reciprocal lattice basis vectors $\mathbf{a}_1^*$ and $\mathbf{a}_2^*$ are also shown.

Besides, honeycomb lattice is not a Bravais lattice and the corresponding Bravais lattice will be a triangular[1]one with 2 atoms per unit cell, denoted A and B, yielding two sublattices A and B, as represented in fig. 1.1.a. In that case the Bravais lattice basis vectors are:

$$\mathbf{a}_1 = \sqrt{3}a\mathbf{e}_x \qquad \text{and} \qquad \mathbf{a}_2 = \frac{\sqrt{3}a}{2}\left(\mathbf{e}_x + \sqrt{3}\mathbf{e}_y\right). \tag{1.2}$$

The following vectors link any atom from A sublattice to its next neighbours, which are necessarily atoms from B sublattice (for any atom from B sublattice it suffices to change the sign):

$$\boldsymbol{\delta}_1 = \frac{a}{2}\left(\sqrt{3}\mathbf{e}_x + \mathbf{e}_x\right), \qquad \boldsymbol{\delta}_2 = \frac{a}{2}\left(-\sqrt{3}\mathbf{e}_x + \mathbf{e}_x\right), \qquad \boldsymbol{\delta}_3 = -a\mathbf{e}_y. \tag{1.3}$$

The equivalent of Bravais lattice in the reciprocal space ($\mathbf{k}$-space) is called *Reciprocal Lattice* and it is no less important in the band structure calculations. As Bravais lattice it is generated in two-dimensional reciprocal space by an ensemble of such vectors:

$$\mathbf{K}_{\boldsymbol{\lambda}} = \lambda_1\mathbf{a}_1^* + \lambda_2\mathbf{a}_2^* \tag{1.4}$$

[1]In most literature (see [84] for exemple) it is this lattice, that is referred as honeycomb, but we will use the above-mentioned denomination to avoid confusion.

that a plane wave of any of these wave vectors $\mathbf{K}_{\boldsymbol{\lambda}}$ will have the same periodicity as the initial Bravais lattice. This appears in the following conditions: $e^{i\mathbf{K}_{\boldsymbol{\lambda}}\mathbf{R}_{\boldsymbol{\ell}}} = 1$ for any $\mathbf{R}_{\boldsymbol{\ell}}$, which constrains λ_i to be integers and gives the following relation for reciprocal lattice basis vectors $\mathbf{a}_j^*$:

$$\mathbf{a}_i \cdot \mathbf{a}_j^* = 2\pi\delta_{ij}$$

Another consequence is that two waves of wave vectors that differ from each other by any reciprocal lattice vector $\mathbf{K}_{\boldsymbol{\lambda}}$ are equivalent. Thus all quantum states of the system are described by the wave vectors inside the *First Brillouin Zone* (FBZ) — a primitive cell consisting of all points of reciprocal space, that are nearer to the given site of the reciprocal lattice than to all other sites of the lattice.

The reciprocal lattice of graphene crystal is spanned by the following vectors:

$$\mathbf{a}_1^* = \frac{2\pi}{\sqrt{3}a}\left(\mathbf{e}_x - \frac{\mathbf{e}_y}{\sqrt{3}}\right) \qquad \text{and} \qquad \mathbf{a}_2^* = \frac{4\pi}{3a}\mathbf{e}_y. \tag{1.5}$$

The FBZ is represented in fig. 1.1.b. As we will see in the next section, the low-energy excitations wave vectors belong to the vicinity of the two particular points K and K', situated on the corners of FBZ and represented by the vectors:

$$\pm\mathbf{K} = \pm\frac{4\pi}{3\sqrt{3}a}\mathbf{e}_x. \tag{1.6}$$

1.2 Graphene Band Structure

In this section we will discuss the electronic properties of graphene, obtained within the tight-binding approximation. As it was mentioned previously it is π electrons, that constitute the valence band, therefore the discussion will be reduced to these states only. In particular, we will consider low-energy excitations, as they are relevant for instance for mesoscopic transport description.

1.2.1 Basic Principles

Tight-binding model is one of the most basic approaches to electronic band structure calculation, that carries a certain number of approximations. It is however sufficiently powerful to describe in the case of graphene the most prominent aspects of its electronic properties.

This approach considers a solid as a collection of almost isolated, only very few interacting atoms. In such a vision it is rather natural to take the orbital states of a single isolated atom as a basis for construction of the electronic states of the solid. The simplest approximation is to consider only highest occupied (valence)

level of the atom E_v and its wavefunction $\chi_v(\mathbf{r})$, assuming that in the solid the energies $E_\mathbf{k}$ of the eigenstates $\varphi_\mathbf{k}(\mathbf{r})$ are situated in the very vicinity of E_v, but far from E_{v-1} and E_e — first excited state.

Consider a single particle Hamiltonian for the $\mathbf{R}_\ell$ lattice site:

$$H_\ell = \frac{\mathbf{p}_\ell^2}{2m_0} + \sum_{\substack{m_1=1 \\ m_2=1}}^{N_1,N_2} V_{\text{at}}\left(\mathbf{r}_\ell - \mathbf{R}_\mathbf{m}\right) \tag{1.7}$$

with $N_1 \times N_2$ — total number of atoms in the crystal. In some cases, we will also use another representation of the single particle Hamiltonian in which it is decomposed in sum of a single atomic Hamiltonian $H_\ell^{\text{at}} = \frac{\mathbf{p}_\ell^2}{2m_0} + V_{\text{at}}\left(\mathbf{r}_\ell - \mathbf{R}_\ell\right)$ and the residual potential term $\Delta V = H_\ell - H_\ell^{\text{at}}$.

It is then reasonable to write trial wavefunction for these eigenstates as a *Linear Combination of Atomic Orbitals*[2]:

$$\varphi_\mathbf{k}(\mathbf{r}) = \frac{1}{\sqrt{N_1 N_2}} \sum_\mathbf{m} a_{\mathbf{k},\mathbf{m}} \chi_v\left(\mathbf{r} - \mathbf{R}_\mathbf{m}\right). \tag{1.8}$$

As it was discussed in the previous section, crystal lattice exhibits several translational symmetries. Obviously, the trial wavefunctions have to respect these symmetries. These considerations are formalized by *Bloch's Theorem*. This very important theorem of the solid state physics exploits the following facts. Because a translation by any Bravais lattice vector $\mathbf{R}_\ell$ will leave the physical problem invariant, the corresponding translational operator $\mathcal{T}_{\mathbf{R}_\ell}$ should commute with the Hamiltonian, $\left[\mathcal{T}_{\mathbf{R}_\ell}, H\right] = 0$. Hence the eigenstates of latter are necessarily also eigenstates of $\mathcal{T}_{\mathbf{R}_\ell}$. In particular, Bloch's Theorem stipulates that these eigenstates are so called Bloch waves, functions that can be written as a product of a plane wave and a periodic function of the same periodicity as the Bravais lattice. One can easily check, that the following trial wavefunction fulfills the above-mentioned requirement, i.e. it is an eigenstate of the translation operator $\mathcal{T}_{\mathbf{R}_\ell}$ and moreover, it can be decomposed in a product of a plane wave and a periodic function:

$$\varphi_\mathbf{k}(\mathbf{r}) = \frac{1}{\sqrt{N_1 N_2}} \sum_\mathbf{m} e^{\imath \mathbf{k}\mathbf{R}_\mathbf{m}} \chi_v\left(\mathbf{r} - \mathbf{R}_\mathbf{m}\right). \tag{1.9}$$

So the electronic band structure calculations in the next section will be based on these trial wavefunctions.

[2]The sum $\sum_\mathbf{m}$ is a short notation for $\sum_{m_1,m_2}^{N_1,N_2}$.

1.2.2 Band Structure Calculations

We now apply the above-presented model to the case of the graphene honeycomb lattice. As it was already mentioned, lattice symmetry is reflected by Bravais lattice, while honeycomb lattice can only be generated by a Bravais lattice with two atoms per unit cell, or in other words by two sublattices each having the same translational symmetry as the initial lattice. Thus a trial wavefunction, that exhibits the lattice symmetry should in general be described by a linear combination of Bloch waves of two sublattices:

$$\psi_{\mathbf{k}}(\mathbf{r}) = a_{\mathbf{k}}\varphi^A_{\mathbf{k}}(\mathbf{r}) + b_{\mathbf{k}}\varphi^B_{\mathbf{k}}(\mathbf{r} - \boldsymbol{\delta}_{\mathrm{AB}}) \tag{1.10}$$

Here, we have chosen the A sublattice sites to coincide with the sites of Bravais lattice, whereas the B sublattice sites are shifted by $\boldsymbol{\delta}_{\mathrm{AB}}$ with respect to them, hence this component appearance in the second function's argument. Both functions $\varphi^A_{\mathbf{k}}(\mathbf{r})$ and $\varphi^B_{\mathbf{k}}(\mathbf{r})$ are given by (1.9), as the atoms of two sublattices are identical, the A and B indices are put here for pedagogical reason, we will omit them from now on.

We may now search the solutions of the Schrödinger equation

$$H\psi_{\mathbf{k}} = \epsilon_{\mathbf{k}}\psi_{\mathbf{k}}. \tag{1.11}$$

with the Hamiltonian H of the form (1.7), but where the ions of both sublattices contribute to the potential energy. Given that there are two electrons per lattice site (one from each atom A and B), multiplication of eq. 1.11 by $\psi^\dagger_{\mathbf{k}}$ on the left leads to a 2×2 matrices secular equation:

$$\det\left[\mathcal{H}_{\mathbf{k}} - \epsilon_{\mathbf{k}}\mathcal{S}_{\mathbf{k}}\right] = 0 \tag{1.12}$$

with

$$\mathcal{H}^{ij}_{\mathbf{k}} = \int \mathrm{d}^2\mathbf{r}\ \varphi^\dagger_{\mathbf{k}}(\mathbf{r})H\varphi_{\mathbf{k}}(\mathbf{r} - \boldsymbol{\delta}^{ij}) \quad \text{and} \quad \mathcal{S}^{ij}_{\mathbf{k}} = \int \mathrm{d}^2\mathbf{r}\ \varphi^\dagger_{\mathbf{k}}(\mathbf{r})\varphi_{\mathbf{k}}(\mathbf{r} - \boldsymbol{\delta}^{ij}), \tag{1.13}$$

where $\boldsymbol{\delta} = \begin{pmatrix} 0 & \boldsymbol{\delta}_{\mathrm{AB}} \\ -\boldsymbol{\delta}_{\mathrm{AB}} & 0 \end{pmatrix}$ and $\mathcal{H}$ and $\mathcal{S}$ are the Hamiltonian and *overlap* matrices respectively.

In the following, in order to simplify the calculations, we will do two approximations. First, we will neglect the overlaps between atomic orbitals, meaning that $\mathcal{S}$ is just the identity matrix, intention which is quite reasonable, since p_z orbitals have rather limited spatial extension in the xy plane as compared to interatomic distance a. Second, since tunnelling probability diminishes exponentially with the distance, we will restrain the hopping integrals to the nearest-neighbours, meaning that

$$\int \mathrm{d}^2\mathbf{r}\ \chi^\dagger(\mathbf{r} - \mathbf{R}_\ell)\Delta V\chi(\mathbf{r} \pm \boldsymbol{\delta}_{\mathrm{AB}} - \mathbf{R}_\mathbf{m}) \not\approx 0 \tag{1.14}$$

if and only if $\mathbf{R}_{\boldsymbol{\ell}} \pm \boldsymbol{\delta}_{\mathrm{AB}} - \mathbf{R}_{\mathbf{m}} = \boldsymbol{\delta}_1, \boldsymbol{\delta}_2$ or $\boldsymbol{\delta}_3$ from (1.3). Moreover, from symmetry considerations the value of these integrals must be $\boldsymbol{\ell}$ and $\mathbf{m}$ independent.[3] This value is called *hopping amplitude* and we denote it as t:

$$t \equiv \int \mathrm{d}^2\mathbf{r}\ \chi^\dagger(\mathbf{r})\Delta V \chi(\mathbf{r} \pm \boldsymbol{\delta}_{\mathrm{AB}}). \tag{1.15}$$

We also introduce for convenience the following constant:

$$t_0 \equiv \int \mathrm{d}^2\mathbf{r}\ \chi^\dagger(\mathbf{r})\Delta V \chi(\mathbf{r}). \tag{1.16}$$

As it can be seen from fig. 1.1.a, any A atom has three next neighbours: B_1, B_2, B_3, though only one B atom is described by the same Bravais lattice vector $\mathbf{R}_{\boldsymbol{\ell}}$ as the A atom. The other two B atoms correspond to the lattice vector shifted, in notations accepted in fig. 1.1.a, by vectors $\mathbf{a}_2$ and $\mathbf{a}_3 \equiv \mathbf{a}_2 - \mathbf{a}_1$. Therefore, they contribute a phase factors $\exp(\imath\mathbf{k}\cdot\mathbf{a}_2)$ and $\exp(\imath\mathbf{k}\cdot\mathbf{a}_3)$ respectively. So the contribution from a single A atom to the off-diagonal upper (lower) Hamiltonian matrix element will be[4] $t\gamma_{\mathbf{k}}^{(\dagger)} \big/ N_1 N_2$, where we have defined the sum of next neighbours phase factors:

$$\gamma_{\mathbf{k}} \equiv 1 + e^{-\imath\mathbf{k}\cdot\mathbf{a}_2} + e^{-\imath\mathbf{k}\cdot\mathbf{a}_3} \tag{1.17}$$

Finally, denoting as ε_0 the eigenvalue of the atomic Hamiltonian H^{at}, corresponding to $\chi(\mathbf{r})$ orbital, we obtain the secular equation in the following form:

$$\det \begin{bmatrix} \varepsilon_0 + t_0 - \varepsilon_{\mathbf{k}} & t\cdot\gamma_{\mathbf{k}} \\ t\cdot\gamma_{\mathbf{k}}^\dagger & \varepsilon_0 + t_0 - \varepsilon_{\mathbf{k}} \end{bmatrix} = 0 \tag{1.18}$$

with two solutions:

$$\varepsilon_{\mathbf{k}}^{\pm} = \pm t|\gamma_{\mathbf{k}}| = \pm t\sqrt{3 + 2\sum_{i=1}^{3}\cos(\mathbf{k}\cdot\mathbf{a}_i)} \tag{1.19}$$

and we have omitted $\varepsilon_0 + t_0$ constant, the energy band shift, introduced by it being physically irrelevant. The energy dispersion, calculated in the approximation

[3] To verify, whether these approximations are justified, one can perform numerical calculations of the corrections from the further extension of the hopping integrals to the next-nearest-neighbours: t_{nnn}, as well as of the corrections from nearest-neighbours orbitals overlap: s_{nn}. Such calculations, done in [126] as well as tight-binding fit to cyclotron resonance experiments in [39] show that $t_{\mathrm{nnn}} - s_{\mathrm{nn}}t \simeq 0.1t$ (with $t \approx -3\,\mathrm{eV}$), approving the admitted approximations.

[4] $N_1 \times N_2$, being the number of A or B atom, and not the total number of atoms as in the previous section.



Figure 1.2: (a) Graphene energy dispersion obtained within the tight-binding approximation neglecting the next-nearest-neighbours hopping (i.e. $t_{\text{nnn}} = 0$). Right: Dirac cone — energy band near the K and K' (Dirac) points. From [158].(b) Density of states per unit cell as a function of energy (in units of t) also in the assumption of $t_{\text{nnn}} = 0$. From [26].

that takes into account the nearest-neighbour hopping only ($t_{\text{nnn}} = 0$) is plotted in fig. 1.2.a. One distinguishes two bands, that touches each other in several points (though only two of them lay in FBZ and are inequivalent). Lower band called *valence band* and upper — *conductance band* — correspond to $\varepsilon^-_{\mathbf{k}}$ and $\varepsilon^+_{\mathbf{k}}$ respectively. Since there are as many states as electrons, furnished by carbon atoms, but each state can be occupied by two electrons (with a spin-up and a spin-down) the valence band is completely filled, whereas conductance band is empty. This means, that the Fermi layer passes through the points of contact of two bands, which are called Dirac points for reasons, that will become clear in the next section. From (1.19) it is rather obvious that they correspond to wave-vectors $\mathbf{k}^D$, which satisfy:

$$\varepsilon^+_{\mathbf{k}^D} = \varepsilon^-_{\mathbf{k}^D} = 0 \tag{1.20}$$

relation, that is itself satisfied only if $\mathbf{Re}\gamma_{\mathbf{k}^D} = \mathbf{Im}\gamma_{\mathbf{k}^D} = 0$, that leads to solutions:

$$\mathbf{k}^D = \pm\mathbf{K} = \pm\frac{4\pi}{3\sqrt{3}a}\mathbf{e}_x \tag{1.21}$$

in which we recognize two crystallographic points K and K' situated on the FBZ corners, already mentioned in sec. 1.1. Note that due to the time-reversal symmetry, ($\varepsilon_{-\mathbf{k}} = \varepsilon_{\mathbf{k}}$), there are necessarily two inequivalent Dirac points. Therefore, zero-energy states, and by continuity all low-energy states will be doubly degenerate, This degeneracy is referred as *valley degeneracy*. In the following we will often restrain the discussion to one of the valleys only, but the extension of the results to the remaining valley is straight-forward.

1.2.3 Low-Energy Excitations

For the following discussion it can be useful to rewrite the problem in slightly different notations. We first introduce effective tight-binding Hamiltonian:

$$\mathcal{H}_{\mathbf{k}} \equiv t \begin{pmatrix} 0 & \gamma_{\mathbf{k}}^{\dagger} \\ \gamma_{\mathbf{k}} & 0 \end{pmatrix} \tag{1.22}$$

The eigenstates of this Hamiltonian are 2-components vectors, or *spinors*:

$$\Psi_{\mathbf{k}}^{\pm} = \begin{pmatrix} a_{\mathbf{k}}^{\pm} \\ b_{\mathbf{k}}^{\pm} \end{pmatrix} \tag{1.23}$$

The two components $a_{\mathbf{k}}^{\pm}$ and $b_{\mathbf{k}}^{\pm}$ of these spinors coincide with the probability amplitudes of the electron to be found on A or B sublattices respectively (the $\pm$ indicator stands for valence and conductance bands). These eigenstates are easily derivable, taking into consideration the above-found eigenvalues of (1.22):

$$\Psi_{\mathbf{k}}^{\pm} = \frac{1}{\sqrt{2}} \begin{pmatrix} 1 \\ \pm e^{\imath\phi_{\mathbf{k}}} \end{pmatrix}, \tag{1.24}$$

where we have defined the angle

$$\phi_{\mathbf{k}} = \arctan\left(\frac{\mathbf{Im}\gamma_{\mathbf{k}}}{\mathbf{Re}\gamma_{\mathbf{k}}}\right) \tag{1.25}$$

As expected, since both sublattices are composed of the identical atoms, the eigenstates correspond to an equal probability for an electron to be found on A and B sublattices.

We now consider the low energy excitations of the system, that we define as all states with characteristic energy with respect to the Fermi level being much smaller than the band width. Its wave-vectors therefore lay in the vicinity of the Dirac points, so one can expand the dispersion relation around $\mathbf{K}$ ($-\mathbf{K}$ case reasonings are analogous) as following: let $\mathbf{k} = \mathbf{K} + \mathbf{q}$ and we take $\mathbf{q}$, that satisfy $|\mathbf{q}| \ll |\mathbf{K}| \sim 1/a$, so finally the expansion small parameter will be $|\mathbf{q}|a \ll 1$ and we will limit it to the first order in $|\mathbf{q}|a$. The only $\mathbf{k}$ dependent parameter of the effective Hamiltonian and energy dispersion being $\gamma_{\mathbf{k}}$ we first expand it:

$$\begin{aligned} \widetilde{\gamma}_{\mathbf{q}} \equiv \gamma_{\mathbf{k}=\mathbf{K}+\mathbf{q}} =& 1 + e^{\imath\mathbf{K}\cdot\mathbf{a}_2} e^{\imath\mathbf{q}\cdot\mathbf{a}_2} + e^{\imath\mathbf{K}\cdot\mathbf{a}_3} e^{\imath\mathbf{q}\cdot\mathbf{a}_3} \\ \simeq& 1 + e^{\imath 2\pi/3}\left[1 + \imath\mathbf{q}\cdot\mathbf{a}_2 + \mathcal{O}(|\mathbf{q}|^2 a^2)\right] \\ &+ e^{\imath 2\pi/3}\left[1 + \imath\mathbf{q}\cdot\mathbf{a}_3 + \mathcal{O}(|\mathbf{q}|^2 a^2)\right] \\ =& -\frac{3a}{2}(q_x + \imath q_y) \end{aligned} \tag{1.26}$$

here we also took advantage of the fact, that by definition $\widetilde{\gamma}_0 \equiv \gamma_{\mathbf{K}} = 0$, removing all $\mathbf{q}$ independent terms. As a consequence, the linearised effective low-energy Hamiltonian will be given by:

$$\widetilde{\mathcal{H}}_{\mathbf{q}} = \hbar v_{\mathrm{F}} \mathbf{q} \boldsymbol{\sigma} \tag{1.27}$$

with v_{F} — *Fermi velocity* defined as:

$$v_{\mathrm{F}} = -\frac{3ta}{2\hbar} \tag{1.28}$$

and $\boldsymbol{\sigma} \equiv (\sigma^x, \sigma^y)$ — Pauli matrices vector ($\boldsymbol{\sigma}' \equiv (\sigma^x, -\sigma^y)$ in the case of K' valley):

$$\sigma^x = \begin{pmatrix} 0 & 1 \\ 1 & 0 \end{pmatrix}, \qquad \text{and} \qquad \sigma^y = \begin{pmatrix} 0 & -\imath \\ \imath & 0 \end{pmatrix}. \tag{1.29}$$

The energy dispersion, therefore, reads (for both valleys):

$$\varepsilon_{\mathbf{q}}^{\pm} = \pm \hbar v_{\mathrm{F}} |\mathbf{q}|, \tag{1.30}$$

which means that the double degeneracy indeed persists also for the low-energy excitations. This result also confirms the equivalence between $|\mathbf{q}|a \ll 1$ and $|\varepsilon_{\mathbf{q}}| \ll t$ conditions, since $|\varepsilon_{\mathbf{q}}| = 3ta|\mathbf{q}|\big/2 \ll t$.

A very useful quantity for thermodynamical and transport properties calculations is the *Density of States*, which allows to switch from discrete summation over all states to integration over energy spectra. Thus $D(\varepsilon)\,\mathrm{d}\varepsilon$ equals to the number of states with the energy in the interval between ε and $\mathrm{d}\varepsilon$. We will calculate it in the low-energy limit, considering both valleys, so in all we have to append a factor of 4 to our calculations to take spin and valley degeneracies into account. The common approach to the density of states calculations is to identify in the thermodynamical limit:

$$\sum_{\mathbf{q}\,|\,\varepsilon_{\mathbf{q}} \leqslant \varepsilon} \simeq 4 \times \frac{(N_1 a \cdot N_2 a)}{(2\pi)^2} \int_0^{\mathbf{q}(\varepsilon)} \mathrm{d}\mathbf{q} \tag{1.31}$$

since $\mathbf{q}$ vectors in quasi-continuum are spanned by $2\pi\big/N_1 a$ and $2\pi\big/N_1 a$ in x and y directions. Then[5]:

$$\int D(\varepsilon)\,\mathrm{d}\varepsilon = 4 \times \frac{1}{(2\pi)^2} \int \mathrm{d}\mathbf{q} = 4 \int \frac{2\pi q}{(2\pi)^2}\,\mathrm{d}q = \int \frac{2|\varepsilon|}{\pi(\hbar v_{\mathrm{F}})^2}\,\mathrm{d}\varepsilon \tag{1.32}$$

[5]In such a way defined density of states is in fact density of states per unit surface

where we performed a beforehand integration over all $\mathbf{q}$, corresponding to the same energy. One obtains directly:

$$D(\varepsilon) = \frac{2|\varepsilon|}{\pi(\hbar v_{\mathrm{F}})^2} \tag{1.33}$$

Note that the density of states vanishes linearly at zero energy, this fact has an important impact on transport properties as it will be seen in the Chapter 3.

The full density of states, extended to higher energies is represented in fig. 1.2.b. One notice, in particular, the presence of van-Hove singularities due to the saddle points of the energy dispersion at the M points of FBZ (see fig. 1.2.a and fig. 1.1.a).

For further details on electronic properties of graphene the reader is referred to [26].

1.3 Properties of Dirac Fermions

The form of the linearised effective Hamiltonian (1.27) strongly reminds the Hamiltonian from the *Dirac Equation* — well known in particle physics relativistic wave equation for spin-½ particle, formulated by Paul Dirac in 1928[43][6]

$$H = c\mathbf{p}\boldsymbol{\sigma} + m\sigma^z \tag{1.34}$$

if we assume the mass m being equal to zero (here c is the speed of light). This equation predicts in particular the existence of a new kind of particle — positron, indeed observed for the first time by Carl Anderson in 1932[6]. This similarity by the way explains the appellation "Dirac Points". Also, it is rather common in graphene community to call π-electrons in graphene *massless pseudo-relativistic fermions* or simply *Dirac Fermions*.

Note, that this Hamiltonian acts on the already mentioned 2-components vectors or spinors. In the particle physics, the direction of such vector reflects the direction of particle spin in the basis of spin up and down states, while in the case of graphene we will call the related observable pseudo-spin (to distinguish it from its "proper" counterpart), and the up and down states will correspond to two sublattices A and B.

In the following we will reveal several curious properties of Dirac equation, that do not occur in the case of ordinary, non-relativistic Schrödinger equation.

[6] This is a two-dimensional version of the equation

1.3.1 Probabilty Current Density

In non-relativistic quantum mechanics the probability current density is calculated as follows:

$$\mathbf{j}(\mathbf{r},t) = \frac{\hbar}{2\imath m}\left(\psi^\dagger \boldsymbol{\nabla}\psi - \psi\boldsymbol{\nabla}\psi^\dagger\right). \tag{1.35}$$

In the relativistic case this quantity is derived in the same manner. From Dirac equation, making use of Pauli matrices hermicity, we have

$$\frac{\partial\Psi}{\partial t} = -c\boldsymbol{\sigma}\boldsymbol{\nabla}\Psi \qquad\qquad \frac{\partial\Psi^\dagger}{\partial t} = -c\boldsymbol{\nabla}\Psi^\dagger\boldsymbol{\sigma} \tag{1.36}$$

then the time derivative of probability density is given by

$$\begin{aligned}\frac{\partial\rho}{\partial t} &= \frac{\partial}{\partial t}\left(\Psi^\dagger\Psi\right) = \Psi^\dagger\frac{\partial\Psi}{\partial t} + \frac{\partial\Psi^\dagger}{\partial t}\Psi \\ &= -c\left(\Psi^\dagger\boldsymbol{\sigma}\cdot\boldsymbol{\nabla}\Psi + \boldsymbol{\nabla}\Psi^\dagger\cdot\boldsymbol{\sigma}\Psi\right) \\ &= -\boldsymbol{\nabla}\cdot\left(c\Psi^\dagger\boldsymbol{\sigma}\Psi\right).\end{aligned} \tag{1.37}$$

Since from continuity equation

$$\frac{\partial\rho}{\partial t} = -\boldsymbol{\nabla}\cdot\mathbf{j}(\mathbf{r},t) \tag{1.38}$$

we finally obtain

$$\mathbf{j} = c\Psi^\dagger\boldsymbol{\sigma}\Psi \tag{1.39}$$

a result, that is different from (1.35).

1.3.2 Zitterbewegung, Chirality and Klein Tunneling

Another intriguing consequence of Dirac equation, named by Erwin Schrödinger with German term *Zitterbewegung*[133], in other words jittery or trembling motion, states that any attempt to localize a relativistic quantum particle will fail, since it is inevitably accompanied by creation of particle-antiparticle pairs at the position of localization. Indeed, the momentum uncertainty of a confined relativistic particle impacts its energy uncertainty, in contrast to the non-relativistic case, where position-momentum and energy-time uncertainties are unrelated. As a consequence, such confined particle will be described by a wave-packet containing both particle (positive energy) and antiparticle (negative energy) components, which moreover will interfere, causing rapid oscillations of the particle. It is hence

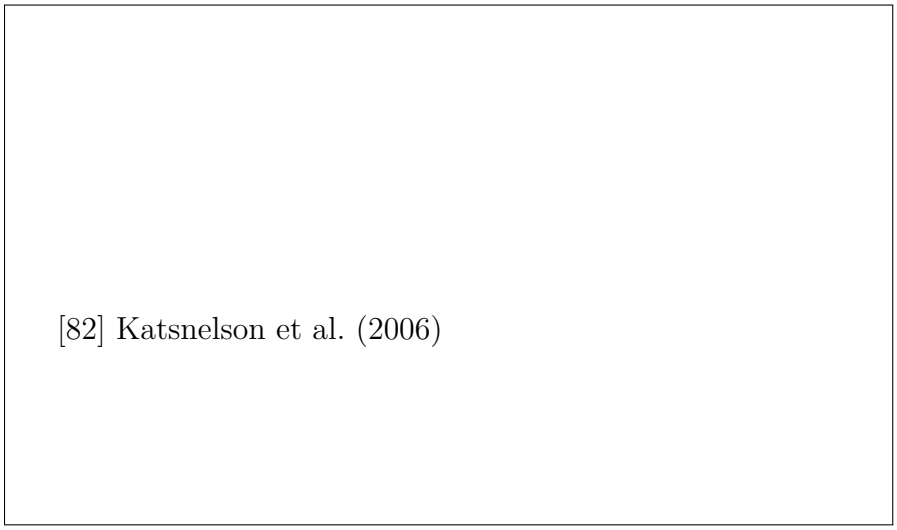

Figure 1.3: (a) Sketch illustrating Klein tunnelling through potential barrier. On top: energy bands filling (blue) in different regions, energy branches of the same color are related to the same spin direction. (b) Transmission probability T through a 100 nm-wide barrier as a function of the incident angle for barrier heights of 200 meV (red curve) and 280 meV (Fermi energy of incident electrons ≈ 80 meV. From [82].

impossible to measure the coordinates of a relativistic particle. In a condensed matter system, this phenomena is manifested by the means of special kind of inter-band transitions with creation of virtual electron-hole pairs.

Before considering the phenomenon of *Klein Tunneling*, it is expedient to first introduce one important property of Dirac fermions, namely *Chirality* or (helicity), defined as the projection of its spin onto the direction of propagation. The corresponding operator reads

$$h_{\mathbf{p}} = \frac{\mathbf{p} \cdot \boldsymbol{\sigma}}{p} \tag{1.40}$$

The eigenvalues of this operator are ± 1, and moreover it obviously commute with the Hamiltonial meaning that the chirality is a constant of motion. The particle-like eigenstates have eigenvalue $+1$, while anti-particle-like states have eigenvalue -1 (in graphene this is the case for K valley, for K' value it is the other way round). Dirac particles are thus called *chiral*. This singular property of Dirac fermions leads to what is known as *Klein Paradox*[86], a phenomenon which can be resumed as the absence of backscattering from a potential barrier. Consider for simplicity a Dirac particle in a one-dimensional space, which hits a potential barrier (see fig. 1.3.a). One would naturally suppose the particle to be scattered back by the barrier. Yet this would mean that the particle have changed

its propagation direction to the opposite without changing its spin, hence inverting the chirality. This is however impossible, since the latter is the constant of motion. As a consequence, such particle penetrates the barrier. Two-dimensional case is a bit more complicated, the transmission probability depends on the incidence angle, as it can be seen in fig. 1.3.b. This effect was experimentally observed in graphene independently by Young and Kim and by Stander et al.

Chapter 2

Transport in Mesoscopic Systems

By *Mesoscopic System* (from Ancient Greek μεσος/mesos — middle, intermediate) one generally understands a condensed matter system of "intermediate" length scale, i.e. a scale over which quantum phase coherence of states is still preserved. In this regime three effects start to play an important role: quantum fluctuations, quantum interferences and in certain conditions also the interactions. Furthermore, many macroscopic rules do not hold in the mesoscopic regime. Experimental research in this field emerged in early 80s, when the progress in micro-fabrication achieved by microelectronics industry as well as the advances of very low temperature cryogenics made possible the implementation of experimental conditions and experimental devices, able to explore the mesoscopic regime. Simultaneously, *Scattering Approach* pioneered by R. Landauer [91, 93, 94, 19, 92] and greatly enriched by M. Büttiker[19, 20, 92, 16, 17, 18], Y. Imry[72, 19, 20, 73, 141, 74] and others, provided a theoretical tool for comprehensible description of transport phenomena in this regime. Nowadays with a vast development of various nano-fabrication techniques more and more ambitious experiments are imagined, able to probe quite intricate quantum effects.

The present chapter is divided in three sections. In the first section we will provide a more detailed description of *coherent conductors* and related phenomena. In the following section scattering approach is presented and calculations of several quantities based on this approach are detailed. To a bit more specific *quantum Hall regime* a separate section is dedicated.

2.1 Mesoscopic Scale

2.1.1 Classical Discription of Transport

Before going deeper into discussion of electronic transport in mesoscopic conductors, let us recall the classical description of electronic transport in solids, given by Drude model. This model considers the ensemble of electrons as a ideal gas of classical particles, moving with randomly distributed velocities and regularly undergoing collisions (with immobile nuclei, as Drude believed). Moreover, after each collision an electron acquires a new random velocity totally independent from the one before collision. In absence of any external force the average velocity is of course zero, but if, for instance, an electric field is applied, the electrons are accelerated and will drift against its direction. However collisions will prevent them from developing an infinite drift velocity. As a results, a stationary regime will be established in which electrons move with a constant average drift velocity, as we expect from Ohm's law. This average drift velocity for given electric field $\mathbf{E}$ depends on *scattering time* τ — average time between two subsequent collisions, and writes (e and m being electron charge and mass):

$$\mathbf{v}_{\text{drift}} = -e\mathbf{E}\tau/m = -\mu\mathbf{E} \tag{2.1}$$

The quantity μ is the *electron mobility*. Then, if n is the electron density, the current density is given by $\mathbf{j} = -ne\mathbf{v}_{\text{drift}}$. Current density is related to $\mathbf{E}$ according to Ohm's law: $\mathbf{j} = \sigma\mathbf{E}$. Thus we obtain the familiar Drude conductivity formula:

$$\sigma = \frac{e^2 n\tau}{m} = en\mu \tag{2.2}$$

Despite its extreme simplicity, this model (especially when combined with the results of quantum theory of solids) is still relevant for transport description in metals and semiconductors. In return, from quantum theory of solids, we know, that an ideal immobile lattice of ions will be seen as a perfect background by a Bloch electron, being by construction an eigenstate of the periodic potential. Consequently, such ideal lattice can not give rise to any scattering, in contrast to what Drude believed. So let us see, what are the real mechanisms of the electrons scattering in solids and compare related characteristic length and time scales.

It is quite obvious that any deviation of the lattice from its perfect order is able to perturb Bloch wave propagation. For example, displacement of a lattice ion from its equilibrium position can be seen as an electric dipole on top of the perfect periodic background, that can interact with an electron. As we know, at non-zero temperature the ions execute collective vibrational motions around their equilibrium positions, described by a wave-like modes, known as phonons. Accordingly, an electron can be inelastically scattered from one state to another emitting

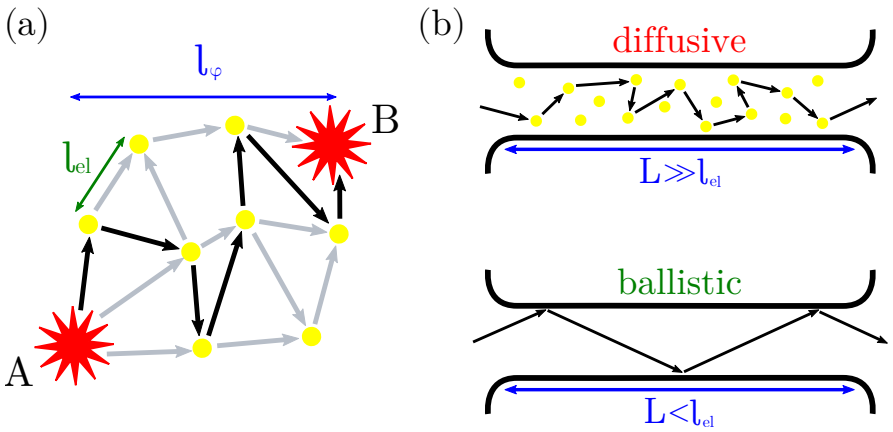

Figure 2.1: (a) Illustration of electron travelling from point A to point B in a diffusive conductor between two inelastic shocks represented by two red stars. Yellow dots represent elastic scatterers, black arrows indicate the direction of electron movement after each collision, grey arrows showing the alternative paths allowing to get from point A to point B. By l_{el} is denoted the elastic scattering length, by l_ϕ — the coherence length. (b) Illustration of electron travelling through diffusive (top) and through ballistic (bottom) conductor of length L.

or absorbing a phonon (this inelastic scattering is responsible, for instance, for the Joule heating). Above Debye temperature, the number of scatterers increase linearly with temperature T, therefore associated scattering time $\tau_{\text{e-ph}}$ in metals scales as $1/T$ (below Debye temperature it scales rather as $1/T^3$), explaining the well-known linear dependence of the resistivity with temperature. Besides, it is also useful to introduce *scattering length* corresponding to the average distance by which an electron travels between two subsequent collisions: $l_{\text{e-ph}}$. At low temperature only low frequency and thus long wave-length modes are excited, meaning that the associated scattering length is also quite large, so the effectiveness of this mechanism comes to naught.

On the other hand, any lattice defects (e.g. impurities, structural lattice defects, crystal boundaries, etc.) always present in the crystal, will also break lattice translational symmetry and cause Bloch electron scattering. However, in contrast to the previous case this scattering mechanism is elastic, due to the defects' lack of degrees of freedom with which electrons can exchange energy, resulting only in the deflection of trajectory of the electron, attempting to avoid the defect. Moreover these processes are usually temperature independent and the associated scattering time $\tau_{\text{e-d}}$ and length $l_{\text{e-d}}$ rather depend on the defects concentration in given sample, hence at low temperature scattering on lattice defects will be the dominant mechanism.

In addition to the lattice related scattering mechanisms, Coulomb interaction between electrons can also give rise to electron-electron scattering, which is by the way inelastic. To have more insight into this mechanism let us compare two energy scales: typical electron kinetic and potential energies per particle in a three-(two-)dimensional system with mean distance between electrons $\bar{d} \propto n^{-\frac{1}{3}}$ ($\propto n^{-\frac{1}{2}}$). We have $E_{\text{kin}} \propto n^{\frac{2}{3}}$ ($\propto n$), while $E_{\text{pot}} \simeq e^2/\bar{d} \propto n^{\frac{1}{3}}$ ($\propto n^{\frac{1}{2}}$), thus giving the following result:

$$\frac{E_{\text{pot}}}{E_{\text{kin}}} \propto n^{-\frac{1}{3}} \left(\propto n^{-\frac{1}{2}}\right) \tag{2.3}$$

meaning that the importance of electron-electron interactions diminishes with increasing electron density[1]. However, in the most cases, this will be a dominant inelastic mechanism at low temperature. As before, we note corresponding time and length scales respectively $\tau_{\text{e-e}}$ and $l_{\text{e-e}}$.

2.1.2 Quantum Phase Coherent Systems

In certain conditions a physical system manifests properties, that can not be explained within (semi-)classical framework, introduced in the previous section, since one has to account for wave-like effects, e.g. interferences, so the quantum mechanical description should be used. For such regime to be reached, the system has to be *quantum coherent*. By that we understand that the quantum phase of electronic wave-functions is preserved at least on the scale of the system. If we denote coherence length and time by t_ϕ and l_ϕ, this means that system size $L \ll l_\phi$.

The coherence is lost when the system interacts with the environment (phonons, other electrons, magnetic impurities, electromagnetic fields, etc.), since this will result in projection of system eigenstates into corresponding interaction operators eigenstates, that are not necessarily the formers. Moreover, these are usually inelastic processes, except in the cases where the environment is modified without energy transfer (e.g. magnetic impurity's spin flip). On the other hand, during an elastic scattering process the phase is modified in a well-defined way, thus quantum coherence is preserved.

As it was discussed in the previous section, the inelastic scattering rate decreases with temperature so, in order to attain such regime experimentally, in addition to a small size and reduced dimension, a very low temperature is required. As mentioned before, the main inelastic scattering mechanism at low temperature is electron-electron interaction. Hence $l_\phi \simeq l_{\text{e-e}}$. Elastic scattering length $l_{\text{el}} \simeq l_{\text{e-d}}$ is also important since it allows to distinguish between two sub-regimes: *diffusive* in which electron propagation through the system is accompanied by many elastic collisions and *ballistic* in which electrons propagate without scattering (except the

[1]Note that, in the case of the Dirac fermions, this ratio is density independent

Table 2.1: Typical length scales in metallic sysmes, GaAs-heterostructures and graphene

	Metal	GaAs/AlGaAs	Graphene
λ_F (nm)	~ 0.1	$\sim 40 - 50$	~ 40
l_{el} (µm)	~ 0.2	10 up to $200 - 300$	0.05 up to 1
l_ϕ(µm) ($T < 1\,K$)	~ 1	idem	$1 - 5$

system boundaries). Typical length-scales in different systems are given in the table:

Multiple are the devices in which at low temperature quantum coherence is attained. These are usually based on *two-dimensional electron gases* obtained at the interface of two semi-conductors or in graphene, one-dimensional conductors represented by various nano-wires or carbon nanotubes, quasi-0-dimensional nano-particles or point defects. In the next section we will give examples of such devices and related mesoscopic phenomena.

2.1.3 Effects of the Coherence on Transport Properties

In the coherent conductors all transport processes can be described in terms of electronic waves transmission taking into account eventual interference effects. Here we will give several examples of the most prominent transport phenomena that arise in quantum coherent systems. Maybe the best known manifestation of the quantum effects in transport properties of a coherent conductor is the conductance quantization. This phenomenon can be observed in *Quantum Point Contacts* (QPC) — ingenious devices in which the number of electronic wave propagation modes can be controlled externally by applying depleting gate voltage. In such systems, conductance, defined at mesoscopic scale as the sum of electron waves transmission probabilities over all modes, behaves as a step function of gate voltage as it can be seen in fig. 2.2.a, each new plateau corresponding to addition of a new mode to the total transmission. The plateaus are equally spaced by $2g_0$, where g_0 is a value called *conductance quantum*, defined by fundamental physical quantities only: $g_0 = \frac{e^2}{h}$ (the factor of 2 comes from the spin degeneracy). Another situation in which conductance quantization emerges is *Quantum Hall Effect*. Both effects will be detailed in the following sections.

Other very vivid examples of wave interference effects in coherent systems are *Weak localisation* and *Aharonov-Bohm effect*. The first effect manifests itself in disordered systems and is commonly interpreted in terms of *coherent backscat-*

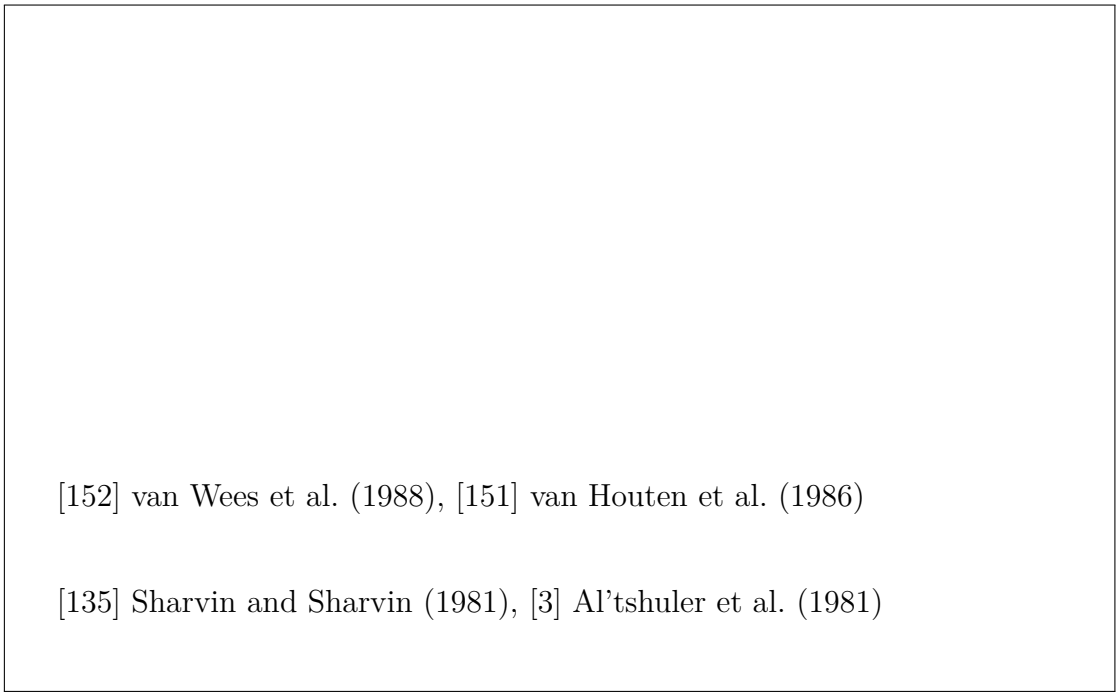

Figure 2.2: (a) First observation by van Wees et al. (simultaneously with Wharam et al.) of the conductance quantization in a GaAs/AlGaAs heterojunction based QPC. From [152]. (b) Manifestation of weak localisation and its destruction by temperature in GaAs/AlGaAs heterojunction based narrow channels of width $W = 1.5\,\mu\text{m}$ (squares) and $W = 0.5\,\mu\text{m}$ (triangles), the channel length $L = 10\,\mu\text{m}$. From [151]. (c) First observation of Aharonov-Bohm effect in a cylindrical magnesium film by Sharvin and Sharvin. From [135]. (d) Sketch of the sample used by Sharvin and Sharvin, suggested by Al'tshuler et al. From [3]. (e) Illustration for the conventional Aharonov-Bohm ring.

tering. To understand the origin of this effect consider such disordered coherent system depicted by the sketch of fig. 2.1.a. Then, to calculate the probability P_{AB} for a particle to travel from point **A** to point **B**, one has to account for all possible trajectories, leading from **A** to **B** (shown on the sketch in grey). Moreover, coherence of the system requires that the calculation of the total probability be done in terms of probability amplitudes A_i of each classical trajectory, rather than classical probabilities $|A_i|^2$:

$$P_{\text{AB}} = \left| \sum_i A_i \right|^2 = \sum_i |A_i|^2 + \sum_{i \neq j} A_i A_j^* \tag{2.4}$$

Here the first term corresponds to the classical diffusion probability, while the

second one reflects the contribution of quantum interferences. Yet, in such diffusive system the number of trajectories contained in this sum is huge and it is therefore quite clear, that in most of the cases the interference term will average out. The exception would be the instance, when the points **A** and **B** coincide, i.e. when we want to calculate the probability for a particle to return to its origin. Indeed, the probability amplitudes for any two trajectories, related by the time-reversal symmetry are identical: $A^{\circlearrowleft} = A^{\circlearrowright} \equiv A$ (which is precisely the consequence of the time-reversal symmetry) and the backscattering probability $|A^{\circlearrowleft} + A^{\circlearrowright}|^2 = 4|A|^2$ is then twice the classical result. This means that apparently the quantum interferences tend to localize the particle, reducing the diffusion constant and hence the conductivity. This effect is called *weak localization*. Figure 2.2.b shows how the effect of the temperature will destroy the weak localization effect, by reducing the coherence length: the resistance decreases first, when temperature is increased and the coherence length falls below the sample length. After the coherence length is sufficiently reduced, the resistance changes the behaviour and starts to grow as it is predicted by the classical Drude model. Another way to destroy this effect is obviously the application of magnetic field that will break the time-reversal symmetry.

The last mentioned effect has quite similar origin. It can be observed for example in a micrometer-size metallic ring (see fig. 2.2.e) in which an electron can follow two distinct paths to arrive from one "end" of the ring to another. Two possible trajectories of the electron — clockwise and counter-clockwise — will interfere, leading to the transmission probability $T = |t^{\circlearrowleft} + t^{\circlearrowright}|^2$, where $t^{\circlearrowleft}$ and $t^{\circlearrowright}$ are the corresponding transmission coefficients. When magnetic field B is applied, these coefficients acquire an additional field-dependent phase factors, that read

$$\psi^{\circlearrowleft} = \int_{\circlearrowleft} \frac{e}{\hbar}\mathbf{A}\,\mathrm{d}\mathbf{l} \quad \text{and} \quad \psi^{\circlearrowright} = \int_{\circlearrowright} \frac{e}{\hbar}\mathbf{A}\,\mathrm{d}\mathbf{l} \tag{2.5}$$

where **A** is the vector potential, associated with the field B. This yields a field dependent phase difference

$$\Delta\psi(B) = 2\pi\frac{e}{h}\Phi \tag{2.6}$$

Φ being the magnetic flux through the loop. We also introduce the notation $\Phi_0 = \frac{h}{e}$, called flux quantum.

On the other hand, the new, field dependent transmission probability will have the following form:

$$T(B) = |t^{\circlearrowleft}e^{\imath\psi^{\circlearrowleft}} + t^{\circlearrowright}e^{\imath\psi^{\circlearrowright}}|^2 = |t^{\circlearrowleft}|^2 + |t^{\circlearrowright}|^2 + \mathbf{Re}\left\{t^{\circlearrowleft}t^{\circlearrowright *}e^{\imath\Delta\psi}\right\} \tag{2.7}$$

$$= |t^{\circlearrowleft}|^2 + |t^{\circlearrowright}|^2 + |t^{\circlearrowleft}||t^{\circlearrowright}|\cos\left(\Delta\psi_0 + \Delta\psi(B)\right) \tag{2.8}$$

where $\Delta\psi_0$ is the eventual phase difference between two paths in the absence of magnetic field. The transmission thus oscillates with the period equal to the quantum of flux Φ_0. The far reaching consequence of this is that counter-intuitively, the transmission through the ring is field-dependent even if the magnetic field in the two arcs of the ring is zero. This effect was observed for the first time by Sharvin and Sharvin but in a cylindrical magnesium film (see fig. 2.2.d) for which the period of oscillations is $\Phi/2$. The result of this study is shown in fig. 2.2.c.

Finally, two more experiments spectacularly pointing out the wave-like aspect of electrons in coherent systems are electronic Fabry-Perrot[30, 22] and Mach-Zehnder[163, 76, 128] interferometry, totally inspired by their optical analogue.

2.2 Scattering Approach

In this section we will formulate scattering approach (also referred to as Landauer approach) to coherent transport, to date prevalent method of the transport description in mesoscopic regime. Its main idea, concisely, is to relate transport properties of the studied system (e.g. conductance, current fluctuations) to its scattering properties, which are assumed to be known from a quantum-mechanical calculation. We first evoke the general principles of the scattering approach and then use its results for calculation of several basic macroscopic quantities. More details about this approach and its consequences can be found for instance in ref. [14].

2.2.1 Framework, Hypotheses, Formulation

For the sake of simplicity we consider a one-dimensional, two-terminal coherent conductor to which two reservoirs of fermions — the "left" (L) and the "right" (R) — are connected and in addition we will omit the spin degree of freedom (the extension to multi-terminal, multi-mode case with spin being more or less straightforward). The system is considered to be in stationary regime and, furthermore, at thermal equilibrium. Moreover we neglect electron-electron interactions effects. The reservoirs are infinitely long and much larger than the conductor, they can be characterized by temperature T and chemical potentials $\mu_{\mathrm{L(R)}}$ and obey Fermi-Dirac statistics: $f_{\mathrm{L(R)}}(\varepsilon) = \left[\exp\left((\varepsilon - \mu_{\mathrm{L(R)}})/k_{\mathrm{B}}T\right) + 1\right]^{-1}$. In addition, they are supposed to be perfect sources and sinks of electrons such that entering particle looses immediately its phase. From this point of view the specified problem is irreversible. On the other hand, the coherent conductor can be seen as a kind of stochastic "frontier guard" transferring the particles from one reservoir to another with certain (generally energy dependent) probability or otherwise rejecting them

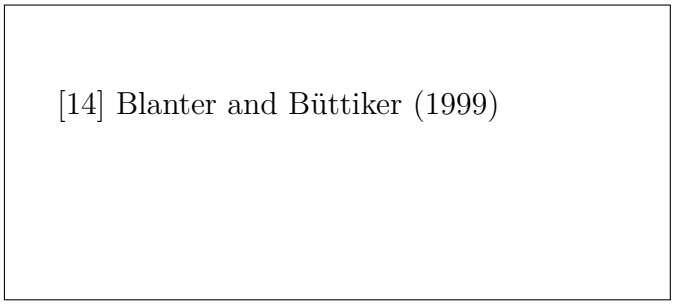

Figure 2.3: Example of two-terminal scattering problem for the case of one transverse channel. From[14].

back to their reservoir of origin (such transfer processes being of course energy conservative). Mathematically this is expressed by *scattering matrix* that we will introduce soon.

In the following it is convenient to introduce particular creation and annihilation operators for electrons in scattering states of given energy ε: $\hat{a}^\dagger_{\mathrm{L(R)}}(\varepsilon)$, $\hat{a}_{\mathrm{L(R)}}(\varepsilon)$ — incident upon conductor from left (right) reservoir, $\hat{b}^\dagger_{\mathrm{L(R)}}(\varepsilon)$ and $\hat{b}_{\mathrm{L(R)}}(\varepsilon)$ — outgoing from conductor towards left (right) reservoirs. Being fermionic operators, they obey canonical anticommutation relation and Fermi-Dirac distribution (for conciseness, the same relations for b operators are omitted):

$$\left\{\hat{a}_{\mathrm{L(R)}}(\varepsilon), \hat{a}^\dagger_{\mathrm{L(R)}}(\varepsilon')\right\} = \delta(\varepsilon - \varepsilon'), \quad \left\langle \hat{a}_{\mathrm{L(R)}}(\varepsilon)\hat{a}^\dagger_{\mathrm{L(R)}}(\varepsilon')\right\rangle = f_{\mathrm{L(R)}}(\varepsilon)\delta(\varepsilon - \varepsilon') \tag{2.9}$$

These operators are related by scattering matrix

$$\begin{pmatrix} \hat{b}_{\mathrm{L}}(\varepsilon) \\ \hat{b}_{\mathrm{R}}(\varepsilon) \end{pmatrix} = \mathcal{S} \begin{pmatrix} \hat{a}_{\mathrm{L}}(\varepsilon) \\ \hat{a}_{\mathrm{R}}(\varepsilon) \end{pmatrix}, \quad \text{where} \quad \mathcal{S} = \begin{pmatrix} r(\varepsilon) & t'(\varepsilon) \\ t(\varepsilon) & r'(\varepsilon) \end{pmatrix} \tag{2.10}$$

In view of current conservation this matrix has to be unitary, meaning that $|t'|^2 = |t|^2 = D$, $|r'|^2 = |r|^2 = R$, with $D + R = 1$.

We define field operators $\hat{\Psi}$ and $\hat{\Psi}^\dagger$ for instance in the left reservoir (far from conductor) as

$$\hat{\Psi}^{(\dagger)}_{\mathrm{L}}(x,t) = \int \frac{\mathrm{d}\varepsilon}{\sqrt{2\pi\hbar v(\varepsilon)}} \left\{\hat{a}^{(\dagger)}_{\mathrm{L}}(\varepsilon)\exp(\imath kx) + \hat{b}^{(\dagger)}_{\mathrm{L}}(\varepsilon)\exp(-\imath kx)\right\} \exp\left(-\imath\frac{\varepsilon}{\hbar}t\right) \tag{2.11}$$

with electron wavenumber $k = \sqrt{2m\varepsilon}/\hbar$ and velocity $v(\varepsilon) = \hbar k/m$. If we then write current operator for the same reservoir (which is equal to current density

operator in one dimension):

$$\begin{aligned}\hat{I}_{\mathrm{L}}(x,t) &= \frac{e\hbar}{2\imath m}\left[\hat{\Psi}^{\dagger}_{\mathrm{L}}(x,t)\frac{\partial\hat{\Psi}_{\mathrm{L}}(x,t)}{\partial x} - \hat{\Psi}_{\mathrm{L}}(x,t)\frac{\partial\hat{\Psi}^{\dagger}_{\mathrm{L}}(x,t)}{\partial x}\right] \\ &= \frac{e}{h}\int \mathrm{d}\varepsilon'\,\mathrm{d}\varepsilon \frac{e^{-\imath(\varepsilon-\varepsilon')t/\hbar}}{2\sqrt{v(\varepsilon)v(\varepsilon')}} \\ &\times\Big\{(v(\varepsilon)+v(\varepsilon'))\left[\hat{a}^{\dagger}_{\mathrm{L}}(\varepsilon)\hat{a}_{\mathrm{L}}(\varepsilon')e^{\imath(k'-k)x} - \hat{b}^{\dagger}_{\mathrm{L}}(\varepsilon)\hat{b}_{\mathrm{L}}(\varepsilon')e^{\imath(k-k')x}\right] \\ &+ (v(\varepsilon)-v(\varepsilon'))\left[\hat{a}^{\dagger}_{\mathrm{L}}(\varepsilon)\hat{b}_{\mathrm{L}}(\varepsilon')e^{-\imath(k+k')x} - \hat{b}^{\dagger}_{\mathrm{L}}(\varepsilon)\hat{a}_{\mathrm{L}}(\varepsilon')e^{\imath(k+k')x}\right]\Big\} \\ &\simeq \frac{e}{h}\int \mathrm{d}\varepsilon'\,\mathrm{d}\varepsilon e^{-\imath(\varepsilon-\varepsilon')t/\hbar}\left[\hat{a}^{\dagger}_{\mathrm{L}}(\varepsilon)\hat{a}_{\mathrm{L}}(\varepsilon') - \hat{b}^{\dagger}_{\mathrm{L}}(\varepsilon)\hat{b}_{\mathrm{L}}(\varepsilon')\right]\end{aligned} \tag{2.12}$$

in the last computational step we neglected velocity dependence on energy, which is reasonable for energies in the viscinity of Fermi level.

2.2.2 Scattering Approach at Work

The obtained result allows us to calculate various quantities, but we will limit the discussion only to the quantities studied in this work — conductance and noise.

a. Conductance Calculation

Conductance is defined as $G = I/V$, where I is the average current ($I = \langle I_{\mathrm{L}}\rangle = \langle I_{\mathrm{R}}\rangle$) and V — chemical potentials difference ($\mu_{\mathrm{L}} - \mu_{\mathrm{R}} = eV$). We can calculate average current (without neglecting energy dependence of velocity):

$$\langle I_{\mathrm{L}}\rangle = \frac{e}{h}\int \mathrm{d}\varepsilon\left\{\left\langle \hat{a}^{\dagger}_{\mathrm{L}}(\varepsilon)\hat{a}_{\mathrm{L}}(\varepsilon)\right\rangle - \left\langle \hat{b}^{\dagger}_{\mathrm{L}}(\varepsilon)\hat{b}_{\mathrm{L}}(\varepsilon)\right\rangle\right\} \tag{2.13}$$

using scattering matrix relations and operator's statistics we finally obtain:

$$\langle I_{\mathrm{L}}\rangle = \frac{e}{h}\int \mathrm{d}\varepsilon\, D(\varepsilon)(f_{\mathrm{L}}(\varepsilon) - f_{\mathrm{R}}(\varepsilon)) \tag{2.14}$$

For applied voltages, small as compared to Fermi energy E_{F}, we can, to begin with, neglect transmission dependence on energy and, moreover, do following approximation:

$$\langle I_{\mathrm{L}}\rangle = \frac{e}{h}\int \mathrm{d}\varepsilon\,\frac{\partial f(\varepsilon)}{\partial\varepsilon}D(\varepsilon) = \frac{e^2}{h}D(E_{\mathrm{F}})V \tag{2.15}$$

We hence obtain the conductance given by:

$$G = \frac{I}{V} = \frac{e^2}{h}D \tag{2.16}$$

where we find already mentioned conductance quantum as multiplying pre-factor. In multi-mode case, taking the spin degeneracy into account, the conductance reads:

$$G = \frac{2e^2}{h} \sum_n D_n \tag{2.17}$$

b. Noise Power Calculation

We remain in the case of one-dimensional two-terminal conductor. Let us derive the expression for current noise, that is current fluctuations away from its average value. We define thereby operators $\Delta\hat{I}_{\mathrm{L(R)}}(t) = \hat{I}_{\mathrm{L(R)}}(t) - \langle\hat{I}_{\mathrm{L(R)}}\rangle$, that will allow us to introduce correlation matrix

$$S_{\alpha\beta}(t-t') = \frac{1}{2}\left\langle \Delta\hat{I}_\beta(t')\Delta\hat{I}_\alpha(t)\right\rangle, \qquad \alpha,\beta = \mathrm{L,R}. \tag{2.18}$$

Let us see the properties of this matrix. First of all in the absence of time-dependent external fields its elements are only $t-t'$ dependent. Furthermore, current conservation implies that they satisfy following relations: $S_{\mathrm{L,R}} = S_{\mathrm{R,L}} = -S_{\mathrm{L,L}} = -S_{\mathrm{R,R}}$. The diagonal elements correspond to autocorrelations in respective contacts, whereas non-diagonal — to cross-correlations between two contacts. Henceforth, without loosing generality, we will continue the derivation only for autocorrelation in left reservoir and keep notation $S_{\mathrm{LL}}(t-t') = S(\tau)$. We define *noise power* as a Fourier transform of $S(\tau)$, that after some algebra can be written as:

$$S_{\mathrm{I}}(\omega) = 2\int \left\langle \hat{I}(0)\hat{I}(\tau)\right\rangle e^{\imath\omega\tau}\,\mathrm{d}\tau \tag{2.19}$$

The results of the first section (eq. 2.12) allow us to compute this quantity:

$$\begin{aligned}
S_{\mathrm{I}}(\omega) =& \frac{2e^2}{h}\int e^{\imath\omega\tau}\,\mathrm{d}\tau \int \mathrm{d}\varepsilon\ \mathrm{d}\varepsilon'\ \mathrm{d}\varepsilon''\ \mathrm{d}\varepsilon'''\, e^{-\imath(\varepsilon''-\varepsilon''')\tau/\hbar} \\
&\cdot\left\langle \left[\hat{a}^\dagger_{\mathrm{L}}(\varepsilon)\hat{a}_{\mathrm{L}}(\varepsilon') - \hat{b}^\dagger_{\mathrm{L}}(\varepsilon)\hat{b}_{\mathrm{L}}(\varepsilon')\right]\left[\hat{a}^\dagger_{\mathrm{L}}(\varepsilon'')\hat{a}_{\mathrm{L}}(\varepsilon''') - \hat{b}^\dagger_{\mathrm{L}}(\varepsilon'')\hat{b}_{\mathrm{L}}L(\varepsilon''')\right]\right\rangle \\
=& \frac{2e^2}{h}\int \mathrm{d}\varepsilon\ \mathrm{d}\varepsilon'\ \mathrm{d}\varepsilon''\left\{ \left\langle \hat{a}^\dagger_{\mathrm{L}}(\varepsilon)\hat{a}_{\mathrm{L}}(\varepsilon''-\hbar\omega)\right\rangle\left\langle \hat{a}^\dagger_{\mathrm{L}}(\varepsilon'')\hat{a}_{\mathrm{L}}(\varepsilon')\right\rangle |t|^4\right. \\
&+\left\langle \hat{a}^\dagger_{\mathrm{R}}(\varepsilon)\hat{a}_{\mathrm{R}}(\varepsilon''-\hbar\omega)\right\rangle\left\langle \hat{a}^\dagger_{\mathrm{R}}(\varepsilon'')\hat{a}_{\mathrm{R}}(\varepsilon')\right\rangle |t|^4 + \left\langle \hat{a}^\dagger_{\mathrm{R}}(\varepsilon)\hat{a}_{\mathrm{R}}(\varepsilon''-\hbar\omega)\right\rangle \\
&\times\left\langle \hat{a}^\dagger_{\mathrm{L}}(\varepsilon'')\hat{a}_{\mathrm{L}}(\varepsilon')\right\rangle |r|^2|t|^2 + \left\langle \hat{a}^\dagger_{\mathrm{L}}(\varepsilon)\hat{a}_{\mathrm{L}}(\varepsilon''-\hbar\omega)\right\rangle\left\langle \hat{a}^\dagger_{\mathrm{R}}(\varepsilon'')\hat{a}_{\mathrm{R}}(\varepsilon')\right\rangle |r|^2|t|^2\Big\}
\end{aligned} \tag{2.20}$$

that, after a long calculations that we skip here, leads to

$$S_{\text{I}}(\omega) = \frac{2e^2}{h}\Big[2D^2\hbar\omega\mathcal{N}(\omega)+RD\Big\{(\hbar\omega - eV)\mathcal{N}(\omega - eV/\hbar) +(\hbar\omega + eV)\mathcal{N}(\omega + eV/\hbar)\Big\}\Big] \tag{2.21}$$

where $\mathcal{N}(\omega) = \left[\exp\left(\hbar\omega k_{\text{B}}T\right) - 1\right]^{-1}$ is Bose-Einstein distribution.

In the present work we study so called *zero-frequency noise*, i.e. noise at such frequencies, that $\hbar\omega \ll eV$, $k_{\text{B}}T$. In these conditions eq. 2.21 simplifies to

$$S_{\text{I}} = 4\frac{e^2}{h}D^2k_{\text{B}}T + 2e\frac{e^2}{h}D(1-D)V\coth\left(\frac{eV}{2k_{\text{B}}T}\right) \tag{2.22}$$

As previously, the general expression of zero-frequency noise for multi-mode two-terminal conductor, taking into account the spin degeneracy, is obtained by summing up over all propagation modes (with factor of 2 for spin), since the noise, generated by one mode is supposed to be decorrelated from the other ones:

$$S_{\text{I}} = 4\frac{2e^2}{h}\sum_n D_n^2k_{\text{B}}T + 2e\frac{2e^2}{h}\sum_n D_n(1-D_n)V\coth\left(\frac{eV}{2k_{\text{B}}T}\right) \tag{2.23}$$

We can now study different contributions to the total noise in (2.22) by admitting subsequently T and V to be zero (still remaining in one-dimensional configuration). At equilibrium, when no voltage or temperature difference is applied to the reservoirs, the only possible sources of noise are thermal fluctuations of energy levels population in the reservoirs, weighted by D^2 factor, as well as partitioning of thermally emitted particles by the conductor, weighted by $D(1-D)$, resulting in final expression in D pre-factor[2]

$$S_{\text{I}} = 4\frac{e^2}{h}Dk_{\text{B}}T = 4Gk_{\text{B}}T \tag{2.24}$$

This noise is called *Johnson-Nyquist noise* and its expression can also be obtained from the Fluctuation-Dissipation theorem. The contribution of this noise to the output signal is unavoidable.

On the other hand, if we suppose the temperature to be zero and a bias V to be applied, we recover pure transport partition noise, which is given by

$$S_{\text{I}} = 2\frac{e^2}{h}D(1-D)eV = 2eI(1-D) = 2eI\mathfrak{F} \tag{2.25}$$

[2]Note that as in (2.22) the spin degree of freedom here is again omitted.

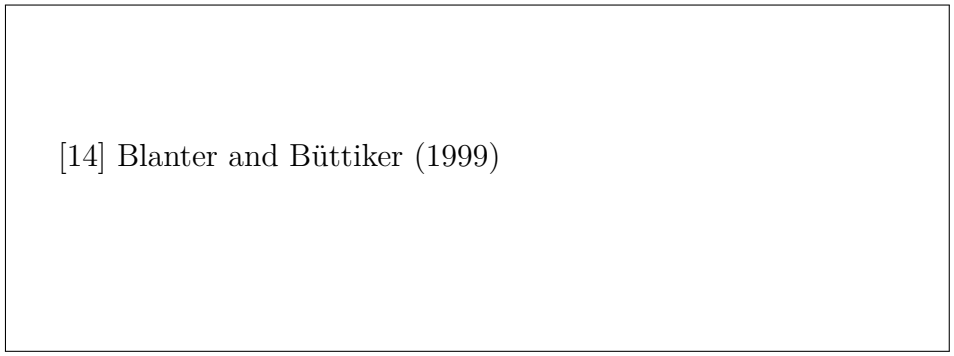

Figure 2.4: (a) Schematic variation of current noise expressed in terms of sample effective noise temperature T_s, showing the cross over from thermal equilibrium to pure shot noise. In these convenient units, the asymptote at large bias has a slope equal to the Fano factor. From [60]. (b) Distribution function of transmission coefficients for $L/l_{el} = 10$. From [14].

where we introduced the *Fano Factor* $\mathfrak{F}$, which, in general case of multi-mode conductor, reads

$$\mathfrak{F} = \frac{\sum_n D_n(1 - D_n)}{\sum_n D_n} \tag{2.26}$$

This quantity is specific to a given type of conductor and, as it is clear from (2.26), can take values only between 0 and 1. To illustrate, in a ballistic conductor, where no scattering is present, Fano Factor is obviously zero. Classical Schottky formula for noise corresponds to Fano factor of 1 and this result can be attained as well in coherent conductors with all transmission coefficients D_n very small, e.g. in a tunnel junction. Another specific case is diffusive and chaotic conductors in which the transmission coefficients T can be discussed only in terms of probability distribution. For instance, a typical distribution for a diffusive conductor of conductance G (see fig. 2.4.b) was calculated by Dorokhov:

$$P(T) = \frac{l}{2L} \frac{1}{T\sqrt{1-T}} \tag{2.27}$$

with L — sample length and l — mean free path, and it leads to Fano factor equal to 1/3. Fano factor in chaotic cavities was found to be 1/4.

The transition from Johnson-Nyquist noise dominant regime to transport noise dominant regime is depicted in fig. 2.4.b. One can, in particular, find the sample temperature very precisely if applied voltage is well known or vice versa, by simply fitting this curve.

2.3 Quantum Hall Effect

In this section we will present a somewhat singular though rather widespread phenomenon in the mesoscopic domain which is Quantum Hall Effect (QHE), more particularly Integer QHE (IQHE). We will first briefly introduce Landau quantisation — a necessary tool for QHE understanding and, in what follows, will explain the mechanisms that lead to Hall conductance quantisation and other related properties. For further information on this subject the reader is referred to [59] and more recent [61].

Hall effect, discovered in its classical form by Edwin Hall in 1879, can be perceived as a result of the Lorentz force, that acts on the charged particles, moving in magnetic field. This force bends the electron trajectories towards the conductor's edges, so that accumulation of charges on each edge but with opposite sign occurs until the established electric field compensates totally the Lorentz force. This results in a voltage drop (called *Hall voltage*) in the direction, perpendicular to the injected current and the *Hall resistance* R_{H} can be defined as a ratio between this transverse Hall voltage and the injected current.

The most convenient way to describe transport properties in the Hall effect regime is to introduce conductivity and resistivity tensors $\sigma_{\mu\nu}$ and $\rho_{\mu\nu}$. Note that in two dimensions the resistance and the resistivity are expressed in the same units and moreover Hall resistance R_{H} is equal precisely to the non-diagonal component of resistivity tensor ρ_{xy}, Hall resistivity in other words. The resistivity tensor is defined in a similar way as the usual resistivity (the conductivity tensor being just its inverse):

$$E^{\mu} = \rho_{\mu\nu} j^{\nu} \tag{2.28}$$

To clarify the origin of the Hall effect let us consider a simple model of two-dimensional electron gas in xy plane in absence of any defects and with no electric field applied, whereas a homogeneous magnetic field points in the direction of z axis. Such a system is invariant under translations so we can switch to a frame of reference moving with velocity $-\mathbf{v}$ relative to the lab frame. In this frame of reference the electrons appear to move with the opposite velocity, that corresponds to a current density $\mathbf{j} = -n_{\mathrm{e}} e \mathbf{v}$ (where $-e$ and n_{e} are electron charge and density respectively) and to the related to this movement Lorentz force $-e\,\mathbf{v} \times \mathbf{B}$, absent in the lab frame. For that reason, in the moving frame of reference an electric field in the direction perpendicular to the current has to appear, in order to compensate exactly the Lorentz force:

$$\mathbf{E} = -\mathbf{v} \times \mathbf{B} = \frac{1}{n_{\mathrm{e}} e}\, \mathbf{j} \times \mathbf{B} \tag{2.29}$$



Figure 2.5: (a) Sketch of a Hall bar. From [61]. (b) First observation of the Quantum Hall Effect by Klitzing et al. From [88].

Thereof follows, that the resistivity and conductivity tensors can be written as:

$$\rho = \frac{B}{n_{\mathrm{e}} e} \begin{pmatrix} 0 & 1 \\ -1 & 0 \end{pmatrix}, \qquad \sigma = \frac{n_{\mathrm{e}} e}{B} \begin{pmatrix} 0 & -1 \\ 1 & 0 \end{pmatrix} \tag{2.30}$$

leading to a classical results for the Hall resistance:

$$R_{\mathrm{H}} = \frac{B}{n_{\mathrm{e}} e} \tag{2.31}$$

In the quantum regime, however, this resistance is quantized, exactly in the same manner as this can be observed in a quantum point contact:

$$R_{\mathrm{H}} = \frac{1}{\nu} \frac{h}{e^2} \tag{2.32}$$

where ν, called *filling factor*, is integer and corresponds to the filling of Landau levels, as it will be explained in the next section. The two following sections will help to understand the reasons of such a peculiar behaviour.

2.3.1 Landau Quantization

Let us study the quantum description of the electron dynamics in presence of magnetic field. To begin with, consider one particle Hamiltonian, at first, in absence of magnetic field

$$H^0 = \frac{\mathbf{p}^2}{2m_{\mathrm{e}}} \tag{2.33}$$

m_{e} being electron's effective mass, related to the specific band. Then, in presence of magnetic field, the Lorentz force effect on electron dynamics can be included in the Hamiltonian by simply replacing the canonical momentum $\mathbf{p}$ with a gauge-invariant one $\mathbf{\Pi}$ (proportional to the velocity) as follows:

$$\mathbf{p} \to \mathbf{\Pi} = \mathbf{p} + e\mathbf{A}(\mathbf{r}) \tag{2.34}$$

that yields to a Hamiltonian

$$H^{\mathrm{B}} = \frac{[\mathbf{p} + e\mathbf{A}(\mathbf{r})]^2}{2m_{\mathrm{e}}} = \frac{1}{2m_{\mathrm{e}}}\left(\Pi_x^2 + \Pi_y^2\right) \tag{2.35}$$

Note that, in contrast to the canonical momentum, the components of the gauge-invariant momentum no longer commute themselves:[3]

$$\begin{aligned}\left[\Pi_x, \Pi_y\right] =& e\left(\left[p_x, A_y\right] - \left[p_y, A_x\right]\right) = e\left(\frac{\partial A_y}{\partial x}\left[p_x, x\right] - \frac{\partial A_x}{\partial y}\left[p_y, y\right]\right) \\ =& -\imath e\hbar\left(\frac{\partial A_y}{\partial x} - \frac{\partial A_x}{\partial y}\right) = -\imath e\hbar(\boldsymbol{\nabla}\times\mathbf{A})\cdot\mathbf{e}_z = -\imath e\hbar B\end{aligned} \tag{2.36}$$

As a consequence, the Hamiltonian (2.35) can be seen as describing one-dimensional harmonic oscillator in gauge-invariant momentum phase-space. As usual, in this case we use ladder operators substitution to find eigenvalues of the Hamiltonian:

$$a = \frac{l_{\mathrm{B}}}{\sqrt{2}\hbar}\left(\Pi_x - \imath\Pi_y\right), \qquad a^\dagger = \frac{l_{\mathrm{B}}}{\sqrt{2}\hbar}\left(\Pi_x + \imath\Pi_y\right) \tag{2.37}$$

where we introduced the *magnetic length* $l_{\mathrm{B}} = \sqrt{\hbar/eB}$ — the radius of semi-classical cyclotron orbit. It is expedient as well, to introduce the *cyclotron frequency* $\omega_{\mathrm{C}} = \hbar/m_{\mathrm{e}}l_{\mathrm{B}}^2$ — the angular velocity of cyclotron precession. These two

[3]Here we used the relation $\left[O_0, f(O_1,\ldots,O_N\right] = \sum_{j=1}^{N}\frac{\partial f}{\partial O_j}\left[O_0, O_j\right]$, valid if $\left[\left[O_0, O_j\right], O_0\right] = \left[\left[O_0, O_j\right], O_j\right] = 0$ for any $j = 1,\ldots,N$.

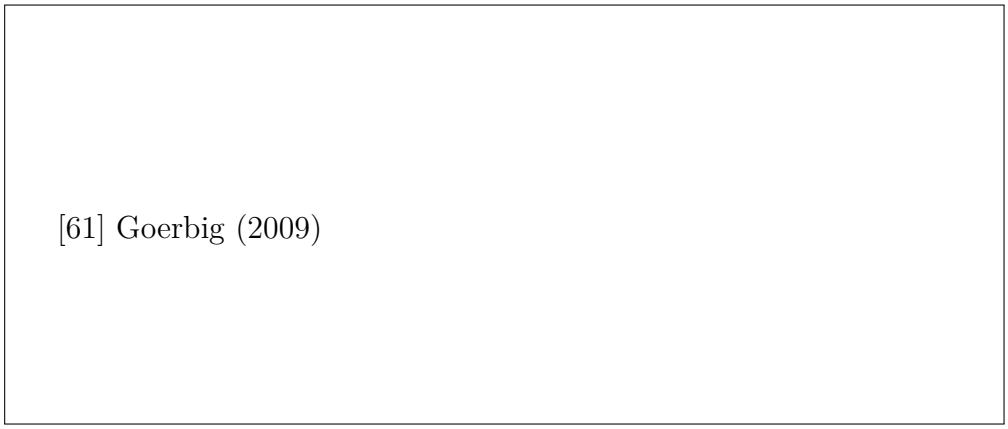

Figure 2.6: (a) Landau levels as a function of the magnetic field: $\varepsilon_n = \hbar\omega_{\mathrm{C}}\left(n+\frac{1}{2}\right) \propto B\left(n+\frac{1}{2}\right)$. From [61]. (b) Density of states (DOS). In a clean system, the DOS consists of equidistant delta peaks (grey) at the energies ε_n, whereas in a sample with a stronger impurity concentration, the peaks are broadened (dashed lines). The continuous black line represents the sum of overlapping peaks, and E_{F} denotes the Fermi energy. From [61].

quantities provide the characteristic length and energy scales of the system in presence of magnetic field. The Hamiltonian can thus be written under the customary form

$$H^{\mathrm{B}} = \hbar\omega_{\mathrm{C}}\left(a^{\dagger}a + \frac{1}{2}\right), \tag{2.38}$$

giving directly the energy eigenvalues

$$\varepsilon_n = \hbar\omega_{\mathrm{C}}\left(n + \frac{1}{2}\right) \tag{2.39}$$

The far reaching conclusion of this result is that in presence of magnetic field the spectrum consists of discrete energy levels, referred as *Landau levels*, so electron kinetic energy can not be varied in a continuous way, which means, as we know, that electric conductance is impossible. Nevertheless, this is a result one can expect, combining the fact of localization of particles on cyclotron orbits by magnetic field with the Heisenberg principle which counterbalances any spatial localization by momentum and thus kinetic energy quantization.

Now let us assess the degeneracy of a single Landau level. Following considerations can help finding the answer. First of all, it seems reasonable that application of magnetic field should not change average density of states if taken over sufficiently large energy range. Initially average DOS was equal to $m_{\mathrm{e}}/2\pi\hbar^2$ times

sample area S, whereas when split into Landau levels it is simply $1/\hbar\omega_{\mathrm{C}}$. It follows that the degeneracy of a Landau level is given by

$$N = \hbar\omega_{\mathrm{C}}(S\frac{m}{2\pi\hbar^2}) = \frac{BS}{h/e} \tag{2.40}$$

Here again the result is rather curious, since it argues that any Landau level contains the number of states N equal to the number of flux quanta h/e penetrating the sample or, in other terms, each state from any Landau level captures one quantum of flux. The Landau levels are thus massively degenerate.

Finally, the eigenstates form depends on the gauge choice, which is often related to the symmetry or geometry considerations. In the next section we will mostly deal with a long and narrow system, in which the translation invariance is preserved, but in one direction only. As a consequence the choice of Landau gauge is the most appropriate, so here we illustrate the eigenstates form in this gauge only. However, in general other geometries can require other gauge choices (e.g. symmetrical gauge for Corbino geometry). Landau gauge is represented by vector potential $\mathbf{A}(\mathbf{r}) = -yB\mathbf{e}_x$ and, as it can be easily seen, indeed preserves the translation invariance in the x direction. In this particular case the momentum $p_x = \hbar k$ is a good quantum number. The Hamiltonian (2.35) then reads

$$H^{\mathrm{B}} = \frac{p_y^2}{2m} + \frac{1}{2}m\omega_{\mathrm{C}}^2(y - y_0)^2, \text{ where } \quad y_0 = kl_{\mathrm{B}}^2 \tag{2.41}$$

so we can separate the variables and write the wavefunction of the n-th Landau level eigenstate in the form

$$\psi_{k,n}(x, y) = exp(\imath kx) \times \phi_n(y - y_0) \tag{2.42}$$

where $\phi_n(y)$ is the n-th oscillator state wavefunction, which exact form is irrelevant for the following discussion. Note, that y_0 plays a role of oscillator center in y direction, whereas in the x direction the state is spread over the whole sample length.

2.3.2 Integer Quantum Hall Effect

The situation in real samples is somehow different from the ideal one described above. First of all, because of the disorder, always present in real samples. In addition, in the following we will consider long and narrow geometry, hence we have to include the lateral confinement into discussion. The experimental results prove however, that Hall resistance quantization is independent of the given geometry or disorder configuration. To anticipate, these two ingredients: the obligatory presence of disorder and of the sample edges of arbitrary shape, but yet the robustness

of the phenomena against these factors, are crucial for the understanding of the mechanisms of the QHE, as it will become clear soon.

To begin, let us consider a long, narrow sample without disorder, as before, connected to two reservoirs on the left and on the right. The lateral confinement can be expressed in terms of a confinement potential $V_{\mathrm{c}}(y)$ such that, it is zero in the bulk, but rapidly increases near the sample edges. Besides, for simplicity we assume that on the scale of magnetic length this potential varies smoothly. Note also, that a potential of this form will not break translation invariance in the x direction. We then develop the confinement potential around the oscillator center $y_0 = kl_{\mathrm{B}}^2$

$$V_{\mathrm{c}}(y) \simeq V_{\mathrm{c}}(y_0) - eE(y_0)(y - y_0) + \mathcal{O}\left(\frac{\partial^2 V}{\partial y^2}\right), \tag{2.43}$$

where we introduced the local electric field E. Neglecting second-order terms in E yields to Hamiltonian

$$H^{\mathrm{B}} = \frac{p_y^2}{2m} + \frac{1}{2}m\omega_{\mathrm{C}}^2(y - y_0')^2 + V_{\mathrm{c}}(y_0') \tag{2.44}$$

with $y_0' = y_0 + eE(y_0)/m\omega_{\mathrm{C}}^2$, and energy spectrum

$$\varepsilon_{n,y_0} = \hbar\omega_{\mathrm{C}}\left(n + \frac{1}{2}\right) + V_{\mathrm{c}}(y_0) \tag{2.45}$$

Here we can omit the prime, since the variation of confinement potential between y_0 and y_0' is of the second order in E.

We infer from this result that the Landau levels structure is preserved under confinement, with the exception of the fact that the energy of a given state now depends on the confinement potential value at its center position y_0.

We can now calculate the current of the n-th Landau level in x direction

$$I_n^x = -\frac{e}{L_x}\sum_k \langle n, k\,|v_x|\,n, k\rangle \tag{2.46}$$

Matrix elements are easily evaluated

$$\langle n, k\,|v_x|\,n, k\rangle = \frac{1}{\hbar}\frac{\partial \varepsilon_{n,k}}{\partial k} \tag{2.47}$$

and one notice straight away that, due to the form of the confinement potential $V_{\mathrm{c}}(y)$ which is zero everywhere apart near the sample edges, the only non-zero matrix elements are those of so called *edge states*[64], i.e. the states having their centres y_0 situated within narrow bands near the edge, in which confinement potential is not constant. The concept of edge states plays a key role in QHE theory. Moreover,

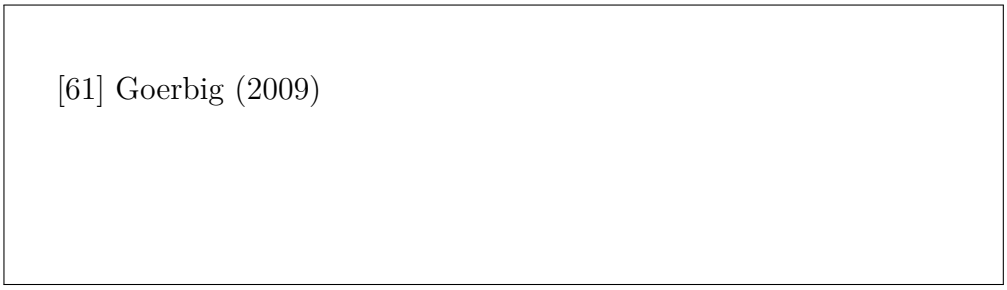

Figure 2.7: (a) Potential landscape of an electrostatic potential in a sample. The metallic contacts are described by the chemical potentials μ_{L} and μ_{R} for the left and right contacts, respectively. The sample is confined in the y-direction between $y_{\max}$ and $y_{\min}$. The thin lines indicate the equipotential lines. When approaching one of the sample edges, they become parallel to the edge. The green lines indicate the electronic motion with the guiding centre moving along the equipotential lines. The electron turns clockwise around a summit of the potential landscape, which is caused e.g. by a negatively charged impurity ($-$), and counter-clockwise around a valley ($+$). At the sample edges, the equipotential lines due to the confinement potential connect the two contacts on the left and on the right hand side. From [61]. (b) The Landau levels are bent upwards when approaching the sample edge, which may be modeled by an increasing confinement potential. One may associate with each Landau level n a maximal value $y^n_{\max}$ of the y-component where the Landau level crosses the chemical potential $\mu_{\max}$. From [61].

it is clear, that the derivative in (2.47) is of the opposite sign for upper and lower edges, meaning that the current flow direction is also opposite on the two edges, as though the current was circulating around the sample. This property is called *chirality* and is of huge consequence, because it so to say forbids the backscattering in the edge channels[17], since the only states of the opposite propagation direction into which an electron can be scattered are situated on the opposite edge, that is macroscopically far. Furthermore, the absence of backscattering implies also the absence of dissipation in the edge channels, that was by the way experimentally confirmed[85]. Indeed, the longitudinal resistance was measured to be zero whenever the Hall resistance draws a plateau, but rise up to several order of magnitude at the moment of transitions between plateaus.

We now switch from continuous to discrete derivative using wave vector quantisation condition $k_m = 2\pi m/L_x$, with m integer obtaining

$$\langle n, k_m \left| v_x \right| n, k_m \rangle = \frac{L_x}{2\pi\hbar}\frac{\Delta\varepsilon_{n,m}}{\Delta m} = \frac{L_x}{h}(\varepsilon_{n,m+1} - \varepsilon_{n,m}) \tag{2.48}$$

Thus the total current of n-th Landau level reads

$$I_n^x = -\frac{e}{L_x}\sum_m \frac{L}{h}(\varepsilon_{n,m+1} - \varepsilon_{n,m}) = -\frac{e}{h}(\varepsilon_{n,N} - \varepsilon_{n,0}) \tag{2.49}$$

since all intermediate terms cancel out. N and 0 indices correspond to states centred near upper and lower edge of the sample (N also being the degeneracy of a Landau level). This means that the transmitted current is given by the balance of counter-propagating edge currents on both edges, each of them depending on the given edge's chemical potential. Thus the current is non-zero only if there is a difference in chemical potentials between two edges. This difference can be identified with Hall voltage: $-eV_{\text{H}} = \mu_{L_y} - \mu_0$, leading to

$$I_n^x = -\frac{e^2}{h}V_{\text{H}} \tag{2.50}$$

From the obtained relation it appears that each Landau level contributes one quantum of conductance g_0 to the total conductance G that is therefore given in the case of ν filled levels by

$$G = \nu\frac{e^2}{h} \tag{2.51}$$

Now let us examine in short how the disorder affects the transport in quantum Hall regime. As it was already mentioned above, Hall resistance quantisation not seem to depend on the specific configuration or magnitude of disorder. This can be understood in the following way. Note first, that arbitrary disorder correspond to an arbitrary potential, that will break translation invariance also in x direction. This potential will have "pits" and "hills" and the density of states of a Landau level will be significantly enlarged, such that the kinetic energy is not reduced to a single value any more even in bulk, although most of states are still localized. Indeed, increasing of filling factor will result first in filling by the electrons of potential pits and thus formation of localized states in spatially separated zones. These zones become more and more extended with increasing filling until eventually zones connecting both edges are formed, when average filling is reached. If so, the backscattering becomes possible and the longitudinal resistance rises sharply, while transition between plateaus occurs in Hall resistance. If we continue to increase the filling factor, electrons will fill the potential hills, hence, similarly, zones of localized states will be formed and backscattering is again suppressed. At the same time a new edge channel is opened and a new plateau will be drawn. This is a percolation vision of QHE.

Chapter 3

Mesoscopic Transport in Graphene

3.1 Conducance and Shot Noise in Graphene

In this section we examine conductance and noise properties of coherent graphene conductor. These calculations were done by Tworzydlo et al. and also partially by Katsnelson.

Consider a simple model of ideal, quite narrow graphene strip of length L and width W, connected to two reservoirs. For the sake of simplicity, we consider a confinement potential in transversal direction to be smooth on the scale of the lattice spacing, since in this case two valleys are decoupled. Hence in the low energy excitation limit, that we discuss here, we can operate with a two-component wavefunction $\Psi = (\Psi_1, \Psi_2)$, taking into account valley (and spin) degeneracy in our calculations. Besides, the usual electrostatic potential confinement term is not applicable in the framework of Dirac equation for massless particles, because of the existence of anti-particles band and absence of gap between two bands, and a mass confinement approach is used instead. Consider the following Dirac equation

$$\left[v_{\mathrm{F}}\ \mathbf{p}\cdot\boldsymbol{\sigma} + v_{\mathrm{F}}^2 M(y)\sigma_z + \mu(x)\right]\Psi(\mathbf{r}) = \varepsilon\Psi(\mathbf{r}) \tag{3.1}$$

as it can be seen, it follows from the σ_z matrix diagonality, that the mass term induces a gap in the graphene spectrum. Therefore, an infinite mass term in Dirac equation is equivalent to infinite potential term in non-relativistic case, so we take $M(y)$ to be zero inside the strip and to go to infinity outside it. As for electrostatic potential energy term $\mu(x)$, it is used to account for carriers density in the strip, varied by gate voltage: $\mu(x) = \mu$ for $0 < x < L$, as well as to model the reservoirs. Indeed, the reservoirs by definition are assumed to contain a much larger number of modes than the conductor, so putting $\mu(x) = \mu_\infty$, with $|\mu_\infty| \gg |\mu|$ in the reservoirs ($x < 0$ and $x > L$), this condition is satisfied.

The infinite mass confinement correspond to the boundary condition [12]:

$$\Psi_1\Big|_{y=0} = \Psi_2\Big|_{y=0}, \qquad \Psi_2\Big|_{y=W} = -\Psi_2\Big|_{y=W} \tag{3.2}$$

and following transversal momenta quantisation

$$q_n = \frac{1}{W}\pi(n+\frac{1}{2}), \quad n = 0, 1, 2\ldots \tag{3.3}$$

To calculate the transmission probabilities of each mode as a function of electrostatic potential energy μ in the strip, we use textbook approach of modes matching at the interfaces between the strip and the reservoirs ($x = 0$ and $= L$). However, once again in the relativistic case there is a slight difference one should be aware of. As it follows from density current conservation

$$\mathbf{j}(\mathbf{r}) = ev_{\mathrm{F}}\Psi^{\dagger}(\mathbf{r})\boldsymbol{\sigma}\Psi(\mathbf{r}) \tag{3.4}$$

the only matching condition is the continuity of two components of Ψ.

An eigenstate of the system is described by two quantum numbers: one continuous — longitudinal wave vector k and one discrete — n, related to the quantized transversal momentum. The transversal wave vectors q_n depend only on the boundary conditions, assumed to be the same in the conductor and in the reservoirs and the eigenenergy in different parts of the system reads

$$\varepsilon_n = \begin{cases} \mu_\infty \pm \hbar v_{\mathrm{F}}\sqrt{k^2+q_n^2}, & x<0 \text{ and } L<x \\ \mu \pm \hbar v_{\mathrm{F}}\sqrt{\tilde{k}^2+q_n^2}, & 0<x<L \end{cases} \tag{3.5}$$

with k real and $\tilde{k}$ that can be both real and imaginary. Plus and minus signs stand for conductance and valence bands respectively. It follows from this discussion, that the transmission and reflection processes, being elastic, will not mix the modes and, as previously, separate transmission probabilities for each mode can be defined: $D_n = |t_n|^2$, where t_n are transmission amplitudes, obtained from modes matching calculations.

For the details of these calculations one is referred to the Appendix A in [149]. They yield the transmission probabilities D_n, that in the limit of $|\mu_\infty| \to \infty$ are given by

$$D_n = \left| \frac{k_n}{k_n \cos(k_n L) + \imath(\mu/\hbar v_{\mathrm{F}}) \sin(k_n L)} \right|^2, \tag{3.6}$$

with $k_n = \sqrt{(\mu/\hbar v_{\mathrm{F}})^2 - q_n^2}$.

In a model QPC modes are subsequently "opened", i.e. their transmission becomes perfect, when Fermi level position is changed progressively, while transmissions of "unopened" modes — those above Fermi level — is negligible most of the

time, giving rise to step-like transitions in the conductance. As it can be seen from eq. 3.6, this is not what we expect in a graphene strip (at least in the limit of $W/L,\ N \to \infty$, N being the total number of modes in the reservoirs), since in that case, in the opposite to the situation with a model QPC, a great number of modes above Fermi level have a transmission different from zero.

This aspect ratio constraint, i.e. the necessity for the conductor to be short and large, can be easily understood by considering a simple one-dimensional barrier tunnelling problem. Transmission probability decreases exponentially with both barrier length and height. Barrier length obviously corresponds to the strip length L, while barrier height is given by the energy difference between the Fermi level and the given unopened mode. This quantity is proportional to the transversal momentum quantum, which decreases itself as $\propto 1/W$. Therefore, in order for the above discussed condition of a great number of unopened modes with transmission different from zero to be accomplished, suitable aspect ratio is required.

So let us see, what do the described form of transmission probabilities imply in particular in terms of the conductance G and the Fano factor $\mathfrak{F}$. These quantities can be calculated in a straight forward manner, using already discussed expressions (2.17) and (2.26) (note, however, that the conductance quantum pre-factor g_0 now equals $\frac{4e^2}{h}$ in order to account for spin and valley degeneracies).

Besides, the details of calculations of transmission probabilities for other boundary conditions can be found within the same reference. The resulting conductance and Fano factor are nevertheless identical for any type of boundary conditions, at least in the limit of $W/L \to \infty$, condition which is satisfied already for moderate aspect ratios $W/L \gtrsim 4$. There the authors also compare the analytical calculations with numerical tight-binding model simulations, which confirm the analytical results.

In the indicated aspect ratio range these can be summarized as

$$\sigma \to g_0/\pi, \qquad \mathfrak{F} \to 1/3, \qquad \text{at } \mu = 0 \tag{3.7}$$

with conductivity $\sigma \equiv G \times L/W$. Furthermore, at $\mu = 0$, i.e. at Dirac point, the Fano factor exhibits maximum, whereas the conductance exhibits minimum. This is in fact, the most notable results of the presented calculation, that we tend to verify experimentally in our work.

The dependence on the aspect ratio of the conductivity σ and Fano factor $\mathfrak{F}$ at Dirac point ($\mu = 0$) are plotted in fig. 3.1. Both quantities reach the $W/L \to \infty$ limit indeed very quickly. In the opposite limit, the disparity of the behaviour for different boundary conditions can be attributed to the distinctions in the energy spectra. This limit actually reflects the situation, similar to one in a model QPC, discussed above, and therefore, "smooth edge" boundary condition, for instance, for which no modes are present at the Dirac point, leads to zero conductance and

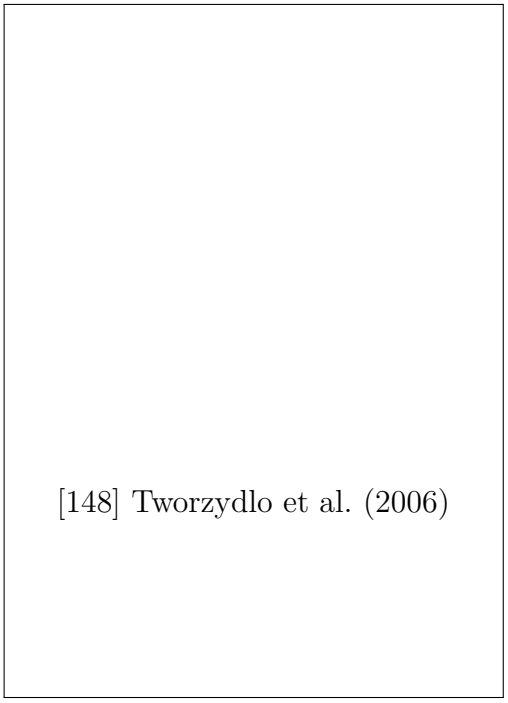

Figure 3.1: Conductivity σ and Fano factor $\mathfrak{F}$ at the Dirac point ($\mu = 0$), as a function of the aspect ratio of the graphene strip. The curves are calculated for two different boundary conditions: smooth edge (solid curves) using eq. 3.6 and "metallic armchair" edge (dashed curves, equation not specified in the text). The limit $W/L \to \infty$ (dotted lines) corresponds to expressions from eq. 3.7, regardless of the boundary condition. The data points for the armchair edge are the result of a numerical solution of the tight-binding model on a hexagonal lattice. From [148].

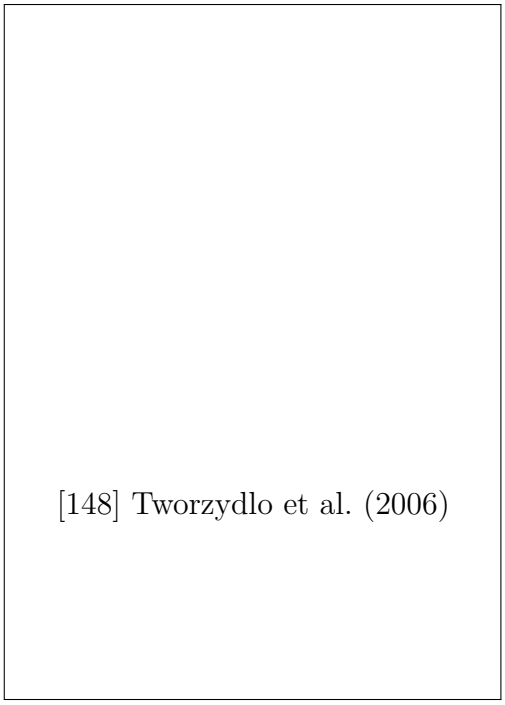

Figure 3.2: Fermi energy dependence of the conductivity σ and the Fano factor $\mathfrak{F}$ at fixed aspect ratio $W/L = 5$ for the case of a smooth edge (solid curves) or metallic armchair edge (dashed curves). The conductivity minimum at the Dirac point corresponds to maximal Fano factor. The oscillations signal the appearance of propagating modes in the graphene strip with increasing potential. From [148].

Fano factor equal to one (QPC closed), just as "metallic armchair edge" boundary condition, for which the spectrum contains exactly one mode at the Dirac point, leads to zero Fano facto and the conductance equal to g_0 (QPC with transmission one).

Figure 3.2 shows the dependence of the conductivity and of the Fano factor on Fermi level position. One sees clearly, that the values in (3.7) are corresponding minimum and maximum of the conductance and the Fano factor. On the other hand, far from the Dirac point, step-like oscillations around classical tendency of the conductance, similar to what can be seen when comparing QPC conductance and classical conductivity, show up. As for the Fano factor, it decreases rapidly if Fermi level move away of the Dirac point and one notices a near-ballistic behaviour, i.e. near zero Fano factor. This is yet not surprising, since in this limit, most of the modes are perfectly transmitting and only few contribute to the partitioning.

It is remarkable, that at the Dirac point the Fano factor attains the value 1/3, which is characteristic for disordered metal conductors (see discussion on diffusive transport in Chapter 2), although the studied graphene strip is defectless. One notes a mathematically similar $1/\coth$ dependence of the transmission probabilities for both cases, that explains the quantitative result. Qualitatively, however, it is difficult to establish any physical analogy between these two very distinct phenomena. In [148] the authors argue, that the result can be attributed to the effect of Zitterbewegung, which would be similar to classical diffusive dynamics. Yet, there was no explicit evidence of this phenomenon in graphene up to now, so such parallels are to be treated with care.

3.2 Quantum Hall Effect in Graphene

Quantum Hall Effect in graphene, referred as *relativistic* in some literature, arises from the same mechanisms as its non-relativistic counterpart. Yet, few differences have to be pointed out. The main distinction, which is moreover at the origin of all others, is Landau levels structure. If one follows the same approach as in the sec. 2.3 of the previous chapter, substitution (2.34) yields

$$H_{\mathrm{D}}^{\mathrm{B}} = v_{\mathrm{F}} \begin{pmatrix} 0 & \Pi_x - \imath\Pi_y \\ \Pi_x + \imath\Pi_y & 0 \end{pmatrix} = \sqrt{2}\frac{\hbar v_{\mathrm{F}}}{l_{\mathrm{B}}} \begin{pmatrix} 0 & a \\ a^\dagger & 0 \end{pmatrix} \tag{3.8}$$

and as previously we introduce the cyclotron frequency, which however this time reads in a different manner: $\omega'_{\mathrm{C}} = \sqrt{2}v_{\mathrm{F}}/l_{\mathrm{B}}$. Like before, the eigenstates of relativistic Hamiltonian are denoted with two-component vectors or 2-spinors

$$\psi_n = \begin{pmatrix} u_n \\ v_n \end{pmatrix} \tag{3.9}$$

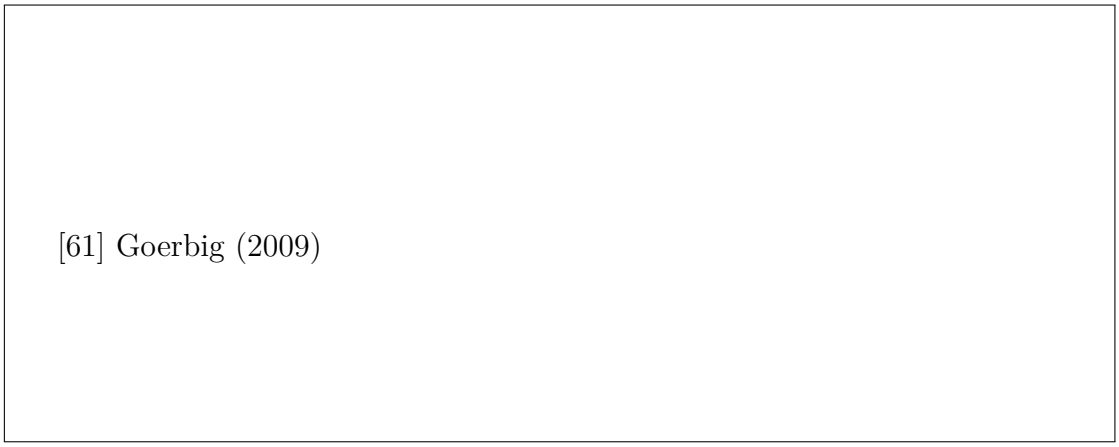

Figure 3.3: (a) Mass confinement for relativistic Landau levels. Whereas the electron-like Landau levels (plus sign in eq. 3.12) are bent upwards when approaching the sample edge ($y_{\max}$), the hole-like Landau levels (plus sign in eq. 3.12) are bent downwards. The fate of the n = 0 Landau level depends on the valley (parity anomaly) – in one valley (K), the level energy decreases, whereas it increases in the other valley (K'). From [61]. (b) Filling of the bulk Landau levels at $\nu = 0$. All electron-like Landau levels are unoccupied whereas all hole-like Landau levels are completely filled. The n = 0 Landau level is altogether half-filled. From [61].

and the eigenvalue equation leads to the relation

$$a^\dagger a \; v_n = \left(\frac{\varepsilon}{\hbar\omega'_{\rm C}}\right)^2 v_n \tag{3.10}$$

whereas the first component of the vector is related to v_n by the expression $\hbar\omega'_{\rm C} a \, v_n = \varepsilon_n u_n$. It is clear from eq. 3.10, that v_n is the eigenfunction of number operator $n = a^\dagger a$, namely $v_n \sim |n\rangle$ (and $u_n \sim a v_n \sim |n-1\rangle$), while the eigenvalues satisfy $\varepsilon_n^2 = (\hbar\omega'_{\rm C})^2 n$. This yields eigenvectors

$$\psi_{n=0} = \begin{pmatrix} 0 \\ |0\rangle \end{pmatrix} \qquad \text{and} \qquad \psi_{n\neq 0} = \frac{1}{\sqrt{2}} \begin{pmatrix} |n-1\rangle \\ \pm\,|n\rangle \end{pmatrix} \tag{3.11}$$

and eigenvalues

$$\varepsilon_n = \pm\hbar\omega'_{\rm C}\sqrt{n} = \pm v_{\rm F}\sqrt{\hbar e B n} \tag{3.12}$$

where plus and minus signs as always stand for conductance and valence bands respectively. Hence, in contrast to non-relativistic case, where Landau level energy is linear in magnetic field and level index, in the relativistic case it disperses as a square root both of these quantities (see fig. 3.3.b). Moreover, particle anti-particle parity is conserved in magnetic field and the Landau levels sequence is



Figure 3.4: Hall resistance (black) and magnetoresistance (orange) as a function of gate voltage at fixed magnetic field $B = 9\,\mathrm{T}$, measured at 1.6 K. The upper inset shows a detailed view of high-filling-factor plateaus measured at 30 mK. From [173].

symmetric about zero of energy. This particular Landau level structure is in fact the reason of all distinctions between conventional integer QHE and relativistic QHE, as it will be briefly demonstrated in the next few paragraphs.

To begin, consider as previously, a conductor of long and narrow geometry, the problem is treated in Landau gauge. We again use the substitution $y_0 = kl_{\mathrm{B}}^2$, with y_0 — the oscillator center in y direction. After a calculation, that can be found for example in [61], one obtains the following expression for energy eigenvalues

$$\varepsilon_{n,y_0} = \pm\sqrt{M^2(y_0) + 2\frac{\hbar^2 v_{\mathrm{F}}^2}{l_{\mathrm{B}}^2}n}, \tag{3.13}$$

represented in fig. 3.3.a. Note first, that edge channels persist in the relativistic case, meaning that the transport mechanism remains the same. In return, there is a Landau level at zero energy, leading to a peak in longitudinal resistance and absence of plateau for Hall resistance at Dirac point. In addition, Landau levels degeneracy is doubled as compared to a simple situation of spin-associated two-degeneracy. These two elements reveal the main feature of relativistic QHE: the Hall resistance quantization is observed at the fillings

$$\nu = \pm 2(2n+1) \tag{3.14}$$

yielding a sequence of plateaus represented in fig. 3.4.

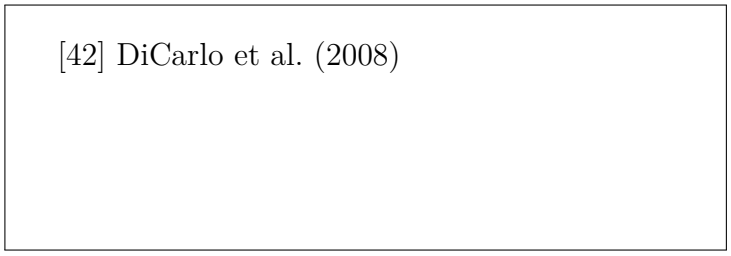

Figure 3.5: The schematics of the experimental setup used by DiCarlo et al..

3.3 Experimental Results

The relativistic Quantum Hall Effect in graphene was quickly validated experimentally. The evidence of the specific sequence of Hall plateaus (3.14), predicted by the above theory, was provided by Novoselov et al. and by Zhang et al. very soon after graphene was discovered. The square root dependence (3.12) of the Landau levels on the magnetic field was demonstrated in the epitaxial graphene by Sadowski et al. Furthermore, observation of the Quantum Hall Effect in graphene at room temperature was reported in [116]. Since then, several experimentalist groups actively studied Quantum Hall Effect in graphene, see refs. [171], [159], [170], [164], [105], [9], [166] for example, all confirming the results described in the previous section. Even the Fractional Quantum Hall Effect was observed in graphene by Dean et al. (on boron nitride), by Feldman et al. and by other groups. For more complete review of the experimental (and theoretical) works in this field reader is referred to [37] for instance.

The situation is rather different with another theoretical results, presented in this chapter. The conclusions of the evanescence modes model proposed by Tworzydlo et al., that we discussed in the sec. 3.1 raised a great interest in the mesoscopic physics community. An empirical confirmation of the predicted effects could serve a robust prove of that graphene pseudo-relativistic physics is indeed attainable for experimentalists. Despite the difficulties of such experimental task, for instance fabrication of ballistic graphene samples or proper measurement of the shot noise, two groups have succeeded to investigate the shot noise in graphene-based devices. However, the results of these two studies lead to somewhat contradictory conclusions as it will be shown in what follows.

One study was carried out by DiCarlo et al. Samples of various aspect ratios and lengths were examined: $W \times L \simeq 2\,\mu\text{m} \times 350\,\text{nm}$, $1.8\,\mu\text{m} \times 1.3\,\mu\text{m}$, $2\,\mu\text{m} \times 300\,\text{nm}$, $1.8\,\mu\text{m} \times 1\,\mu\text{m}$ (presumably multi-layer) and a graphene p-n junction device. The conclusions of this study are that the ballistic regime was not attained, samples in the diffusive regime show Fano factor ≈ 0.35, which however does not vary with gate voltage (up to carrier densities of about $1 \times 10^{12}\,\text{cm}^{-2}$, which the used setup

allow to attain). Only the multi-layer sample demonstrated the variation of the Fano factor with gate voltage, which decreased from .33 at the neutrality point to 0.25 at $n_s \sim 6 \times 10^{12}\,\mathrm{cm}^{-2}$. The universal value of the minimal conductivity $\frac{4e^2}{\pi h}$ was not observed, instead measurements showed a multiplicity of values depending on the sample. Main results of this study are presented in fig. 3.6. In short, this experiment does not provide a clear evidence of the evanescence modes theory, without disapproving it completely.

The key points of this study are:

- The noise was measured with the cross-correlation technique, cryogenic low-noise amplifiers (calibrated with Johnson-Nyquist thermometry) together with resonant circuits were used for noise detection at 1.5 MHz.
- The lowest measurement temperature was 0.3 K.
- Independent measurements in the Quantum Hall regime (however in a separate cryostat) were used to determine carrier density dependence on gate voltage. From that, the mean free path was estimated, varying between ~ 25 and 40 nm depending on the sample. Hence a clear evidence of diffusive transport in all samples was presented.

As drawbacks can be considered the following elements:

- Two-point approach was used for conductance and noise measurements, meaning that in both experiments contact resistance was not avoided.
- The samples were not checked in Raman spectroscope in order to confirm their monolayerness and probably not annealed.
- The effects of the eventual capacitive back-gate shunt at MHz frequency was not discussed in this work.

In the other study carried out by Danneau et al. also samples of various aspect ratios and lengths were examined: $W \times L \simeq 4.8\,\mu\mathrm{m} \times 200\,\mathrm{nm}$, $2\,\mu\mathrm{m} \times 200\,\mathrm{nm}$, $900\,\mathrm{nm} \times 300\,\mathrm{nm}$, $1\,\mu\mathrm{m} \times 500\,\mathrm{nm}$, $4\,\mu\mathrm{m} \times 950\,\mathrm{nm}$ (considered to be in the diffusive regime), $900\,\mathrm{nm} \times 500\,\mathrm{nm}$ (with non-parallel leads). The conclusions of this study are more promising, the variation of the Fano factor was observed in most of their samples. In particularly, one sample showed the minimal conductivity very close to $\frac{4e^2}{\pi h}$ and Fano factor $\simeq 1/3$ at the neutrality point, decreasing when the carrier density increases. In another two samples with large aspect ratio however, the neutrality point was not attained experimentally, but the variation of the Fano factor was still observed (see fig. 3.9). Moreover, the Fano factor in the sample considered to be in the diffusive regime also manifested a variation with the gate voltage. In short, although the results of this study attest the conclusions of the evanescence modes theory, several emphasized issues suggest that a new study

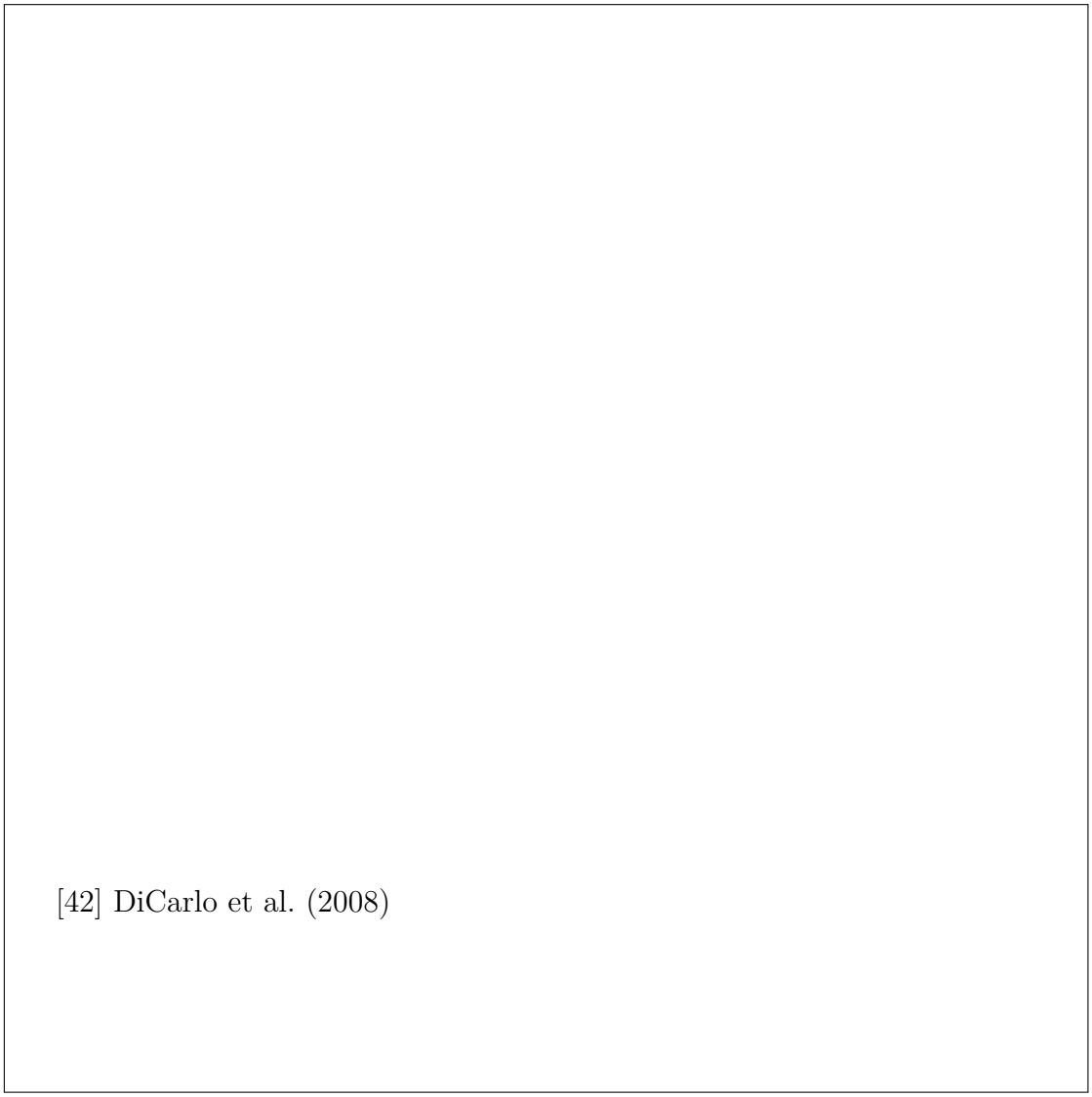

Figure 3.6: Some results of the work by DiCarlo et al.. For Sample A1, wide and short (2 µm×350 nm) differential resistance (a) and Fano factor (b) as a function of the back gate voltage at electron temperature $T_e = 0.3\,\mathrm{K}$ are shown. For Sample A2, more squared (1.8 µm×1.3 µm, patterned on the same graphene sheet as A1) are shown differential resistance and conductance (c) as well as Fano factor (d) as a function of the back gate voltage at two electron temperatures (T_e = 0.3 K and 1.1 K). For Sample D, presumably multi-layer (1.8 µm×1 µm) are shown differential resistance and conductance (e) as well as Fano factor (f) as a function of the back gate voltage at the same two electron temperatures. From [42].

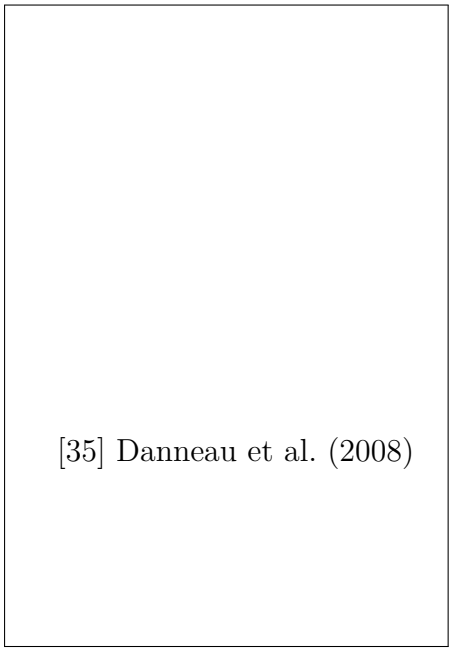

Figure 3.7: The schematics of the experimental setup used by Danneau et al..

could shine more light on the validity of this theory.

The key points of this study are:

- Noise measurement at very high frequency (600-850 MHz), without any $1/f$ noise contributions. Use of cryogenic low-noise amplifiers, independent calibration with a tunnel junction (see fig. 3.7).
- Large temperature range: 4.2-30 K

As drawbacks can be considered the following elements:

- Use of the auto-correlation technique and two-point geometry for the noise (and conductance for latter) measurements. (Avoiding the contact resistance contribution to the measurement is particularly important in the case of the minimal conductivity determination).
- The correspondence between gate voltage and carrier density was not determined separately, this is also the case for the mobility and mean free path. Hence the assumption of ballistic regime was not verified independently.
- Quantitative agreement with the theory was not obtained even for the best measurement, factor ~ 9 discrepancy between gate capacitance estimated from the evanescence modes theory and the one estimated from a simple two plane capacitor model.

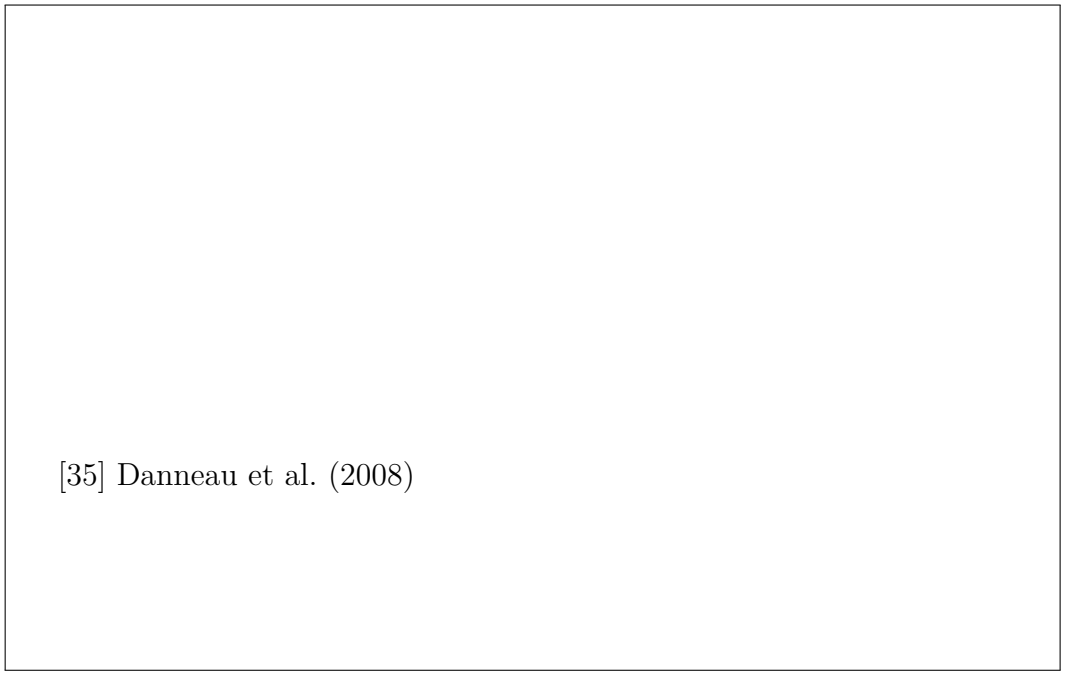

Figure 3.8: Some results of the work by Danneau et al.. For Sample A ($4.8\,\mu m \times 200\,nm$): (a) differential resistance (in green, left axis) and conductance (in blue, right axis) as a function of the back gate voltage, (b) Fano factor as a function of the back gate and the bias voltages at $T = 8.5\,K$. For Sample D ($1\,\mu m \times 500\,\mu m$): (c) differential resistance (in green, left axis) and conductance (in blue, right axis) as a function of the back gate voltage, (d) Fano factor as a function of the back gate and the bias voltages at $T = 5\,K$. For Sample E, presumably in diffusive regime ($4\,\mu m \times 950\,nm$): (e) differential resistance (in green, left axis) and conductance (in blue, right axis) as a function of the back gate voltage, (f) Fano factor as a function of the back gate and the bias voltages at $T = 12\,K$. From [35].

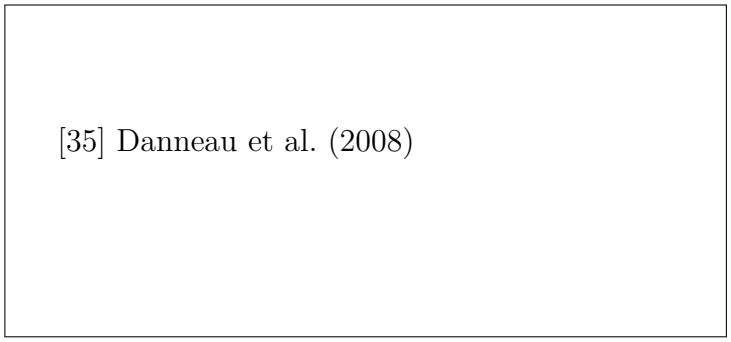

Figure 3.9: Fano factor for samples A (blue dots), B (orange dots) and C (green dots), all having $W/L \geq 3$, as a function of $\delta V = V_G - V_D$, V_G being the back gate voltage and V_D — its value at which the Dirac point is reached. From [35].

- Neutrality point is not reached experimentally in two samples, claimed to be in ballistic regime (estimated gate voltage values corresponding to the neutrality point are 145 and 100 V).
- Only in one sample, where the neutrality point was attained experimentally, the correct value of the minimal conductivity was observed.
- Samples probably not checked in Raman spectroscope for monolayerness and probably not annealed.
- High voltage used for the sample biasing (up to 50 mV)
- The effects of the eventual capacitive back-gate shunt at almost GHz frequency was not discussed in this work.

On the whole, two experimental works tried to validate the evanescence modes theory proposed by Tworzydlo et al. Two works disagree in several points, quantitative agreement with this theory was not obtained in both cases. As far as we know, no other experiments were performed in this subject, while the question remains opened. This fact motivated the need to design a new experiment, eventually free of the above-mentioned drawback elements. This is the purpose of this work, that we present in what follows.

Part II

Experimental Setup and Device

Chapter 4

Measurement System Principle

4.1 Experimental Requirements and Techniques

4.1.1 Typical Scales

We start with an overview of the typical scales observed in graphene samples on SiO_2. At the end we will also touch upon the suspended graphene and graphene on hBN.

Typical graphene samples, obtained by mechanical exfoliation, are usually p-doped. To be able to vary the carrier density, in particular to reach the Dirac point, one usually gates the graphene sample. Back-gate is often preferred because of the relative simplicity of fabrication. Carrier densities as high as $1 \times 10^{-13}\,\mathrm{cm}^{-2}$ are attained. It is important to have an estimate of the sample resistance, when conceiving a measurement system. The resistivity of graphene is very low at high carrier density (hundreds of ohms), while at the Dirac point it reaches its maximum. In ballistic samples it is predicted to be $\frac{\pi h}{4e^2} \approx 20\,\mathrm{k}\Omega$. For samples in diffusive regime, a very extensive study by Tan et al. reports on 19 samples which maximum resistivity lay between $2\,\mathrm{k}\Omega$ and $5\,\mathrm{k}\Omega$ with one sample however showing much higher resistivity of $\simeq 13\,\mathrm{k}\Omega$. Higher values were also reported in refs. [111] and [42].

The aim of our experiment is to probe coherent transport properties in graphene. The key quantity for that is the phase coherence length, given by $l_\phi = \sqrt{D\tau_\phi}$, with D — diffusion constant and τ_ϕ — the time of phase decoherence. D on its turn depends on the elastic mean free path l_{el}: $D = \frac{1}{2} v_{\mathrm{F}} l_{\mathrm{el}}$, while τ_ϕ is temperature and carrier density dependent. The crucial requirement for our samples is thus that their effective dimensions remain beyond the phase coherence length at temperatures we want to conduct our measurements, i.e. at 4 K. This quantity in graphene on SiO_2 was investigated by several groups. Berezovsky et al. found $l_\phi \simeq 500\,\mathrm{nm}$

at 4 K with $l_{\mathrm{el}} \simeq 50\,\mathrm{nm}$ (by the way these same values were observed by Eless et al. but in graphene grown on SiC), Morozov et al. reports $l_\phi \simeq 1\,\mu\mathrm{m}$ at the same temperature. Other studies done at $\simeq 250\,\mathrm{mK}$ find phase coherence length of about $1\,\mu\mathrm{m}$[29] and $3-5\,\mu\mathrm{m}$[108]. Interestingly, investigation of phase coherence length in a graphite wire (7 ± 1 layers) on SiO_2 was carried out by Graf et al., which obtained $l_\phi \simeq 2\,\mu\mathrm{m}$ at 4 K. Finally, another quite surprising result was published by Minke et al., who studied coherence length in very narrow graphene ribbons ($40\,\mathrm{nm} \times 1\,\mu\mathrm{m}$), for the conclusion was that l_ϕ in such particular systems is much shorter that in "bulk" graphene: $\approx 75\,\mathrm{nm}$ at 4 K.

Second crucial requirement we are supposed to fulfil, namely ballistic regime, is characterized by elastic mean free path. This quantity is carrier density dependent so we will consider it for densities $\sim 1-10\times10^{12}\,\mathrm{cm}^{-2}$. Some values, encountered in literature were already mentioned. In the work by Tan et al. one finds l_{el} ranging from 10 nm to 500 nm for most of the numerous samples they studied and for most carrier density ranges, while Morozov et al. reports $l_{\mathrm{el}} \simeq 80\,\mathrm{nm}$. However, values indicated in ref. [108] are even higher: $l_\phi \simeq 0.5-1\,\mu\mathrm{m}$.

Now let us see, how these values can be improved. One technique consists in placing a *hexagonal boron nitride* (hBN) layer between substrate and graphene. This material is quite similar to graphene: it is also a two-dimensional crystal with a hexagonal lattice of close lattice constant, except that each sublattice is occupied by different kinds of atoms, Boron and Nitrogen, making of it a large band gap semiconductor. Thus hBN partially protects graphene from the effect of SiO_2 substrate, without modifying its electronic properties. In the work by Dean et al. mobilities about $60\,000\,\mathrm{cm}^2\,\mathrm{V}^{-1}\,\mathrm{s}^{-1}$ are reported for graphene on hBN, corresponding to the mean free path varying from 200 nm to 700 nm. More recent work by Calado et al., in which graphene synthesised by chemical vapour deposition on copper foil and then transferred on top of a hBN layer on SiO_2 is studied, reports $l_\phi \simeq 200-400\,\mathrm{nm}$. But the most efficient way to obtain high mobility graphene remains fabrication of suspended samples by etching the substrate under the graphene layer or by placing the graphene layer over a trench prepared on the substrate beforehand. In this case mean free paths as long as $1.2\,\mu\mathrm{m}$ can be attained[15].

Given these facts, it seems justified to consider typical values of coherence length l_ϕ to lay between 500 nm and $1\,\mu\mathrm{m}$ and elastic mean free path $\approx 200\,\mathrm{nm}$ attainable. As for the minimal resistivity, it is fixed around $\approx 20\,\mathrm{k}\Omega$ in ballistic systems, while in diffusive systems the dispersion is quite significant. Nevertheless values between $4\,\mathrm{k}\Omega$ and $6\,\mathrm{k}\Omega$ seem reasonable.

4.1.2 Noise Measurement Techniques

In this section we will treat various techniques of noise measurement at zero frequency (i.e. $\hbar\omega \ll eV$)[1]. In this limit, the common approach is to measure the voltage noise across the sample $S_{\mathrm{V}} = S_{\mathrm{I}}/G^2$ (G being its conductance) which echoes the current noise, generated by the sample. The final step of Power Spectral Density calculation is usually done by a commercial spectrometer or by an analog-to-digital conversion PC card together with a software FFT[2] bloc. Just as for the conductance measurement, four-point technique is preferred, since otherwise contribution to the detected noise of the thermal noise generated by the contact resistances will be hard to separate. The most challenging issue is however the noise, added by the detection system itself.

Hereafter, we note as S^{s} the sample (voltage) noise (the noise, one tends to detect) and as S^{d} — the noise due to the detection system or the *detection noise*. This latter is in the most cases much stronger than the sample noise: $S^{\mathrm{s}} \ll S^{\mathrm{d}}$, and it is extremely difficult to eliminate its contribution from the result of the measurement $S^{\mathrm{m}} = S^{\mathrm{s}} + S^{\mathrm{d}}$. Furthermore, S^{s} often represents a too weak signal to be measured directly, and an amplification is then required, being the main source of additional noise. Therefore, the amplifier performance is very important and the amplifier's voltage and current noise characteristics $S^{\mathrm{a}}_{\mathrm{V}}$ and $S^{\mathrm{a}}_{\mathrm{I}}$ (referred to the input of the amplifier) become as relevant as such parameters as its gain or bandwidth. In some rare situations, the detector noise S^{d} can be measured separately, and then subtracted from the final result, but since $S^{\mathrm{d}} \gg S^{\mathrm{s}}$ the uncertainty of obtained result δS^{m} will still be much greater than the S^{s}. These fluctuations usually have a Gaussian statistics and thus by averaging of the spectra over an acquisition time τ_m this uncertainty can be reduced according to the relation

$$\delta S^{\mathrm{m}} = \sqrt{2}\frac{S^{\mathrm{m}}}{\sqrt{\Delta f \tau_m}} \simeq \sqrt{2}\frac{S^{\mathrm{d}}}{\sqrt{\Delta f \tau_m}} \tag{4.1}$$

where Δf is a measurement bandwidth. The efficiency of this approach is however limited by the amplifiers gain fluctuations and the required precision may not be attained.

Commercial room-temperature low noise amplifiers of acceptable performance exist, but their usage has an important drawback: the low to room temperature connection is usually done with long coaxial cables, yielding a significant capacitance to the ground. The sample impedance often being quite high as well, this leads to a notable bandwidth reduction, as a consequence of the RC-cut. $1/f$ noise defines the lower limit of the useful bandwidth. In order to overcome these limitations a cryogenic amplifier can be placed in the proximity of the sample,

[1] More exhaustive survey about the noise measurement techniques can be found in [60].

[2] FFT — Fast Fourier Transform

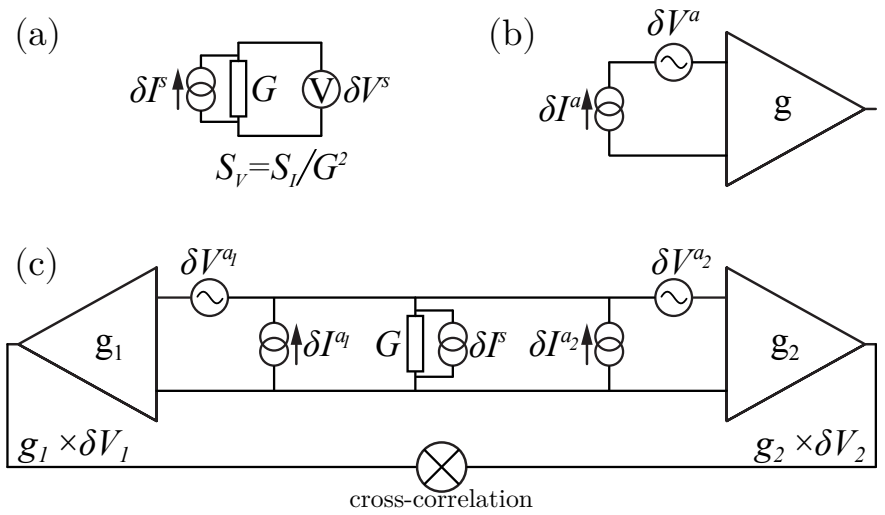

Figure 4.1: Schematic representation of the voltage noise measurement (a) and of an amplifier with its voltage and current noise sources, g designating the amplifier gain (b). On (c) is displayed the principle of cross-correlation measurement with all noise sources explicitly shown, the sample of conductance G being in the center.

therefore reducing the connecting cables length and corresponding capacitance. If however, this is still not sufficient e.g. $1/f$ noise is too high within the measurement bandwidth, adding a RLC resonant circuit to the amplification chain can be a solution. Such circuit shifts the passband to higher frequencies, allowing to attain the regime in which the $1/f$ noise becomes negligible. The resulting passband has a Lorentzian shape of width $1/2\pi RC$ and is centred at the frequency $f_{\text{res}} = 1/2\pi\sqrt{LC}$, with R, L and C — respectively resistance, inductance and capacitance of the resonant circuit. The circuit capacitance can not be reduced below the one of the coaxial cables, just as the resistance is limited by the sample resistance. The inductance is hence the only "free" parameter to control the resonant circuit characteristics. Note also, that the skin effect increases the resistive losses of the inductor, modifying the parameters of the resonant circuit at high frequency.

Yet, the most powerful method remains the cross-correlation detection, represented schematically in fig. 4.1.b. Although, as one notices, a duplication of the detection system is required, at this price one gets a remarkable advantage — such a way of detection directly suppresses the contribution to the measurement results of the detection system voltage noise and in some cases even the current noise contribution is suppressed.

Let us see, how does this method work. First of all, recall that the total

fluctuations at the i-th amplifier input read

$$\delta V_i = \delta V^{\mathrm{a}_i} + G^{-1}(\delta I^{\mathrm{a}_1} + \delta I^{\mathrm{a}_2}) + G^{-1}\delta I^{\mathrm{s}} \tag{4.2}$$

yielding the following expression for the autocorrelation noise (referred to input)

$$S_{\mathrm{V}_i} \propto \left\langle \delta V_i^2 \right\rangle = \left\langle (\delta V^{\mathrm{a}_i})^2 \right\rangle + G^{-2}\left\langle (\delta I^{\mathrm{a}_1})^2 \right\rangle + G^{-2}\left\langle (\delta I^{\mathrm{a}_2})^2 \right\rangle + G^{-2}\left\langle (\delta I^{\mathrm{s}})^2 \right\rangle, \tag{4.3}$$

while the cross-correlation noise is given by

$$S_{\mathrm{V_1V_2}} \propto \langle \delta V_1 \delta V_2 \rangle = G^{-2}\left\langle (\delta I^{\mathrm{a}_1})^2 \right\rangle + G^{-2}\left\langle (\delta I^{\mathrm{a}_2})^2 \right\rangle + G^{-2}\left\langle (\delta I^{\mathrm{s}})^2 \right\rangle \tag{4.4}$$

As it can be seen, the voltage fluctuations term disappears from the expression (4.4) for the cross correlation. Indeed, the cross-correlation measurement contains only the information mutual to both detectors. While the noise currents, generated by the both amplifiers, will run through the sample and the produced voltage noise will be detected also by the both amplifiers, voltage noise of each amplifier, considered uncorrelated, will be detected only by the corresponding amplifier and will not be contained in the cross-correlation. It is then clear, that using of a sample in which the signal propagation is non-reciprocal, like in QHE regime, or separation of the amplifiers from the sample using several resistors will provide a configuration, in which even the amplifiers current noise term is absent.

In return, the uncertainty on the detected noise spectral density will still depend on the detection noise:

$$\delta S^{\mathrm{m}} \simeq \frac{S^{\mathrm{d}}}{\sqrt{\Delta f \tau_m}} \tag{4.5}$$

even though a speed-up by a factor 2 (for a fixed uncertainty) is apparent due to twice as much information detected by two independent measurement lines.

All presented methods were integrated in the measurement system used in this work.

4.2 Technical Realisation

In the following we aim to illustrate the technical aspects of our experimental setup and to justify the technical solutions we opted for in view of the conclusions of the previous section. We start the section with the discussion of the device "architecture". We then explain the principle of the measurement system and present a brief analysis of the corresponding electrical circuit, while the cryogenic amplifiers concept is detailed in a separate paragraph at the end of the section. The description of the cryogenic inset, carrying the measurement circuit, and the noise detection system, based on the rapid analog-to-digital conversion PC card, are both transferred into the Appendices B.1 and B.2 respectively.

4.2.1 Device Design

The graphene-based device is the essential component of the experimental setup and, by the way, its fabrication discussed in details in the next chapter, also presents a great piece of work.

The figure 4.2 shows the sketch of the device. The core element of the device is a graphene sample of particular form, connected to six strip electrodes. The device is thus designed to allow 4-point cross-correlation measurement, that offers a number of obvious advantages (although having as a drawback the difficulty of fabrication). Two additional electrodes (electrically disconnected from the graphene layer) are the side gates, used to vary the carrier density in the graphene layer. The back gate, despite its greater efficiency, was avoided in this design, because of the related shunt capacitance, that can be comparable to the graphene resistance at the frequencies the noise measurements are done, allowing a part of current fluctuations to sink through it. For the same reason, the device substrate material is the intrinsic Si with SiO_2 layer on top.

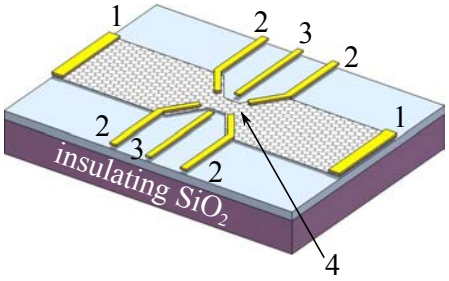

Figure 4.2: Sketch of the graphene-based device: 1 — two current injection electrodes, 2 — four voltage probes, 3 — side-gates (electrically disconnected from the graphene), 4 — nano-constriction, which plays a role of coherent conductor (proportions are not conserved for better visibility). Everything is situated on top of an insulating silicon substrate (in purple), containing a SiO_2 capping layer (in light blue).

The truly critical point, that deserves our special attention is however the shape of the graphene sample. Recall from the previous chapter, that our intention is to study a ballistic graphene conductor of particular aspect ratio, namely width/length above 3.5. Such aspect ratio, way above one, is quite uncommon, so a specific approach is required. Indeed, in subsec. 4.1.1 we specified the value $\approx 200\,\mathrm{nm}$ as a target mean free path value to count on, yielding the optimal dimensions, length$\times$width of about $200\,\mathrm{nm} \times 800\,\mathrm{nm}$. Yet, conductor having such peculiar orientation with respect to the current direction, it would be extremely difficult to reliably contact six electrodes to it. For these reasons, the following solution was suggested.

As it can be seen on the sketch the graphene layer has a constriction in the middle. An essential detail to understand is that in our device what plays a role of the coherent conductor which transport properties we probe, is the zone of the constriction, i.e. this very narrow strip of graphene, whereas the two wide parts of graphene on the both sides correspond to the model reservoirs. Hence, the required dimensions of the conductor can be easily attained, while its contacting remains relatively feasible. On the other hand, the constriction, being much narrower, than the rest of the graphene layer, the transport properties of the latter will be entirely defined by the physics in the constriction. Besides, in that case the two reservoirs are defined as two parts of graphene on both sides of the coherent conductor of length l_ϕ, i.e. phase coherence length. In other words, the reservoirs are everywhere except the segment of length l_ϕ in the middle of the layer.

In addition, such geometry presents second important advantage: the conductor and the reservoirs being a part of the same graphene crystal, the contact between them is perfect, that is extremely difficult to achieve with usual metal deposition technique. The contact resistance between the metallic electrodes and graphene sample is yet still present but at distance from the constriction greater than the phase coherence length, therefore playing no role in the electronic transport through the constriction. Hence, any Fabry-Pérot-type resonances or Coulomb blockade-type effects are avoided.

It is true that within this approach the real dimensions of the coherent conductor are hard to identify, first of all because the fabrication process limits precision for the resulting constriction dimensions and second, because it is difficult in practice to define where the conductor ends and the reservoirs start. On the other hand, we know that the phase coherence length in the exfoliated graphene on SiO_2 ranges between 0.5 µm and 1 µm (see subsec. 4.1.1) giving us the approximate idea of conductor's size. Furthermore, the constriction, because of its high resistance, delimits the effective conductor much better, than simply the distance between the voltage probes. We will anyway keep in mind, that at least the intended length×width dimensions are 200 nm × 800 nm.

4.2.2 Measurement System

Let us start with an overview of the main elements of the system. The schematics of the measurement circuit is given in fig. 4.3. The device design already gives the idea of the required circuitry: two separate lines for current injection and sinking, four identical voltage probe lines, one line to apply the gate voltage (two branches of the side-gates are already shorted in the device). Two 50 kΩ resistors, placed near the device and separating it from current injection and sinking lines will be particularly useful for current biasing of the device at high frequency. In addition, the setup is equipped with two thermometers and two heaters, placed in

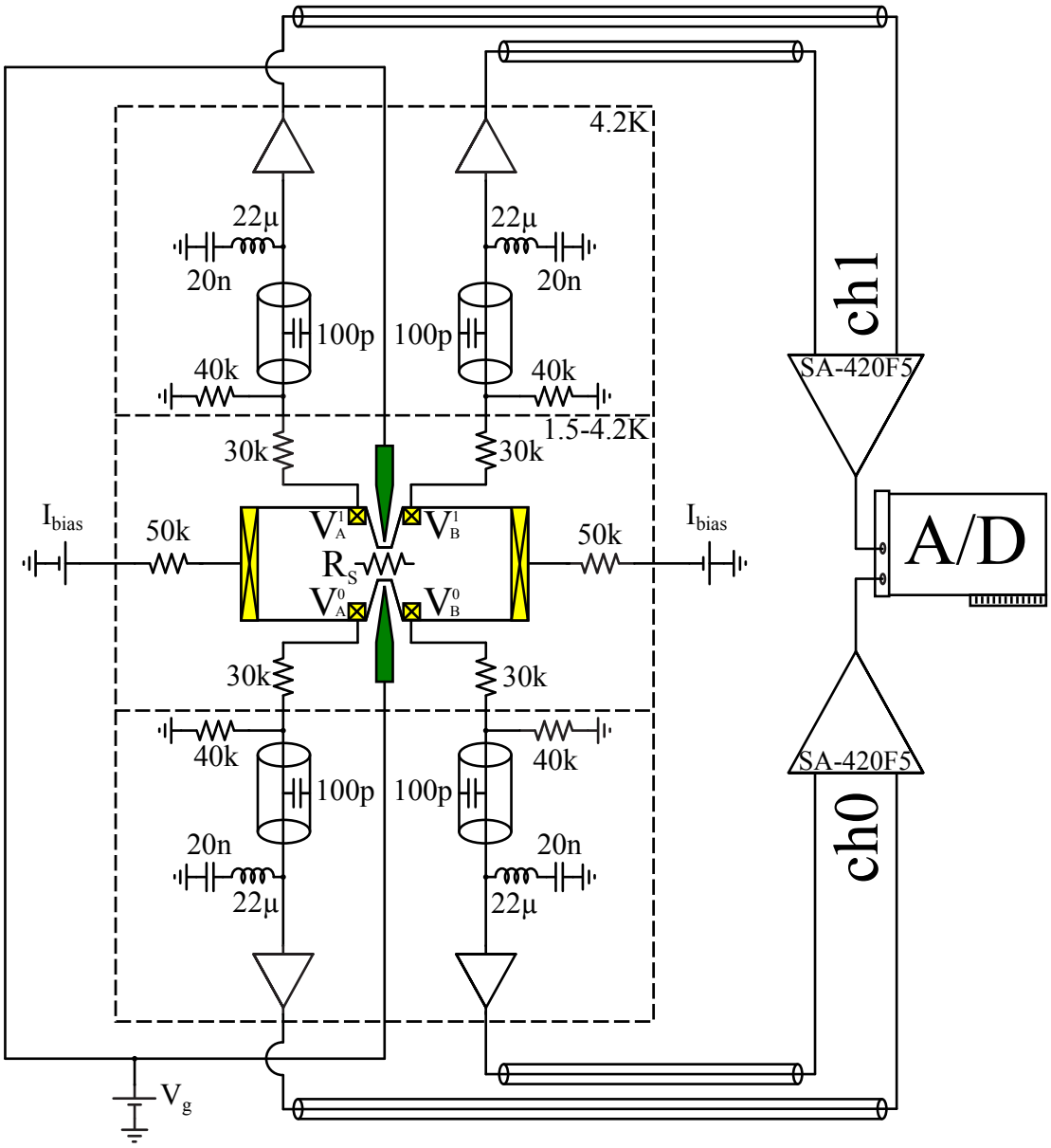

Figure 4.3: Schematics of the measurement circuit with a sketch of the device in the center: six ohmic contacts are coloured in yellow and side-gates are coloured in green, constriction resistance is explicitly shown and denoted R_s. Four identical voltage probing lines are connected to the sample and contain each a resonant circuit and a cryogenic amplifier. They are then connected to two room-temperature differential amplifiers *NF SA-420F5* resulting in two output channels (ch0 and ch1) that are in their turn connected to different instruments, including analog-to-digital conversion PC card, also sketched. All low temperature connections, except those of the voltage probing lines were realized with standard commercial cryogenic Lakeshore coaxial cables. Major part of the circuit is situated inside a low temperature inset (on the schematics delimited with a dashed line) and the possible experimental temperatures are indicated.

different locations (not shown on the schematics).

Now, let us see in details the key component of the measurement system, namely the voltage probe lines. An ideal voltage measurement supposes an infinite input impedance of the voltage probe instrument. To approach at best to these ideal conditions and reduce as possible the current leakage through the voltage probe lines, the 30 kΩ resistors were added at the inputs of each probe followed by 40 kΩ resistor to the ground (see schematics), giving the total DC input impedance of 70 kΩ, to be compared with the constriction resistance, varying between 1 and 8 kΩ. At high frequency the resistance to the ground is governed by the resistive part of the inductor (see the end of this section), that yields total input impedance at 3 MHz of about 51.5 kΩ. Note that such resistors configuration causes signal loss, unravelling why we limited ourself to these values of resistances. Additionally, for the reasons displayed in the previous section, each line contains also a resonant circuit, followed by a cryogenic amplifier (see sec. 4.2.3). Finally, the lines are plugged into corresponding inputs of two room-temperature differential amplifiers *NF SA-420F5* (voltage gain 46 dB). The signals on the outputs of each differential amplifier (to which from here on we will refer as channel 0 and channel 1) are then proportional to the voltage drop across the sample and should be identical up to detection noise component.

In these last paragraphs we will present the characteristics of the resonant circuits. The most basic resonant circuit contains an inductor and a capacitor as well as a resistor (intrinsic resistance of the inductor or additional one). In our circuit, each resonator includes coaxial cables capacitance of about 100 pF, previously mentioned 40 kΩ resistor and 22 µH inductor (*Coilcraft 1812CS*, without magnetic core). Thanks to additional 20 nF capacitor such circuit provides a low-frequency band as well as high-frequency one centred around 3 MHz, allowing to measure in both regimes. The high frequency response of all four lines is plotted in fig. 4.4. One notice a certain disparity between lines, that can be explained by differences in resonant circuits components: differences in lengths of connecting coaxial cables will result in different capacitances, intrinsic resistance of inductors can also vary from one specimen to another. Besides, due to the skin effect that makes the high frequency current flow mostly through a thin surface layer of the conductor, the effect of the inductor's intrinsic resistance on the resonant circuit properties can become significant.

We analysed the resonant circuits with the *LTSpice* simulations software. The corresponding analytical model is presented in the Appendix B.3. The obtained curves fit well the experimental ones (see fig. 4.4), except for the line B1, for which the behaviour couldn't be completely understood. The resulting values of circuit elements are presented in table 4.1. We denote C — total capacitance, r — intrinsic series resistance of the inductor, R — equivalent to it resistance in

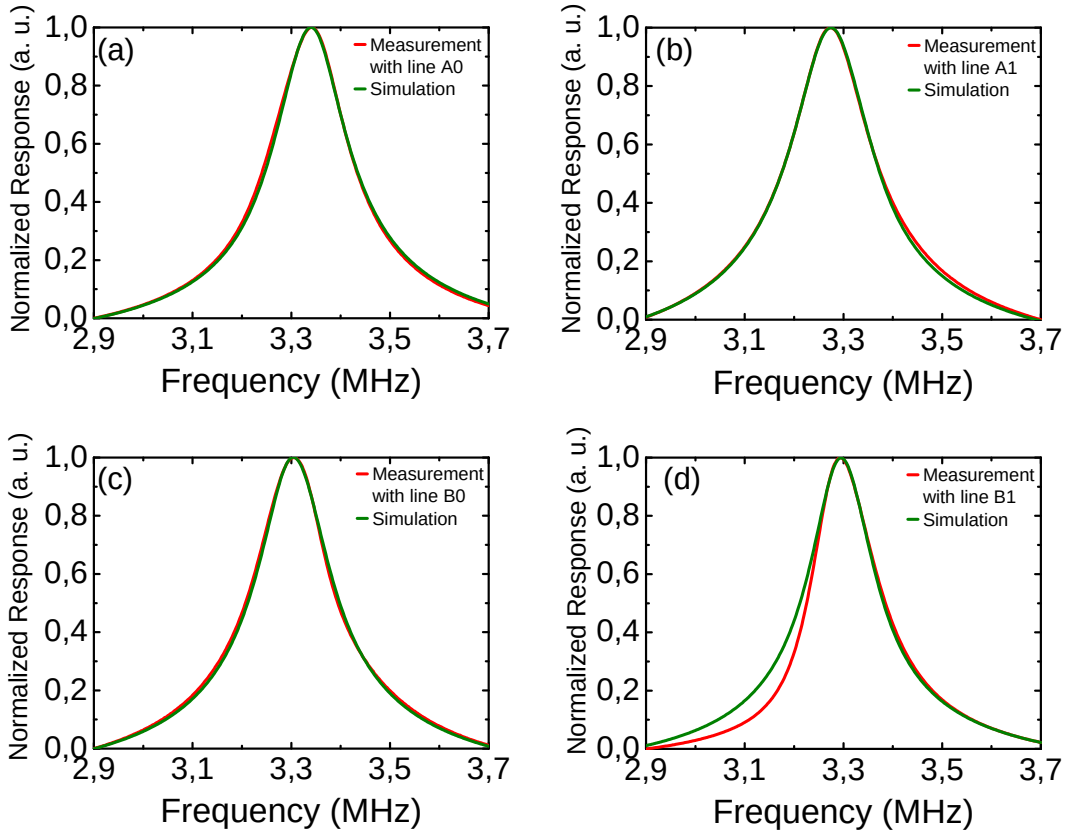

Figure 4.4: High frequency response of the each resonant circuit in arbitrary units (normalized to vary between 0 and 1), in red experimental data, in green the result of simulations with the software LTSpice.

parallel, $R /\!/ 40\,\mathrm{k}\Omega$ — total equivalent resistance to the ground, f_{res} — resonant frequency, f_{cut} — eventual cut frequency, due to the circuitry after the cryogenic amplifiers. The resistance R represents a resistance, which when put in parallel with the ideal inductor L would result in the same total impedance as the resistance r, put in series with the same inductor. In the limit of $r \ll \omega L$, it is simply given by $R = L^2\omega^2/r$.

4.2.3 Cryogenic Amplification System

The cryogenic amplification system was developed within the Nano-electronics group during my PhD work and is used in several experimental systems, including the setup for measuring the shot noise in graphene. Here we explain the principle of this system.

Table 4.1: Values of different components of resonant circuits for each measurement line.

Line	C (pF)	$r(\Omega)$	R (kΩ)	$R/\!/40$ (kΩ)	f_{res} (MHz)	f_{cut} (MHz)
A0	103.95	8	57.5	23.6	3.34	5.7
B0	106.55	16	28.5	16.6	3.3	3.8
A1	109.1	11	41	20.2	3.27	8
B1	107.3	7.5	60.7	24.1	3.29	> 10

The core element of the amplifier is the *High Electron Mobility Transistor* (HEMT) — a field effect transistor (FET) based on semiconductor heterostructure. A FET is a crafty device, with non-linear and moreover gate voltage dependent current-voltage characteristics. One distinguishes two regimes of FET operation: linear and saturation one. In saturation regime the drain-source current I_{DS} is practically independent of the drain-source voltage V_{DS} but strongly depends on the gate-source voltage V_{GS}. This dependence can be considered as linear in the limit of small variations v_{GS} and i_{DS}:

$$g_{\mathrm{m}} = \frac{i_{\mathrm{DS}}}{v_{\mathrm{GS}}} \tag{4.6}$$

The above quantity, called *transconductance*, is an important characteristics of any FET.

Now consider the circuit, represented in fig. 4.5.a and suppose that we add a small modulation v_{i} to the voltage on its input (gate) terminal. Let us calculate the AC response of the circuit, i.e. the alternative voltage that such modulation produces on the output (drain) terminal. We note V_{G} and I_{D} — the DC components of the gate voltage and of the drain-source current (here, for simplicity, the source terminal is grounded). We then have the voltage at the output terminal equal to

$$V_{\mathrm{D}} = V_{\mathrm{DD}} - R_{\mathrm{D}}(i_{\mathrm{D}} + I_{\mathrm{D}}), \quad \text{where } i_{\mathrm{D}} = g_{\mathrm{m}} v_{\mathrm{i}} \tag{4.7}$$

Its AC component v_{o} is obviously given by $-R_{\mathrm{D}} g_{\mathrm{m}} v_{\mathrm{i}}$, meaning that the output signal is simply proportional to the input signal and thus when $R_{\mathrm{D}} g_{\mathrm{m}} > 1$ amplification regime is attained.

Based on this property, an amplification system can be built. For our goals five criteria have to be fulfilled:

- the HEMT as well as the passive components should operate at $T \simeq 4\,\mathrm{K}$ and be temperature stable.
- the HEMT should have low voltage and current noise characteristics (referred to the input)

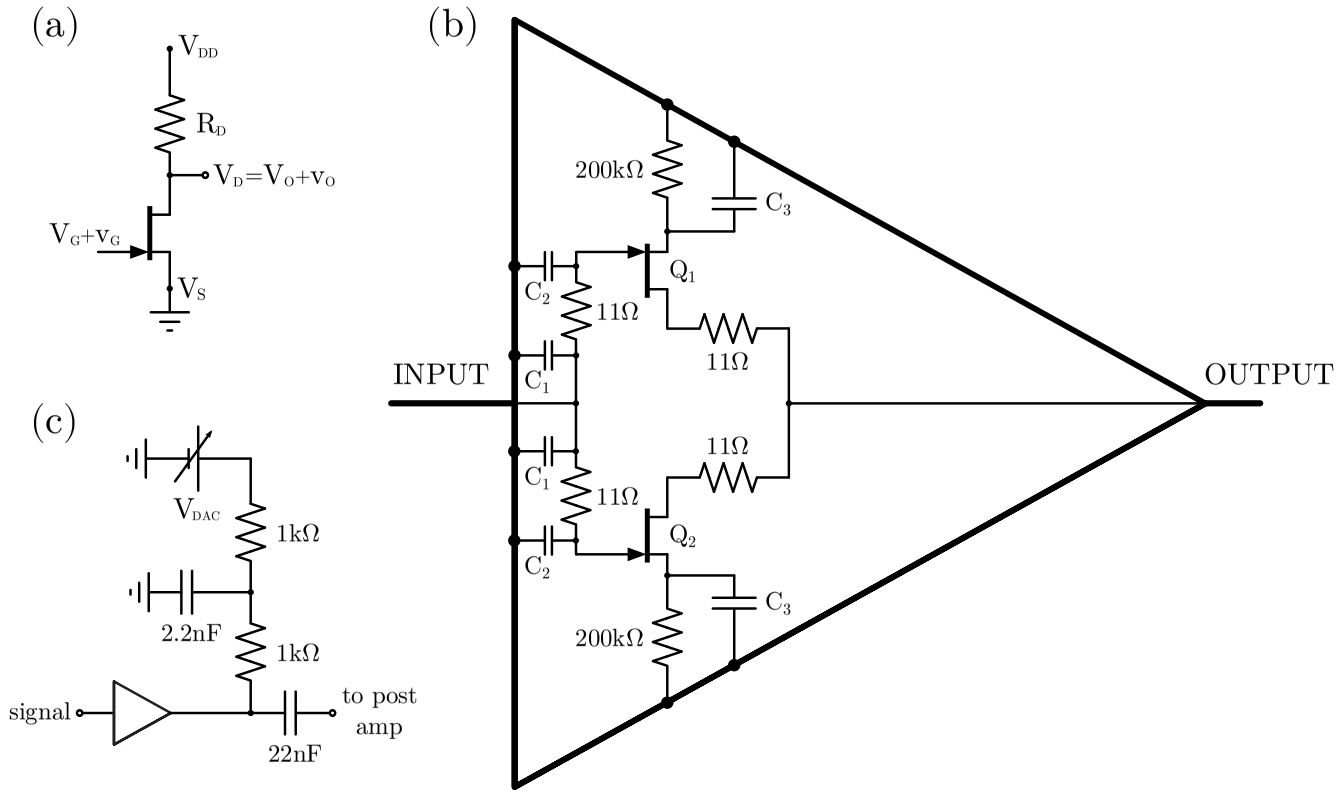

Figure 4.5: (a) Basic amplification circuit. (b) Schematics of the cryogenic amplifier (amplification block). Stabilizing capcitances C_1, C_2 and C_3 correspond to several discrete capacitors distributed along the strip lines of the circuit board. (c) Principle of the signal splitting and amplifier polarization, the supply voltage is V_{DAC}.

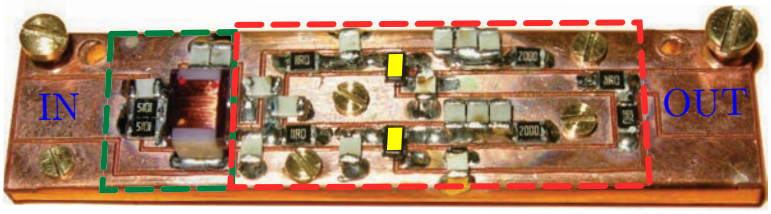

Figure 4.6: Photography of the main circuit board with both resonant circuit (which also includes the coaxial cable capacitance not shown) and two HEMTs (highlighted with yellow colour) cryogenic amplifier, enclosed with green end red dashed lines respectively. Input and output are indicated.

- the HEMT dissipated power should be enough low to avoid the device heating
- simultaneous measurements at several MHz and near DC should be possible
- amplification system should be isolated as good as possible from outside electromagnetic interferences

The amplification system can be divided into amplification and polarisation blocks, the two being connected via a special board, called *Splitter*. Amplification block, as it can be seen in fig. 4.5.b, includes two *ATF-34143* HEMTs Q_1 and Q_2 put in parallel and also several passive components mounted on a circuit board made of machined Copper/Dielectric/Copper (35 µm/50 µm/35 µm) substrate enrolled over a massive copper plate and bolted to it, resonant circuits are situated on the same board (see fig. 4.6). Putting two transistors in parallel presents the following interest. It can be shown[80], that the current noise of N HEMTs in parallel adds linearly, i.e. equals to N times the current noise of a single HEMT, while the voltage noise of N HEMTs in parallel adds like resistances in parallel, i.e. equals to the voltage noise of a single HEMT, divided by N. Since the voltage noise of the used HEMTs is in principle more significant than the current noise even for such quite high input impedances as we have, this allows to improve the signal-to-noise ratio. Extra discrete capacitors, distributed along the strip lines of the circuit board (shown as a single symbols in the fig. 4.5.b) were added for stability to damp eventual resonances in the GHz range.

Polarisation block serves to power the amplification block. To isolate the amplification system from the power network and to avoid additional ground loops, rechargeable batteries are used as a power source. The rest of the polarisation circuit is shielded and is separated from the batteries (non-shielded) by *Murata* filters, which reject all parasitic AC components, induced to the non-shielded part of the circuit by the environment. Voltage regulators are used to accurately tune the working polarisation voltage. Finally, the splitter board (see fig. 4.5.b) serves

to separate the output signal from the DC polarisation voltage V_{DAC}, thus avoiding an extra line from room temperature for transistor supply.

The realized amplification system can be characterised by its gain as well as voltage and current noise characteristics. However, an accurate insitu measurement of these characteristics in our experimental setup was not possible or extremely difficult. For these reasons, we refer ourselves to the results obtained by Jullien in a very similar system carrying a QPC, which allows an accurate analysis of amplifier's characteristics thanks to the well defined conductance plateaus on which the QPC conductance and the Fano factor are well known. In this experiment the amplifiers' current and voltage noise at 3 MHz (referred to the input) were determined to be $15\,\mathrm{fA}/\sqrt{\mathrm{Hz}}$ and $0.22\,\mathrm{nV}/\sqrt{\mathrm{Hz}}$ respectively. The found gain $\approx -4.6\,\mathrm{V/V}$ is higher that what we could estimate for our system (below $-3\,\mathrm{V/V}$). The dissipated power was estimated to be of the order of $2.2\,\mu\mathrm{W}$ to be compared to $\simeq 133\,\mathrm{pW}$, the Joule heating produced at the constriction of the graphene-based device at its maximum resistance (at the Dirac point) with voltage drop across the constriction of 1 mV.

Chapter 5

Device Fabrication

In the present chapter we discuss the methods and related fabrication processes that were adopted in order to produce the graphene nano-structure devices on which the conductance and noise experiments were then carried out. These devices were conceived and developed during my PhD work and their elaboration took an important place in this work. All of them are "home-made" on SPEC nano-fabrication facility that includes among other tools 10 000 class clean room, optical and electron beam lithography systems and various thin-film deposition equipments.

This chapter is organized in the following way. First section provides a summary of methods generally required for the fabrication of a typical graphene-based device and for each method an insight into its physical origins is given. In particular, at the beginning of this section principal techniques of graphene obtaining are reviewed. The first section is thus recommended to a reader only superficially familiar with such kind of methods, whereas the next section could rather attract an advanced reader, concerned with the refinement of his own processes of graphene-based devices fabrication. That section gives a detailed description of all processes, that were worked out for the fabrication of our devices. Besides, one can find the exact recipes for this section in Appendix A.1. Both chapters can be useful to a reader that starts his activities in this field. In addition, for an outline of common nano-fabrication techniques (lithography, thin-film deposition etc.) one is referred to Appendix A.3.

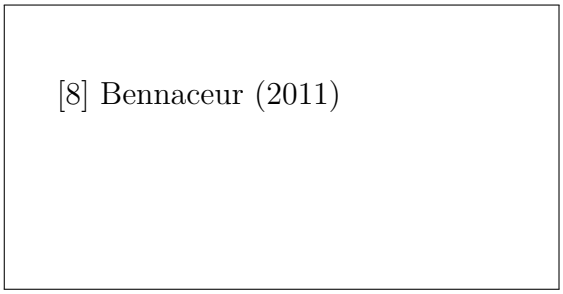

Figure 5.1: Photography of a skotch-tape with exfoliated graphite. From [8].

5.1 Methods

5.1.1 Obtaining Graphene

In this section we propose a brief review of the principal techniques that allow to obtain mono-layer graphene samples. We start with the discussion of the *Mechanical Exfoliation* technique, that was historically the first technique that proved the possibility of obtaining one-atom thick graphene layers[114]. This is also the only technique we used while fabricating our graphene-based devices. Next, we present other approaches and discuss their advantages and drawbacks.

a. Mechanical exfoliation

Mechanical exfoliation is the technique, that allowed the very first reported isolation of a single layer graphene sheet. It was developed at the University of Manchester (UK) and at the Institute of Microelectronics Technology (Chernogolovka, Russia) by Andre Geim and Kostya Novoselov and a Nobel prize was awarded to them in 2010 for "ground-breaking experiments regarding the two-dimensional material graphene"[?].

This technique consists of a mechanical cleavage of highly oriented pyrolytic graphite (HOPG). Since the graphite represents a stack of graphene layers held by rather weak van der Waals forces (interlayer spacing is of 0.335 nm) it is easily peeled off using only scotch-tape. Hence by peeling more and more layers one can eventually obtain a single layer of graphene. Although this technique is easily implemented in laboratory conditions and despite its low cost and the outstanding characteristics in terms of mobility[15, 45], structural defects concentration[140, 75] etc. of the in such a way obtained samples, this method remains a quite artycrafty and largely uncontrollable process and is not appropriate for industrial applications. This technique was used in present work to obtain graphene flakes for subsequent devices fabrication, since our experiment necessitates high electron mobility graphene.

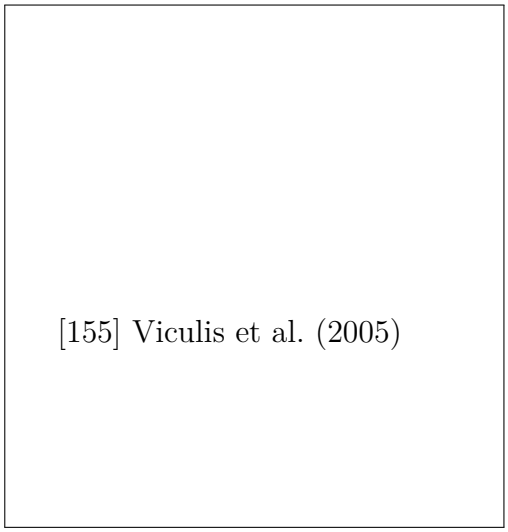

Figure 5.2: Schematic diagram showing the intercalation and exfoliation process. From [155].

Later, another approach to mechanical exfoliation, known as sonification[32], was suggested where graphite is dispersed in a liquid medium, subjected to an ultrasound treatment. As a consequence graphite is exfoliated and , non-exfoliated pieces are eventually separated from graphene by centrifugation. However, this method also has its obvious limitations in terms of fabrication scalability.

b. Chemical exfoliation

The radically different manner of graphite layers separation is intercalation of molecules between adjacent layers to enlarge the interlayer spacing and thereby lower the van der Waals forces. The following step is to rapidly evaporate he intercalated material at elevated temperature, that will result in graphene exfoliation[155, 124, 120]. This process can be further enhanced by combining it with sonification or ball milling. However, in order to obtain a single-layer graphene flakes, this procedure has to be repeated several times eventually with different intercalants. Even though, it is difficult to control the number of layers for thus obtained films, this technique is scalable and may be eventually adopted for some specific applications.

Another approach to graphene fabrication is its growth on various substrates. As it implies deposition on large surfaces it is necessarily scalable and moreover

compatible with conventional techniques of semiconductors based devices manufacturing.

c. SiC sublimation

The advantage of SiC sublimation technique[11, 65] is that the graphene is directly obtained on a wide-gap semiconducting substrate (≈3 eV gap for 6H-SiC polytype).

This technique is based on the following principle. Energy of Si-atoms sublimation is lower than the one of C-atoms, so while heated the silicon atoms leave the surface, whereas carbon atoms stay and reorganize themselves into graphene honeycomb lattice. Often this process of graphitisation is performed under Ultra High Vacuum (UHV) conditions, but additionally an argon atmosphere can be used to slow down the Si sublimation[48]. Because the carbon atoms density in graphene is approximately three times higher than the one in the single atomic plane of a SiC crystal, the Si sublimation over at least three atomic planes is necessary for graphene formation. This is however quite arduous to achieve as Si and C diffusion from bulk to surface is very slow even at temperatures customary to graphitisation process. Moreover the graphitic layer nearest to the bulk SiC is tightly bound to it: it is approximately 0.2 nm distant from the bulk against 0.34 nm distance between graphene sheets in crystalline graphite. Thus this first layer plays a role of a buffer on which graphene layers are formed. The reason, why one is allowed to consider so obtained one-atom thick carbon layer as a mono-layer graphene is that thanks to the buffer layer it is only weakly coupled to the rest of the substrate and even if several graphene layers are formed, the coupling between them is enough weak (interlayer distance 0.39 nm), so that each layer can in certain degree be considered as an independent single layer graphene[137].

Besides, SiC crystal has Si- and C-terminated faces and the growth of graphene and its physical properties differ with the chosen face type (see ref. [138] for comparison of the growth on two faces). For instance, on Si-face the graphitisation process is slow with easier controllable graphene layers number and a single orientation of graphene lattice in regard to the SiC crystal is possible (rotated by 30°)[65]. In contrast, the graphitisation on C-face is very fast and various orientations of the graphene lattice are possible[66], that makes the control of the number of graphene layers difficult and also results in a formation of crystalline domains of different orientations. Unfortunately (and maybe astonishingly) the Si-face grown samples show a much lower electron mobility than their C-face grown counterpart[127, 83].

As a conclusion, an industrial fabrication process based on this technique can be implemented for applications that doesn't require high electron mobility.



Figure 5.3: Sketch of the CVD-grown graphene layer transfer process. From [172].

d. Chemical Vapour Deposition on metal

Chemical Vapour Deposition (CVD) is a technique of thin film deposition, which consists of usage of gaseous precursors that will decompose on the substrate surface to form the desired deposit.

Graphene CVD on metal substrate is often considered as the most promising technique from the point of view of fabrication scalability[172, 106]. The metallic substrate plays a role of catalyst, which when exposed to a continuous flow of carbon contained molecules at elevated temperature (for example CH_4 or C_2H_2) will activate their decomposition and will absorb the produced carbon atoms on the surface or into bulk. At certain conditions a graphene layer is formed on the metal surface. This layer can then be transferred to any substrate as follows: the metal is first coated with polymer on the side, containing the graphene layer, it is then dissolved while the graphene layer remains on the polymer surface. The polymer with attached graphene is then placed on desired substrate and the former is finally also dissolved (see fig. 5.3).

Different metals were studied as a potential catalysing substrates: nickel[153, 150], cobalt[49], ruthenium[143], rhenium[123], platinum[142], iridium[34], stainless steel[78] and copper (see [106] and [172] and the references therein), latter usually regarded as the most hopeful. Further improvements to the standard CVD process are possible, such as DC[5] or microwave plasma[102, 169] enhanced CVD or so called hot-wire CVD[136, 68], in which heated tungsten wires, installed in front of the gas inlet, will decompose directly incoming molecules into reactive species.

e. Other techniques

Among alternative graphene deposition techniques now studied there are molecular beam epitaxy from a graphite source[110, 175, 57], growth from metal-carbon melts[4], in which carbon is dissolved in a molten metal and then precipitated out at a lower temperature or similar to it carbon ions implantation in metallic grains, with subsequent heating and slow cooling causing carbon diffusion and graphene

formation[56] and reduction of graphite oxide powder to graphene flakes[100], the list is not exhaustive.

5.1.2 Making Graphene Visible

One of the most spectacular properties of the graphene is that these one-atom-thick flakes can still be visible with an eye, having only an optical microscope as a tool. This property has certainly played its role in the graphene discovery, making an optical detection of mono- and few-layer graphene possible and even relatively rapid and convenient[58].

Graphene film has a quite high opacity for its thickness: in vacuum it absorbs 2.3% of the incident light. On a silicon substrate with an oxide capping layer (SiO_2/Si) the contrast produced by graphene with respect to an empty wafer can be considerable in certain conditions, as it can be seen in fig. 5.4.a. Indeed, the difference in optical paths in the presence of a graphene flake corresponds in general to a different, compared to a pristine SiO_2, interference color. Moreover, this change in color can be tuned with the thickness of the latter, as it will be illustrated in following. Therefore an appropriate choice of the oxide layer thickness and of the color filter is capital if one wants to render graphene flakes visible.

A simple Fresnel-law-based model from [13] provides an explanation for this remarkable fact and the following calculations furnish the optimal conditions for the graphene observation. In their model Blake et al. consider a normal light incidence from air (refractive index $n_0 = 1$) onto a trilayer structure of graphene, SiO_2 and semi-infinite Si bulk (see fig. 5.4.b). The SiO_2 and Si refractive indices $n_2(\lambda)$ and $n_3(\lambda)$ are wave-length dependent. As for the graphene refractive index n_1, the one of the graphite was assumed to well describe the system. Then relative indices of refraction are introduced as:

$$\begin{aligned} r_1 &= \frac{n_0 - n_1}{n_0 + n_1} \\ r_2 &= \frac{n_1 - n_2}{n_1 + n_2} \\ r_3 &= \frac{n_2 - n_3}{n_2 + n_3}, \end{aligned} \tag{5.1}$$

as well as phase shifts due to changes in optical path:

$$\begin{aligned} \Phi_1 &= 2\pi \cdot \frac{d_1}{\lambda/n_1} \\ \Phi_2 &= 2\pi \cdot \frac{d_2}{\lambda/n_2}. \end{aligned} \tag{5.2}$$

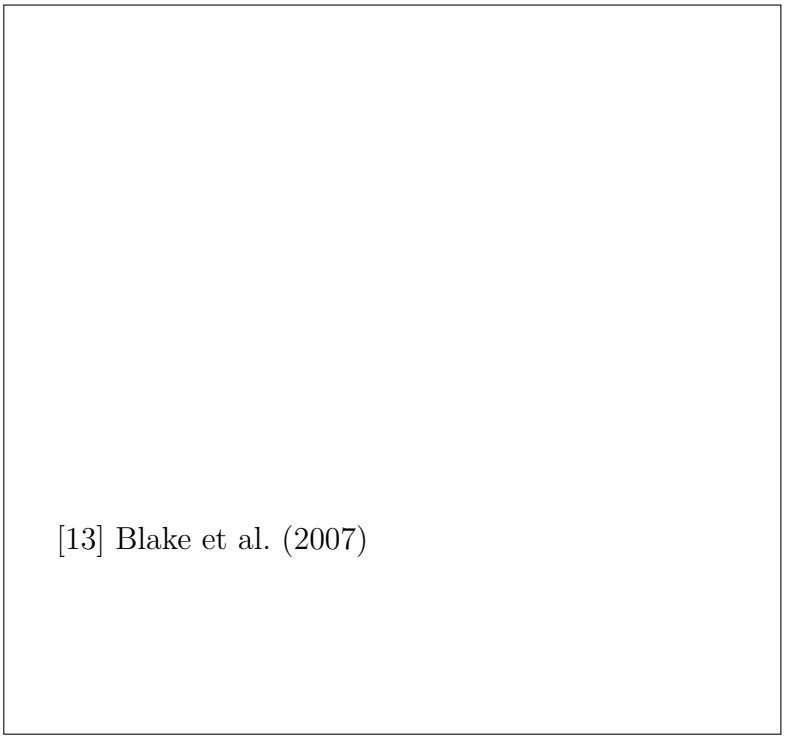

Figure 5.4: (a) Optical microscope picture of mono- (enclosed with dotted line) and multi-layer graphene on the SiO_2/Si wafer, showing the color contrast between graphene of different thickness and the wafer. (b) Sketch of the interference model considered by Blake et al. (c) Obtained color plot of the contrast as a function of wavelength and SiO_2 thickness according to eq. 5.4. The color scale on the right shows the expected contrast. From [13].

The reflected light intensity is written as:

$$I(n_1) = I_{\text{inc}} \left| \frac{r_1 e^{\imath(\Phi_1+\Phi_2)} + r_2 e^{-\imath(\Phi_1-\Phi_2)} + r_3 e^{-\imath(\Phi_1+\Phi_2)} + r_1 r_2 r_3 e^{\imath(\Phi_1-\Phi_2)}}{e^{\imath(\Phi_1+\Phi_2)} + r_1 r_2 e^{-\imath(\Phi_1-\Phi_2)} + r_1 r_3 e^{-\imath(\Phi_1+\Phi_2)} + r_2 r_3 e^{\imath(\Phi_1-\Phi_2)}} \right|^2 \tag{5.3}$$

Finally the contrast is defined as the relative intensity of reflected light in the presence ($n_1 \neq 1$) and in the absence of graphene ($n_1 = n_0 = 1$):

$$C = \frac{I(n_1 = 1) - I(n_1)}{I(n_1 = 1)} \tag{5.4}$$

The results of the numerical simulations based on this model are presented in fig. 5.4.c. They allow to eliminate the thickness below 30 nm as well as the thickness ≈150 nm. The optimal thickness are found to be of 90 and 280 nm. The wafers we used have the thickness between 280 and 300 nm.

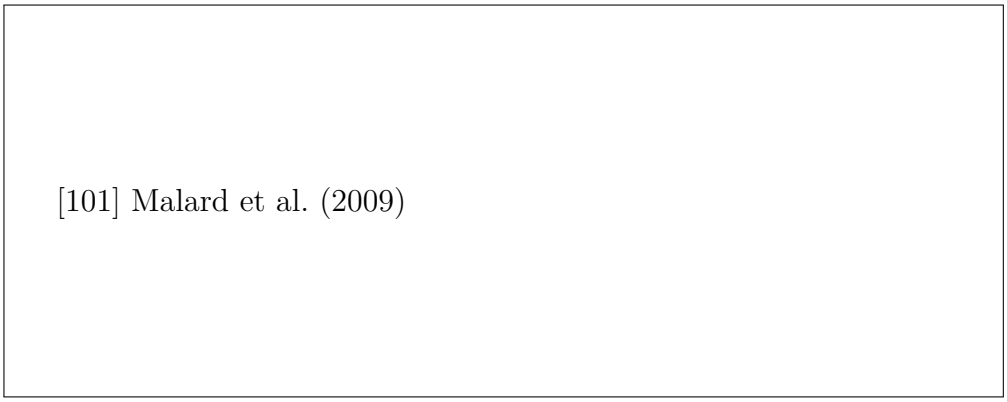

Figure 5.5: (a) Raman spectra of pristine (top) and defected (bottom) graphene. The main peaks are labelled. From [53]. (b) Calculated phonon dispersion relation of graphene showing the iLO, iTO, oTO, iLA, iTA and oTA phonon branches. From [101].

5.1.3 Raman Spectroscopy of Graphene

Raman spectroscopy was found to be a very powerful tool for graphene characterization, since, in particular, it affords a dependable mean of distinguishing between mono- and multilayer flakes, that was first reported by Ferrari et al.

This spectroscopy method relies on so called Raman scattering of monochromatic light on the studied matter[125, 95]. In contrast to Rayleigh scattering process in which photons are elastically scattered by the matter, Raman scattering is inelastic and results in an energy exchange between photons and vibrational (and rotational) degrees of freedom of the nucleus. A brief introduction to this phenomena is given in the Appendix A.2. By Raman spectra one commonly understands the intensity of scattered light as a function of the difference between incident and scattered photon energy, the so called *Raman shift*. Raman spectra provides the knowledge about the material constituents and their state, that makes of it a powerful tool for materials investigation.

In general, a Raman spectrometer contains a laser source and a confocal microscope that allows to focalize the laser beam on a sample. The back-scattered light is then filtered in order to removed the much more intense Rayleigh component and the Raman shift spectra is measured by conventional spectrometry techniques.

The Raman spectras of carbon-based materials are studied since many years and are well characterized and understood (see references 5–19 in [101] for instance). Although all these materials have only few significant peaks in their Raman spectra, their shapes, intensities, and positions provide structural and electronic information about studied carbon allotrope.

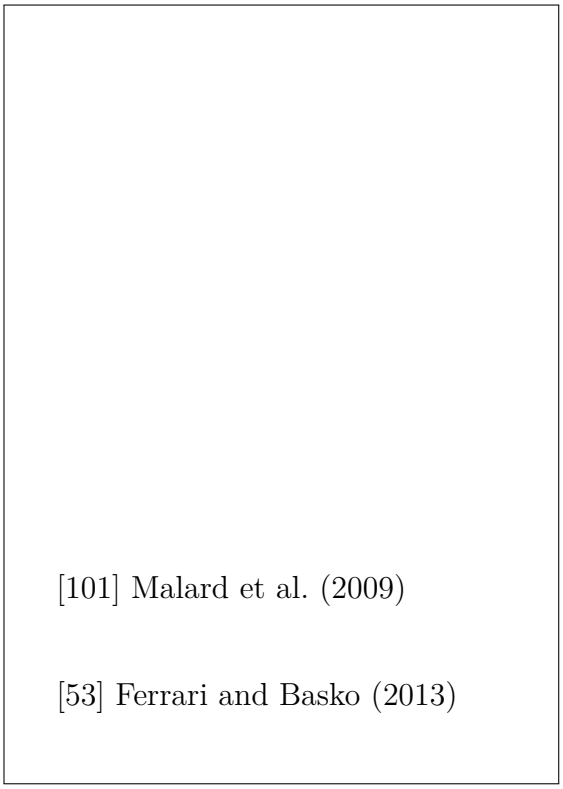

Figure 5.6: The measured G' Raman band with 2.41 eV laser energy for (a) monolayer, (b) bi-layer, (c) tri-layer, (d) four-layer graphene (e) HOP graphite. The multiple Lorentzian fits as well as the individual Lorentzian components are also shown for each case. From [101]. Inset: sketch of the in-plane phonon mode E_{2g}. From [53].

In graphene, for instance, Raman spectroscopy is used to ascertain the number of layers, examine the doping[24, 36] and disorder[52, 129, 23] as well as quality and type of edge[165, 63, 33, 25]. The Raman spectra of graphene, as seen in fig. 5.5.a for pristine (top) and defected (bottom) graphene sample, consist of several peaks, certain features appearing only in samples with defects. Figure 5.5.b shows phonon dispersion in graphene, which contains three acoustic (A) and three optic (O) branches with four in-plane (i) and two out-of-plane (o) modes (L and T stand for longitudinal and transverse modes respectively). The most prominent peaks are so called G and G' (sometimes also called 2D) peaks. Another important features, which are related to disorder of the sample, are D and D' peak. The transitions that generate these peaks are shown in fig. 5.7.

The only peak that originates from non-resonant first order (only one phonon is created) transition is the G one. Due to the fundamental Raman selection rule

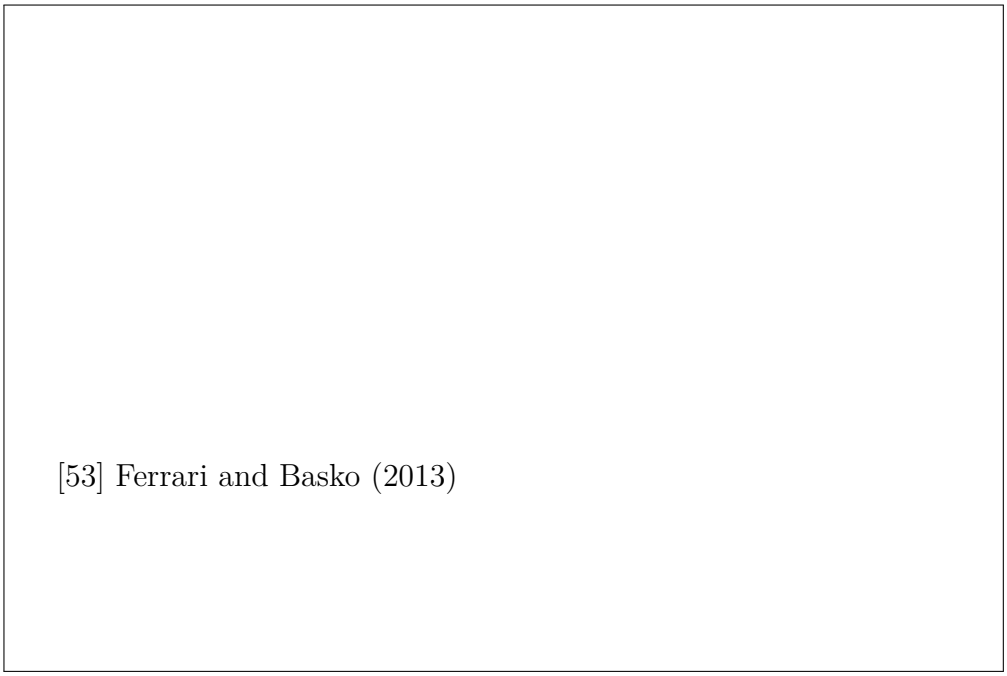

Figure 5.7: Sketches representing different Raman transitions in graphene, denoted with the corresponding peaks' labels. From [53].

(phonon wave vector $\mathbf{q} \approx 0$, see [54]), solely the high-frequency in-plane optical phonons modes of E_{2g} symmetry around Brillouin zone center (Γ point) are excited (see inset of fig. 5.6).

The G' peak on the contrary is the result of a double (two phonons are created) resonance transition, producing two in-plane optical phonons of opposite wave vectors (thus the selection rule is satisfied) near K and K' points, which will connect the electronic states from different valleys. This type of transition is therefore called *intervalley*. This peak is highly sensitive to the number of graphene layers and allows to discern between mono-, bi- and multi-layer samples, as its shape, width and position vary significantly when moving from mono-layer graphene to graphite[51]. The G' peak of mono-layer graphene can be fitted by a single Lorentzian. Since for multi-layer graphene each energy band splits in two with different splitting for electrons and holes, several processes at slightly different frequencies are possible, giving rise to a peak of different shape. For instance the G' peak of bi-layer graphene has four Lorentzian components whereas the one of the graphite has two components, as seen in fig. 5.6.

The last two peaks, D and D', originate from double resonance transition as well (intervalley for former, intra-valley for latter), though with a different mechanism behind: one-phonon defect-assisted scattering process (see corresponding sketches

in fig. 5.7). More particularly, the corresponding scattering process consist of one elastic scattering by a defect and one inelastic scattering with emission of an in-plane optical phonon near K (K') point. Besides, these peaks are strongly dispersive with excitation frequency[121].

5.1.4 Graphene Oxygen Plasma Etch

Plasma cleaning is commonly used in the research as well as in the industry especially to remove the contaminants in order to obtain a pristine surface of a material. Thus, graphene mono- and multi-layers can be easily etched by oxygen plasma. In general, plasma mainly affects the surface layer and its action can be divided into three types: heating, sputtering (mechanical action, the particles have to be accelerated by an applied electric field) and etching (based on the chemical reaction). Since graphene is a very thin material its etching necessitates no heating or electric field application.

The process is usually performed at room temperature and low pressure ($\sim$100 torr): air is pumped out and a weak flow of the oxygen is supplied. The plasma is created by a high frequency (commonly used is the 13.56 MHz frequency) excitation. Though during the process active species are generated, that then react with the surface layer of the material to be etched (e.g. graphene) and finally the products of the reactions are removed from the surface by pumping. The activated species are atoms, molecules, ions, electrons and so called *vacuum UV-photons* (VUV), created by other species deexcitation. First VUV photons break the existing organic bonds (C−C, C=C, C−O, C−H). Then different oxygen species ($O_2^{\pm}$, O, $O^{\pm}$, e^-) enter onto reaction having as products water and carbon oxide and dioxide. These products are volatile and are rapidly evacuated by the pump.

5.2 Processes

In this section we list in order all stages of the devices fabrication process. The exact recipes used can be found in Appendix A.1. The approach we proposed is to first deposit a graphene flake on the substrate, then contact it using common nano-fabrication techniques and finally give a specific shape to the flake using oxygen plasma etching.

5.2.1 Wafers Preparation

The substrates we used are standard commercial 2 inch, 280 µm-thick, intrinsic (undoped) Si wafers with 280 to 300 nm oxide layer. So, prior to graphene device

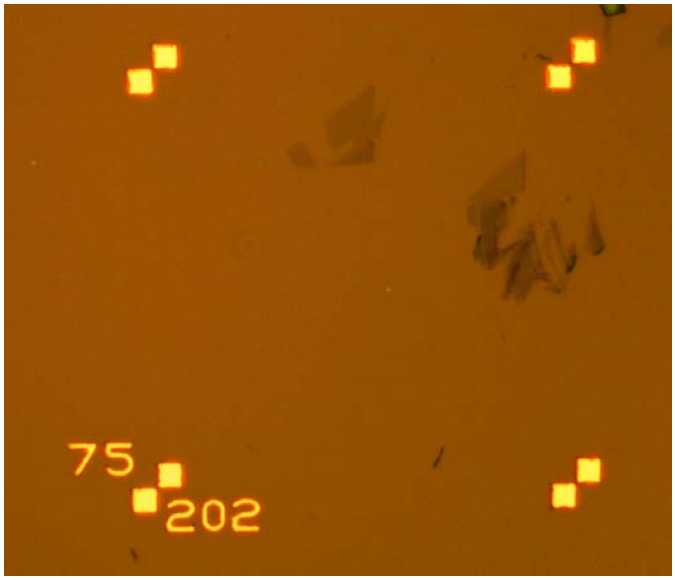

Figure 5.8: Photography of coordinate marks with indication of the coordiante.

fabrication it is crucial to prepare the substrate for the subsequent handling and clean its surface utterly well.

a. Coordinate system marks

As a very first step, we do a sort of improvement to the pristine wafers: for more commodity we furnish them with a coordinate system. The coordinate system represents a grid of special (metallic) marks, for each second one with indication of its coordinates (in arbitrary units), that we deposit on each wafer. Doing that we purpose two aims. First of all, we should be able to easily locate the place where the given graphene flake is situated on the wafer. Another point is that we have to precisely align the wafer while performing electron beam lithography. These two conditions determine the characteristics of the coordinate marks we use.

The coordinate (or alignment) marks are metallic double squares, the form that is perfect for position and angle alignment (see fig. 5.8). The size of a square is $5\,\mu m \times 5\,\mu m$, the distance between two marks is $86\,\mu m$. The choice of the inter-marks distance is related to the size of the smallest working field ($96\,\mu m \times 96\,\mu m$) we use in the electron beam lithography process. Thus, we can have up to four alignment marks in the working field, which provides us a necessary alignment precision (about 50 nm).

In the following the procedure of the coordinate marks deposition is detailed. We pattern the grid of alignment marks by the conventional method of optical

lithography (for the lithography principle see: subsec. A.3.1, A.3.2). The wafers are spin-coated with an UV-sensible positive resist (*Microposit S1813*), after what they are exposed to the UV radiation through a specially fabricated optical mask in the *Karl Süss MJB4* mask aligner (alignment accuracy below 1 µm). Finally the wafers are immersed in *Microposit MF 319* for resist development. We then deposit a golden thin-film (about 100 nm) in the Joule evaporator (see subsec. A.3.3). In order to have a better adhesion of the gold film to the wafer surface we embed a ∼5 nm chrome layer in between.[1] Finally, after lift-off is done we obtain a grid of golden marks.

Before the next fabrication stage, for convenience, we divide the round wafers into four pieces each. Here and in other steps where we need to cleave the wafers, we use a conventional scribing and breaking technique and *Karl Süss HR-100* scriber.

b. Surface treatment

As it was already mentioned above we thoroughly clean the substrate surface before transferring the graphene flakes on it as it is a necessary condition for the flakes to firmly stick to the wafer surface, otherwise the flakes become too fragile to handle. Therefore we perform a wet etching of surface contaminants by putting the wafers in *Piranha* solution (H_2SO_4/H_2O_2 in the ratio 1/5). Alternative approach is oxygen plasma etching, although this approach has several disadvantages: it is less efficient and creates dangling bonds in the silicon oxide, that can dramatically decrease the electron mobility in the graphene[112].

5.2.2 Graphite Deposition

We obtain graphene flakes by graphite exfoliation method using special electrostatic discharge safe scotch-tape. We first pill pristine graphite bulk with scotch and then transfer obtained single- and multi-layer flakes to the beforehand cleaned wafer pieces. We usually perform this step for several wafer quarters at the time as the process is rather cumbersome and time consuming.

a. Exfoliation with scotch tape

It is not desirable to manipulate bulk graphite in the clean room as its powder, which can be easily spread around by electrostatic repulsion, will contaminate the

[1] As it will be described later in the text we use titanium instead of chrome for the same purpose, while depositing the microcircuits. The reason for this difference is that in the next step of fabrication we will clean the wafer surface in an acid solution before transferring the graphene onto it. The acid we use reacts with titanium but not with chromium, so if former were used, acid would deteriorate the adhesion layer and hence the alignment marks.

atmosphere of the clean room. However, doing it under an extraction hood is still suggested to avoid dust deposition onto the scotch-tape.

To pill graphite we put a certain amount of it onto a large piece of scotch-tape and fold and unfold it for several times. While doing that we also tend to distribute the flakes on the scotch surface rather uniformly to reduce their superposition probability. It is also important to use an optimal quantity of graphite otherwise if too few graphite is put, this will decrease the total amount of flakes and hence the probability of finding single-layer flakes. In the opposite case, if too much graphite is put, big graphite cakes will pollute the wafer surface and provoke certain difficulties during the lift-off. If there are still big graphite cakes on the scotch-tape, it is advised to try to remove them (e.g. with tweezers) without spoiling the neighbourhood flakes. Afterwards we transfer the flakes from the large scotch-tape to a smaller individual scotch-tape segments, specially prepared for each wafer piece. Then we fold these tapes to protect the adhesive surface from dust.

The next step is done in the clean room as graphite flakes are not mobile any more and will not pollute the clean room.

b. Transfer to the wafer

The transfer of the graphene flakes on the cleaned wafer is performed in the clean room. The folded scotch-tapes are opened slowly, while the wafers are took out from the "Piranha" solution, rinsed in distilled water and kept under N_2 blow inside the extraction hood to avoid dust deposition until the scotch-tapes are brought into contact with the wafer surface and refolded over it. The scotch is then flatted with the finger. It is very important to have a perfect adhesion of the scotch-tape to the wafer surface and to avoid the creation of air bubbles inside.

Furthermore, the wafers with scotch can be put under press during a couple of days to promote a better adhesion of the flakes to the wafer surface. For this purpose we use lead bricks, that we put over the wafers protected by a layer of paper or rubber. This is a standard recipe used in the group. However it was noticed that one obtains a very good results without applying pressure and even the advantage of the latter method is that fewer graphite "dirt" stay on the wafer after the scotch is removed, probably because the weight is rather applied to the big cakes that are much higher and play a role of piles. The last samples were obtained with the latter approach.

Finally the scotch is removed in the clean room. This also has to be done very slowly ($\sim$1 cm/min) to separate scotch from the flakes in the right way: flakes stay on the wafer and not on the scotch without being damaged. Afterwards, wafers are cleaned in hot acetone in order to remove scotch glue residues as well as the unstable flakes that will not support the following fabrication stages anyway.

5.2.3 Graphene Flakes Detection

It is of high importance to be able to efficiently and reliably detect the mono-layer flakes on wafers. This task is far from being obvious as the typical size of a flake is 5 µm × 10 µm whereas the searching zone is a quarter of a 2 inch wafer. Moreover, one usually finds not more than five to eight mono-layer flakes per wafer quarter over a huge quantity of multi-layer flakes and graphite cakes. Our approach is to combine optical and Raman spectroscopy methods. Optical detection method, meaning finding the flakes with one's eyes using only an optical microscope as a tool, has proven it efficiency, even if, to become as efficient it necessitates a certain experience in that exercise. Raman spectroscopy, on the other hand, is an utterly reliable method if one needs to precisely distinguish between mono- and multi-layer flakes, the task that the optical method is not able to fulfil, so it completes the latter one from this point of view. To summarize, the optical method is exploited for the detection in the strict sense, whereas the Raman spectroscopy provides a mean to verify the "monolayerness" of the found flakes.

a. Wafer scanning with optical microscope

Optical detection supposes a complete scanning of the wafer with optical microscope. We usually used an objective with the magnification ×10 (field diameter $\sim 2400\,\mu m$). The very direct approach is to search for the most translucent flakes, taking into account only those which dimensions are sufficient to be used for device fabrication, and to note their coordinates. It is noticed that usually the areas with the highest probability to find a mono-layer flake are those with the highest flakes density. When the wafer is scanned and the coordinates of all flakes, likely to be mono-layer, are noted we check whether this is indeed the case with Raman spectroscope (see next section). Usually we find 10 to 15 candidates and between 5 and 8 flakes are then confirmed to be mono-layer.

b. Raman spectroscopy of flakes

For Raman spectras acquisition we used *Jobin-Yvon's LabRam Aramis* spectroscope. This instrument is equipped with a CCD camera, that allows to optically scan the wafer, moving the motorized stage on which it is situated. Hence we first optically find the flake, as we know its coordinates, and then perform the spectroscopy. Often it is enough to probe spectra in a one or two points of the flake only. Indeed, the presence on the flake of the regions with different numbers of graphene layers is rather easily recognizable by eye since the disparity in contrasts (even for the difference of one layer in thickness) is sufficiently visible when the regions to compare are situated next to each other. Otherwise, if necessary, the

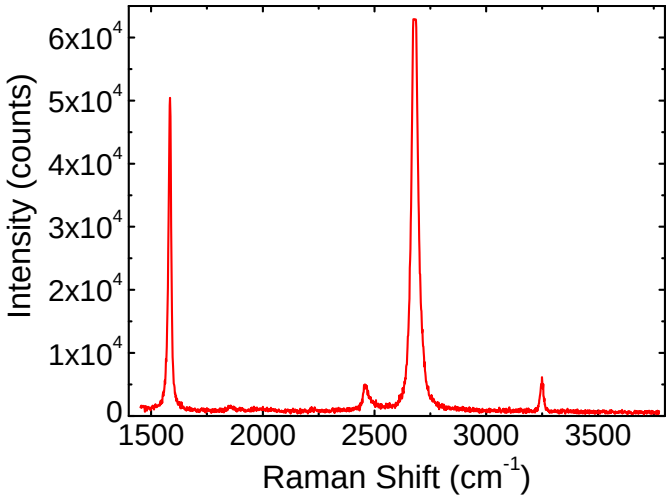

Figure 5.9: Raman spectra of the sample, studied in this work (note the detector saturation at 6.3×10^4 counts for 2D peak).

spectroscopy can be done in several points or even the whole flake can be scanned with the mapping function of the instrument.

Additionally LabRam Aramis spectrometer has a high-speed scanning mode, that provides a relatively fast generation of Raman spectra maps over large surfaces (e.g. over the whole wafer quarter). In this way created maps are supposed to simplify the searching of graphene flakes and even could allow to skip the stage of optical detection. However, while creating such wide maps, the spectrometer moves the stage over macroscopic distances, thus this movement should be extremely precise, otherwise there will be errors in the correspondence between physical coordinates and the coordinate scale on the map. Besides, the configuration of the map color scale, that would make the very rare and small graphene mono-layer flakes stand out against a background of silicon and graphite, can be a tough task.

To summarize, the combination of the optical detection method with local Raman spectroscopy was found to be the most efficient approach for graphene detection.

5.2.4 Microcircuit Deposition

During the following stage a microcircuit (one per graphene flake) will be deposited on the wafer. This microcircuit will be contacted to the graphene flake in different points and it will also contain gate electrodes that are electrically disconnected from the flake (the principle of the device design is discussed in Chapter 4). In such a way obtained *chip* can then be contacted to the macroscopic sample holder by the common wire bonding technique to, in the end, be connected to the

measurement system.

The basic structure of the microcircuit is the same from one sample to another. However, since the shape of each flake is unique and the surrounding flakes are distributed arbitrary, each time we need to adapt the microcircuit pattern in order to take into account flake geometry as well as to avoid surrounding flakes that can cause disconnection of the circuit strips or shorts between two strips. In that situation the optical lithography is inappropriate for microcircuit patterning as discussed in Appendix A.3.2. Moreover the pattern itself requires a higher resolution and alignment precision, than this type of lithography can provide. Accordingly, the microcircuit is patterned by electron beam lithography (see description in the same Appendix).

In the two following sections we will first reveal the microcircuit design and then give some more details on the fabrication processes.

a. Patterns design

The lithography patterns were designed with AutoCAD software and then converted to GDSII — conventional format of most e-beam lithography softwares. We use graphene flake image as a background layer in order to conceive a suitable pattern, adapted to each case. This image is created by superposition of photos with different magnification in order to have flake image in high resolution as well as a global view on the wafer and position of other flakes. The alignment marks on the image allow to define the scale and horizontal correctly in the CAD design.

The microcircuit design was gradually improved during the development period until we obtained an optimal one giving a reproducible output. The main technological constraint was the proximity effect due to the tightness of the microcircuit having a great number of electrodes near the flake, thus all important improvement concerned the finest parts of the pattern. Various designs schemas, satisfying the device principles, discussed in subsec. 4.2.1 of Chapter 4, were tested. As an example, initially, a design with large side-gates (see fig. 5.11.a), that were supposed to be more efficient and less local, was tried unsuccessfully. They were then replaced by local side-gates. Apart form several geometry optimisations, two conceptual improvements were added to the design during development stage. First one consists in additional voltage probes, that can be used if primary ones have lost contacts. Another improvement — supplementary alignment marks, patterned during the same process as graphene contacting electrodes, concerns the following stage of graphene etch, so their utility will be explained in the next chapter.

The device in its final version is sketched in fig. 5.10.a and the SEM micrograph of a similar device can be seen in fig. 5.11.b. The current injection electrodes (in yellow) are large and have notched ends to increase the effective perimeter of contact, since the charges enter especially through this one-dimensional interface.

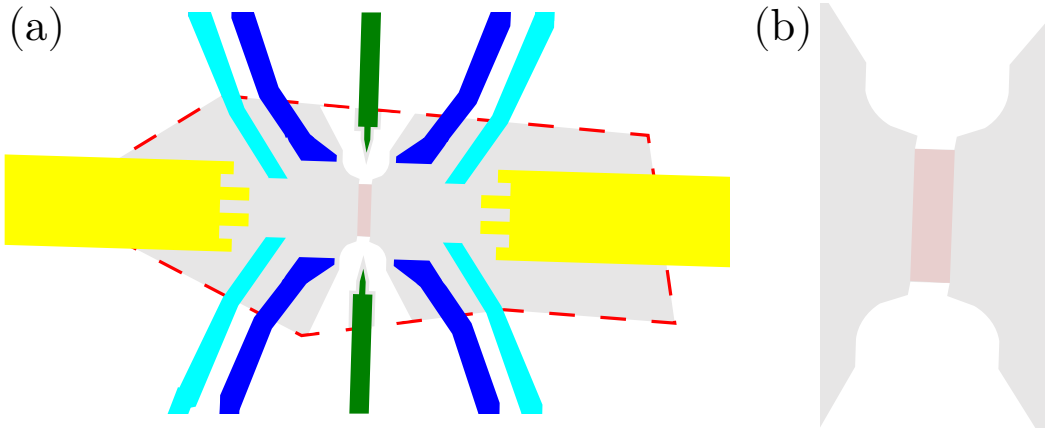

Figure 5.10: (a) Device lithography pattern: two large electrodes for current injection (in yellow), four voltage probes (in blue), four spare probes (in light blue) and two side-gates (in green). Graphene layer with a constriction cut out is shown in grey, dashed line showing the initial layer geometry. The constriction is highlighted with red colour. (b) The blow-up of the region near the constriction.

The eight thin electrodes are voltage probes: four primary (in blue) and four spare probes (in light blue). The two local side-gates (in green) will be disconnected from graphene afterwards by plasma etching. The optical photo of the part of the device containing the graphene layer (before plasma etch) is displayed in fig. 5.12.b, while in fig. 5.12.a the picture shows the macroscopic part of the circuit (different sample). As one can see, each electrode strip is terminated by a large (150 µm × 150 µm) contact pad to which wires then can be bonded.

b. E-beam lithography and metal deposition

The microcircuit deposition is a quite intensive and, at the same time, delicate process and it is recommended to follow the same scenario and implement the same recipe each time in order to avoid any unexpected result. As it was mentioned above the structure of the pattern favours the proximity effect to overdose the pattern and expose spacings between pattern strips. In these conditions it is imperative to find and keep an exact combination of irradiation dose and development time (the obtained sharpness of the pattern also depends on development time).

We start with cleaning the wafer surface in acetone and spin-coating it with 250 nm of *Polymethyl Methacrylate* (Microchem PMMA) — electron-sensible positive resist. The wafer is now ready for the lithography routine, performed in *Philips/FEI XL30S* Scanning Electron Microscope (SEM) controlled by *Elphy*

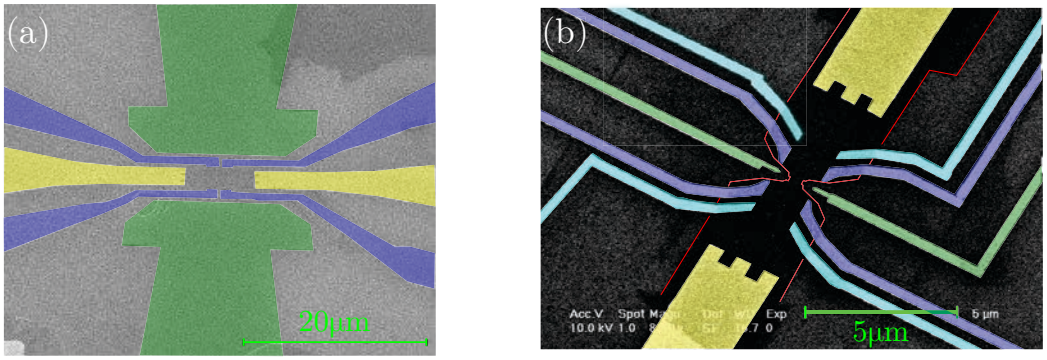

Figure 5.11: (a) False-colour SEM micrograph of one of the first device designs tried. (b) False-colour SEM micrograph of a device similar to the one measured in this work. Colour code of fig. 5.10 was preserved in both pictures.

Quantum lithography software. Note that, the beam pre-configuration and wafer pre-alignment being rather time-consuming, we prefer, if the wafer quarter contains several graphene flakes, to pattern all microcircuits at a time. Moreover, since the pattern contains elements of different scale the irradiation of the resist is done in several steps, each step with different magnification and working area[2], from highest to lowest magnification factor. The utterly precise alignment of the wafer, prior to the exposure, is essential in this process, preserving the graphene touching electrodes from being displaced away from the flake.

As soon as the exposure is completed, we develop the pattern in diluted *Methyl Isobutyl Ketone* (MIBK) and optically check the position of the pattern as well as the development quality. We then evaporate 7 nm-thick titanium adhesion layer with 50 nm-thick gold film on its top. We conclude this stage with the *lift-off* process: we dissolve the resist in hot acetone and then, using a pipette, blow away the golden film, floating over the substrate surface. Prior to removing the wafer from the acetone we check in the stereo microscope if no gold film remained gripped between two strips and, if necessary, repeat the operation with a pipette until a proper result is obtained. The wafer is then rinsed in isopropanol and dried with compressed nitrogen.

Before proceeding to the following stage we verify that the minimal required number of contacts are working using one of two possible test set-ups (see subsec. 5.2.6), otherwise we will ought to restart the fabrication process from the beginning.

[2]The working area — the area, the SEM beam can attain without moving the stage, it obviously depends on magnification factor

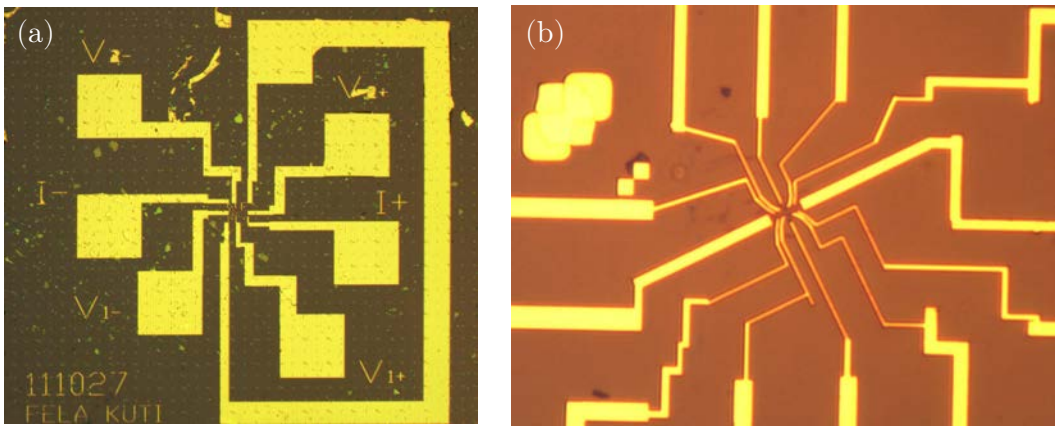

Figure 5.12: (a) Optical microscope picture of a chip with microcircuit. Chip dimensions are about 3 mm × 3 mm. (b) Blow-up of the microcircuit near the graphene flake, picture of the device used in this work.

5.2.5 Nano-Constriction in Graphene

Graphene etch is the last fabrication step. It has the following goals: first of all, according to the requirements of the device design, it is necessary to cut out a constriction in the graphene flake, that should also electrically disconnect side-gates from the flake. Furthermore, we have to remove all other flakes that produce shorts in the microcircuit and that we weren't able to avoid while designing the microcircuit pattern. We design the lithography pattern for this step taking into account two above-mentioned points. Besides, the constriction pattern has a convergent form but its effective size (200 × 800 nm) is defined by two small rectangular cut-outs on each side (see fig. 5.10.b). The sharpness of the real constriction is limited by lithography resolution.

The approach is again to use PMMA with a lithographed pattern as a mask to protect the graphene flake from the effect of the oxygen plasma and let plasma act only on the uncovered regions of the surface. However, one should be cautious while using oxygen plasma cleaning process together with PMMA mask, since PMMA is equally subject to plasma action (etching rate $\sim$ 100 nm/min), so the precise timing of this process is of huge importance.

The new pattern is designed in AutoCAD and it is lithographed with electron beam as the required precision and subtlety of the pattern are even higher than on the stage of the microcircuit deposition. Indeed, the new pattern has to be precisely aligned with the previous, microcircuit pattern, otherwise by etching in the wrong spots we can cut the graphene flake into two separate parts or disconnect it from one or several contacts or, in the opposite way, fail to remove the electric connection between the flake and the side-gates. To sum up, the alignment is a

crucial moment of this process.

Still, the electron beam positioning is limited and even though during each lithography an alignment of the wafer is done, the beam is always slightly shifted in arbitrary direction. Thus, the total mismatch between two successive lithography processes can be up to double of the typical beam shift, which is not acceptable for our purposes. To overcome this obstacle we add to the microcircuit pattern supplementary alignment marks, already mentioned above. These marks, patterned within the same lithography process as the electrodes, will be shifted exactly in the same way as the latter. Hence the wafer alignment using these marks during the second lithography can sufficiently reduce the alignment mismatch between two patterns. Eventually, we can optically check if the pattern is correctly placed, directly after developing it in MIBK, and restart the operation if the shift is unacceptable. Besides, prior to developing the patterns, we usually[3] cut out each microcircuit from the wafer quarter, obtaining in this way several ($\sim 3 \times 3\,\mathrm{mm}$) chips (see fig. 5.12.a), that can be handled separately and suit the sample holder dimensions.

Finally we perform the etching in *SPI Plasma-Prep II* machine. We expose the chip to the oxygen plasma during two minutes (5 minutes if it contains thicker flakes). At this point as well, one can optically check whether the thick flakes were successfully removed, if necessary, repeat etching process and only afterwards, dissolve the resist. The chip is now ready for tests and usage in the experiment.

5.2.6 Device Test

After fabrication is finished we perform basic electrical tests on the device to check if it still has all required contacts for carrying out shot noise experiment. At first, the fabricated devices regularly retained only too few working contacts. But after all, we managed to establish a process, allowed to fabricate devices that had practically all contacts working, otherwise spare voltage probes could also be used. For these tests we had choice between two setups, described below.

a. Probe station

The advantage of a probe station is that it allows to directly (i.e. without bonding the microcircuit) test the device by placing the probe needles on the electrodes pads. However, conventional DC resistance tests with an ordinary ohmmeter are in practice not very safe for such fragile devices as ours. For this reason we equipped a conventional probe station with a lock-in detection system, that provides a possibility to use very low excitations to probe the resistance. It is also safer to apply

[3] In some cases we cut the wafer already before microcircuit pattern developing

current biased excitations, since in a voltage biased device the dissipated power diverges as the inverse of the resistance. For the device safety we also ground the probes each time, before placing them on the pads, to avoid applying a voltage pulse to the device. Nevertheless, the probe station doesn't allow to do more sophisticated tests than a simple two point resistance measurement.

b. Test insert

Test insert allows more advanced studies to be carried out. It has twelve measurement lines that make four point measurement as well as simultaneous gate voltage application possible. Moreover, the sample holder with a device, when connected[4] to the insert, is kept inside a leak-proof chamber from which the atmosphere can be pumped out, hence, it is also appropriate for measurements in a dewar with liquid nitrogen or helium. Although simple contacts tests can also be done with this setup, it requires the bonding of the device to the sample holder, so it is usually more reasonable to do such kind of tests with the probe station before and to use the test insert to measure the response of the device to the gate voltage and to study the effect of the low temperature on the contacts quality. In this setup we also use lock-in detection system with low, current-polarized excitation.

5.2.7 Difficulties and Solutions

In this section we summarise the difficulties we encountered during devices fabrication and solutions proposed to overcome them. First of all, an excessive quantity of graphite used during exfoliation process can result in deposition on the wafer of big graphite cakes (putting the wafers under press (boosts even more this effect). This has several drawbacks: first, it becomes difficult to avoid these cakes while designing the microcircuit pattern and, furthermore, it is very hard to remove such cakes with oxygen plasma, since the PMMA mask will be totally etched before the cakes. Second, these cakes are usually thicker than the PMMA mask for the microcircuit deposition and the resist will not cover them completely. This will hinder from a correct lift-off, as the metallic film will remain gripped to the cakes.

Once again, due to the proximity effect, finding the optimal combination of irradiation dose and development time wasn't a straight-forward task. The pattern geometry optimisation was also required to attain highly reproducible results, albeit occasional deviations in the equipment operation (e.g. SEM, plasma machine) make the complete reproducibility impossible. The beam positioning precision

[4]Note that for the device safety, it is essential to have all measurement lines grounded, while connecting the sample holder to the insert.

was a limiting factor as well, in particular when trying to superpose two successive lithographies. As it was explained our solution was to add supplementary alignment marks to the first pattern.

Still, the most stubborn issue was undoubtedly the control on the quality of the device contacts, for, quite often, at the end of the fabrication process the device had most of its contacts with graphene flake lost, making it unusable. So, furnishing the microcircuit with additional voltage probes was indeed useful. Unfortunately, the reason of the contact quality degradation is rarely evident. Yet, we could identify few possible reasons: foremost, due to flake fragility any mechanical or electrostatic shock can damage the contacts or even completely destroy the device. Hence, the devices at any fabrication stage are to be handled with care. It is also suggested to use electrostatic discharge safe chip box for storing and transporting devices. Besides, the constriction makes the flake even more fragile, although an appropriate shape allows to shrink the mechanical strain: the borders should be rounded and the right angles are not recommended. We equally noticed, that plasma action on uncovered part of electrode (even far from the flake) can significantly worsen the contact quality. Thus, it is important to mind to always keep electrodes strips covered by the mask. Moreover, one should remember, that plasma also etches the mask. By the way, rising of the oxygen pressure in the chamber will increase the etching rate and can even solidify the PMMA, that becomes hardly removable then.

Part III

Experimental Results

Chapter 6

Measurement System Calibration

Recall that our system is designed with the goal of conducting four-point cross-correlation voltage fluctuations measurements. The indicated approach presents several remarkable advantages (e.g. contact resistance contribution is avoided, detection noise is suppressed). Furthermore, the use of cryogenic amplifiers and of a high frequency measurement band (within which the $1/f$ noise is weak), available thanks to resonant circuits, allow a tremendous gain in the measurement duration. At the same time, this approach revealed itself to be also extremely challenging, because of the complications with the device fabrication as well as with, discussed in this chapter, measurement system calibration.

As it was explained in Chapter 4, our measurement system contains four measurement lines, and each of them consists of a resonant circuit and cryogenic amplifier and leads to one of the inputs of two room-temperature differential amplifiers. The gain of commercial amplifiers is assumed to be fixed and well known, that is not the case for cryogenic amplifiers. The gain of a cryogenic amplifier depends on polarisation voltage (see subsec. 4.2.3 for details) and, moreover, at given polarisation voltage, the gain of any two HEMTs is not necessarily the same. In addition, the gain varies with the temperature and after each cooling, the gain characteristics can slightly change as well. That is why after each cooling one has to adjust amplifiers gain and calibrate it. Besides, from time to time, we also checked for eventual drift of the gain and readjusted it if required. Note also, that the electric circuit of each measurement line contains a combination of resistances (including eventual contact resistances a priori unknown), that will form a voltage divider. Its effect is obviously to reduce the signal amplitude, but by a factor, which in not necessarily well-known.

It is clear, that at the output of each measurement line we will detect a signal, which is proportional to the voltage at the point on the sample to which the voltage probe of the given measurement line is connected. Hence, to be able to measure in a correct way the voltage drop between any two such points on the sample, it is

obviously essential to have identical gain on each measurement line. However the gains of the measurement lines depend not only on amplifiers' gain, but also on the exact properties of voltage dividers, that are not always well-known and are not accurately identical for all lines. As a consequence, our main task is to adjust the amplifiers' gains (more exactly the polarisation voltages), in the way, that the gains of all four lines were identical, although this doesn't necessarily mean, that such tuning will result in identical gain of all four amplifiers, because of eventual differences in the voltage dividers for instance, as it was explained. Moreover, it is not possible to determine separately the amplifiers' gains and the losses factors due to the voltage dividers. We present below the approach we used for measurement lines tuning.

First of all note, that the voltage, measured by two voltage probes, situated on the same side with respect to the constriction (e.g. V_{A}^0 and V_{A}^1), is necessarily the same, and so should be for the corresponding output voltages. This gives the first indication of how to adjust the gains. In addition, we use a following trick. By applying the same voltage but of the opposite sign on each side of the sample, we force all current injected into the device through one current electrode to sink essentially through the other current electrode, without skipping along alternative paths, for instance through voltage probes, connected to the ground via several resistances. Hence, ideally the middle of the constriction will be at the ground potential, whereas two voltage probes, situated on different sides of the constriction (e.g. V_{A}^0 and V_{B}^0) will see the voltage of the opposite sign, but of the same magnitude as well, that will allow us to adjust all four lines.

As it will be explained in more details in the dedicated section, the equivalent circuits of measurement lines at low (far from resonant frequency, below RC cut) frequency and at high (near resonant) frequency are different, so it is not guaranteed, that the adjustment, done at low frequency, will hold at high frequency. The noise measurements, as we know, are done at resonant frequency, i.e. at high frequency, thus the system should be tuned at this frequency above all. Yet the measurements at high frequency are far from been obvious, because the signal phase is easily shifted by all capacitances, present in the circuit. For these reasons we first perform tuning and calibration at low frequency and, after having well understood and experimentally confirmed this method at low frequency, we reproduce it at high frequency.

At low frequency we also do a two-point measurement without involving the voltage measurement lines. This has the advantage to be independent of measurement lines' gain, but has obvious yet important drawback: the result of the measurement contains contact resistances. However this measurement is unavoidable and provides one of the elements of the calibration, while the contact resistance value can be established independently, as it will be explained.

From these measurements, constriction resistance and its dependence on the gate voltage can be obtained. Moreover, at high frequency, some measurements allowing to determine the current through the system (which is otherwise unknown) is done.

This chapter is spread into two sections: first one is dedicated to low frequency calibrations, while the last section is dedicated to high frequency calibrations.

6.1 Low Frequency Calibration

In this section we review the measurements, done at low frequency (between 100 and 250 Hz) with the purpose to test our approach of measurement system tuning and calibration.

6.1.1 Lines Tuning

We start with adjustment of measurement lines, as it was explained in introduction. We use *Phase Sensitive Detection* technique to obtain a required signal to noise ratio. The excitation signal is generated by two synchronized lock-ins, with π phase shift between them, in order to apply on each side of the device a voltage of opposite sign. Moreover, it is current biased thanks to the 10 MΩ resistances, as shown in the circuit scheme of fig. 6.1. This simplifies the interpretation of the output signal, measured by the lock-ins, since the current injected in the device is independent of constriction resistance. As a result, the output signal is just proportional to $R_S /\!\!/ 70\,\mathrm{k}\Omega$: the constriction resistance R_S in parallel with 70 kΩ — total input independence of the voltage probing system (see fig. 6.1). The derivation of R_S is then straightforward.

Figure 6.2.a shows the result of lines tuning. As it can be seen, the agreement is quite well. However, all four curves differ by the noise-like variations around the common average value. These are the *Universal Conductance Fluctuations* — reproducible features, related to the precise configuration of the impurities in the sample. At mesoscopic scale, the particles absorbed by a given voltage probe didn't follow exactly the same path as those absorbed by another voltage probe and thus didn't come across the same impurities. This explains, why the Universal Conductance Fluctuations differ for each measurement line.

Figure 6.2.b shows the resulting curve of output signals (proportional to the voltage drop across the constriction, see fig. 6.1 as well as fig. 4.3) measured by the both channels (outputs of two differential amplifiers, indexed 0 and 1), that we note $V^{0/1} = V_A^{0/1} - V_B^{0/1}$ (index A/B stands for one side and another with respect to the constriction), and thus to $R_S /\!\!/ 70\,\mathrm{k}\Omega$. In the following we will explain

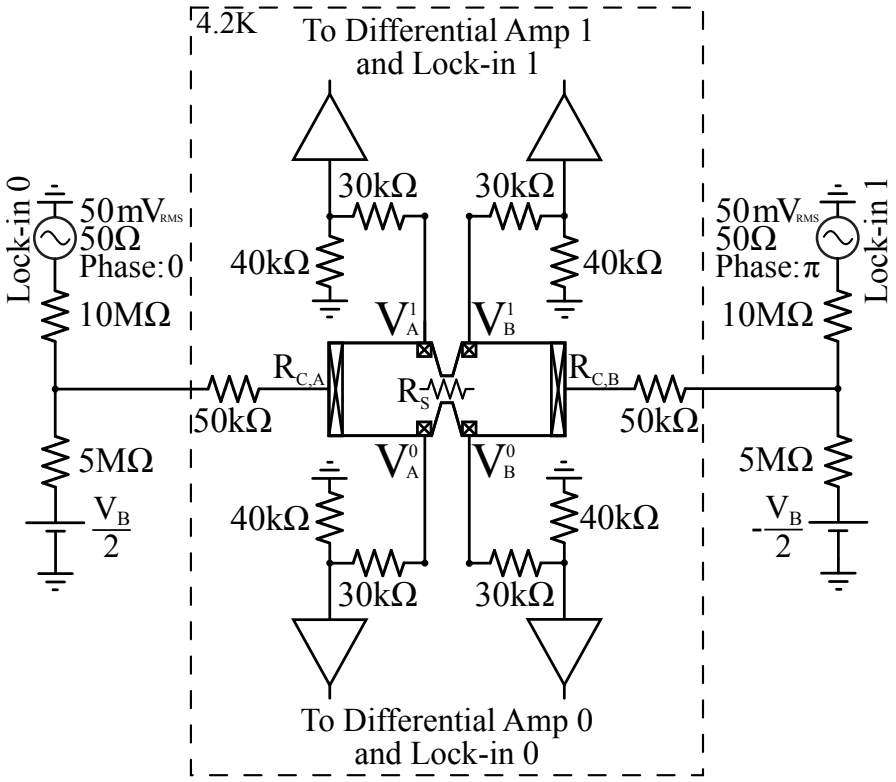

Figure 6.1: Schematics of the low frequency setup, equivalent circuit at corresponding frequency: $f_{\text{LF}} = 137Hz$. Inside the dashed rectangle: low temeperature part with the device in the middle and cryogenic amplifiers, outside of the dashed rectangle: and room temperature part with differential amplifiers omitted. This setup was equally used to measure at low frequency the differential resistance as a function of the bias voltage.

how, from the output voltage signal, it is possible to figure out the constriction resistance value. But for that, additional measurements are required.

6.1.2 Two-point Measurement

Another measurement, that is necessary for the experimental system calibration is a direct (without passing through amplifiers) two-point one. The setup schematics is shown in fig. 6.3. The result of such measurement will obviously contain contacts resistances $R_{\text{C, A}}$ and $R_{\text{C, B}}$ of current injection electrodes, but will provide us exact, gain invariant value of constriction resistance variation, that we can then compare to the variation of the output voltage in order to obtain the conversion coefficient between output voltage and constriction resistance.

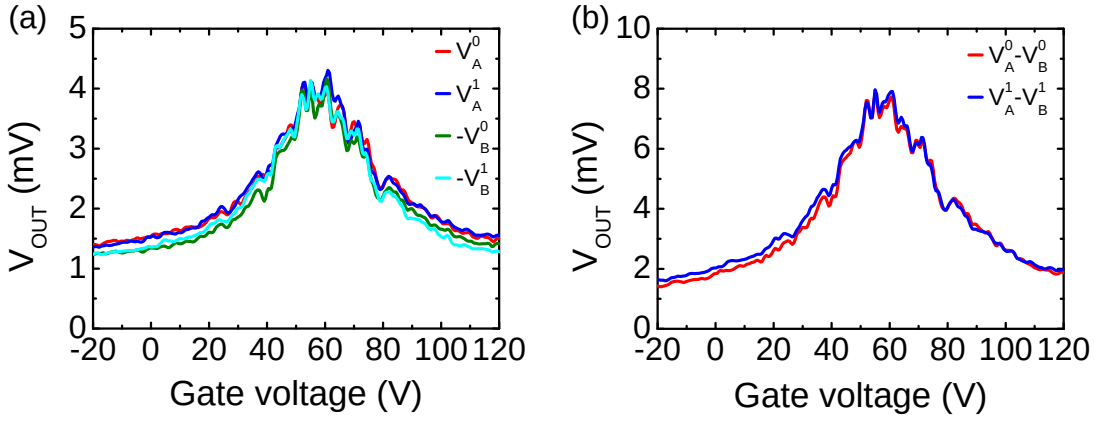

Figure 6.2: Output of all four measurement lines after gain tuning (a) and output differential signal from two channels (b).

We again use the Phase Sensitive Detection technique, and measure the voltage drop V across $R_{\mathrm{M}} = 50\,\mathrm{k}\Omega$, that will allow to find the current through the setup: $\frac{V_{\mathrm{e}}-V}{R_{\mathrm{M}}} = I = 2\frac{V_{\mathrm{e}}}{R_{\mathrm{tot}}}$, where by R_{tot} we obviously noted the total resistance of the circuit. As seen from the circuit schematics total resistance reads

$$R_{\mathrm{tot}} = 2 \times R_{\mathrm{M}} + 2 \times 50\,\mathrm{k}\Omega + R_{\mathrm{C,\,A}} + R_{\mathrm{C,\,B}} + R_{\mathrm{s}} /\!/ 70\,\mathrm{k}\Omega \tag{6.1}$$

so, since R_{M} is known, the measurement provides us $R = R_{\mathrm{C,\,A}} + R_{\mathrm{C,\,B}} + R_{\mathrm{s}} /\!/ 70\,\mathrm{k}\Omega$ as a function of gate voltage V_{G}, that we plotted in fig. 6.4.a. Let us define ΔR as a variation of R on the interval of gate voltages between $-20\,\mathrm{V}$ and $60\,\mathrm{V}$: $\Delta R = R(60\,\mathrm{V}) - R(-20\,\mathrm{V})$. Then $\Delta R = \Delta(R_{\mathrm{s}} /\!/ 70\,\mathrm{k}\Omega)$, since with a certain degree of approximation we can consider that $R_{\mathrm{C,\,A}} + R_{\mathrm{C,\,B}}$ is gate voltage independent[1].

6.1.3 Calibration

It is clear that since $V^{0/1} = \eta \times R_{\mathrm{s}} /\!/ 70\,\mathrm{k}\Omega$, the variation of this value on the interval between $-20\,\mathrm{V}$ and $60\,\mathrm{V}$ will be $\Delta V^{0/1} = \eta \times \Delta(R_{\mathrm{s}} /\!/ 70\,\mathrm{k}\Omega)$, where $\Delta(R_{\mathrm{s}} /\!/ 70\,\mathrm{k}\Omega)$ on the other hand we know from two-point measurement. By combining these two measurements we can in principle find η. In return, we should mind the eventual offsets in the output signal of the four-point measurement, that gives us a second parameter to find out. To do that in an independent manner, we make use of the linear dependence of conductivity on the charge density $\sigma \propto n_{\mathrm{el}} \propto \Delta V_{\mathrm{G}} =$

[1]Contact resistance is usually due to Schottky barrier formed between the metal and semiconductor and indeed depends on charge density, proportional to the gate voltage. However, we can assume that the effect of the side-gates is of reduced extension and doesn't influence the local charge density near current electrode/graphene interface, which is not the case, for instance, for the contact resistances of voltage probes, situated in the proximity of the local gates.

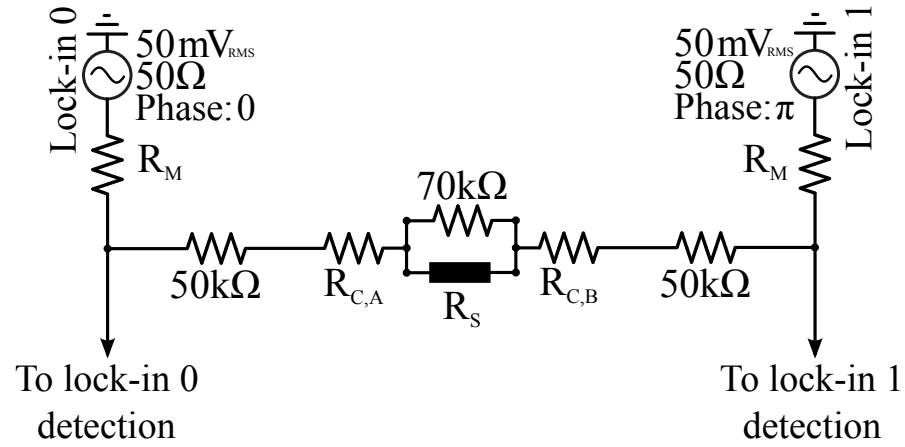

Figure 6.3: Schematics of the equivalent circuit for the two-point low frequency measurement setup ($f_{\text{LF}} = 137Hz$), measurement resistance $R_{\text{M}} = 50\,\text{k}\Omega$.

$V_{\text{G}} - V_{\text{D}}$, with V_{D} — gate voltage, corresponding to the Dirac point, since at the Dirac point the charge density is zero. This can be rewritten as

$$R \propto \frac{1}{\Delta V_{\text{G}}} \to 0, \text{ when } \Delta V_{\text{G}} \to \infty \tag{6.2}$$

Then, if what we measure is a certain resistance $R^* = R + R_{\text{OFFS}}$, where R_{OFFS} is a constant offset resistance,

$$R^*\Big|_{\Delta V_{\text{G}}^{-1} \to 0} \longrightarrow R_{\text{OFFS}} \tag{6.3}$$

meaning that by extrapolating the curve $R^*\left(\Delta V_{\text{G}}^{-1}\right)$ to zero we will find R_{OFFS}. In the four-point measurement, the R_{OFFS} will correspond to a certain measurement artefact (V_{OFF}/η), whereas in the two-point measurement, this will be the contact resistance $R_{\text{C, A}} + R_{\text{C, B}}$.

Such ideal classical behaviour will appear mostly far from Dirac point, since at weak charge density appearance of the electron-hole puddles involves more complicated processes. Hence, on the signal versus $[V_{\text{G}} - V_{\text{D}}]^{-1}$ plot the curve becomes linear only near zero (see fig. 6.5.a for instance). We perform linear fit of each branch of the curve and the offset is given by the intercept of obtained straight lines. Two lines should obviously have the same intercept and V_{D} was used as a free parameter to obtain this. Note that this plot is not symmetric relative to zero, that is not completely unusual, as we do not expect the same dependence of conductivity on charge density for holes and for electrons.

The result of the application of this method to two-point measurement situation can be seen in fig. 6.4.b. We find $R_{\text{C, A}} + R_{\text{C, B}} = 296.75\,\text{k}\Omega$ and $V_{\text{D}} = 59.5\,\text{V}$,

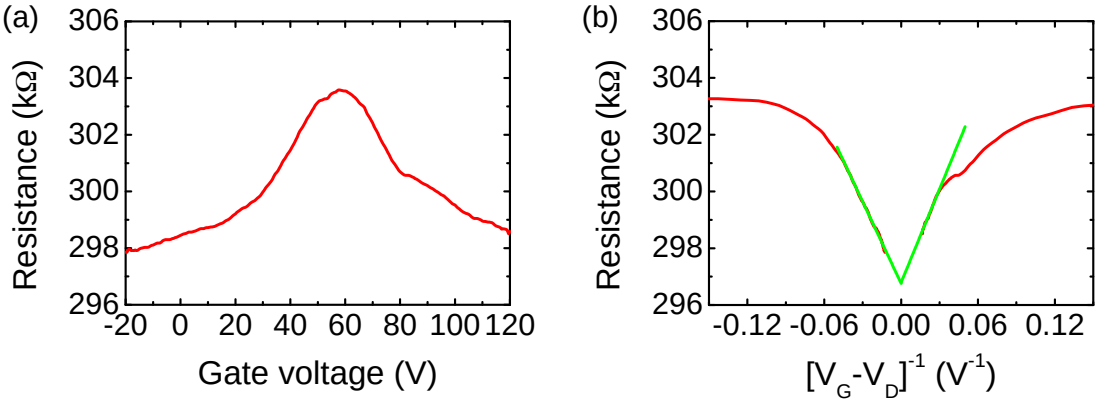

Figure 6.4: Two-point resistance $R_s /\!\!/ 70\,\mathrm{k\Omega} + R_{C,\,A} + R_{C,\,B}$ (smoothed) as a function of gate voltage (a) and as a function of inverse charge density with linear fit in green (b).

meaning at least $\simeq 150\,\mathrm{k\Omega}$ per contact, which is quite high value for contact resistance.

As for four-point measurement with amplifiers, since we are using Phase Sensitive Detection technique, we do not expect any significant offset in our measurements. As seen from the plot in fig. 6.5.a, we indeed obtain an offset of $\approx 0.28\,\mathrm{mV}$ which is not more than 5% of the signal. The output signal with corrected offset is plotted in fig. 6.5.b. The Dirac point was found to be at $V_D = 60.5\,\mathrm{V}$ which is slightly different from the previous result. The position of Dirac point depends essentially on impurities configuration over and under graphene, which could slightly evolve with time and because of other measurements performed on the device. Since there indeed was a long delay between two measurements, such slight disparity is considered as usual. In addition, because of the disorder puddles at low density, the Dirac point position is only locally well defined, the fact that also explains the plateau formation around the Dirac point.

We now know $R_s /\!\!/ 70\,\mathrm{k\Omega}$ from two-point measurement and can determine the proportionality factor η that allows to convert the output signal of four-point measurements to resistance units. Note first, that on the interval for the gate voltage between -20 and $60\,\mathrm{V}$ the constriction resistance varies by $5.75\,\mathrm{k\Omega}$, whereas on the same interval the output signal varies by $6\,\mathrm{mV}$, leading to $\eta \simeq 5.75/6\,\mathrm{k\Omega\,mV^{-1}}$.

We can finally calculate and plot together the R_s, obtained from the two- and four-point measurements, as the function of V_G in fig. 6.6. The achieved agreement seem fully convincing. These curves will be analysed in a separate chapter.

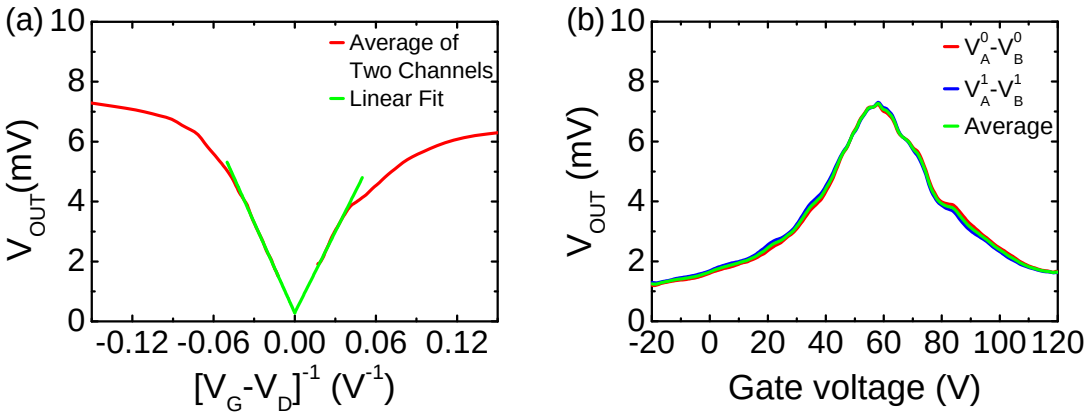

Figure 6.5: Average of output signals of two channels (smoothed) as a function of inverse charges density with linear fit (a) and the output signal of both channels and their average (all smoothed) with corrected offset as a function of gate voltage (b).

6.2 High Frequency Calibration

6.2.1 Lines Tuning

From the studies we performed at low frequency we concluded that our tuning and calibration approaches work well. We next applied these same approaches at frequencies, at which we intended to perform noise measurements, i.e. around 3 MHz. More precisely, we chose measurement frequency to be 3.33 MHz, which is the frequency on which the cross-correlation response passband is centred. Inasmuch as our main goal is to measure noise with cross-correlation method, the choice of this frequency for tuning and calibration of the measurement system seems expedient. Once again, the previous tuning will not necessarily hold when passing from hundred Hertz to several MHz — two frequency ranges at which quite a few circuit parameters could differ — and a separate tuning and calibration are indeed required. Probably the most important difference to point out between these two ranges is due to the variation with the frequency of the intrinsic resistance of the inductors, expected from the well known *skin effect*. Also, a capacitive shunt of certain circuit elements is possible. On the other hand, with the increase of the frequency, the measurements become more and more tricky and the appropriate techniques have to be applied. Hence, here we do not detail anew the basic principles of the used approach, being unchanged, but rather discuss some technical details that differ it from the previous case and then directly present the results.

Now let us see, what distinguishes measurement approach used here from the low frequency case. First of all, use of high resistances for current polarisation is

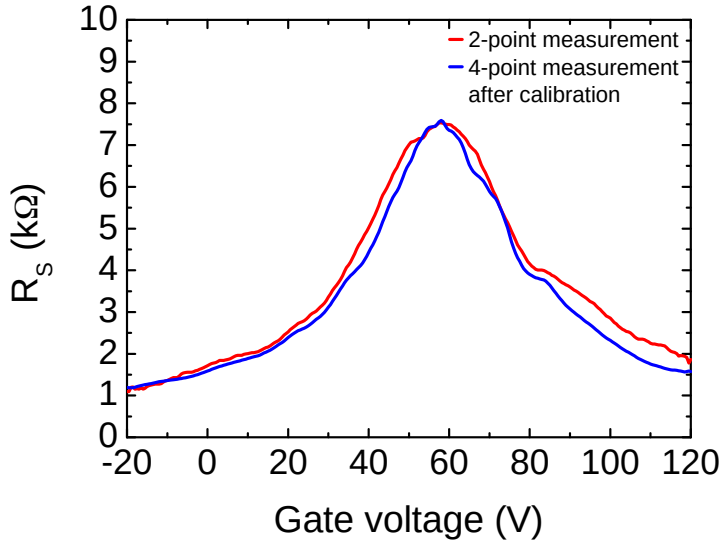

Figure 6.6: Constriction resistance obtained from two-point measurement (in red) and from four-point measurements with amplifiers (in blue) as a function of gate voltage.

not appropriate, since this leads to a cut frequency[2], much lower, than the working frequency. In return, our system already contains 50 kΩ resistors near the device and, moreover, as we saw, the contact resistance of current leads is very high as well, hence, adding high resistances at room temperature is not necessary to have a current polarized excitation. Next, since the commercial lock-ins, adapted for this frequency range were not available, we used for the Phase Sensitive Detection two synchronized high frequency generators, but, as before, with a difference in phase of π, combined with a home-made lock-in, that we built up from our analog-to-digital conversion card (see. sec. B.2) and that we tested beforehand by comparing it to a commercial lock-in. The schematics of the measurement is shown in fig. 6.7. One can also notice the -30 dB attenuators on each side, which are required simply because the minimal power the voltage generators can deliver is too strong, so that otherwise it could be unsafe for the device. Finally, at these frequencies, the parasitic capacitances become non-negligible and the signal arrives in some sense with an arbitrary phase to the detector. Moreover, we noticed that the output signal contains an important offset, which is probably due to the cross-talk between the measurement lines via inductive coupling for instance. As a consequence, in

[2]The low temperature part of the setup is connected to the high temperature part via special coaxial cables of about 2.5 m, that in addition have high capacitance. Their capacitance is thus estimated to be about 400 pF. If we use for example a 1 MΩ resistors, the resulting cut frequency will be given by $f_c = 1/2\pi RC \approx 400$ Hz

this situation the absolute value of the resulting signal is not a representative quantity any more and a treatment of the signal is required, which consists in following. We numerically adjust the phase of the signal in order to transfer all variation of the signal to the real part, whereas the imaginary part then remains practically constant. So if we note by X^*_{OUT} and Y^*_{OUT} the real and imaginary parts of the measured signal, mathematically this corresponds to applying the formula below

$$\begin{aligned} X_{\text{OUT}} &= Y^*_{\text{OUT}} \sin(\theta + \pi) - X^*_{\text{OUT}} \cos(\theta + \pi) \\ Y_{\text{OUT}} &= Y^*_{\text{OUT}} \sin\theta - X^*_{\text{OUT}} \cos\theta \end{aligned}$$

with θ such that the above condition is satisfied. In addition for the convenience, we shift all curves to begin at the same value (we choose zero). We now can consider the real part X_{OUT} only and tune the lines by requiring, as previously, a perfect superposition of all curves. The result of this operation is shown in fig. 6.8.

The next step is to find and subtract the offset and thus obtain the true physical signal coming from the device, that we can then convert to the constriction resistance. To do that we apply exactly the same method as described in the previous section (see subsec. 6.1.3 and eq. 6.2 and 6.3 there). However, one detail should be mentioned. As one could already notice, the response of the lines VA0 and VB0 at $V_{\text{G}} \approx 75\,\text{V}$ start to deviate from the symmetric regime we observe with the lines VA1 and VB1 and that we also observed at low frequency with all four lines. Indeed the sample was probably slightly damaged between two measurements, that introduced a supplementary contact resistances to the voltage probes of lines VA0 and VB0, which moreover vary with gate. The corresponding model will be exposed in another section, but for the moment what matters, is that the method from subsec. 6.1.3 can not be applied for the channel 0, since the required hypotheses become inaccurate in this case. Nevertheless we consider that all four lines can be well tuned, using only the parts of the curves below the Dirac point, whereas the offset can be determined from the correctly working channel, i.e. channel 1. As for the channel 0, it is supposed to have the same offset. Furthermore, it is clear, that our method can still be applied to the part of the data from the channel 0 below Dirac point, and we obviously obtain the same result as with the channel 1. The resulting offset equals $-6.85\,\text{mV}$ as seen from fig. 6.9.a. Figure 6.9.b shows the corrected outputs of both channels, i.e. without the offset.

This finally provides us all necessary elements to derive the constriction resistance R_{s} from the measurements at high frequency. An important remark to be done is, that at high frequency the resistance in parallel with the constriction, coming from the measurement lines, is reduced to $\approx 51.5\,\text{k}\Omega$, due to the skin effect

(see subsec. 4.2.2 of Chapter 4 for details). Hence, the output signal is proportional to $R_s /\!\!/ 51.5\,k\Omega$, the quantity, which can be calculated from the previous measurements (we suppose that the constriction resistance didn't change from one measurement to another). Then, as before, since $V_{OUT} = \eta \times R_s /\!\!/ 51.5\,k\Omega$, the same is true for the variation of these quantities on the interval of gate voltages between -20 and $60\,V$: $\Delta V_{OUT} = \eta \times \Delta R_s /\!\!/ 51.5\,k\Omega$. If that is the case, to find out the proportionality coefficient η, it is again cautions to, instead of comparing the quantities themselves, compare their variation on the above mentioned interval, thus avoiding any offset related drawbacks. This becomes the only constraint we apply, whereas the offset is obtained independently. We then calculate R_s and its comparison with the previous results, as seen in fig. 6.10, convinces us that the result in the fig. 6.9.b indeed contains no offset. This confirms once again the relevancy of our method. Note however, that near the Dirac Point, the orange curve (measurement at high frequency with channel 1) is slightly larger than the reference one in blue (measurement at low frequency, average of channels 0 and 1). This is probably due to the evolution that the device has undergone between the two measurements. All these curves will be discussed in details in Chapter 7.

6.2.2 Current Measurement

As it was already mentioned, in low frequency measurements we used high resistances to generate a current polarized excitation. These resistances dominated the remaining resistances of the system, making the current calculation easy. At high frequencies however this approach was not appropriate and we considered the two $50\,k\Omega$ resistances, situated near the device, together with the current leads contact resistances be sufficient to obtain the current source, independent of the constriction resistance. In that case, yet, a straight-forward calculation of the current is not possible, since not all resistances are known and, in addition, eventual capacitive shunt can also interfere. Though, it is still very important to know the exact value of the current, passing through the device. For this reason we do a new independent measurement, that will allow to calculate the current. The setup schematics is represented in fig. 6.11.

We now will explain its principle: the non-linearity of the device conductance can be of a great use. For instance, if we measure the differential resistance as a function of the DC bias voltage, with gate voltage being fixed, the response will not be a constant function, but rather something of the type, one can see in fig. 7.9 (green curve). By the way, in this measurement we will use low frequency detection system, since in practice, the fact that the setup is not tuned to work at low frequencies is not a problem, as it will be seen. Now, if we replace the DC bias by the high frequency excitation (while the differential resistance measurement is still done at low frequency), the non-linearities should still manifest themselves

in the response. If we manage to relate the non-linear response to the DC bias and the one to the high frequency excitation, by comparing the two we will be able to find the current at high frequency, because the corresponding DC current is well known. In short, we first measure the system response, proportional to the differential resistance, at different bias voltages V_{B}, while no high frequency excitation is applied: $V^{\mathrm{HF}} = 0$. We then measure the same response, but at zero bias voltage and with high frequency excitation of different amplitudes (we know only the RMS voltage applied to the entire system, but not the voltage across the constriction). Finally, thanks to the relation below, the result of the first experiment allows us to calculate the response that we are supposed to detect during the second experiment for any given AC current. Matching the outcome of these calculations with the results of the second experiment, will provide us the sought correspondence between the RMS value of the high frequency excitation V^{HF} and the AC current I_{AC}, which it generates.

Let us see, how these two experiments are related. We first note as $R_{\mathrm{d}}(I)$ the differential resistance, which depends on the current, passing through the device. This dependence is known from the first experiment (DC current can be calculated in the straight-forward manner: $I = V_{\mathrm{B}}/10\,\mathrm{M\Omega}$). We also know that during the second experiment this value was obviously time dependent according to the expression $R_{\mathrm{d}}\left(I_{\mathrm{AC}}\sin(\omega t)\right)$ (ω being the excitation angular frequency). Yet, since the detection is done at low frequency, i.e. $f^{\mathrm{LF}} \ll f^{\mathrm{HF}}$, the measured signal will correspond to a certain time average of the previous expression $\overline{R_{\mathrm{d}}\left(I_{\mathrm{AC}}\sin(\omega t)\right)}$.

In order to calculate these averages of the differential resistance $\overline{R_{\mathrm{d}}}$ for different AC current amplitudes I_{AC}, we make use of the results of the first experiment (with the DC current). It is however clear, that a sinusoidal excitation will not vary the device resistance regularly, but instead the resistance will obviously remain more time near $R_{\mathrm{d}}(I_{\mathrm{AC}})$ or $R_{\mathrm{d}}(-I_{\mathrm{AC}})$ values, than near $R_{\mathrm{d}}(0)$, meaning that a kind of weighted average should be used in such calculation. To account for that, we take the values of R_{d} interpolated on the sinusoidal grids of the time-varying current for each amplitude I_{AC}. It is evident, that a usual average over such irregularly spaced array of values is equivalent to the mentioned weighted average. As a result, we obtain the response we are supposed to detect with our system when a given AC current is injected into the device. If the same response was indeed detected during the second experiment (with the HF excitation), this same current was injected into the device, hence allowing us to relate high frequency voltage and current. Note, that we use RMS values in all our measurements, so the AC current values are also converted to these units (dividing by $\sqrt{2}$).

Both experiments were done at $V_{\mathrm{G}} = 55\,\mathrm{V}$, the results of the procedure we have just discussed are presented in fig. 6.12. Experimental and numerical results are plotted with independent scales, but in the way that the two ensembles of points

are superimposed. Two scales are thus related, just as are the voltage and the current. The RMS value of the full high frequency excitation, that we applied to the circuit ($2V^{\text{HF}}$) in all other measurements is 200 mV. Our method yields the corresponding RMS value of the high frequency current ≈ 16.7 nA, when calculated using the measurement with channel 0, and ≈ 16 nA, when calculated using the measurement with channel 1. For the following calculations, we take the average value of 16.35 nA (RMS) and will keep in mind 4.5% error that we will include in the error bar henceforth.

Besides, this result is confirmed by a straight-forward calculation of the injected AC current. Indeed, the RMS value of the full high frequency excitation after the -30 dB attenuators is $200\,\text{mV} \times 10^{-3/2} \simeq 6.32$ mV, the total contact resistances as we saw in subsec. 6.1.2 is $R_{\text{C, A}} + R_{\text{C, B}} \simeq 300\,\text{k}\Omega$. Taking into account the two series 50 kΩ resistors, the AC current reads: $6.32\,\text{mV}/400\,\text{k}\Omega \simeq 15.8$ nA (RMS).

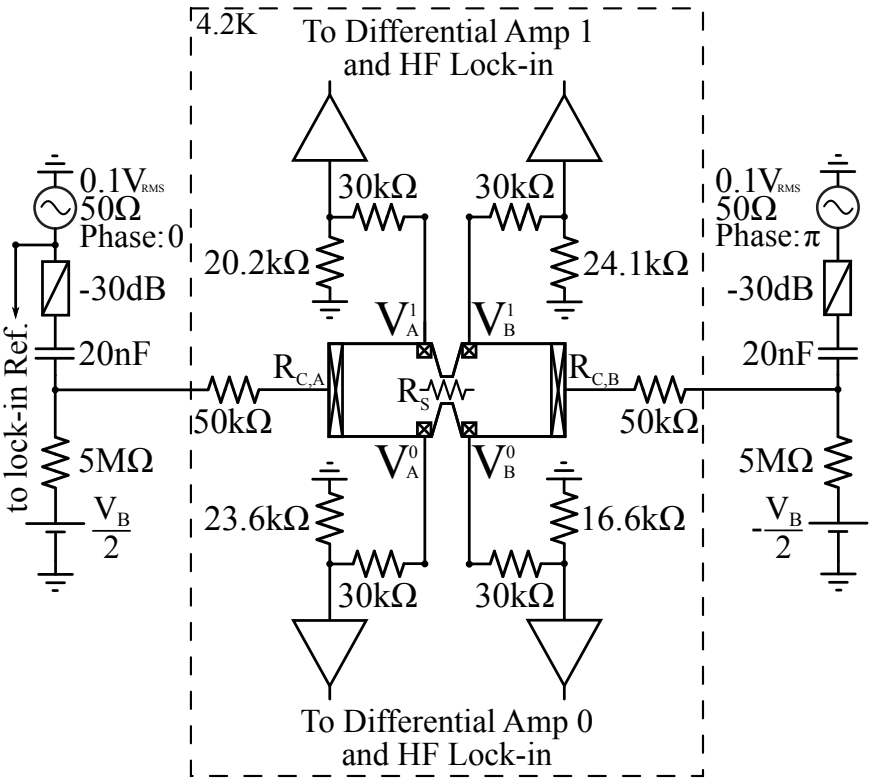

Figure 6.7: Schematics of the high frequency setup, equivalent circuit at corresponding frequency: $f^{\mathrm{HF}} = 3.33\,\mathrm{MHz}$. Inside the dashed rectangle: low temperature part with the device in the middle and resonant circuits replaced by equivalent resistances, determined in subsec. 4.2.2 of Chapter 4. Outside of the dashed rectangle: room temperature part with differential amplifiers omitted. The 20 nF capacitors serve to protect the 50 Ω high frequency generators from direct currents. This setup was equally used to measure at high frequency the differential resistance as a function of the bias voltage.

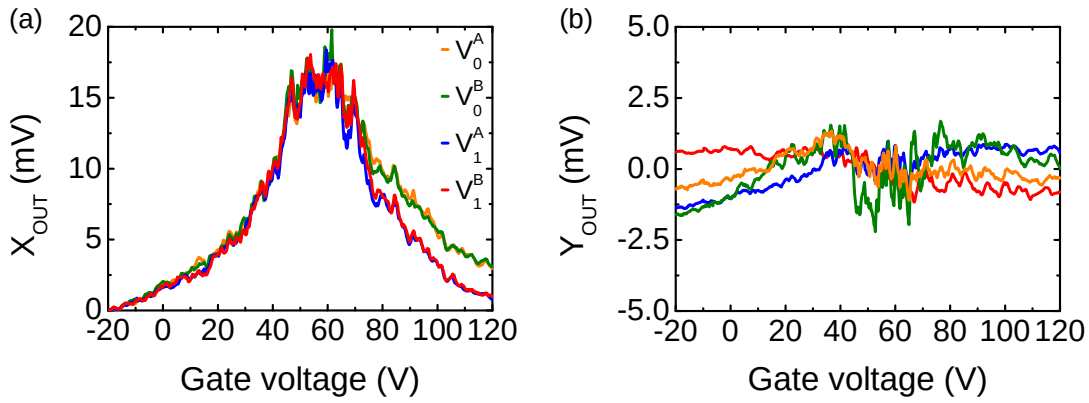

Figure 6.8: Real (a) and imaginary (b) parts of the output signal after phase correction for all four measurement lines, result of the tuning.

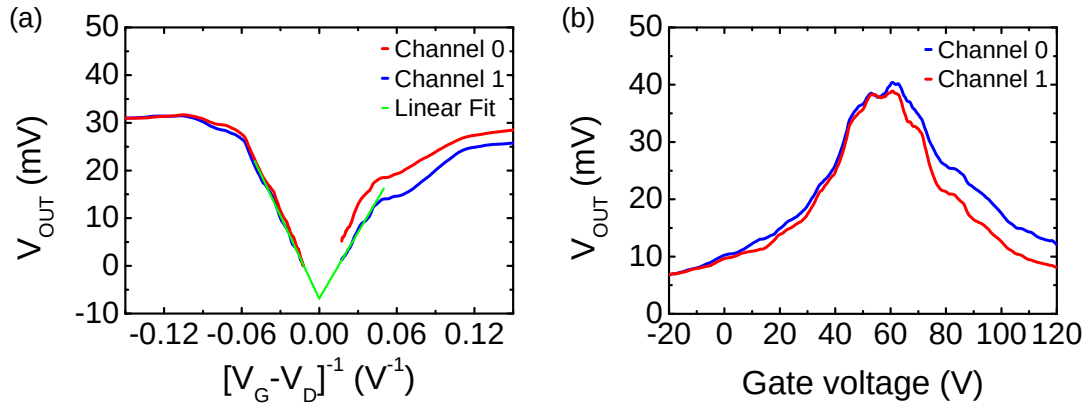

Figure 6.9: Real part of the output signal (channel 0 in red and channel 1 in blue, both smoothed) after phase correction plotted versus the inverse charges density (a). Linear fit intercept (in green) points out the offset of the signal. On the figure (b) the offset is subtracted from the signals (smoothed) plotted versus the gate voltage.

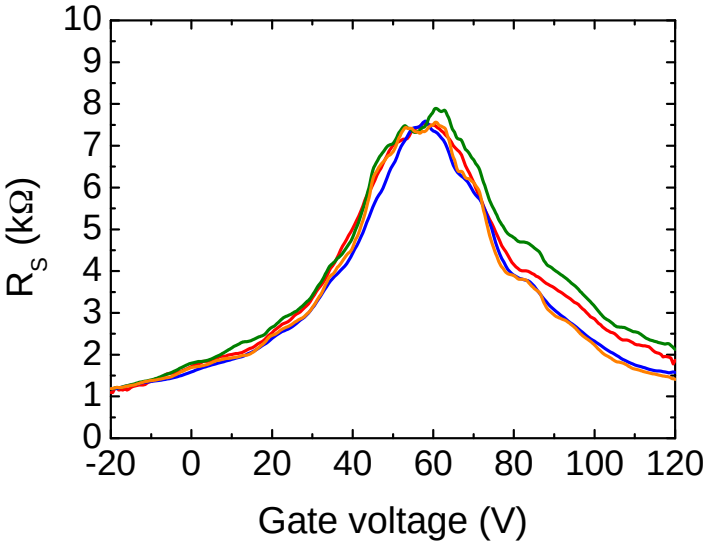

Figure 6.10: Constriction resistance R_S obtained with different methods: in red 2-point measurement, in blue 4-point measurement at low frequency (average between two channels) and in green and orange 4-point measurement at high frequency through channels 0 and 1 respectively.

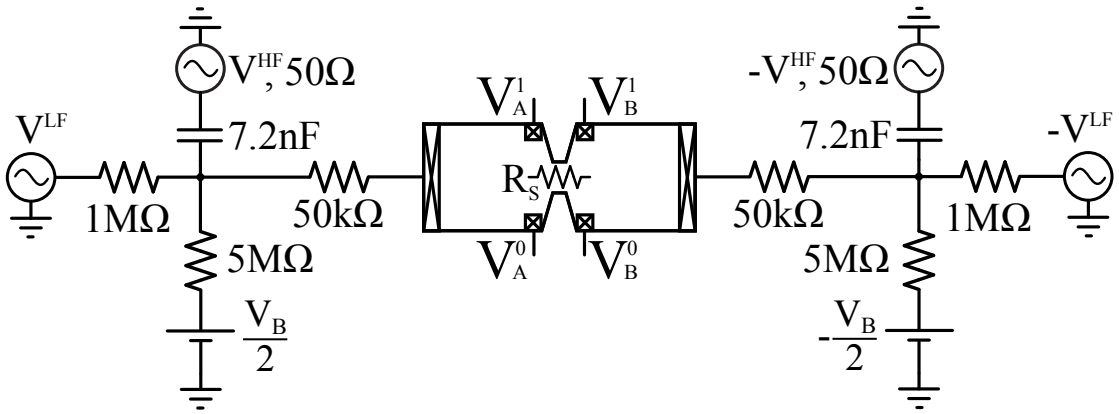

Figure 6.11: Schematics of the circuit with the device in the center. Measurement lines as well as $-30\,\mathrm{dB}$ attenuators are omitted, $\pm V^{\mathrm{LF/HF}}$ notation is used to emphasize the π phase discrepancy between corresponding sources. $V^{\mathrm{LF}} = 50\,\mathrm{mV_{RMS}}$, V^{LF} is variable, used frequencies are $f^{\mathrm{LF}} = 137\,\mathrm{Hz}$ and $f^{\mathrm{HF}} = 3.33\,\mathrm{MHz}$ respectively.

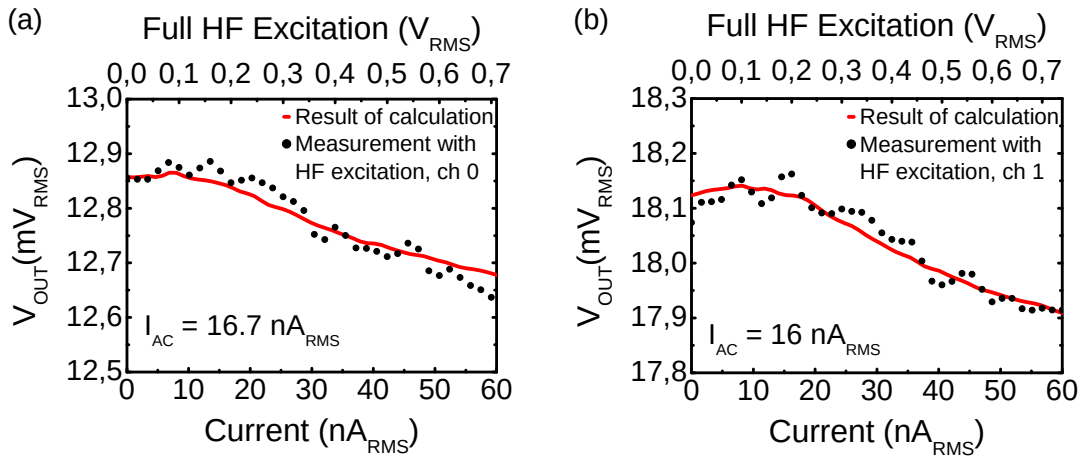

Figure 6.12: Superposition of the result of calculation (red line, lower scale) and the high frequency measurement (black dots, upper scale) for channel 0 (a) and channel 1 (b).

Chapter 7

Conductance Measurements at Zero Magnetic Field

7.1 Conductance at Zero Bias

In this section we try to establish a theoretical basis for the results of conductance measurements by verify different hypotheses one after another. This is also the way this section is organized: we dedicate a separate subsection to each theoretical model and afterwards provide arguments, confirming one of them.

But before going deeper into the subject, remember that in the previous section we indicated several divergences in the device behaviour due to its evolution in time. In the last subsection we will present a model giving the possible scenario of this evolution (see section 7.1.4), which we consider to be extrinsic to the constriction conductance properties. Therefore the broad analysis of the device conductance that we present here will concern exclusively the curves, that seem not to have any extrinsic issues. These are the curves provided by the 4-point measurement at low frequency as well as by the measurement of the same principle, but at high frequency and using only channel 1.

These curves are shown in the fig. 7.1.a (while the curves with altered behaviour are shown in fig. 7.1.b). First important aspect, visible on all curves, is that the Dirac Point is shifted to about 60 V, in other words, the graphene sample is highly p-doped, which is expected for an unbaked pristine graphene on SiO_2 substrate and after all nano-fabrication steps. Moreover one notices that the sample does not reach the minimal conductivity in one point but rather saturates on a certain range of gate voltages. By the way, the curves are also symmetric about the neutrality point. The saturation value of the resistance is about 7.5 kΩ while on the flanks of the curve the resistance shows excellent $\propto 1/\Delta V_G$ behaviour, where $\Delta V_G = V_G - V_D$ with $V_D \simeq 61\,V$, almost attaining a value of 1 kΩ at −20 V of gate

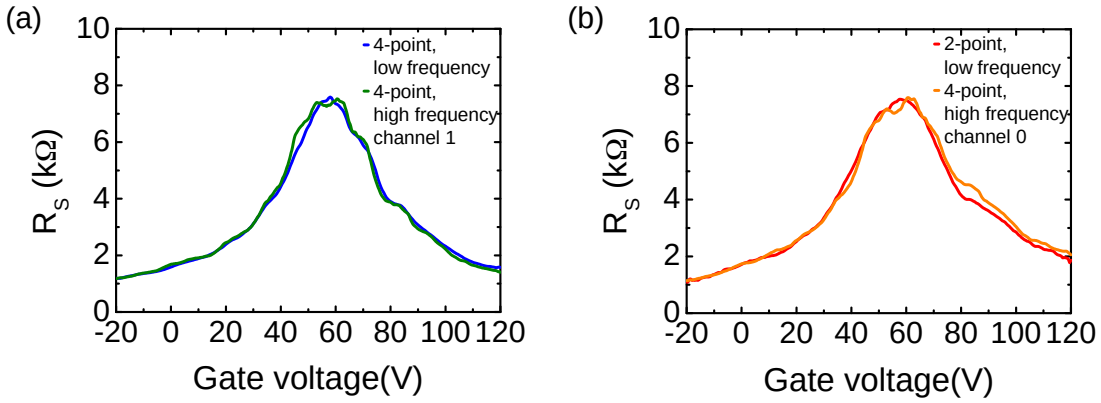

Figure 7.1: Results of the conductance measurements with different setups: in blue — four-point measurement at low frequency (average of two channels), in green — four-point measurement at high frequency with the channel 1, in red — two-point measurement at low frequency, in yellow — four-point measurement at high frequency with the channel 0. The curves in figure (a) are considered to not to have any extrinsic issues as opposed to those in figure (b).

voltage.

Now let us confront this data to several theoretical models.

7.1.1 Ballistic Regime Hypothesis

First of all we would like to test the ballistic model presented in Chapter 3, because the original intention of our work was to probe transport properties in this regime. Although, it is not likely that the ballistic regime was attained, since the device has not been baked, and because for the calibration we already noted the variation of the resistance $\propto 1/\Delta V_{\mathrm{G}}$.

We estimate the aspect ratio of the constriction, using the relations (3.7). Indeed, the conductivity value at the Dirac point in ballistic regime is universal and reads

$$\sigma = G \times \frac{L}{W} \to \frac{4e^2}{h}\frac{1}{\pi}, \tag{7.1}$$

with G — constriction conductance and W and L — its width and length respectively. This corresponds to constriction resistance

$$R_{\mathrm{s}} \to \frac{L}{W}\frac{\pi}{2}\frac{h}{2e^2} = \frac{L}{W}\frac{\pi}{2} \cdot 12.9\,\mathrm{k\Omega} \tag{7.2}$$

Taking into account the saturation value of the differential resistance $\simeq 7.5\,\mathrm{k\Omega}$, (7.2) yields aspect ratio $\frac{W}{L} \simeq 2.7$, that is much less than intended 4 value and even

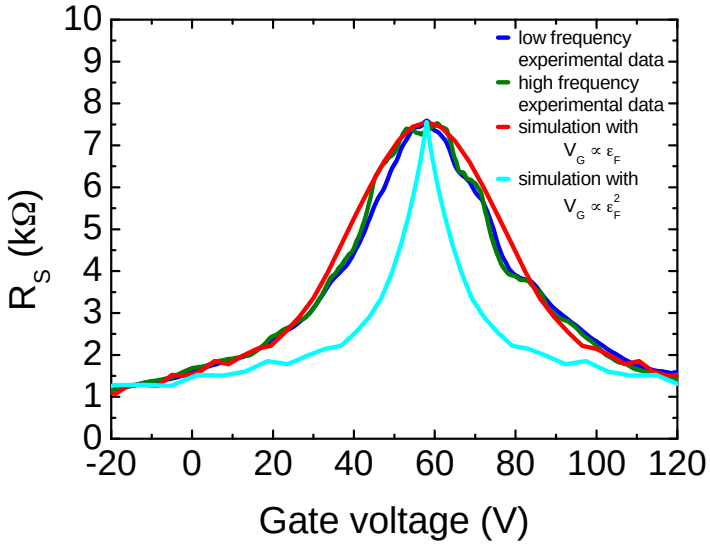

Figure 7.2: The results of the fit using the conclusions of the ballistic model within two assumptions: $\Delta V_{\mathrm{G}} \propto \varepsilon_{\mathrm{F}}$ (in red) and $\Delta V_{\mathrm{G}} \propto \varepsilon_{\mathrm{F}}^2$ (in light blue). The experimental data is plotted in green and blue.

less than 3.5, aspect ratio after which the Fano factor converges to the universal value 1/3. The conductance at this aspect ratio is, however, already very close to the universal value, as it can be seen in fig. 3.1.a, that allows the application of the relations above. We now have two free parameters. The first one is the constriction width, that we nevertheless fix to $W = 800\,\mathrm{nm}$ — the value given by the lithography design and that does not suppose to vary more than by $\pm 20\%$. Yet the main free parameter is the one that relates the gate voltage relative to the Dirac point ΔV_{G} with the Fermi energy ε_{F} in the constriction. Here two cases are possible. In the total absence of screening the electrostatic potential and thus the Fermi energy in the constriction is entirely defined by the gate voltage that is $\Delta V_{\mathrm{G}} \propto \varepsilon_{\mathrm{F}}$. This case is however not very realistic in particular for the high carrier density. On the other hand, in the presence of screening the charges in the conductor shield the gates' field and the better way to describe the effect of the gates is to consider the conductor-gates system as a capacitor, that means that it is the number of carriers and thus their surface density n_{s} that are proportional to the gate voltage ΔV_{G}. From (1.32) the carrier density depend on the Fermi energy as follows

$$n_{\mathrm{s}} = \frac{\varepsilon_{\mathrm{F}}^2}{\pi (v_{\mathrm{F}} \hbar)^2} \tag{7.3}$$

We note the conductor-gates capacitance per unit area as C, i.e. $C = e n_{\mathrm{s}} / \Delta V_{\mathrm{G}}$.

Then the relation between the Fermi energy and the gate voltage reads

$$\Delta V_{\mathrm{G}} = \frac{e\,\varepsilon_{\mathrm{F}}^2}{\pi C(v_{\mathrm{F}}\hbar)^2} \tag{7.4}$$

namely $\Delta V_{\mathrm{G}} \propto \varepsilon_{\mathrm{F}}^2$, a relation totally different from the previous one. Of course, only one of these two incompatible assumptions will allow to describe correctly the experimental curves. It is not very hard to guess that, since the experimental conductance has linear dependence on the gate voltage far from the Dirac point, which is also the case for the theoretical conductance, which is however linear with the Fermi energy (see fig. 3.2.a), the assumption $\Delta V_{\mathrm{G}} \propto \varepsilon_{\mathrm{F}}$ will be confirmed. Performing a numerical fit of the conductance curves, with both assumptions we conclude that this is indeed the case (see fig. 7.2). Moreover the fit obtained in the assumption of no screening is surprisingly perfect. Hence, based on the results of this fit, we can evaluate the parameter β relating the Fermi energy with the gate voltage and defined as $\varepsilon_{\mathrm{F[eV]}} = \beta \Delta V_{\mathrm{G}}$. It equals $\approx 2.8 \times 10^{-4}$.

To conclude, the hypothesis of ballistic transport seems to hold only when the screening in the conductor is weak, which is not very realistic. A more exhaustive discussion about this subject will be presented in the subsec. 7.1.3.

7.1.2 Diffusive Regime Hypothesis

Most of the studies of the graphene transport properties reported on samples in the diffusive regime. It is quite obvious, that the transport properties of such one atom-thick layer are easily affected by the underlying substrate and by the surface residues which are difficult to remove totally. Ideally, suspended sample, thoroughly baked is required to probe the ballistic regime. Several common features were observed in these studies: conductance, at first linear with the carrier density, saturates to its minimal value on a certain range of carrier densities around the Dirac point. Some studies suggested universality of the minimal conductivity even in the diffusive regime, but this early assumption was latter rejected. Yet, conductance saturation at finite value when the carrier density is low can seem somehow puzzling because it can not be taken into account by a naive Drude transport theory, since in the intrinsic graphene the carrier density (to which the Drude conductivity is proportional) simply vanishes at the Dirac point. This in particular means, that whenever the Dirac point is reached, the Drude-type transport is impossible.

However, this is not what was observed experimentally. The explanation for this inconsistency is quite simple: charged impurities in the substrate generate carrier density fluctuations, often referred to as puddles in the literature, making the ubiquitous cancellation of carrier density experimentally inaccessible in available samples. These density puddles were indeed observed using Scanning Single

Electron Transistor by Martin et al. On the other hand, Adam et al. developed a self-consistent theory for graphene transport in the diffusive regime, starting from puddles hypothesis. This work combines *Random Phase Approximation*(RPA) and *Boltzmann Equation* formalisms and provides quite exhaustive picture of transport that handles pretty well both high and low carrier density limits.

a. RPA Model for Diffusive Conductance

The main results of the model proposed by Adam et al. can be formulated as follows

$$\sigma(n_{\mathrm{s}} - \bar{n}) = \begin{cases} \frac{20e^2}{h}\frac{n^*}{n_{\mathrm{imp}}} & \text{if } n_{\mathrm{s}} - \bar{n} < n^*, \\ \frac{20e^2}{h}\frac{n_{\mathrm{s}}}{n_{\mathrm{imp}}} & \text{if } n_{\mathrm{s}} - \bar{n} > n^* \end{cases} \tag{7.5}$$

Here, n_{s} is the surface carrier density, n_{imp} is the impurities density, n^* is the residual carrier density — value below which the carrier density becomes highly inhomogeneous so that it is not possible to define it as a global quantity, $\bar{n}$ is the gate voltage offset related to the sample doping, expressed in terms of carrier density: $\bar{n} = \alpha V_{\mathrm{D}}$, α being conversion coefficient.

Note that this model in particular allows to estimate the impurities density. The charged impurities in this model are supposed to be situated in oxide at the distance d away from the graphene plane and to be arbitrary distributed. Knowing n^* one can also estimate d.

In order to obtain this result, first the scattering time τ was calculated as follows

$$\frac{\hbar}{\tau(\mathbf{k})} = \frac{n_{\mathrm{imp}}}{4\pi}\int \mathrm{d}\mathbf{q}\left[\frac{V(q)}{\epsilon(q)}\right]^2 [1-\cos^2\theta]\delta(\varepsilon_{\mathbf{k}+\mathbf{q}} - \varepsilon_{\mathbf{k}}), \tag{7.6}$$

where $V(q) = 2\pi e^{-qd}e^2/(\kappa q)$ is the Fourrier transform of bare Coulomb potential, κ being the dielectric constant of the surrounding material (SiO_2 and air), θ is the angle between $\mathbf{k}$ and $\mathbf{k}+\mathbf{q}$ and ϵ is RPA graphene dielectric function. Its approximate expression reads

$$\epsilon(q) = \begin{cases} 1 + q_{\mathrm{TF}}/q & \text{if } q < 2k_{\mathrm{F}} \\ 1 + \pi r_{\mathrm{s}}/2 & \text{if } q > 2k_{\mathrm{F}} \end{cases}, \tag{7.7}$$

where $q_{\mathrm{TF}} = \frac{4e^2}{\hbar}\frac{k_{\mathrm{F}}}{\kappa}$ — Thomas-Fermi wave-vector and $r_{\mathrm{s}} = \frac{e^2}{\hbar v_{\mathrm{F}}\kappa} \approx 0.8$[1] is the interaction parameter which in graphene is carrier density independent. Charged impurities-induced electrostatic potential fluctuations can also be calculated:

$$\overline{\delta V^2} = n_{\mathrm{imp}}\int \frac{\mathrm{d}^2 q}{(2\pi)^2}\left[\frac{2\pi e^2 e^{-qd}}{\kappa q \epsilon(q)}\right]^2 = 2\pi n_{\mathrm{imp}}\left(\frac{e^2}{\kappa}\right)^2 C_0(r_{\mathrm{s}},\ a = 4k_{\mathrm{F}}d) \tag{7.8}$$

[1]Calculated for graphene on the SiO_2 substrate ($\kappa = (3.9+1)/2$)

where

$$C_0(r_\mathrm{s}, a) = -1 + \frac{4E_1(a)}{(2+\pi r_\mathrm{s})^2} + \frac{2e^{-a}r_\mathrm{s}}{1+2r_\mathrm{s}} + \left(1+2r_\mathrm{s}a\right)e^{2r_\mathrm{s}a}\left(E_1\left(2r_\mathrm{s}a\right) - E_1\left(a(1+2r_\mathrm{s})\right)\right) \tag{7.9}$$

with $E_1(z) = \int_z^\infty t^{-1}e^{-t}\,\mathrm{d}t$ — exponential integral function.

Finally, the residual density can be related to the impurity density (self-consistently) by admitting that the chemical potential fluctuations magnitude $\overline{\varepsilon_\mathrm{F}^2} = \hbar^2 v_\mathrm{F}^2 \pi n^*$ should equal to the electrostatic potential fluctuations induced by the charged impurities $\overline{\delta V^2}$, yielding

$$\frac{n^*}{n_\mathrm{imp}} = 2r_\mathrm{s}^2 C_0(r_\mathrm{s}, a = 4d\sqrt{\pi n^*}) \tag{7.10}$$

b. Numerical Simulations

We used this model (in particular the eq. 7.5), to fit our experimental data. Two free parameters were required to obtain the fit shown in fig. 7.3 (in light violet): the impurities density n_imp and the residual carrier density n^*, while other quantities were determined independently. The aspect ratio, allowing to relate the resistance and the per square conductivity, was estimated from the lithography design. Note, that this model deals with the classical diffusion of charges and the area of the whole region between voltage probes (including the wider parts on both sides of the constriction) should be considered for the per square conductivity calculation. This leads to the aspect ratio $\frac{L}{W} \simeq 1.35$. Another quantity — α, relating carrier density and the gate voltage as following $n_\mathrm{s} = \alpha V_\mathrm{G}$, can be found from the separate measurement in Hall Effect regime (see Chapter 8 for details). This yields $\alpha = 2.53 \pm 0.07 \times 10^{10}\,\mathrm{cm}^{-2}\,\mathrm{V}^{-1}$, corresponding to the capacitance per unit area of $C_\mathrm{gate} \approx 4\,\mathrm{nF\,cm}^{-2}$.

This model is very useful, since it provides us several important quantities and takes into account both regimes: at low and at high carrier density. However, as one notices, the cross-over between these two regimes is not taken into account in a very accurate manner, leading to the fit curve, that deviates quickly from the experimental data, matching it only at its maximum and on the flanks. It is obvious that in the reality this switchover is progressive. To account for that we exploit the ansatz, formulated in [107]

$$n_\mathrm{s} = \sqrt{n^{*2} + \left[\alpha(V_\mathrm{G} - V_\mathrm{D})\right]^2} \tag{7.11}$$

and the conductance then reads

$$\sigma = \frac{20e^2}{h}\frac{n_\mathrm{s}}{n_\mathrm{imp}} \tag{7.12}$$

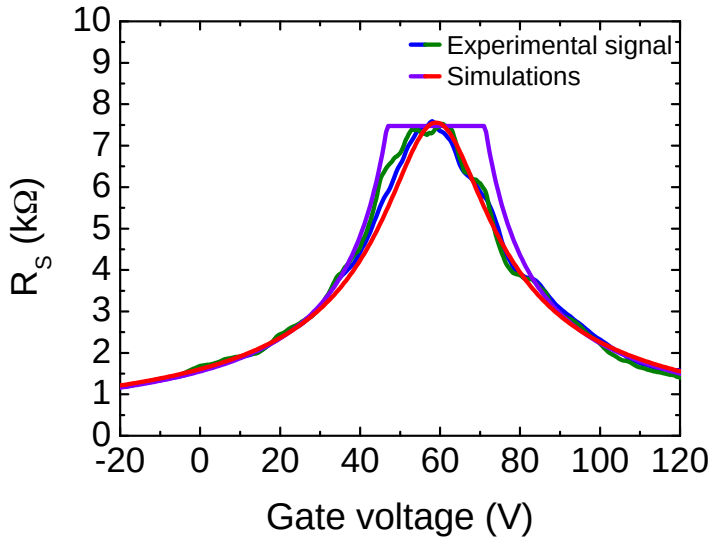

Figure 7.3: The results of the fit using the conclusions of the diffusive model: direct application of the eq. 7.5 (in violet) and $\sigma \propto \sqrt{(n_s - \bar{n})^2 + n^{*2}}$ (in light red). The experimental data is plotted in green and blue.

With (7.12) we obtain the curve plotted in red in the fig. 7.3. The fit is now much better, although we had to modify only very slightly the fit parameters (given in table 7.1 between parenthesis).

7.1.3 Discussion

We now review these two incompatible hypothesis in order to settle, which one should be considered a the correct. Let us first discuss the assumption of weak screening in our graphene layer. The only reason for non-capacitive behaviour in such low-dimensional systems is the limited density of states, which in some cases makes the energy cost of adding new particles to the system higher, than the induced by applied field change in the potential energy of the particles already present in the system. The convenient quantity to evaluate this effect is the quantum capacitance, defined as $C_Q = e^2 \frac{\partial n_s}{\partial \mu} = e^2 D(\mu)$, where μ is the chemical potential and $D(\mu)$ is the density of states. In the graphene the density of states is given by the expression (1.33), which yields

$$C_Q = e^2 \frac{2}{\pi} \frac{\mu}{(\hbar v_F)^2} \tag{7.13}$$

Using the coefficient $\beta \approx 2.8 \times 10^{-4}$ defined in one of the previous subsections we can calculate the quantum capacitance at the given gate voltage. The result is shown in the fig. 7.4

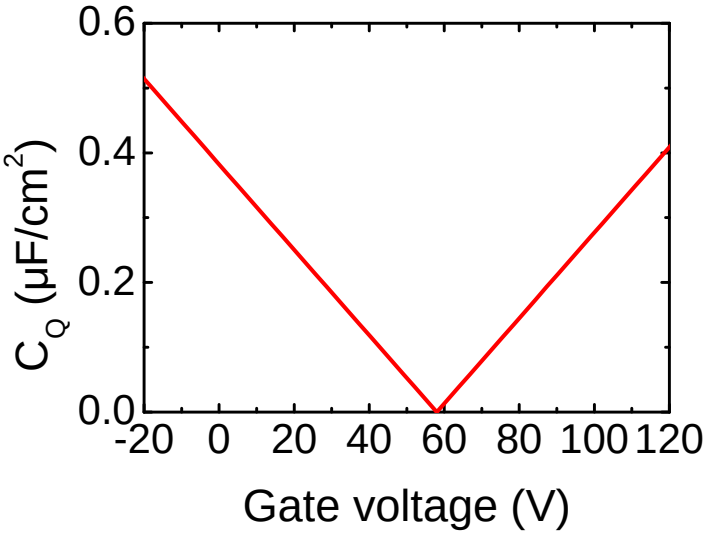

Figure 7.4: Quantum capacitance of a graphene layer as a function of the gate voltage in the assumption of no screening.

The effect of the gate is then modeled by the series capacitance of the geometric and quantum capacitance. The estimated values of the quantum capacitance are of several hundreds of nF cm^{-2}. While the geometric capacitance (certainly estimated in different assumptions in the previous subsection, yet this value is quite realistic) equals 2.56 nF cm^{-2}, which is some orders of magnitude smaller. Two values become comparable only ± 1 V around V_{D}. Hence, the total capacitance is entirely defined by its geometric compound which contradicts the weak screening assumption.

In addition to that, the energy scale, deduced from the experiment with non-zero bias presented in the sec. 7.2 does not agree with the energy scale estimated using the ballistic fit. The results of the experiment at non-zero magnetic field also strongly attest the capacitive behaviour of carrier density with the gate voltage. All that means, that we should rather trust the results of the analysis in which we considered our device to be in the diffusive regime.

Let us discuss the quantities, provided by this analysis and shown on the table 7.1. First of all note, that the mean free path l_{e} (see fig. 7.5(b)), estimated using the Drude conductivity formula, even at high carrier density is only about 50 nm $\ll$ 200 nm — the constriction length, confirming the diffusive regime hypothesis. The found impurities concentration 1.33×10^{12} cm^{-2} seems to be a typical value for a quite dirty sample (the hierarchy proposed in ref. [2] is from 2×10^{11} cm^{-2} — very clean to 3.2×10^{12} cm^{-2} — very dirty) and is close to the largest values obtained in the similar work by [144]. The parameter n^* is basi-

Table 7.1: Quantities extracted from the result of the fit (approximative values). We denoted as l_e the mean free path and as τ the elastic scattering time of fig. 7.5.b, as μ the mobility of fig. 7.5.a and as σ_{min} the minimal conductivity (appearing at the Dirac point).

Parameter	Value (approx.)
n_{imp}	$1.33\ (1.41) \times 10^{12}\,\mathrm{cm}^{-2}$
n^*	$3.1\ (3.25) \times 10^{11}\,\mathrm{cm}^{-2}$
l_e	30 to 60 nm
τ	30 to 60 fs
σ_{min}	$4.65\frac{e^2}{h}$
μ	$3660\,\mathrm{cm}^2\,\mathrm{V}^{-1}\,\mathrm{s}^{-1}$
d	1.27 nm

cally related to n_{imp} via the distance at which the impurities are situated in the oxide (see eq. 7.10). The found value $n^* \simeq 3.1 \times 10^{11}\,\mathrm{cm}^{-2}$, corresponding to the smearing energy bandwidth of $\varepsilon_F^* \simeq 81\,\mathrm{meV}$ is not far from the one reported in [104] and yields $d \simeq 1.27\,\mathrm{nm}$ that is also rather reasonable (value considered in the literature is $\approx 1\,\mathrm{nm}$). Estimated mobility $\mu \simeq 3660\,\mathrm{cm}^2\,\mathrm{V}^{-1}\,\mathrm{s}^{-1}$, shown in the fig. 7.5(a), is also similar to the values found in [144] for one of their samples. The minimal conductivity $\sigma_{min} \simeq 4.65\frac{e^2}{h}$ is close to $4\frac{e^2}{h}$, mistaken in the early works for a universal value, but rather explained by the poor samples quality used in these works. Adam et al. affirm that for very clean samples ($n_{imp} \approx 2 \times 10^{10}\,\mathrm{cm}^{-2}$) value $8\frac{e^2}{h}$ is attained, according to their calculations. More recent experiments indeed revealed larger magnitudes and larger spread of σ_{min} even in the samples on SiO_2, for example Tan et al. find values between $5\frac{e^2}{h}$ and $10\frac{e^2}{h}$. Measurements in graphene samples on boron nitride carried out by Dean et al. yielded $\sigma_{min} \simeq 6\frac{e^2}{h}$ but also $n^* \approx 10 \times 10^9\,\mathrm{cm}^{-2}$ and most notably $\mu \simeq 60\,000\,\mathrm{cm}^2\,\mathrm{V}^{-1}\,\mathrm{s}^{-1}$ which is a great improvement of samples quality. Du et al. performed a comparative study of the transport properties of suspended and not suspended graphene samples. In this work they claim approaching the ballistic regime, obtaining in the suspended samples $\sigma_{min} \simeq 1.7\sigma_0$, where $\sigma_0 = \frac{4e^2}{\pi h}$ is the ballistic, "truly" minimal conductivity[2]. The obtained mobility is of the order of $120\,000\,\mathrm{cm}^2\,\mathrm{V}^{-1}\,\mathrm{s}^{-1}$, $n^* \simeq 4 \times 10^9\,\mathrm{cm}^{-2}$. In their non suspended samples in return, $\sigma_{min} \simeq 6\frac{e^2}{h}$, $\mu \simeq 20\,000\,\mathrm{cm}^2\,\mathrm{V}^{-1}\,\mathrm{s}^{-1}$ and $n^* \simeq 6 \times 10^{10}\,\mathrm{cm}^{-2}$. Comparing these values with those derived in our experiment, we conclude that the quality of our sample is not especially great, that is not surprising since our sample was not annealed.

[2]Remember that the result $\sigma_0 = \frac{4e^2}{\pi h}$ was obtained by Tworzydlo et al. for aspect ratios $W/L \gtrsim 4$. In the work by Du et al. the discussed ballistic sample has length $L = 0.5\,\mu\mathrm{m}$ and width $W = 1.4\,\mu\mathrm{m}$.

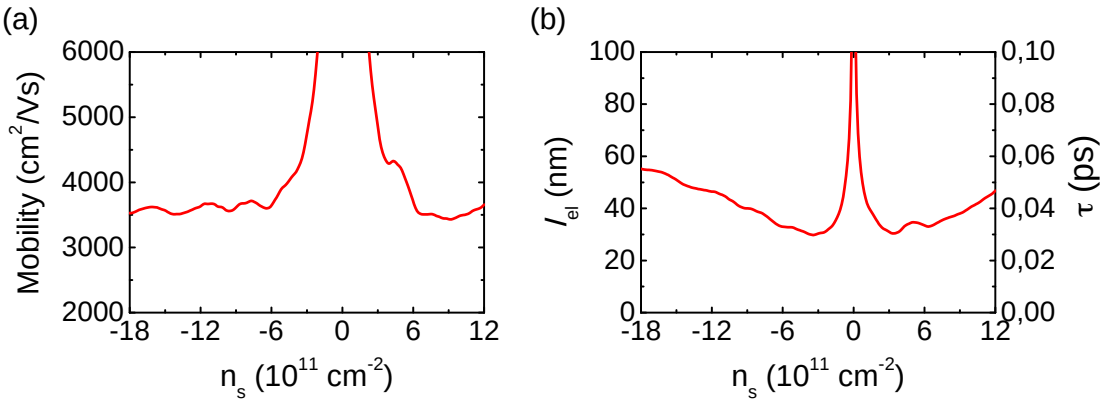

Figure 7.5: Calculated mobility (a) and mean free path/elastic scattering time (b) as a function of the carrier density in our sample. The analysis is only valid for densities below $\simeq -4 \times 10^{11}\,\mathrm{cm}^{-2}$ and above $\simeq 4 \times 10^{11}\,\mathrm{cm}^{-2}$.

7.1.4 Model for the "altered" Curves

In this section we will develop a simple model, that tends to explain the difference in the responses of the channel 0 and channel 1, and which is also valid in the case of the two-point measurement.

To begin, let us have a look on the curves we plotted in fig. 7.6. They show the response of each measurement line as a function of the gate voltage. Two details can be discerned on these curves. First of all, up to gate voltage of about 45 V the signals of all four lines follow one another quasi-perfectly and (with few exceptions) reproduce the all UCF-related structures in details. Next, on the span of gate voltages between 45 and 65 V, four curves seem to have more or less the same average value, which moreover do not vary much with the gate voltage. On the other hand, the fluctuations around this average value are much stronger, than what we see on the left part of the curves. At the gate voltage value of about 65 V the signal of the line V_{A}^1 starts to decrease quicker, than the others, while the response of the line V_{B}^1 keeps following the lines V_{A}^0 and V_{B}^0 until $V_{\mathrm{G}} \simeq 72\,\mathrm{V}$ when it passes above them to join the V_{A}^1 line at $V_{\mathrm{G}} \simeq 80\,\mathrm{V}$. The same reproducible UCF structures, however, are still present in all four responses, the peaks at the gate voltages of approximately 69, 72.5, 78, 84, 92 and 103 V attest it. The question to address is: what can be the reason for the lines V_{A}^0 and V_{B}^0 to measure the higher voltage than their two other counterparts?

The most apparent explanation is that the corresponding resistance is also higher, because of some additional resistances in series with the constriction, that moreover appear only above the Dirac Point and are detected exclusively by the probes of channel 0. We argue that these resistances appear when a *p-n junction*

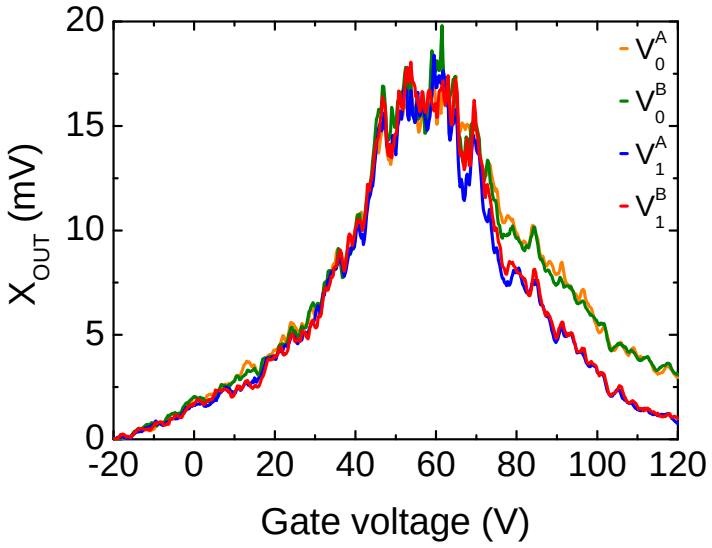

Figure 7.6: Real part of the output signal as a function of gate voltage for each measurement line after phase correction and arbitrary offset subtraction. Measurements done at high frequency. Note the difference in the behaviour of the blue and red curves comparing to the orange and green ones.

is formed between the n-doped constriction and the specific locations at which the voltage is probed, latter still being p-doped in the case of the lines V_{A}^0 and V_{B}^0. Below the Dirac Point this junction is obviously absent, since all area of the graphene sample is p-doped and no distinctions in the response of the probes arise. The expected scenario is sketched in fig. 7.7.

Note that unlike to what is shown on these idealistic sketches, from our measurement it seems that the n-region attains the probe V_{A}^1 slightly before V_{B}^1. This can be simply explained by the dissymmetry in the position of two probes with respect to the side gates, possibly the result of the lithography process lack of precision. On the other hand, the responses of the lines V_{A}^0 and V_{B}^0 were initially similar to the one of V_{A}^1 and V_{B}^1, but changed with time: the response of V_{A}^0 changed first, and after several measurements the line V_{B}^0 followed (here we presented only the last measurements). As a consequence, the difference in responses can not be explained by the position of the probes V_{A}^0 and V_{B}^0. We consider two options to explain what is keeping the n-region from propagating until these probes. First explanation is that some residues could change their position and come near the probes hence screening the field of the gates. The second option is that cracks appeared between these probes and the constriction in the graphene layer, meaning that the points at which the voltage is really probed were shifted towards the "bulk" part of the layer. Finally, it is also straightforward to see that in a two-point

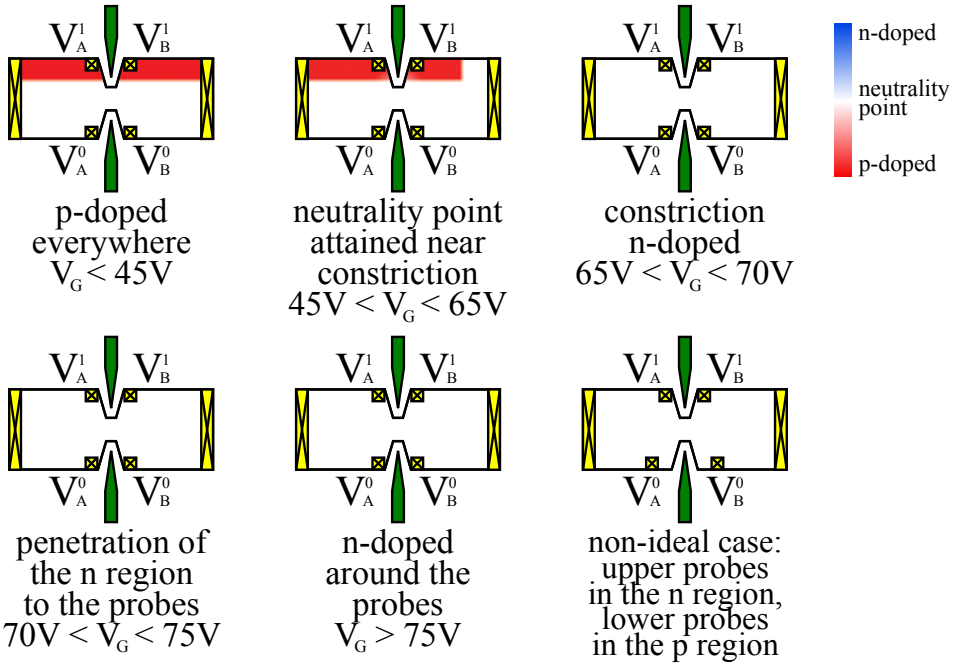

Figure 7.7: Illustration of the side-gates effect on the local carrier density. Different possibilities are shown, lower right sketch proposes a potential reason for the divergences of the V_A^0 and V_B^0 probes behaviour. Density puddles, occurring on the interval of gate voltages between 45 V and 65 V, are not shown on the corresponding sketch.

measurement an additional p-n junction resistance is unavoidable.

7.2 Conductance Spectroscopy

It is often interesting to study the dependence of transport properties on the energy of injected electrons. Such study can reveal several useful quantities. First of all, it provides a reliable energy scale for the system. Some quantities become more recognizable as it is the case for the UCF. Last but not least, the results of this experiment allow us to derive the non-linear current-voltage characteristics of the system. This information will be essential for us during the analysis of the shot noise data.

The schematics of the experimental setup is shown in the fig. 6.7, the principle of this measurement is the following: a DC current $I = V_B/10\,\mathrm{M}\Omega$ is injected into the device, resulting in a voltage drop V_{ds} across the constriction. In addition, this voltage drop is modulated by a small AC excitation V_{exc}. The response of the device to this modulation for a given DC current, i.e. the differential resistance,

is observed as always using Phase Sensitive Detection at 3.33 MHz. Besides, in order for the differential resistance measurement to remain in the linear regime, independent on the $V_{\rm exc}$ value, the latter should verify $eV_{\rm exc} \lesssim k_{\rm B}T,\ eV_{\rm ds}$. On the other hand, when the drain-source bias exceeds the thermal energy ($eV_{\rm ds} > k_{\rm B}T$), the mesoscopic conductance may depend on $V_{\rm ds}$ itself (but not on $V_{\rm exc}$ since it is too small), manifesting the non-linearities.

Several reasons can give rise to a non-linear behaviour of the conductor. First, a DC bias $V_{\rm ds}$ applied to the conductor shifts the energy of the electrons in one reservoir above the electrochemical potential by $V_{\rm ds}$, changing the number of propagating modes which contribute to the total transmission. As a consequence the conductance is enhanced. In that sense, the effect of the bias voltage on the *differential* conductance is similar to the effect of the gate voltage, except that $eV_{\rm ds}$ exactly equals to the energy shift of the electrons providing us a relevant energy scale. Under other conditions, the shift of the energy at which the carriers are injected modifies their coherence length and thus the distance over which the phenomena such as weak localization take place. As a consequence, the differential conductance increases with $V_{\rm ds}$, since the effect of weak localization decreases.

Besides, one particularity of our experimental setup should be pointed out, before we start analysing the data. Indeed, if one glances at the circuit schematics of the fig. 6.7, one will note that the device in our setup is biased in some unusual way: the application of voltage $+V_{\rm B}/2$ and $-V_{\rm B}/2$ to two 5 MΩ resistors situated on each side of the device leads to the "drain" voltage $V_{\rm d} = V_{\rm ds}/2$, and the "source" voltage $V_{\rm s} = -V_{\rm ds}/2$, instead of the more conventional $V_{\rm ds}$ and 0 values. Obviously, the voltage drop across the constriction is still $V_{\rm ds}$, the injected DC current is still $V_{\rm B}/10\,{\rm M}\Omega$, but the voltage of the constriction middle is zero (relative to the ground).

The main reason for such particular biasing technique is to reduce the effect of applied DC voltage on the gain of the cryogenic amplifiers. As it was explained in subsec. 4.2.3, the gain of these amplifiers depends on their transconductance, which itself is FET's gate-source voltage dependent. Yet, a shift of the voltage of a probe and as a consequence of the FET's gate will modify the amplifier gain. Our approach allows to reduces significantly the voltage by which each individual probe is shifted[3] and thus the impact of the above mentioned effect on the measurement result.

[3]Indeed, in that case the induced voltage shift is only of $\pm V_{\rm ds}/2$ for the respective probes. On the other hand, the conventional approach would consist in shorting to the ground potential of one of the room-temperature inputs, used for the device biasing. As seen from the schematics 6.7, these are separated from the device by 50 kΩ resistors as well as by eventual contact resistances. Hence, in that case the induced voltage shift would be equal to $V_{\rm ds} + I(R_{\rm C} + 50\,{\rm k}\Omega)$ and $I(R_{\rm C} + 50\,{\rm k}\Omega)$ for the respective probes. Since the constriction resistance $R_{\rm s} \ll R_{\rm C}+50\,{\rm k}\Omega$, the advantage of our approach is evident.

By the way, from the transmission viewpoint, such approach is rather equivalent to the application of the bias V_{ds} in the usual way, simultaneous to the electrostatic potential shift by $V_{\mathrm{ds}}/2$ in the opposite direction. Hence, the resulting transmission enhancement arises only from the half of the applied drain-source voltage. To derive this relation in a more rigorous way, let us first calculate the DC current through the sample, when a bias V_{ds} is applied in such a peculiar way. Since the total transmission vary on this energy range, the current reads

$$I = \frac{4e}{h} \int\limits_{-eV_{\mathrm{ds}}/2}^{eV_{\mathrm{ds}}/2} T(\varepsilon + \mu_{\mathrm{G}})\, \mathrm{d}\varepsilon \tag{7.14}$$

where $T(\varepsilon)$ is the total transmission ($T = \sum T_n$) at the energy ε and by μ_{G} we denoted eventual gate induced shift of the electrostatic potential. From that

$$\frac{\mathrm{d}I}{\mathrm{d}V_{\mathrm{ds}}} = \frac{4e^2}{h} \left(\frac{1}{2} T(eV_{\mathrm{ds}}/2 + \mu_{\mathrm{G}}) + \frac{1}{2} T(-eV_{\mathrm{ds}}/2 + \mu_{\mathrm{G}}) \right) \tag{7.15}$$

and at the Dirac point, where $\mu_{\mathrm{G}} = 0$, this yields simply

$$\frac{\mathrm{d}I}{\mathrm{d}V_{\mathrm{ds}}} = \frac{4e^2}{h} T(eV_{\mathrm{ds}}/2) \tag{7.16}$$

since from symmetry considerations $T(\varepsilon) = T(-\varepsilon)$.

The measured conductance value is indeed $\frac{\mathrm{d}I}{\mathrm{d}V_{\mathrm{ds}}}$, because the AC excitation is applied in the same way as the DC voltage (i.e. $\mathrm{d}V_{\mathrm{ds}} = V_{\mathrm{exc}}$, not $2V_{\mathrm{exc}}$). So if we denote by $\frac{\mathrm{d}V_{\mathrm{ds}}}{\mathrm{d}I}\Big|_{V_{\mathrm{G}},V_{\mathrm{ds}}}$ the value of the differential resistance at bias and gate voltages equal to V_{G} and V_{ds} respectively, the case when $\frac{\mathrm{d}V_{\mathrm{ds}}}{\mathrm{d}I}\Big|_{V_{\mathrm{G}},0} = \frac{\mathrm{d}V_{\mathrm{ds}}}{\mathrm{d}I}\Big|_{0,V_{\mathrm{ds}}}$ corresponds to the energies relation $\mu_{\mathrm{G}} = eV_{\mathrm{ds}}/2$.

Next, since what we control in the experiment is the injected DC current I and since we expect the device resistance to be non-linear, the drain-source voltage (DC voltage drop across the constriction) should be calculated as following

$$V_{\mathrm{ds}} = \int\limits_{0}^{I} \mathrm{d}I \left\{ \tfrac{\mathrm{d}V_{\mathrm{ds}}}{\mathrm{d}I} /\!/ 51.5\,\mathrm{k}\Omega \right\} \tag{7.17}$$

(the current injected into the device also passes through the measurement lines). The carrier density, on its turn, is calculated as $n_{\mathrm{s}} = \alpha \Delta V_{\mathrm{G}}$, with $\alpha = 2.53 \pm 0.07 \times 10^{10}\,\mathrm{cm}^{-2}\,\mathrm{V}^{-1}$ obtained from the independent measurement in the Quantum Hall regime.

Finally, we extract the differential resistance $\frac{\mathrm{d}V_{\mathrm{ds}}}{\mathrm{d}I}$ from the detected signal using the approach, presented in sec. 6.2. This approach allows in particular to

determine the non-physical offset (that we then subtract) by extrapolating the resistance curves to infinite carrier densities, where the resistance tends to zero. This is equivalent to focus on $\Delta V_{\mathrm{G}}^{-1} \to 0$ limit, where the Dirac voltage V_{D} is the free parameter such as offset values obtained from electrons and holes branches of the curve coincide. In the present case, this condition should be fulfilled for any V_{ds}. The obtained value from channel 1 data analysis is $V_{\mathrm{D}} = 61.75\,\mathrm{V}$ (the average deviation is less than 0.1%). The channel 0 data does not allow to estimate V_{D}, since above the Dirac point the measurement result includes the additional resistance of the p-n junction. For that reason we take the same value of V_{D} as in the case of channel 1 and determine the offset using only the holes branch of the resistance curve.

In addition, despite our effort, the effect of the DC voltage on the amplifiers gain is still not negligible. This results in an extra slope of the differential resistance curves for a fixed gate voltage. To get rid of this artefact, we symmetrize these curves

$$\left.\frac{\mathrm{d}V_{\mathrm{ds}}}{\mathrm{d}I}^{*}\right|_{V_{\mathrm{ds}}} = \left.\frac{1}{2}\frac{\mathrm{d}V_{\mathrm{ds}}}{\mathrm{d}I}\right|_{V_{\mathrm{ds}}} + \left.\frac{1}{2}\frac{\mathrm{d}V_{\mathrm{ds}}}{\mathrm{d}I}\right|_{-V_{\mathrm{ds}}} \tag{7.18}$$

We now can plot the differential resistance as a function of parameters, controlling the transport properties of the system: carrier density in the conductor and the energy of injected particles. We also performed the numerical simulations in the both assumptions: of ballistic and diffusive regimes, combining the results of zero-bias simulations with the relation (7.15). The quantity μ_{G} used in this relation can be found in the ballistic regime assumption with the help of previously determined coefficient β, whereas in the diffusive regime assumption with the help of coefficient α and relation (7.3). Figure 7.8 shows the experimental (a and b) and numerical (c and d) results.

First, to understand the color plots, recall that what we control is the injected current, that we sweep always over the same values. Since the device differential resistance decreases with the carrier density, the generated voltage drop V_{ds} is swept over lower values at higher carrier density. Note that both channels show very similar behaviour with the bias voltage for $n_{\mathrm{s}} > 0$. Above this value channel 0 deviates from channel 1, as it was seen at zero-bias. Besides, if we increase bias voltage at fixed carrier density, the differential resistance in general drops rather quickly until the value $V_{\mathrm{ds}} \sim 4\,\mathrm{mV}$ is reached and then saturates, i.e. varies very little with the bias. At this same value of V_{ds} the fluctuations are also smeared. On the other hand, the variation of the differential resistance with carrier density around the neutrality point differs at low bias and at high bias ($V_{\mathrm{ds}} \gtrsim 4\,\mathrm{mV}$). At low bias it is quite pronounced, similar to what is observed in zero-bias experiment. Whereas at high bias this variation is very weak and the differential resistance seems to saturate around the neutrality point, as it was predicted by Adam et al..

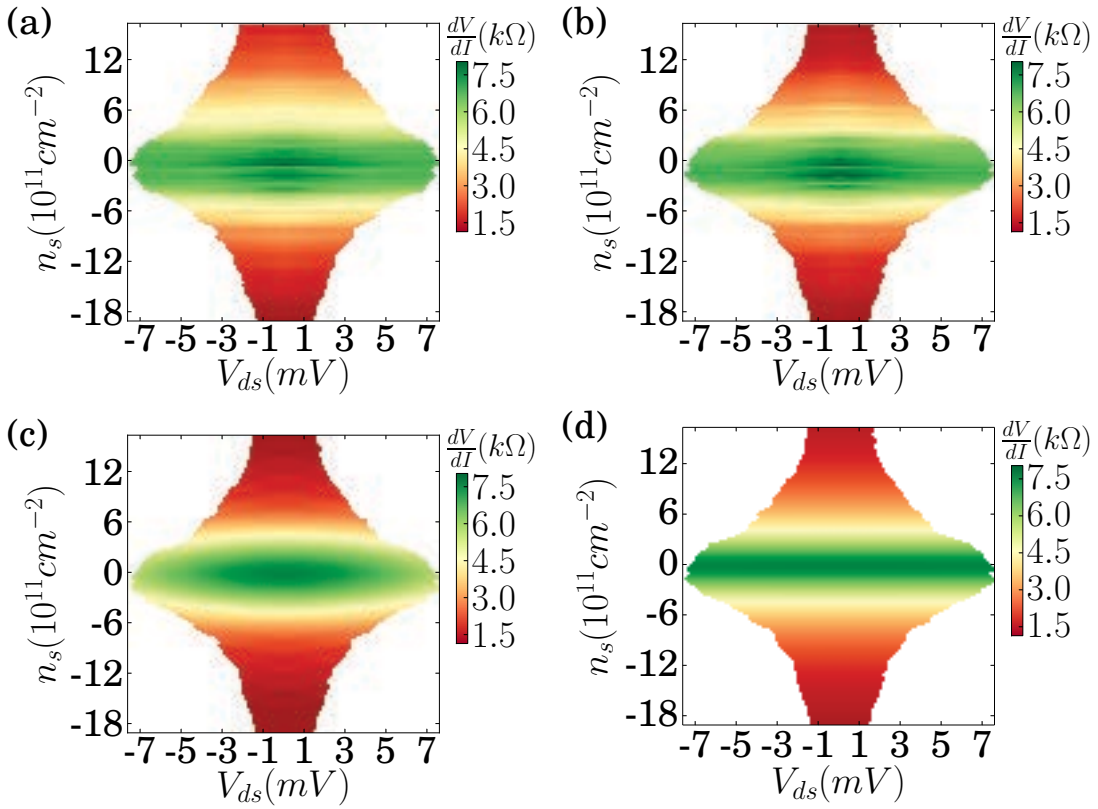

Figure 7.8: Differential resistance as a function of carrier density and drain-source voltage (DC voltage across the constriction) extracted from the measurements with channel 0 (a) and channel 1 (b) or calculated in the hypotheses of ballistic (c) and diffusive (d) regime using the parameters, extracted from the fits at zero bias.

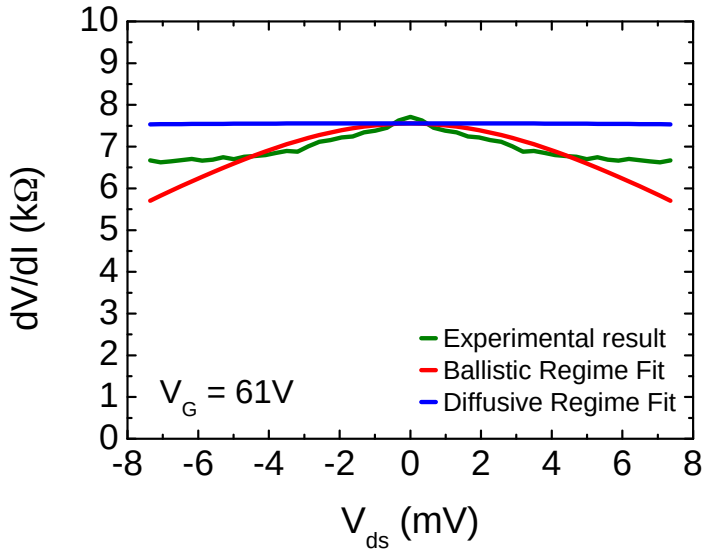

Figure 7.9: Differential resistance as a fuction of the bias voltage across the constriction at $V_G = 61\,V$. Ballistic and diffusive simulations (red and blue) and the experimental results (in green).

Let us now examine the results of the simulations and compare them to what we detect experimentally. We start with the ballistic regime assumption. It is quite striking, how strongly the differential resistance drops with bias voltage. In addition, at high carrier density (electrons or holes) a sort of coulomb diamonds (although slightly bent) can be distinguished. These are simply more pronounced manifestation of the oscillations that are already quite noticeable at high carrier density in the zero bias conductance graph 3.2 of the Chapter 3. So when combined with the relation (7.15), these oscillations form aforementioned bent diamonds, to which the relation

If we look at the results of another simulations, in diffusive regime assumption, we see that at fixed n_s the differential resistance is quasi-constant with V_{ds}, while at fixed V_{ds} the variation with n_s is sharp for any V_{ds}, in the opposite to what we observe experimentally. Yet, the obtained color plot is exactly what we would naively expect when combining diffusive model from subsec. 7.1.2 with the expression (7.15). This suggests that in our model not all phenomena are taken into account.

For the sake of visibility we plotted the variation of the differential resistance with bias voltage at $V_G = 61\,V$. It is clear that the differential resistance, calculated with ballistic model, does not show any saturation behaviour and drops continuously, thus disagreeing with the experiment. This fact confirms that this

assumption is wrong. On the other hand the differential resistance, calculated with diffusive model, does not show the peak between −4 and 4 mV and remains constant over the whole range of drain-source voltages. Such inconsistency may seem a bit puzzling from the first glance, yet another phenomena already discussed in subsec. 2.1.3 of the Chapter 2, namely the weak localization, was not taken into account up to now.

Let us see if the peaks in the differential resistance at zero bias can indeed be explained by the effect of the weak localization. First of all, we spread the total conductivity σ into the classical, Drude component and the component originating from the weak localization correction:

$$\sigma = \sigma_{\mathrm{Drude}} + \delta\sigma_{\mathrm{loc}} \tag{7.19}$$

Latter can be written as[7]

$$\delta\sigma_{\mathrm{loc}} = -2\frac{e^2}{\pi h}\ln\left(1+\frac{\tau_\phi}{\tau_{\mathrm{e}}}\right) \simeq -2\frac{e^2}{\pi h}\ln\left(\frac{\tau_\phi}{\tau_{\mathrm{e}}}\right), \quad \text{when} \quad \tau_\phi \gg \tau_{\mathrm{e}} \tag{7.20}$$

where τ_ϕ is the phase coherence time, τ_{e} — elastic scattering time and the 2 prefactor comes from valley degeneracy. Then, if we denote as σ^0 ($\delta\sigma^0_{\mathrm{loc}}$) and σ^1 ($\delta\sigma^1_{\mathrm{loc}}$) the total conductivity (the weak localization correction) at $V_{\mathrm{ds}} = V^0_{\mathrm{ds}}$ and V^1_{ds} respectively, considering σ_{Drude} and τ_{e} to be drain-source voltage independent, we have

$$\sigma^1 - \sigma^0 = \delta\sigma^1_{\mathrm{loc}} - \delta\sigma^0_{\mathrm{loc}} = \frac{e^2}{\pi h}\ln\left(\frac{\tau^0_\phi}{\tau^1_\phi}\right). \tag{7.21}$$

It is now clear, that if we are able to calculate the phase coherence time at different drains-source voltages, we can try to fit our data. The phase coherence time will depend essentially on the electronic temperature T_{e} and $\delta\varepsilon$ — the quasiparticle energy with respect to the Fermi level at which it is injected. Calculations, done for graphene by Li and Das Sarma using GW and random phase approximations, show that the temperature-dependent phase coherent time can be written as

$$\frac{1}{\tau_\phi^{\mathrm{temp}}} \simeq -\frac{\pi(k_{\mathrm{B}}T_{\mathrm{e}})^2}{4\hbar\varepsilon_{\mathrm{F}}}\left[\ln\left(\frac{k_{\mathrm{B}}T_{\mathrm{e}}}{8\varepsilon_{\mathrm{F}}}\right) + 1.08387\right] \tag{7.22}$$

while the injection energy-dependent phase coherence time reads

$$\frac{1}{\tau_\phi^{\mathrm{energy}}} \simeq -\frac{\delta\varepsilon^2}{4\pi\hbar\varepsilon_{\mathrm{F}}}\left[\ln\left(\frac{\delta\varepsilon}{8\varepsilon_{\mathrm{F}}}\right) + 0.5\right] \tag{7.23}$$

The total phase coherence time is obviously given by

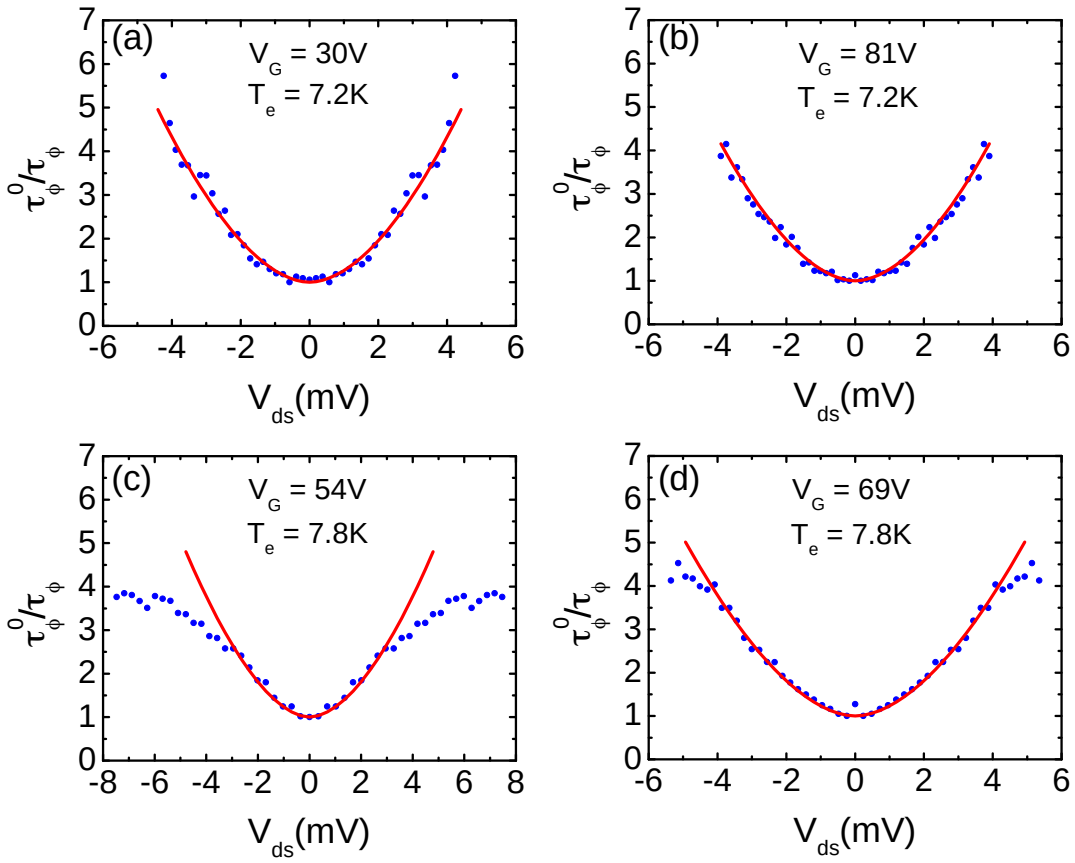

Figure 7.10: (a) – (d) τ_ϕ^0/τ_ϕ as a function of $V_{\rm ds}$ for $V_{\rm G} = 30,\ 81,\ 54$ and $69\,\rm V$ respectively. Blue dots show experimental data, red line — fit curve. Used parameter $T_{\rm e}$, electronic temeprature is indicated on correponding graph.

$$\frac{1}{\tau_\phi} = \frac{1}{\tau_\phi^{\rm temp}} + \frac{1}{\tau_\phi^{\rm energy}} \tag{7.24}$$

(in this simple approximation we consider the temperature to be bias independent).

We can now fix $V_{\rm ds}^0 = 0\,\rm V$ and plot $\tau_\phi^0/{\tau_\phi}^4$, extracted from our experimental data, as a function of $V_{\rm ds}$ and fit it using the above formulas (7.22 – 7.24) having the electronic temperature as the only free parameter. Note that fixing $V_{\rm ds}^0 = 0\,\rm V$ yields $\tau_\phi^0 = \tau_\phi^{\rm temp}$. Here the following remark is however necessary: because of the disorder induced "puddles", the description of transport at the Dirac point $V_{\rm D}$ can be rather complex and not well described by our simple model. For this reason we limit our study to the points rather far form $V_{\rm D} \approx 58\,\rm V - 61\,\rm V$. The obtained

[4]We therefore omit the 1 superscript index over τ_ϕ henceforth.

agreement for several gate voltages is shown on fig. 7.10. Note the expected saturation of the phase coherence time at V_{ds} above $\pm 4\,\mathrm{mV}$ for the data nearest to the Dirac point ($V_{\mathrm{G}} = 54$ and $69\,\mathrm{V}$). The resulting electronic temperature at zero DC bias T_{e} ranges between $\simeq 7.2\,\mathrm{K}$ and $7.8\,\mathrm{K}$, which is higher, than the helium bath temperature, but consistent with the values, we extracted from the noise measurement when the Joule heating was not taken into account. This suggests that the heating effects should be included in our model. One also sees that the condition from the eq. 7.20 is satisfied, since τ_ϕ is of the order of $10\,\mathrm{ps}$, while τ_{e} is of the order of $50\,\mathrm{fs}$ (see subsec. 7.1.3). The phase coherence length at zero bias is estimated to be $\approx 600 - 800\,\mathrm{nm}$ which is in agreement with the values found in the literature[111, 10].

Chapter 8

Conductance in the Magnetic Field

In this chapter we present the results of the conductance measurements in the magnetic field. Although our experimental system does not allow to attain high magnetic field values, required for the appearing of several Quantum Hall plateaus, these measurements can still be useful providing the information about carrier density in the sample for instance. Strong disorder, revealed in our samples, makes the observation of the usual magneto-transport signatures as Shubnikov-de-Haas oscillations difficult. Another obstacle we faced in this experiment is the inhomogeneity of the electrostatic doping of the graphene sheet by the side-gates, which leads to the formation of the regions with different filling factors, hence complicating the analysis of the data. However, as it will be shown, the plateaus formed by the Hall resistance of the constriction can be observed if the right combination of the voltage probes is chosen. For other combinations of the voltage probes, specific data treatment can be applied in order to confirm the corresponding values of the filling factor. The derivation of the filling factor in the constriction as a function of the gate voltage and the magnetic field is the main purpose of these measurement, since this allows to establish the correspondence between the gate voltage and the carrier density in this region.

8.1 Measurement Principle

In this experiment we used the setup, described in the sec. 7.2 (measurement frequency 3.33 MHz), except that no finite DC bias is applied, and we swept the gate voltage and the magnetic field.

As one can see, in such setup three different types of voltage probes combination are possible. If we refer ourselves to the notations of fig. 8.1, we can discern the

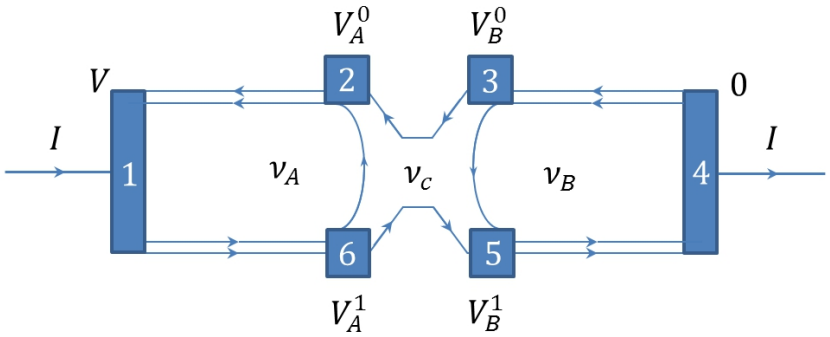

Figure 8.1: Sketch of a Hall bar with a constriction and three regions with different filling factors ν_{A}, ν_{B} and ν_{c}.

combination $V_{\mathrm{A}}^1 - V_{\mathrm{B}}^1$, i.e. the longitudinal one, the combination $V_{\mathrm{A}}^0 - V_{\mathrm{A}}^1$ — the transversal one, and finally the combination to which we refer as crossed: $V_{\mathrm{A}}^1 - V_{\mathrm{B}}^0$. Other possible probes combinations are obviously equivalent to one of these three. Note, that on the sketch the direction of the chiral current in the edge channels is shown for a given magnetic field direction and carriers' sign. For the opposite magnetic field direction or for the opposite carriers' sign, just permute 0 and 1 indices of probes on the sketch. If both parameters are changed for their opposite values, the sketch will remain valid without changes.

In the case of an ideal Hall bar the longitudinal and the transversal probe combinations correspond to the measure of the longitudinal R_{xx} and Hall R_{H} resistances respectively. Yet, our device can not be considered as an ideal Hall bar for the following reason: the carrier density induced by the field effect of the side-gates depends on the distance from the latter. As a consequence, the carrier density and thus the filling factor is different near the probes and in the constriction. This has a peculiar effect on the measured voltages: for instance the transversal combination of probes will measure the Hall voltage, which is defined by the filling factor value between the probes, not by the one of the constriction. In addition, we should have in mind that since the input impedance of the voltage probe lines can in some cases be comparable with the measured resistance, the current can sink through them yielding an additional voltage drop (which is however quite difficult to take into account).

Let us now address the problem of spatial variation of the filling factor in a Hall bar, by dividing it into three regions with a different filling factor each, as sketched in the fig. 8.1 (here, we neglect the effects of the current sinking through voltage probes). Such model can seem too simplistic, but it helps to build up an intuition about the measured quantities. We can relate the voltage measured by any probes pair to the filling factors with the help of the Landauer-Buttiker relations for the

multi-terminal devices (see [16]):

$$I_p = \frac{e^2}{h} \sum_q [T_{q \leftarrow p} \mu_p + T_{p \leftarrow q} \mu_q] \tag{8.1}$$

where p and q are the indices of terminals, I_p — the current, which enters the terminal p and μ_p is the electrochemical potential of this terminal, $T_{q \leftarrow p}$ is the transmission from the terminal p to the terminal q.

We use the notation of the sketch 8.1: by ν_{A} and ν_{B} we note the filling factors in the proximity of the probes $V_{\mathrm{A}}^0/V_{\mathrm{A}}^1$ and $V_{\mathrm{B}}^0/V_{\mathrm{B}}^1$ respectively and by ν_{c} — the filling factor in the constriction. The injected current is denoted by I and we chose the terminals 1 and 4 to be at the voltage V and 0 for the simplicity (this obviously will not change the result). According to (8.1) we can write

$$I_1 = \quad I = \quad \frac{e^2}{h} \left(\nu_{\mathrm{A}} V - \nu_{\mathrm{A}} V_{\mathrm{A}}^0 \right) \tag{8.2}$$

$$I_2 = \quad 0 = \quad \frac{e^2}{h} \left(\nu_{\mathrm{A}} V_{\mathrm{A}}^0 - \nu_{\mathrm{c}} V_{\mathrm{B}}^0 - (\nu_{\mathrm{A}} - \nu_{\mathrm{c}}) V_{\mathrm{A}}^1 \right) \tag{8.3}$$

$$I_3 = \quad 0 = \quad \frac{e^2}{h} \left((\nu_{\mathrm{c}} + \nu_{\mathrm{B}}) V_{\mathrm{B}}^0 - 0 \right) \tag{8.4}$$

$$I_4 = \quad -I = \quad \frac{e^2}{h} \left(0 - \nu_{\mathrm{B}} V_{\mathrm{B}}^1 \right) \tag{8.5}$$

$$I_5 = \quad 0 = \quad \frac{e^2}{h} \left(\nu_{\mathrm{B}} V_{\mathrm{B}}^1 - \nu_{\mathrm{c}} V_{\mathrm{A}}^1 - \nu_{\mathrm{B}} V_{\mathrm{B}}^0 \right) \tag{8.6}$$

$$I_6 = \quad 0 = \quad \frac{e^2}{h} \left((\nu_{\mathrm{c}} + (\nu_{\mathrm{A}} - \nu_{\mathrm{c}})) V_{\mathrm{A}}^1 - \nu_{\mathrm{A}} V \right) \tag{8.7}$$

These equations lead to the following results:

$$V = \frac{h}{e^2 \nu_{\mathrm{c}}} I \tag{8.8}$$

$$V_{\mathrm{A}}^1 - V_{\mathrm{A}}^0 = \frac{h}{e^2 \nu_{\mathrm{A}}} I \tag{8.9}$$

$$V_{\mathrm{B}}^1 - V_{\mathrm{B}}^0 = \frac{h}{e^2 \nu_{\mathrm{B}}} I \tag{8.10}$$

$$V_{\mathrm{A}}^0 - V_{\mathrm{B}}^0 = \left(\frac{h}{e^2 \nu_{\mathrm{c}}} - \frac{h}{e^2 \nu_{\mathrm{A}}} \right) I \tag{8.11}$$

$$V_{\mathrm{A}}^1 - V_{\mathrm{B}}^1 = \left(\frac{h}{e^2 \nu_{\mathrm{c}}} - \frac{h}{e^2 \nu_{\mathrm{B}}} \right) I \tag{8.12}$$

$$V_{\mathrm{A}}^1 - V_{\mathrm{B}}^0 = \frac{h}{e^2 \nu_{\mathrm{c}}} I \tag{8.13}$$

$$V_{\mathrm{A}}^0 - V_{\mathrm{B}}^1 = \left(\frac{h}{e^2 \nu_{\mathrm{c}}} - \frac{h}{e^2 \nu_{\mathrm{A}}} - \frac{h}{e^2 \nu_{\mathrm{B}}} \right) I \tag{8.14}$$

One sees that the probes pairs $V_{\mathrm{A}}^1 - V_{\mathrm{A}}^0$ and $V_{\mathrm{B}}^1 - V_{\mathrm{B}}^0$ will indeed sense the filling factors in the proximity of the corresponding electrodes, ν_{A} and ν_{B} respectively, while, less obviously, the crossed combination of probes $V_{\mathrm{A}}^1 - V_{\mathrm{B}}^0$ will sense the filling factor in the constriction ν_{c}. Furthermore, the longitudinal combinations of probes $V_{\mathrm{A}}^0 - V_{\mathrm{B}}^0$ and $V_{\mathrm{A}}^1 - V_{\mathrm{B}}^1$, in the opposite to what one would intuitively expect, will not measure no voltage drop each time the Hall resistance of the constriction shows a plateau. Instead it will have a more complicated behaviour depending both on ν_{c} and ν_{A} (ν_{B}), which is less straight-forward for the analysis. Aforementioned behaviour, due to the spatial variation of the filling factor, is well-known and was previously observed in other systems, namely in GaAs/AlGaAs heterostructures, see ref. [67] for example. What differs graphene from these systems is that formation of the regions with opposite polarities of charge carriers is possible. In such *p-n-p* junction, the edge states counter-circulate in the *p*- and *n*-regions and at the interface between regions a full equilibration arises. A *p-n-p* system can thus be seen simply as three conductors in series. Here we do not consider this unusual situation due to its complexity in the case of four point device, but the reader can refer to the work by Özyilmaz et al., where graphene *p-n-p* junctions under magnetic field are studied in two point geometry and the filling factor in different regions is controlled by independent top- and back-gates. Other theoretical and experimental results on Quantum Hall Effect in graphene *p-n* junctions can be found in refs. [1, 160, 70].

In this work we performed the analysis of all probes combinations at the maximum field ($\simeq 7.5\,\mathrm{T}$). The study of the system response to the gate voltage and magnetic field sweep was done with the $V_{\mathrm{A}}^1 - V_{\mathrm{B}}^0$ and $V_{\mathrm{A}}^1 - V_{\mathrm{B}}^1$ voltage probes combinations. These experiments are presented in the next section.

8.2 Results and Discussion

Here we show the results of the experiment in which both the gate voltage and the magnetic field were swept and the voltage was measured with the crossed and longitudinal probes combinations $V_{\mathrm{A}}^1 - V_{\mathrm{B}}^0$ and $V_{\mathrm{A}}^1 - V_{\mathrm{B}}^1$. We represented them on the color plots displayed in the fig. 8.2. Here we chose the notation for the gate axis, that seemed us the most appropriate for this representation: $\Delta V_{\mathrm{G}} = V_{\mathrm{G}} - V_{\mathrm{D}}$, where $V_{\mathrm{D}} = 61\,\mathrm{V}$ is the voltage required to attain the neutrality point. Besides, it should be emphasized, that the shown color plots contain two parts, that can be distinguished by the sign of the charge carriers: for $\Delta V_{\mathrm{G}} < 0$ these are holes (*p*-region), while $\Delta V_{\mathrm{G}} > 0$ these are electrons (*n*-region). Yet, recall from the previous discussion, that changing of the carriers' sign is equivalent to the permutation of 0 and 1 indices. This means that for example in the fig. 8.2a, the electrons part is described by the formula (8.13), while for the holes part by the formula (8.14).

In addition, near $\Delta V_{\mathrm{G}} = 0$ formation of *p-n-p* junction is probable. One should always keep in mind these subtleties, while analysing the plots below.

As one could remember from the theoretical description of magneto-transport (see sec. 2.3), the transport properties of the system, for enough high magnetic fields, are in general determined by the filling factor $\nu = \frac{n_{\mathrm{s}}}{eB/h}$ and should remain unchanged under the variation of parameters that preserves the filling factor constant. This condition is satisfied if the ratio n_{s}/B remains constant, which on the color plot corresponds to radial lines going from zero magnetic field and carrier density. Hence, in a conventional system, Shubnikov-de-Haas oscillations of the longitudinal resistance or step function of the Hall resistance produce a fan-shaped picture (e.g. [166]). In our system, however, step like transitions appear only for the crossed combination of probes and when carriers are electrons (i.e. $\Delta V_{\mathrm{G}} > 0$), where fan-shaped picture is indeed observed. In the case of the longitudinal combination of probes, two filling factors enter into the competition, see (8.11) and (8.12), bluing the picture. Nevertheless, we believe that, since this measurement presents the superposition of two plots of the same type, fan-shaped structures should still manifest themselves at least partially.

Besides, if the data is plotted as a function of the gate voltage (and not carrier density) and of the magnetic field, the appearance of the radial lines on the color plot, would strongly confirm the good screening assumption according to which $\Delta V_{\mathrm{G}} \propto n_{\mathrm{s}}$. As it can be readily observed, the radial lines indeed show up in the color plots 8.2. As a consequence, we can infer that the hypothesis of ballistic regime in our device is incorrect.

Moreover, since the radial lines are constant filling factor lines, and the measured resistance is supposed to depend only on the filling factor(s), averaging along the radial lines would simply give the resistance value with fluctuations removed. We performed this operation between 6 and 7.565 T. We add on top of the color plots the resistance curves at 7.565 T (in red) and the results of the averaging along the radial lines at corresponding filling factors (in green).

On the other hand, the color plots obviously should allow us to find out the coefficient α, already defined previously as $n_{\mathrm{s}} = \alpha \Delta V_{\mathrm{G}}$. For that, however, we should be able to attribute to any or at list to certain radial lines the value of correspondent filling factor. Then, according to the previous formulas, this constant will be defined by the relation

$$\alpha = \frac{eB}{h} \frac{\nu}{\Delta V_{\mathrm{G}}} \tag{8.15}$$

The filling factor in the constriction can be easily determined in the electrons part of the fig. 8.2a, where the plateaus are observed (see also the top graph). As it was explained in sec. 3.2, the Hall resistance in graphene manifests plateaus at

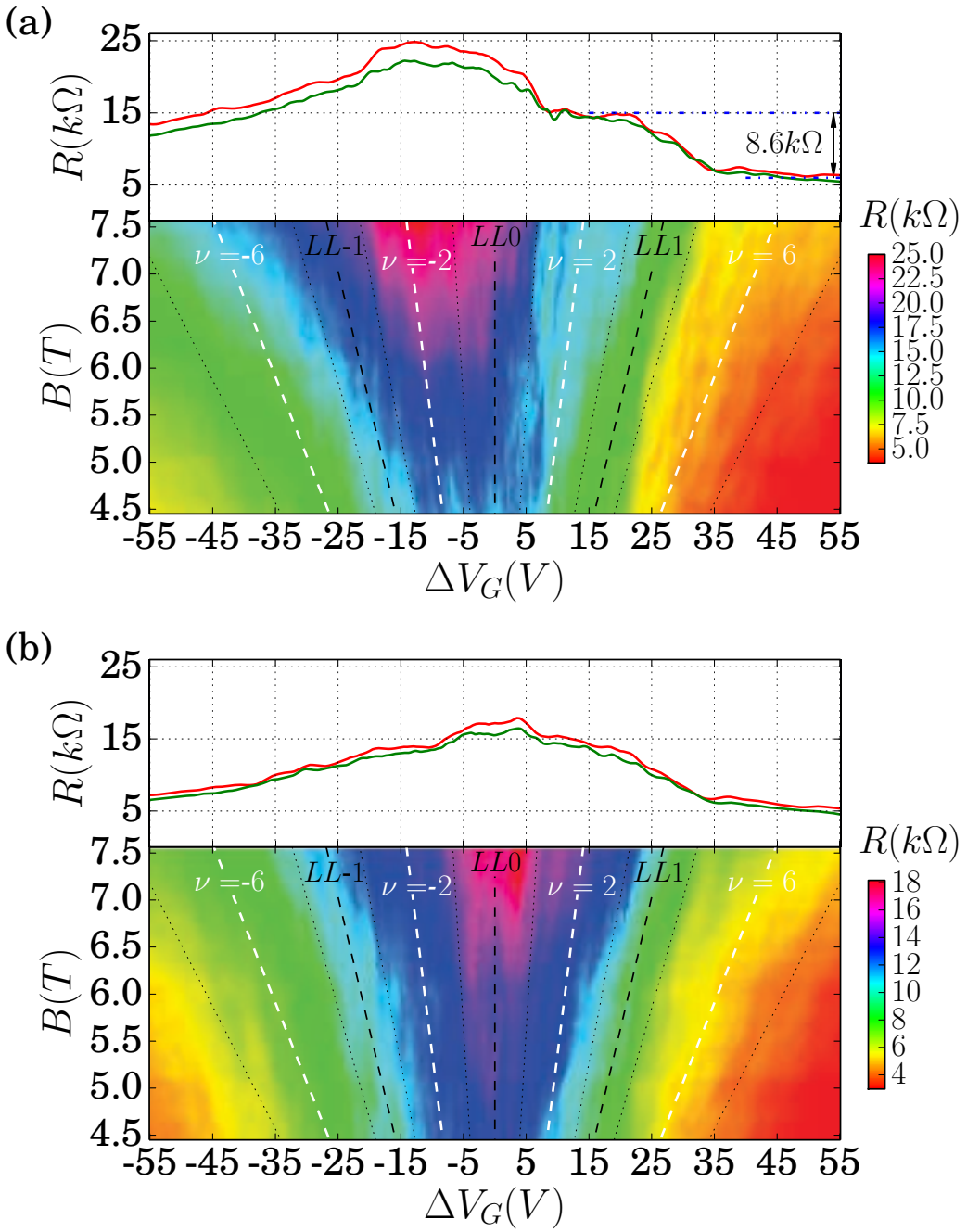

Figure 8.2: Color plots of the resistance measured with the crossed (a) and longitudinal (b) probes combinations as a function of $\Delta V_{\mathrm{G}} = V_{\mathrm{G}} - V_{\mathrm{D}}$ and magnetic field B. Top graphs show the variation of the resistance at maximum magnetic field $B = 7.565\,\mathrm{T}$ (red curves) as well as the values of the resistance, averaged along the constant filling factor lines, at the same filling factor (green curves). Black dotted lines, marking the boundaries of plateaus that appear in the electron part of the figure (a), were also transposed in the holes part and on the figure (b). White dashed constant filling factor lines correspond to the filling factors -6, -2, 2, 6, black ones to the centers of the Landau Levels -1, 0, 1.

filling factors given by

$$\nu = \pm 2(2n+1), \quad \text{i.e.} \quad \nu = 2, 6, 10, 14 \ldots \tag{8.16}$$

From that we can conclude, that the plateaus we observe correspond to $\nu_c = 2$ and $\nu_c = 6$. Furthermore, the difference between the values of resistance on the two plateaus equals $\approx 8.6\,\mathrm{k}\Omega$. This value is exactly $\frac{h}{2e^2} - \frac{h}{6e^2}$ — difference between the plateaus with $\nu_c = 2$ and $\nu_c = 6$, confirming this hypothesis. Our data hence contains $\approx 3\,\mathrm{k}\Omega$ offset, that we were not able to explain.

It is reasonable to expect that the complete filling of a Landau level is attained at the middle of a Hall plateau. Thus with a certain degree of precision we can claim that the bisectors of radial lines limiting the Hall plateaus (shown in the fig. 8.2a by black dotted lines) are the lines of filling factor 2 and 6 for the first and the second plateau respectively. These bisectors are shown in the fig. 8.2a. by the white dashed lines. We also transposed both types of lines to the holes part of the plot (using symmetry considerations) and to the fig. 8.2b.

The α coefficient can be obtained from the bisector slope θ using the formula

$$\alpha = \frac{\nu_c}{\tan\theta}\frac{e}{h} \tag{8.17}$$

leading to α values $\simeq 2.6 \times 10^{10}\,\mathrm{cm}^{-2}\,\mathrm{V}^{-1}$ and $\simeq 2.46 \times 10^{10}\,\mathrm{cm}^{-2}\,\mathrm{V}^{-1}$ obtained for filling factors 2 and 6 respectively. We take average of this value: $\alpha \simeq 2.53 \pm 0.07 \times 10^{10}\,\mathrm{cm}^{-2}\,\mathrm{V}^{-1}$.

Note that even though, no plateaus are observed on the holes part of the color plot, one is still able to recognize the zones of different colors, separated by the same radial lines (black dotted lines), limiting the Hall plateaus on the electrons part. This can be understood by looking on the formula (8.14), that demonstrates, that the measured signal is a combination of Hall resistances of all three regions. When one of these resistances exhibits a step transition from one plateau to another, this is necessarily reflected on the color plot. Here the transitions of the Hall resistance of the constriction are especially recognizable. This is also the case for the measurement with the longitudinal combination of probes $V^1_{\mathrm{A}} - V^1_{\mathrm{B}}$, see fig. 8.2b. Nevertheless, we can not give a clear explanation for the measured values.

In order to enhance the visibility of these transitions, we plotted the derivative of the data along the gate voltage direction in the fig. 8.3. First, note that the radial translational symmetry of our data is seen even better on these graphs. Furthermore, it is quite clear, that the result of the analysis of Hall plateaus from the electrons part of the plot fig. 8.2a holds in both of new color plots.

Finally, using the results of the averaging along the radial lines, described above, we reconstructed the color plots, replacing all values on given radial line by

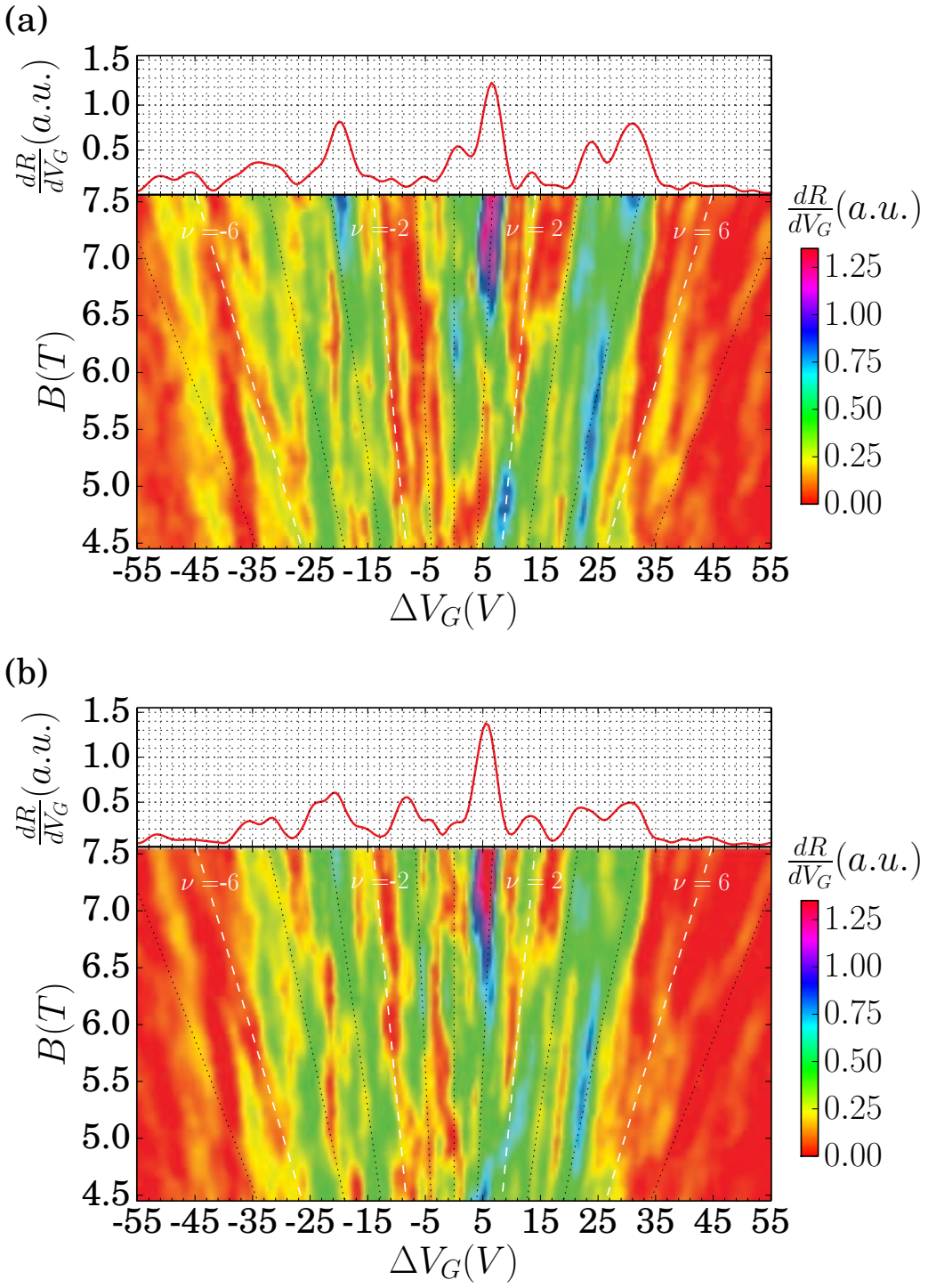

Figure 8.3: Color plots of the absolute values of the resistance derivative along the gate voltage direction measured with the crossed (a) and longitudinal (b) probes combinations as a function of $\Delta V_{\mathrm{G}} = V_{\mathrm{G}} - V_{\mathrm{D}}$ and magnetic field B. Top graphs show the variation of the derivative at maximum magnetic field $B = 7.565\,\mathrm{T}$. Black dotted lines, transposed from the fig. 8.2, mark the boundaries of plateaus. White dashed constant filling factor lines correspond to the filling factors -6, -2, 2, 6.

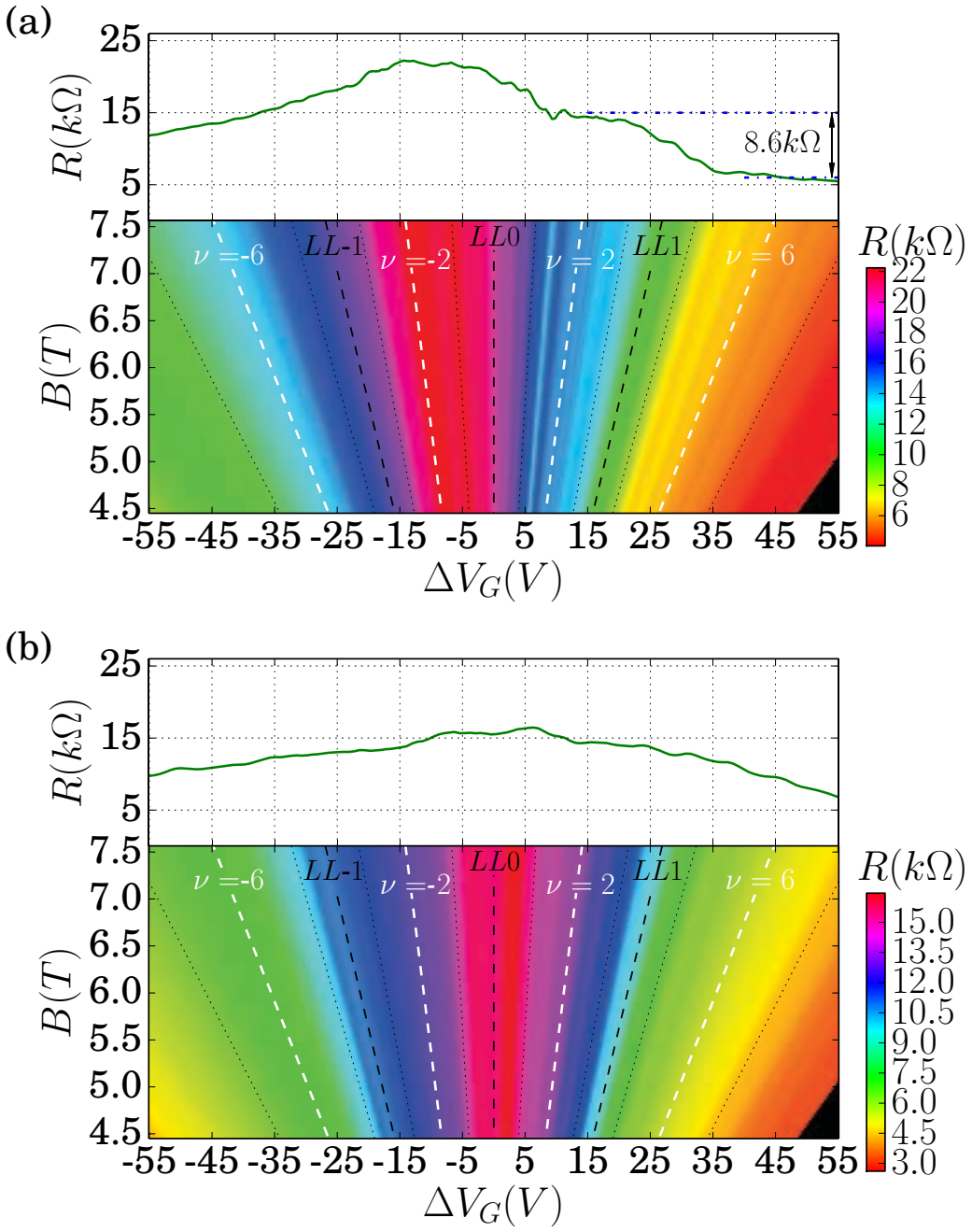

Figure 8.4: Color plots reconstructed with the results of the averaging along the radial lines, replacing all values on given radial line by its average, for crossed (a) and transversal (b) probes combinations as a function of $\Delta V_{\mathrm{G}} = V_{\mathrm{G}} - V_{\mathrm{D}}$ and magnetic field B. Top graphs show the values used for the color plots reconstruction. Black dotted lines, transposed from the fig. 8.2, mark the boundaries of plateaus. White dashed constant filling factor lines correspond to the filling factors -6, -2, 2, 6, black ones to the centers of the Landau Levels -1, 0, 1.

its average. The outcome is shown in fig. 8.4. This is the most appropriate way of data smoothing in such kind of experiments.

To conclude, the study of the transport properties of our device in the magnetic field helped us to confirm the hypothesis of diffusive regime and good screening evoked in subsec. 7.1.2 as well as determine the α coefficient, required for the conversion between gate voltage and carrier density. Nevertheless, we do not have a complete understanding of all the results and several questions remain open.

Chapter 9

Shot Noise in Graphene

In this chapter we get to the heart of the matter: in the following we will present the result of the noise measurements on our graphene-based device. The main purpose of this experiment is to determine the Fano factor and study its possible variation with Fermi energy (i.e. carrier density). We first discuss the measurement principle and explain how the current noise spectral density was extracted from the acquired data. Next, we expose the obtained results and confront them with the conclusions of previous experiments as well as with numerical simulations, found in the literature.

9.1 Measurement Principle

The principle of this measurement was already presented in the sec. 4.2 of the chapter Measurement System Principle (see in particular the fig. 4.3). Here we propose a brief reminder of employed method. First, the present study is based on four-point and cross-correlation noise measurement technique. This is attained in the following way: a DC current is injected into the device via separate electrodes, the fluctuations of this current due to the transmission properties of the sample result in the fluctuations of the voltage drop across the constriction. These voltage fluctuations are detected by two pairs of voltage probes situated on both sides of the constriction (see fig. 4.2) and the cross-correlation approach is used. This method is certainly more challenging than a conventional two-point current noise measurement, but allows to get rid of the contact resistance related issues and partially of the parasitic noise appended to the signal by the detection system.

Let us see how these principles were implemented technically. In fact, the used setup is somehow similar to the one described by the schematics 6.7. The device is current biased by applying a DC voltage to two $5\,\mathrm{M}\Omega$ resistors placed before and after the device, the double detection of the voltage fluctuations across

the constriction is done with the help of four voltage probes, connected to four cryogenic amplifiers and the difference between corresponding signals is taken by two room-temperature differential amplifiers. The RLC filters, added to each detection circuit serve to shift the pass-band to frequencies at which $1/f$-noise is negligible. The two obtained signals are then digitized by the two-inputs analog-to-digital conversion board *Spectrum* at 10 MSamples/s into a 2^{15} Samples buffer (thus a 1 MHz band contains 6553 or 6554 points). Finally, the FFT is performed by the software module, developed for this purpose and the crosscorrelation as well as the autocorrelation of each signal are calculated. The crosscorrelation contains real and imaginary part, in our calculations we take the absolute value of it.

In addition, to reduce the uncertainty on the noise, the spectra were averaged over 40 000 acquisitions each and the noise at zero bias was subtracted, yielding what is called the excess noise. This was done in order to remove all bias-independent parasitic contributions (which is usually the case for parasitic electromagnetic peaks appearing due to the ground loops unavoidable in complex measurement systems). The still persisting peaks were removed numerically. Finally, the best fit of the bandpass filtered signal was done in order to extract the filter independent noise level. The Autocorrelation spectra were fitted with a single Lorentzian-type function:

$$S^{\mathrm{A}}(f) = \frac{S_0^{\mathrm{A}}}{1 + (f^2 - f_0^2)^2/(f\Gamma)^2} \tag{9.1}$$

where f_0 is the resonance frequency. We obtain that two channels have slightly different resonant frequencies: $f_1 \approx 3.29\,\mathrm{MHz}$ for the channel 0, while $f_2 \approx 3.36\,\mathrm{MHz}$ for channel 1, yielding $\Delta f \approx 70\,\mathrm{kHz}$, to be compared to the bandwidths of the respective channels: $\Gamma_1 \approx 158\,\mathrm{kHz}$ and $\Gamma_2 \approx 164.5\,\mathrm{kHz}$. Therefore, the crosscorrelation was fitted with a double Lorentzian-type function:

$$S^{\mathrm{C}}(f) = \frac{S_0^{\mathrm{C}}}{1 + \frac{\Gamma_2^2(f^2-f_1^2)^2 + \Gamma_1^2(f^2-f_2^2)^2}{f^2\Gamma_1^2\Gamma_2^2} + \frac{(f^2-f_1^2)^2(f^2-f_2^2)^2}{f^4\Gamma_1^2\Gamma_2^2}} \tag{9.2}$$

(the derivations of both formulas are given in the Appendix B.3). A typical excess noise crosscorrelation spectra and its fit are shown in fig. 9.2.

The clearest way to understand how the Fano factor was extracted from the obtained data is to consider the equivalent electric circuit, shown in fig. 9.1. The capacitors C_0 on the schematics represent the capacitances of coaxial cables used for device DC biasing and estimated to be $\simeq 300\,\mathrm{pF}$. These, compared to the adjacent $50\,\mathrm{k\Omega}$ resistors, can be neglected at frequencies of about 3 MHz, giving the simplified variant of the circuit shown on the right of the figure. Here Z_0 depicts the total impedance of the voltage probes and Z_1 depicts the impedance of the part of the circuit used for injection of the DC and AC currents. However,

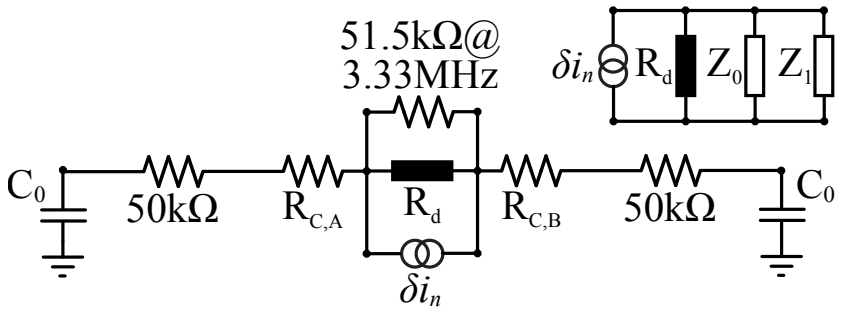

Figure 9.1: Main: Equivalent electric circuit for the noise measurement, C_0 — capacitances of coaxial cables, $R_{\mathrm{C,\,A/B}}$ — contact resistances. Inset: simplified variant of the same circuit.

in sec. 6.1 we saw that the total series contact resistance $R_{\mathrm{C,\,A}} + R_{\mathrm{C,\,B}} \simeq 300\,\mathrm{k\Omega}$, which is also the case at 3 MHz. Hence the impedance Z_1 which is essentially the contact resistance in series with two 50 kΩ resistors is negligible in parallel with R_d and Z_0.

Now recall, that our data corresponds to the voltage noise spectral density at the output of the amplifiers so we need first to find the corresponding noise at the input of the measurement circuit and then convert voltage noise to current noise. Our method consists of the following steps. Let us note by K_0 and K_1 the gain coefficients of the both measurement channels, and by $S_{\mathrm{VV}}^{\mathrm{OUT}}$ and $S_{\mathrm{VV}}^{\mathrm{IN}}$ the crosscorrelation voltage noise referred to the output and to the input of the measurement channels respectively. Then the following relation holds:

$$S_{\mathrm{VV}}^{\mathrm{OUT}} = K_0 K_1 S_{\mathrm{VV}}^{\mathrm{IN}} \tag{9.3}$$

Moreover if R_d is the differential resistance of the constriction the current noise is given by $S_{\mathrm{II}} = S_{\mathrm{VV}}^{\mathrm{IN}}/(R_\mathrm{d} /\!\!/ Z_0)^2$, which leads to

$$S_{\mathrm{II}} = \frac{S_{\mathrm{VV}}^{\mathrm{OUT}}}{K_0 K_1 (R_\mathrm{d} /\!\!/ Z_0)^2} \tag{9.4}$$

On the other hand, the gain coefficients are simply given by the ratio of the output and input voltages, i.e. $K_{0,1} = V_{0,1}^{\mathrm{OUT}}/V^{\mathrm{IN}}$. From the measurements described in sec. 7.2, we know $V_{0,1}^{\mathrm{OUT}}$, while $V^{\mathrm{IN}} = I_{\mathrm{AC}} R_\mathrm{d} /\!\!/ Z_0$, where $Z_0 = 51.5\,\mathrm{k\Omega}$ at measurement frequency (3.33 MHz). The differential resistance as well as the AC excitation current I_{AC} are both known. All this means that the precise knowledge of gain coefficients is not necessary, since the current noise spectral density is expressed as

$$S_{\mathrm{II}} = \frac{S_{\mathrm{VV}}^{\mathrm{OUT}}}{V_0^{\mathrm{OUT}} V_1^{\mathrm{OUT}}} \times I_{\mathrm{AC}}^2 \tag{9.5}$$

and, to remain in the same experimental conditions, we obviously should take the value of S_{VV}^{OUT} at 3.33 MHz that we know from the best fit of the spectra.

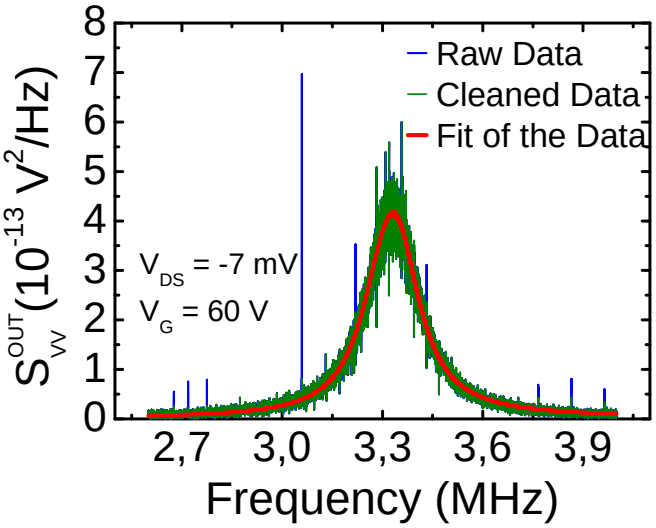

Figure 9.2: Measured crosscorrelation spectra of the excess voltage noise S_{VV}^{OUT} (blue and green with suppressed peaks) around resonance frequency near the Dirac point (at gate voltage $V_G = 60\,V$) and at drain-source voltage $V_{DS} \simeq -7\,mV$. Thickness of the best fit line (red) reflects the standard error of the fit.

Calculation of the exact DC current through the constriction is also straightforward. Let I_{DC} be the DC current, injected in the device and V_{ds} — corresponding drain-source voltage, that was calculated as a function of I_{DC} for all gate voltages in sec. 7.2 of Chapter 7 (see (7.17) in particular). The part of the current passing through the constriction (drain-source current) is given by $I_{DS} = I_{DC} - V_{ds}/70\,k\Omega$, since at low frequency Z_0 equals $70\,k\Omega$, while Z_1 is almost infinite.

Finally, note that thanks to the use of the 4-point approach together with the cross-correlation detection, the contribution of the thermal noise of different resistances present in the measurement circuit can be neglected. The exception can be made for the series contact resistance ($R_{C,\,A} + R_{C,\,B} \simeq 300\,k\Omega$), which is grater than the remaining part of the impedance Z_1. This means that a part of the current fluctuations generated by this contact will pass through the constriction and thus will be detected by our measurement system despite the use of the cross-correlation technique. Nevertheless, this parasitic contribution remains very small[1].

[1]If we assume about 3/4 of these current fluctuations to pass through the constriction, this will lead to the contribution $S_{par} = 3k_B T_e/(R_{C,\,A} + R_{C,\,B}) \approx 1.4 \times 10^{-26}\,A^2\,Hz^{-1}$ at $T_e \simeq 100\,K$, maximum temperature we expect at the contact (at maximum DC current, see subsec. 9.2.3). This rather lavish estimate correspond to 10 to 15% of the total detected noise at the same value of DC current.

9.2 Shot Noise in Presence of Joule Heating

We thus obtain the noise curves, shown in fig. 9.4 (red dots). Estimation of the electron temperature T_e using the Johnson-Nyquist to shot noise crossover, $eV = 2k_B T_e$, V being the intercept of the pure shot noise asymptote with the drain-source voltage axis (in the case of the excess noise), yields values ranging mostly between 7 and 9 K (see fig. 9.5.a, green squares).

In that way estimated electron temperature is clearly well above 4.2 K — the temperature of the helium bath. One possible reason for such elevated temperature could be the insufficient thermal anchoring to the helium bath of the cryogenic amplifiers, which dissipation will raise the temperature of the stage where the device is situated. This situation being possible, it is however quite difficult to provide any quantitative estimation of this effect. Still, the obtained temperature range appears too high.

Another possibility is the dissipation in the device itself. In that case the electron temperature will depend on the injected DC current I_{DC} as well as on how good this heat can sink from the device. The most important source of dissipation in the device is certainly the high contact resistance between graphene and one (or both) of the injection electrodes, which is $\simeq 300\,\mathrm{k}\Omega$. The impact of such high resistance should unavoidably be seen in the measurement. On the other hand, the coldest points are situated near the metallic electrodes in which the electrons are well coupled to the phonons. The electrons in the metal are hence considered to be at the temperature of the stage T_0. By the way, there is an important detail to be reminded here: as it was explained in Chapter 5, our device has four additional (spare) probes (electrically disconnected from the measurement system) obviously also at the stage temperature T_0, which contribute to the heat sink as well. Remember moreover, that only half of the heat, dissipated by $\simeq 300\,\mathrm{k}\Omega$ resistance goes to the sample, while another half is returned to the bath directly.

9.2.1 Cooling by Electron Diffusion

The quantitative estimation of this effect can be obtained by writing the heat balance. To begin, let us consider only the heat transport due to the electron diffusion in the graphene. In that case the thermal conductivity κ_e is given by the Wiedemann-Franz relation:

$$\kappa_e = \mathcal{L}\frac{T_e}{\rho}, \quad \text{where} \quad \mathcal{L} = \frac{\pi^2}{3}\left(\frac{k_B}{e}\right)^2 \tag{9.6}$$

where T_e is the local electron temperature, while ρ is the local electrical resistivity and $\mathcal{L}$ is called Lorentz number. In this problem, many parameters are unknown, especially the resistances between the hot points and the cold ones. For this reason,

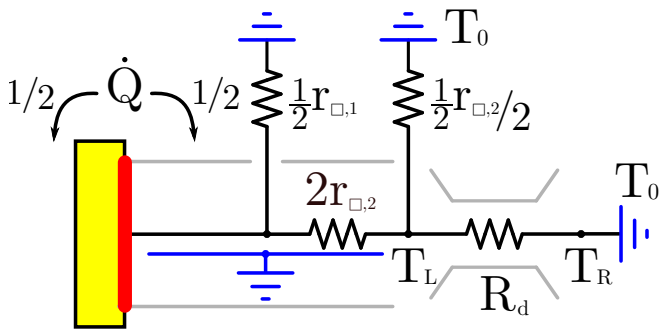

Figure 9.3: Schematics for the simplest heat transfer problem. The hottest area in the device in which the dissipation takes place is marked with red colour, the coolest areas (at the temperature T_0 of the stage where the device is situated) is marked with blue colour. The blue wire below symbolizes the phononic bath.

we simplify our model as much as possible by doing the following assumptions. First of all, the heat generation takes place in one location only, which is the $\simeq 300\,\mathrm{k}\Omega$ contact resistance between the metal and the graphene layer. Next, because of its high resistance the heat flow through the constriction is very weak, hence the electrons on its right can be seen as thermally isolated from their counterparts on the left of the constriction: $T_\mathrm{R} = T_0$. Finally, since near the current injection electrodes, the side gates are weakly efficient, the graphene layer is strongly hole-doped between the current injection electrode and the spare probes. For the sake of simplicity, we consider the sheet resistance in this region to be constant and denote it as $r_{\square,1}$, while between the principal probes and the constriction, the sheet resistance $r_{\square,2}$ is also put to be constant. The latter region is obviously more resistive, it is reasonable to take $r_{\square,2}/r_{\square,1} \simeq 3$. The different aspect ratios can be roughly estimated from the lithography design (see fig. 5.10). This yields the picture represented by the schematics, shown in fig. 9.3.

The temperature T_L in this simplistic model can be found from the following equation[131]

$$\dot{Q} = \frac{\pi^2}{3}\left(\frac{k_\mathrm{B}}{e}\right)^2 \frac{T_\mathrm{L}^2 - T_0^2}{2}\frac{1}{r_{\square,2}/4}, \quad \dot{Q} = \frac{1}{2}300\,\mathrm{k}\Omega \times I_\mathrm{DC}^2 \frac{r_{\square,1}}{r_{\square,1} + 4.5 r_{\square,2}} \tag{9.7}$$

with $\dot{Q}$, the fraction of the heat, that did not sink through the spare probes. This equation leads to the expression:

$$T_\mathrm{L} = \left[\frac{300\,\mathrm{k}\Omega \times I_\mathrm{DC}^2}{25\,\mathrm{nW}}\gamma + T_0^2\right]^{1/2}, \quad \gamma = \frac{r_{\square,1} r_{\square,2}}{4 r_{\square,1} + 18 r_{\square,2}} \tag{9.8}$$

9.2.2 Data Fit

We can now embed this calculation into the formula describing the excess noise dependence on the drain-source voltage and try to fit our data using the new relation. At constant temperature the former reads

$$S_{\mathrm{II}}^{\mathrm{e}}(V_{\mathrm{ds}}) = 2eR_{\mathrm{d}}^{-1}\mathfrak{F}V_{\mathrm{ds}}\coth\left(\frac{eV_{\mathrm{ds}}}{2k_{\mathrm{B}}T}\right) - 4R_{\mathrm{d}}^{-1}\mathfrak{F}k_{\mathrm{B}}T \tag{9.9}$$

Besides, since T_{L} can be very different from $T_{\mathrm{R}} = T_0$, we take the electron temperature in the constriction T_{c} to use with (9.9) given by $T_{\mathrm{c}} = \frac{T_{\mathrm{L}}+T_{\mathrm{R}}}{2}$, that finally yields, when latter depends on the drain-source voltage V_{ds}:

$$\begin{aligned} S_{\mathrm{II}}^{\mathrm{e}} =& 2eR_{\mathrm{d}}^{-1}\mathfrak{F}V_{\mathrm{ds}}\coth\left(\frac{eV_{\mathrm{ds}}}{2k_{\mathrm{B}}T_{\mathrm{c}}(V_{\mathrm{ds}})}\right) \\ &+ 4R_{\mathrm{d}}^{-1}\left(1-\mathfrak{F}\right)k_{\mathrm{B}}T_{\mathrm{c}}(V_{\mathrm{ds}}) + 4R_{\mathrm{d}}^{-1}k_{\mathrm{B}}T_0 \end{aligned} \tag{9.10}$$

We thus perform the numerical fit of all curves using (9.10), having the Fano factor $\mathfrak{F}$, stage temperature T_0 and γ as free parameters. Choosing the parameter $\gamma \simeq 10\,\Omega$ we succeed to fit the excess noise curves (see fig. 9.4), with the stage temperature T_0, ranging mostly between 4.8 and 5.5 K as shown in fig. 9.5.a (blue triangles), i.e. only slightly above 4.2 K, what can be attributed to the external sources of heat as, for instance, already discussed cryogenic amplifiers dissipation. The dependence of the electron temperature in the constriction on the bias DC current I_{DC} estimated at $V_{\mathrm{G}} = 55\,\mathrm{V}$ is displayed in fig. 9.5.b. By the way, note that the temperature near the contact, at which the dissipation takes place, may be very high, the thermal noise of the contact will have only minor contribution to the noise we measure, that would not hold in case of a simple two-point measurement. This demonstrates once again the advantage of our method.

Besides, note from (9.8), that the temperature T_{c} at high drain-source voltages will be proportional to V_{ds} and its variation with the latter quantity will contribute to the increase of the noise power in addition to the shot noise component. As a consequence, the Fano factor extracted from the fit with (9.10) will be lower than the apparent one, obtained simply from the slope of the linear part of the noise curve.

The value of the parameter γ (if we hold to our assumption $r_{\square,2}/r_{\square,1} \simeq 3$) corresponds to $r_{\square,1} \approx 200\,\Omega$ and $r_{\square,2} \approx 600\,\Omega$, which is about factor of $3-6$ lower as compared to what we could estimate from our measurements of the device resistance. Recall yet, that our model was intentionally greatly simplified to allow for a simple analytical solution. For that reason, it may eventually underestimate the sheet resistances $r_{\square,1}$ and $r_{\square,2}$, that give rise for the variation of T_{c}, shown on fig. 9.5.b. In addition, another possible mechanism of the heat transfer was not

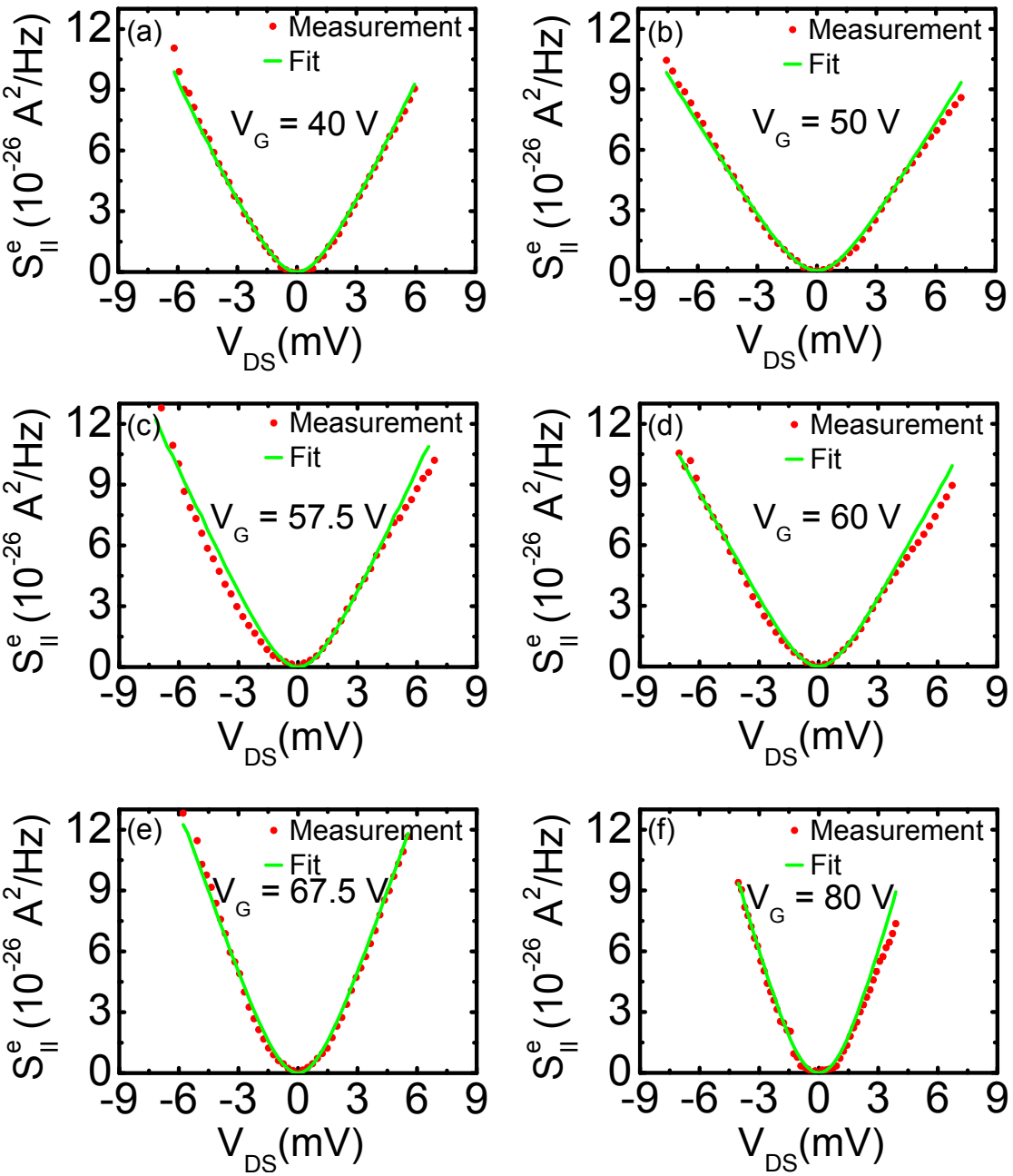

Figure 9.4: Excess current noise S_{II}^{e} through the constriction for different gate voltages (red circles, their size exceeds the standard error) as a function of the drain-source voltage and the three-parameters best fit (green solid curve).

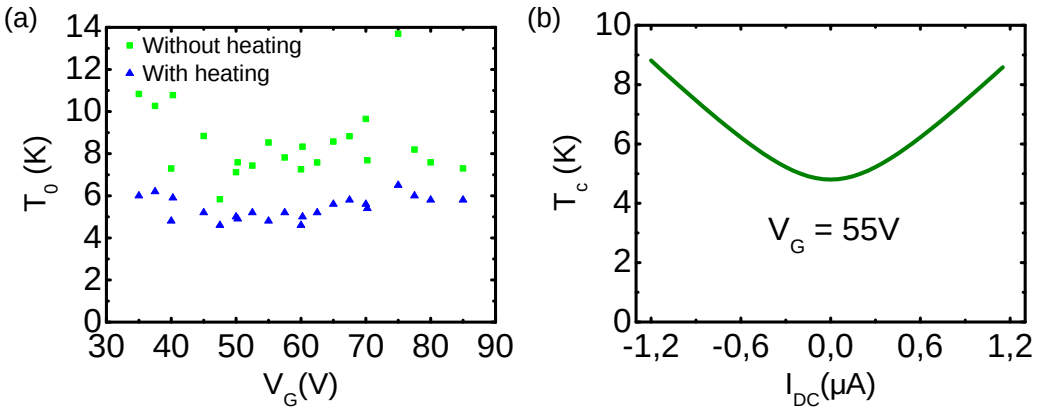

Figure 9.5: (a) T_0, estimate of the temperature of the stage to which the device is thermalized as a function of the gate voltage. Green squares: estimated from the Johnson-Nyquist and the shot noise crossover, without taking the heating into account. Blue triangles: extracted from the excess noise fit, that includes the heating. (b) Electron temperature in the constriction T_c at $V_G = 55V$ as a function of the DC bias current I_{DC}.

considered so far: the cooling by phonon emission, that we discuss in the next section.

9.2.3 Cooling by Phonon Emission

At low temperature, only the coupling to longitudinal acoustic phonons is relevant. We also assume that the energy transfer between the lattice and the substrate is much stronger than the electron-phonon energy exchange rate, so that the lattice is at the temperature of the substrate and hence of the stage: $T_p = T_0$. As a consequence, the heat flux is out of plane and is proportional to the effective surface. Per unit area, it is typically given by the relation

$$\dot{Q}_{ep} = \Sigma_{ep}\left(T_e^{\delta} - T_p^{\delta}\right) \tag{9.11}$$

The parameter δ was predicted to equal to 4 in the clean graphene[90, 156] or, what is equivalent, at temperatures well above the disorder temperatures $T_{dis} = \frac{h}{k_B}\frac{s}{l_e}$[28], with $s = 2 \times 10^4\,\mathrm{m\,s^{-1}}$ the sound velocity and l_e the electronic mean free path. Below the disorder temperature and in the assumption of weak screening δ is reduced to 3[28]. The quantity Σ_{ep} is the electron-phonon coupling constant, which within two latter hypothesis reads[28]

$$\Sigma_{ep} = \frac{2\zeta(3)}{\pi^2}\frac{\varepsilon_F}{v_F^3\rho_M}\frac{D^2k_B^3}{\hbar^4 l_e s^2} \tag{9.12}$$

where $\rho_{\mathrm{M}} \approx 7.26 \times 10^{-7}\,\mathrm{kg\,m^{-2}}$ is the graphene mass per unit area and D is the deformation potential. There still a debate about the magnitude of the deformation potential and values between 10 and 30 eV can be found in the literature (see Refs. [71, 28] and the references therein). Besides, this prediction (including $\delta = 3$) was experimentally confirmed by Fong et al., that studied different mechanisms of the heat transfer in disordered graphene using the Johnson-Nyquist thermometry.

The local electron temperature now obeys the equation (written here for a constant sheet resistance $r_\square$):

$$-\frac{\partial}{\partial x}\left(\frac{\mathcal{L}}{r_\square}T_{\mathrm{e}}\frac{\partial T_{\mathrm{e}}}{\partial x}\right) + \Sigma_{\mathrm{ep}}\left(T_{\mathrm{e}}^3 - T_0^3\right) = 0 \tag{9.13}$$

The relation (9.13) does not allow for a simple analytical result in the case of our system, but we can still estimate the effectiveness of the cooling due to the electron-phonon coupling mechanism. For instance, let us consider the characteristic distance λ, above which the electron temperature starts to approach the lattice temperature T_0. In our system the dissipated power is important and it is reasonable to assume $T_{\mathrm{e}} \gg T_0$. Then, λ can be found by taking an approximate solution of (9.13), with the term T_0^3 neglected, of the form

$$T_{\mathrm{e}}(x) = T_{\mathrm{m}}\frac{1}{(1 + x/\lambda)^2} \tag{9.14}$$

T_{m} being the temperature of the hottest point. This yields

$$\lambda = \left(\frac{\mathcal{L}}{r_\square}\frac{10}{\Sigma_{\mathrm{ep}}}\right)^{1/2} T_{\mathrm{m}}^{-1/2} \tag{9.15}$$

At low DC currents another regime is established, when $T_{\mathrm{e}} - T_0 \ll T_0$. The electron temperature decreases exponentially in that case, while the characteristic length reads

$$\tilde{\lambda} = \left(\frac{\mathcal{L}}{3r_\square}\frac{1}{\Sigma_{\mathrm{ep}}}\right)^{1/2} T_0^{-1/2} \tag{9.16}$$

Now note that when this length becomes of the order of the distance between the hottest point of the sample and the cold metallic contacts, the transition from electron diffusion (Wiedemann-Franz) dominated to electron-phonon coupling dominated regimes is observed: in that situation the electrons start to be more efficiently thermalized by exchanging their energy with the phonons than by diffusing until the metallic contacts. Fong et al. indeed observed a cross-over between two regimes of the heat transfer, when measuring the thermal conductance with varied temperature.

We express the thermal length λ taking an intermediate value of the deformation potential $D \simeq 20\,\mathrm{eV}$, by the way close to the value considered by Hwang and Das Sarma in their calculation and also to what was estimated experimentally by Fong et al. for their device D1 (which has similar characteristics as our device). We start by writing the coupling parameter in the following form

$$\Sigma_{\mathrm{ep}} \simeq 0.09\,\mathrm{W\,m^{-2}\,K^{-3}}\frac{\sqrt{n_{\mathrm{s}[10^{12}\mathrm{cm}^{-2}]}}}{\left(\frac{l_{\mathrm{e}}}{40\,\mathrm{nm}}\right)} \tag{9.17}$$

where $n_{\mathrm{s}[10^{12}\mathrm{cm}^{-2}]}$ is the carrier density in the units of $10^{12}\mathrm{cm}^{-2}$. Above expression together with Lorentz number value $\mathcal{L} \simeq 2.44 \times 10^{-8}\,\mathrm{W\,\Omega\,K^{-2}}$ lead to

$$\lambda \simeq \frac{1645\,\mu\mathrm{m}\Omega^{1/2}\mathrm{K}^{1/2}}{\sqrt{r_{\square}}}\frac{1}{T_{\mathrm{e}}^{1/2}}\sqrt{\frac{l_{\mathrm{e}}}{40\,\mathrm{nm}}}\frac{1}{(n_{\mathrm{s}[10^{12}\mathrm{cm}^{-2}]})^{1/4}} \tag{9.18}$$

Let us evaluate λ in our system, when the current I_{DC} injected into the device equals to $1\,\mu\mathrm{A}$, which is the near-maximum current we applied in this experiment[2]. We first estimate the electron temperature at the hottest point of the device (we take $r_{\square,2}/r_{\square,1} \simeq 3$ with $r_{\square,1} \simeq 1.5\,\mathrm{k\Omega}$, $T_0 \simeq 5\,\mathrm{K}$):

$$\begin{aligned} T_{\mathrm{m}} &= \left[\frac{300\,\mathrm{nW}}{25\,\mathrm{nW}}\frac{9r_{\square,1}r_{\square,2}}{2r_{\square,1}+18r_{\square,2}} + T_0^2\right]^{1/2} \\ &= \left[12\cdot 750\,\Omega + (5\,\mathrm{K})^2\right]^{1/2} \simeq 100\,\mathrm{K} \end{aligned} \tag{9.19}$$

and then, using $1 \times 10^{12}\,\mathrm{cm}^{-1}$ as the order of magnitude for the carrier density, 40 nm as a typical mean free path and assuming the average sheet resistance to be $\sim 3\,\mathrm{k\Omega_{\square}}$, we get at $T_{\mathrm{m}} \simeq 100\,\mathrm{K}$

$$\lambda \approx 3\,\mu\mathrm{m} \tag{9.20}$$

and at $T_0 \simeq 5\,\mathrm{K}$

$$\tilde{\lambda} \approx 2.5\,\mu\mathrm{m} \tag{9.21}$$

which are both actually comparable to the distance between the hottest point and the constriction.

This result proves the importance of the electron-phonon coupling mechanism in the heat transfer in our system. Indeed, as one can see, in that case the characteristic thermal length λ starts to approach the distance between the hottest point and the constriction, while the electron temperature near constriction starts to approach the lattice (and thus the stage) temperature. In the previous section we found the variation of the electron temperature in the constriction T_{c}, that

[2]The maximum applied current equals to $1.2\,\mu\mathrm{A}$.

allowed us to fit our noise curves with (9.10) yielding a reasonable temperatures of the stage. Assuming only the Wiedemann-Franz mechanism of heat transfer such variation of T_c leads to the sheet resistances of the graphene much lower, than what we estimate from the conductance measurement (see discussion at the end of subsec. 9.2.2). It is clear from above, that if the electron-phonon exchange mechanism is included into the heat balance equation, this variation of T_c will result in the sheet resistances of higher value, probably much closer to our estimations.

9.3 Noise Power Fluctuations

In this section we draw reader's attention to the apparent fluctuations of the measured noise power around mean value, represented by the fit curves (see fig. 9.4). The noise power fluctuations in disordered systems is something known and these are of the same origin as the Universal Conductance Fluctuations. In a disordered conductor the electronic waves interferences, that obviously depend on the injected particles energy, impact the corresponding transmission coefficients. This is reflected in the reproducible fluctuations of the conductance (already men-

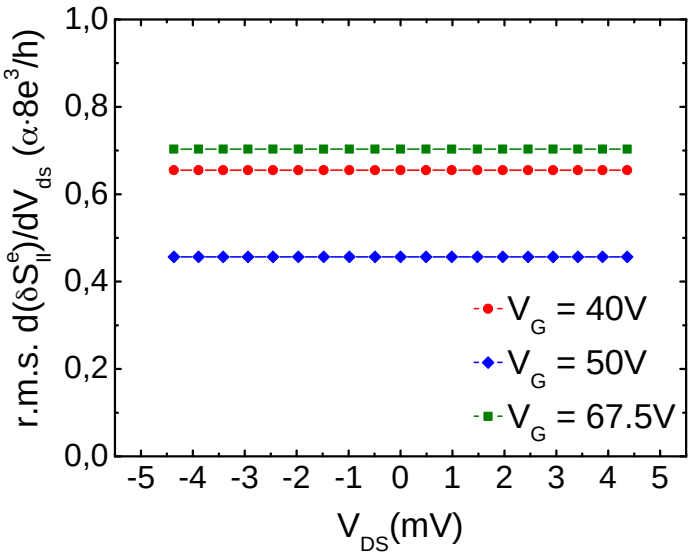

Figure 9.6: Study of noise power fluctuations at three gate voltage values, according to the relation (9.23). The theoretical value corresponds to 1 in the graph, $\alpha = \sqrt{\frac{46}{2835}}$.

tioned in Chapter 6), but also in the fluctuations of another transmission coefficients dependent quantity, the Fano factor. The former fluctuations are produced

(approximately) by the opening or closing of an additional electronic channel over the total N channels, yielding the magnitudes of the order of conductance quantum. In return, the impact of this process on the Fano factor is less straightforward.

The phenomenon of the noise power fluctuations in conventional diffusive conductors was studied theoretically by de Jong and Beenakker within the framework of the random-matrix theory. They obtain (for the conductors that however must be much longer than wide) the root-mean-square fluctuations of the noise power given by[38]:

$$\text{r.m.s. } \delta S_{\text{II}} = 2e|V_{\text{ds}}|\frac{2e^2}{h}\sqrt{\frac{46}{2835}} \tag{9.22}$$

Just as it is for the UCF, the magnitude of these fluctuations is independent of the conductor size, particular disorder configuration or number of channels and by analogy with the formers may be called "universal noise fluctuations"[38]. Note that in the case of graphene, in addition to the spin degeneracy related 2 pre-factor, the same pre-factor accounting for the valley degeneracy has to be added.

We are not aware of any theoretical or experimental work reported on this subject in graphene. Nevertheless, we are going to verify whether this prediction can be confirmed by our data. It is clear that for the graphene

$$\text{r.m.s. } \frac{\mathrm{d}\delta S_{\text{II}}}{\mathrm{d}V_{\text{ds}}} = \frac{8e^3}{h}\sqrt{\frac{46}{2835}} \tag{9.23}$$

In fig. 9.6 this quantity is plotted in units of $\frac{8e^3}{h}\sqrt{\frac{46}{2835}}$ for three values of gate voltages (for a given gate voltage the root-mean-square value was calculated over all points of the noise curve laying out of thermal noise domination region and then plotted against a fixed V_{ds} range for clearness, the theoretical value being equal to 1 in these units). As one can notice, the results obtained at $V_{\text{G}} = 40$ and $67.5\,\text{V}$ show very similar values, and moreover are approaching the theoretical value, in the opposite to what is observed at $V_{\text{G}} = 50\,\text{V}$, closer to the Dirac point, where the electron-hole "puddles" are formed. It is thus obvious that the relation (9.23) is not completely confirmed by our data and a deeper theoretical and experimental investigation of this phenomena is required. The reasons, why the result by de Jong and Beenakker does not seem to completely hold in graphene, might be for instance the effects related to the pseudo-relativistic nature of the quasi-particles in this material or to the already mentioned electron-hole "puddles", but other reasons are also possible (without mentioning that the graphene conductor we study is large and short, while the above result was obtained for long and narrow conductors).

9.4 Results and Discussion

The resulting dependence of the Fano factor on the gate voltage, that we found in subsec. 9.2.2, is depicted in fig. 9.7. Markedly, the Fano factor varies only slightly with the gate voltage, remaining near value ≈ 0.25 and the behaviour predicted by Tworzydlo et al. and shown in fig. 3.2 is not seen on this graph.

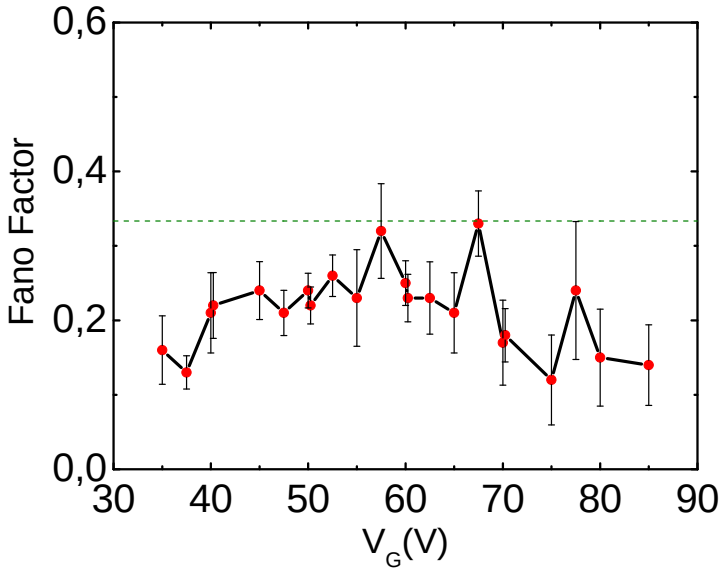

Figure 9.7: Fano Factor as a function of gate voltage extracted from the three-parameter fit of the experimental data with (9.10), horizontal dashed line corresponds to the value 1/3. The Dirac point is estimated to lay between 58 and 61 V.

Such inconsistency with the evanescent modes model is although not so surprising, since these predictions were obtained for an ideal, ballistic graphene ribbon, while our sample, as it was established in Chapter 7, has a significant level of disorder and the electron transport in it is believed to be diffusive. To settle the doubt, see that $V_G \simeq 30\,\mathrm{V}$ on our graph corresponds to carrier density $n_s \simeq 7 \times 10^{11}\,\mathrm{cm}^{-2}$, which on its turn corresponds to energies of about 97 meV. In the units of fig. 3.2 and for $W = 800\,\mathrm{nm}$ this gives $\simeq 120$ which is greatly far away from the region in this figure, where the variation of the Fano factor is weak (± 5 units).

As a consequence, we will compare our data with other experimental results by Danneau et al. (in particular with their Sample E, presumably diffusive, see fig. 3.8.f on page 56) and by DiCarlo et al., rather than with the conclusions of Tworzydlo et al. Furthermore, several theoretical and numerical studies were done on the subject of current fluctuations and Fano factor in disordered graphene. We will see the conclusions of these works as well.

Let us have a look once again on our data. On the holes part of the curve the Fano factor is quasi-constant down to $V_G \simeq 40\,V$, after what it starts to diminish. On the electrons part, in return, the fluctuations are significant and the Fano factor seems to diminish already for the gate voltages above $\simeq 65\,V$. However, because of the fluctuations, it is quite difficult to see, when the mean value of the Fano factor starts to decrease. Finally, near the Dirac point ($V_G \simeq 58\,V$), the Fano factor reaches its maximum ≈ 0.32, showing a pretty pronounced peak to which one should equally draw attention.

Now, if we make a comparison with the results by Danneau et al. discussed in Chapter 3, our data obviously disagree with what is represented in fig. 3.8.b (see page 56), which is however expected, since this graph displays the behaviour of a ballistic sample. On the other hand, fig. 3.8.f of the page 56 shows the behaviour of a diffusive sample so such comparison is absolutely pertinent. Our data indeed agree in several aspects with the above-mentioned result. Even though, the Fano factor behaviour, observed in this work is more stable, i.e. no fluctuations can be noticed, apart from that the two graphs are qualitatively similar: the Fano factor is constant over a large plateau, and decreases outside of it. Moreover, the Fano factor in fig. 3.8.f seems to reach its maximum near the Dirac point, as it is the case for our data, although the variation is smooth without a pronounced peak. The values measured by Danneau et al. are however lower, $\approx 0.19 - 0.2$ as compared to $\approx 0.24 - 0.25$ that we found, and the Fano factor decrease they observe is also sharper.

Besides, it would be interesting to check, if our data remains constant within the same limits as the one in fig. 3.8.f. However, without knowing the corresponding carrier densities (or alternatively back-gate capacitance of the Sample E), it is difficult to estimate the extent of the plateau. Considering the plateau to persist up to $V_D \pm 10\,V$ and taking the values of capacitance, mentioned for the Sample A ($C_{gate} \sim 12\,aF\,\mu m^{-2}$ and $115\,aF\,\mu m^{-2}$, depending on hypothesis[3]) we obtain corresponding carrier density $\simeq \pm 0.85 \times 10^{11}\,cm^{-2}$ and $\simeq \pm 7.2 \times 10^{11}\,cm^{-2}$ respectively for the two mentioned values, while in our case $V_G = 40\,V$ corresponds to $n_s \simeq 5 \times 10^{11}\,cm^{-2}$. Hence, if we believe the second hypothesis, the two results agree. Good agreement with the results of this study is an encouraging sign.

The results reported by DiCarlo et al. on their turn differ from our data in some details. In particular, they found rather constant behaviour of the Fano factor around ≈ 0.35, 45% higher, than what we measured, which in addition seems more stable, with weaker fluctuations. On the other hand, at least in fig. 3.6.b (Chapter 3, page 54), one distinguishes a peak near the Dirac point,

[3]The first value was obtained as a free parameter in the fit by the theoretical predictions of the data for Sample A, while the second value was obtained from the two infinite plane capacitor model.

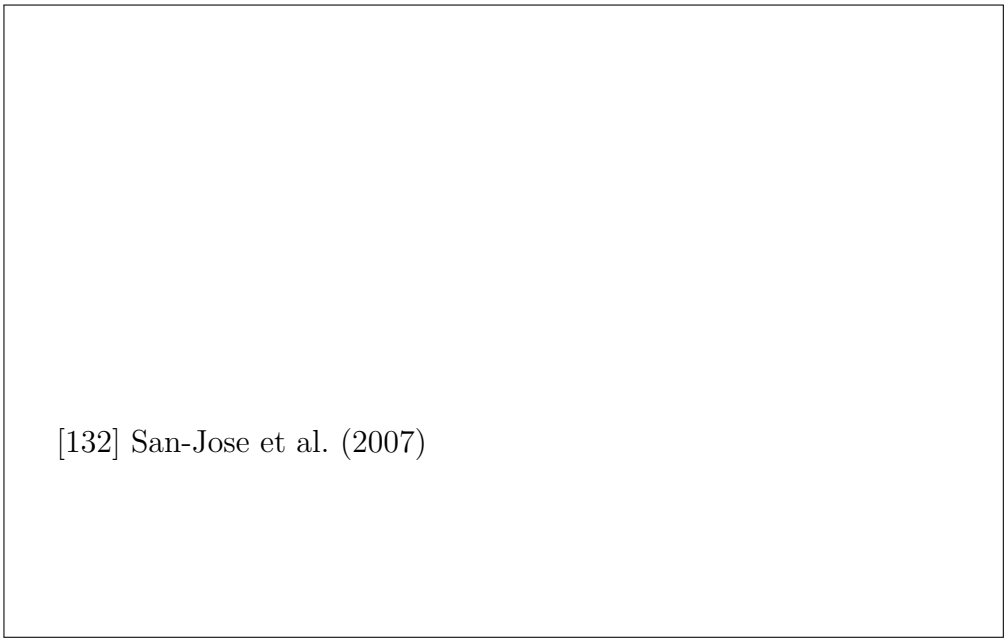

Figure 9.8: Top figures: sketches of two types of disorder realisations considered in the work by San-Jose et al.: one-dimensional disorder (a) and two-dimensional disorder, i.e. charge puddles (b). Under each sketch the result of corresponding simulation of the Fano factor dependence on the graphene sheet length to typical size of charge puddles ratio. The Fano factor saturates to the system independent values in both cases: $F_{1D} = 0.243$ and $F_{2D} = 0.295$, for large system sizes. From [132].

while in fig. 3.6.d the fluctuations look more important on the electrons side than on the holes side, as it is also the case for our data. Finally, the result for Sample D (fig. 3.6.f), presumably multi-layer, has to be discussed. The Fano factor, measured at $T_e = 1.1\,\mathrm{K}$ in this sample certainly approaches the values we also observed (maximum ≈ 0.27) and in addition varies with the gate voltage. Yet, this variation is much slower (remember that the back-gate in this sample is almost three times more efficient than the side-gates of our device). It is hence hard to speak about agreement between two results.

Such disparity between our data and the conclusions of the work by DiCarlo et al. can be attributed to the difference in the degree of disorder of the samples used in two experiments. This is confirmed by the numerical results, as it will be explained in what follows. In return, the mean free path, reported in [42] is $\approx 40\,\mathrm{nm}$, very close to what we could estimate, suggesting a similar degree of disorder.

In the following we present a brief review of theoretical and numerical works

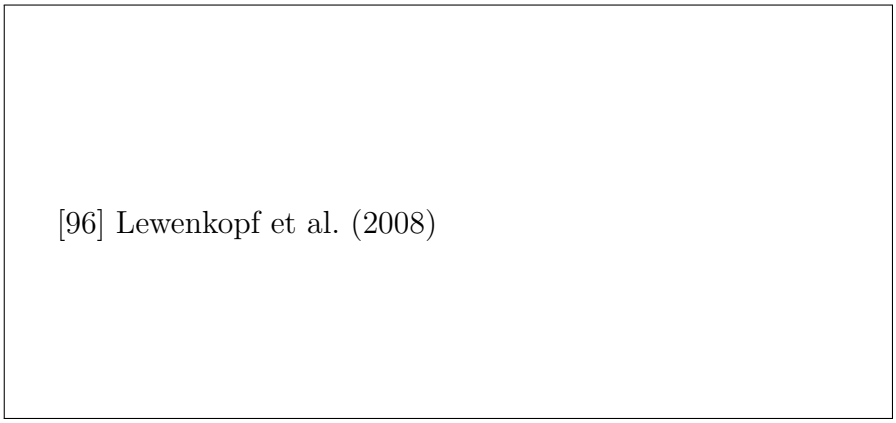

Figure 9.9: Results of the work by Lewenkopf et al. Average Fano factor as a function of carrier density for several disorder strengths and $\xi = 2a_0$. The number of realizations ranges from 100 to 5000. (a) Square sheets ($W/L = 1$) with $L/\xi = 40$. (b) Rectangular sheets ($W/L = 3.1$) with $L/\xi = 26$. The dashed lines represent F=1/3. From [96].

investigating the current fluctuations in diffusive graphene and compare the conclusions of these works with our results. The first study by San-Jose et al. examines current fluctuation in disordered graphene within the transfer matrix formalism. Considering a smooth puddle disorder of two types — one-dimensional and two-dimensional (see fig. 9.8) — they conclude that in both cases, when the characteristic system length L becomes much greater, than the range of the disorder potential ξ (typical size of charge puddles) the Fano factor saturates to the universal value, but different for two cases: $F_{1D} = 0.243$, while $F_{2D} = 0.295$. The dependence of the Fano factor on system length is shown in fig. 9.8 for the both cases. Note, that the average value of the Fano factor we observe is very close to F_{1D}, yet the case of 2D disorder seems more realistic. Different type of disorder could also explain the disparity between our results and the results of DiCarlo et al.

Another work by Lewenkopf et al. used the recursive Green's function method for studying transport properties of a graphene sample having a long-range disorder. In this work was introduced a special dimensionless parameter K_0, characterizing the disorder strength. This parameter is defined as a pre-factor of the impurity potential correlation function and from the quantitative point of view expresses the magnitude of the disorder fluctuations. In addition, within Born approximation, this parameter can be related to l_e, the mean free path far from the Dirac point, according to

$$l_e = 2\lambda_F/(\pi K_0) \tag{9.24}$$

with λ_F — Fermi wavelength. Considering the values of l_e obtained in subsec. 7.1.3 of the previous chapter, see in particular fig. 7.5.b, we estimate that in our case this parameter ranges from 0.5 to 1. The results of the simulations can be seen in fig. 9.9. First point to note is that the values of Fano factor obtained in this work are situated around $0.25 - 0.29$ for the same values of the disorder parameter K_0. What is more remarkable is that the simulations of Lewenkopf et al. predict the appearance of a peak at the neutrality point in the case of a moderate disorder, that we also observe.

The last work we discuss was accomplished by Logoteta et al. The authors investigate the dependence of Fano factor on the energy of injected electrons by the means of envelope function approach and Fourier-based method used to solve numerically the Dirac equation[103]. The simulations are done for two impurities concentrations $n_{imp} = 5 \times 10^{11}\,cm^{-2}$ and $5 \times 10^{13}\,cm^{-2}$ (this same quantity in our system is $\simeq 1.35 \times 10^{12}\,cm^{-2}$) and for various disorder amplitude ranges δ (see [99] for more details). Three aspect ratios of the graphene sheet were studied. Some results the authors obtained are presented in fig. 9.10. Note by the way, that the energy range considered in these simulations almost coincides with the one in our experiment.

For the aspect ratio and impurity concentration, relevant for our study ($W = 200\,nm$, $L = 40\,nm$ and $n_{imp} = 5 \times 10^{11}\,cm^{-2}$, see blue solid curve in fig. 9.10.a) Fano factor exhibits the values, oscillating around 0.25 with a rather prominent peak at the Dirac point, reaching 0.35 value, which is consistent with our data (the asymmetry of the theoretical curve with respect to zero energy is due to the use in the simulations of non-infinite potential energy in the contacts, compare refs. [148] and [99] for this detail). In addition, for the positive energies the oscillations are rapidly damped (it is however not very clear, whether this is not due to the same reasons as the global asymmetry of the curve). Whether or not the Fano factor manifests a decrease far from the Dirac point is also less apparent. Yet, it is difficult, to know if the disorder amplitude ranges δ used in these simulations are appropriate in the case of our system. Besides, the simulations for other aspect ratios (the same figure, graphs (b) to (d)) show higher values of the Fano factor ($0.3 - 0.4$), than what we measured, but on the other hand, especially in fig. 9.10.c, a peak at zero energy is clearly seen as well as the strong fluctuations at positive energies. As a consequence, an important point is that this study also confirms the appearance of a peak at the neutrality point, that we observe.

In summary, our results confirm to some extent the existing theories for current fluctuations in the diffusive graphene as well as the experimental result by Danneau et al. for their diffusive sample and also indirectly the one by DiCarlo et al. On the other hand, they are not able to confirm or refute the results by Tworzydlo et al.

just as it is for the results by Danneau et al. for their ballistic samples, because they were obtained for a different transport regime. Finally, the remarkable peak in the Fano factor at the Dirac point observed in the numerical simulations and in our data would deserve further investigation both theoretically and experimentally. Its elucidation would certainly provide an important insight in the nature of the transport through "puddles" region near the Dirac point.



Figure 9.10: Fano factor in graphene as a function of the injection energy, determined by Logoteta et al. (a) Simulations for a ribbon with $W = 200\,\text{nm}$ and $L = 40\,\text{nm}$ in the absence of potential disorder (red dotted curve), or in the presence of disorder with $n_{\text{imp}} = 5 \times 10^{11}\,\text{cm}^{-2}$ and an amplitude range $\delta = 0.2\,\text{eV}$ (blue solid curve), or with $n_{\text{imp}} = 5 \times 10^{13}\,\text{cm}^{-2}$ and an amplitude range $\delta = 0.02\,\text{eV}$ (green dashed curve), the horizontal dotted line correspond to the value 1/3. (b) Simulations for a rectangular sheet with $W = 200\,\text{nm}$ and $L = 600\,\text{nm}$, $n_{\text{imp}} = 5 \times 10^{11}\,\text{cm}^{-2}$ and with δ equal to $0.5\,\text{eV}$. (c) and (d) Simulations for a square sheet with $W = 200\,\text{nm}$ and $L = 200\,\text{nm}$, $n_{\text{imp}} = 5 \times 10^{11}\,\text{cm}^{-2}$ and with δ equal to $0.16\,\text{eV}$ and $0.5\,\text{eV}$ respectively. From [99].

Conclusion

This thesis investigates transport properties of mono-layer graphene samples, namely conductance (Chapter 7) and quantum shot noise (Chapter 9), which is actually the main purpose of this study. Conductance in the in-plane magnetic field is also studied (Chapter 8).

The starting point, that initially motivated this work, were the evanescence wave theory proposed by Tworzydlo et al. together with two experimental works by DiCarlo et al. and Danneau et al., attempted to verify this theory, since the conclusions of the two latter studies suggested, that a further investigation of this question is required.

In our experiment we intended to improve the experimental conditions of the noise measurement, by applying several techniques, that we describe in Chapter 4. In particular, we use four-point voltage measurement and cross-correlation method, that allow to significantly reduce the contributions of the measurement system to the detected signal. In addition, home-made cryogenic low-noise amplifiers together with band-pass filters were used in this experiment to further improve the experimental conditions.

Following our intentions, a specific graphene-based experimental device, meeting the principles of our measurement approach, was conceived and fabricated. The major originality of this device is the constriction in the center of graphene layer as well as the use of side-gates instead of back-gate, both elements dictated by the ideology of our measurement approach. Device architecture presentation can be found in the section 4.2 of Chapter 4, while its fabrication is described in Chapter 5. Also, the experimental setup was built-up and then the measurement system was thoroughly tuned and calibrated, which however, appeared to be rather difficult.

All these points made the experiment preparation very challenging and time-consuming. As a result, some experiments were left for future research. Nevertheless, quite extensive study of the conductance properties of our sample were carried our at near DC and high frequency ($\approx 3\,\mathrm{MHz}$) in order to well characterize them. In particular, it was shown that transport regime in our sample is diffusive and not ballistic as required. The investigation of noise in this regime is however

not without interest and, as far as we know, no experimental works in this regard except the already mentioned[42, 35] were reported. We thus continued working on this sample and performed noise measurements in order to investigate the Fano factor behaviour as a function of the particles energy.

Although our results answer the initial question only partially, since the ballistic regime was not reached in the present experiment, they are nevertheless of great interest by themselves: they are consistent with the conclusions of Danneau et al. and DiCarlo et al., and moreover shows a good agreement with the theoretical calculations of Fano factor in diffusive graphene. In particular, the peak at Dirac point, predicted by Lewenkopf et al., was observed and merits further investigation. Besides, our data of conductance measurement is also confirmed by the previous results reported in literature.

In addition to that, we demonstrated the importance of the Joule heating in our device. We argued, that the reason for that is dissipation in one of the contacts and evoked different mechanisms of heat transfer in graphene.

Finally, our results proved the advantage of our approach and the conformity of our noise measurement systems to the requirements of the experiment. The principal direction for further development of this project is the improvement of the samples quality first by means of a special very careful annealing and especially by suspending the central part of the graphene layer, containing the constriction. Improvement of amplifiers calibration procedure is also desirable. Also, investigation of noise in Quantum Hall Regime is very attractive kind of experiment.

Appendices

Appendix A

Device Fabrication

A.1 Recipes

A.2 Introduction to Raman scattering

The full description of the Raman scattering process requires a quantum-mechanical treatment. Yet a classical interpretation can also be helpful as it provides a physical intuition for this complex phenomena.

The electric field will polarize the atoms of the matter that will result in a microscopic dipole moments μ which depend on the matter's polarizability α:

$$\mu(t) = \alpha(t)E(t) \tag{A.1}$$

where $E(t)$ is time varying electromagnetic field. In the case of an isotropic medium and if we consider the nucleus frozen, α is just a constant. Thus, an incident electromagnetic wave of angular velocity ω_{i} will induce dipoles, oscillating at the same angular velocity and re-emitting an electromagnetic wave of this angular velocity in an arbitrary direction. This leads to an elastic scattering process, commonly referred as *Rayleigh scattering*.

If instead we take into account the nucleus vibration, the polarizability can not be considered as a time-independent constant any more because it varies with a bond length. Indeed, electrons experience a stronger interaction when tightly surrounded by short-bond nucleus and hence are less perturbed by the electromagnetic field. On the other hand if bonds are long electrons are more easily displaced by the electromagnetic field. Note that the heavy nucleus will not respond to the rapidly changing electromagnetic field.

Given these facts and assuming the motion of nucleus to be that of a classical

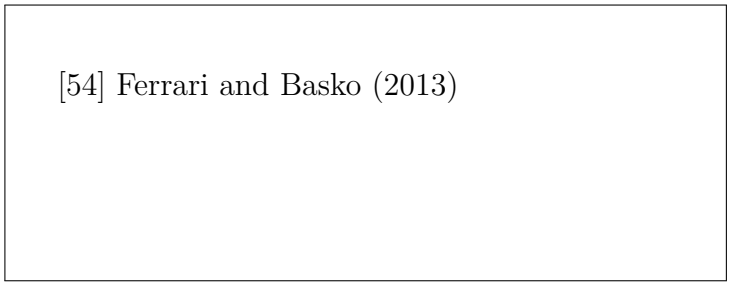

Figure A.1: Rayleigh and Raman scattering in resonant and non resonant conditions. From [54].

harmonic oscillator, we can write:

$$Q(t) = Q_0 \left[e^{\imath \omega_{\mathrm{n}} t + \imath \phi} + \mathrm{c.c.} \right] \tag{A.2}$$

for the coordinate Q of the nucleus oscillating with angular velocity ω_{n}.

Furthermore, in the presence of nuclear modes, the electronic polarizability α can be expressed in terms of the nuclear coordinate Q, and expanded in a Taylor series as follows:

$$\alpha(t) = \alpha_0 + \left(\frac{\delta \alpha}{\delta Q} \right) \Bigg|_{t=0} Q(t) + \dots \tag{A.3}$$

With the incident electromagnetic wave of angular velocity ω_{i} written as $E(t) = Ae^{-\imath \omega_{\mathrm{i}} t} + \mathrm{c.c.}$, the dipole moment is found as:

$$\mu(t) = \alpha_0 A e^{-\imath \omega_{\mathrm{i}} t} + A \left(\frac{\delta \alpha}{\delta Q} \right) \Bigg|_{t=0} Q_0 \left\{ e^{-\imath(\omega_{\mathrm{i}} - \omega_{\mathrm{n}})t + \imath \phi} + e^{-\imath(\omega_{\mathrm{i}} + \omega_{\mathrm{n}})t - \imath \phi} \right\} + \mathrm{c.c.} \tag{A.4}$$

Thence, according to this result the dipole moment will oscillate at several frequencies. The first term on the right-hand side describes the above mentioned elastic Rayleigh scattering, whereas the last term expresses inelastic Raman scattering which as we see shifts the re-emitted radiation frequency to $\omega_{\mathrm{i}} + \omega_{\mathrm{n}}$ and $\omega_{\mathrm{i}} - \omega_{\mathrm{n}}$, called Stokes and anti-Stokes, contributions respectively.

The detailed quantum-mechanical description of this phenomena exploit the perturbation theory and is beyond the scope of this work. In a nutshell, the perturbation induced by the photon of energy $\hbar \omega_i$ increases the energy of the system by the same amount. The new energy level does not necessarily correspond to a stationary state of the system, that is then said to be in a virtual state with a considerably short lifetime. As a result, the system rapidly returns to a new stationary state emitting a photon of different energy $\hbar \omega_s$, while the remaining

energy goes to create (annihilate) one or several vibrational excitations of the system.

The process accompanied by an increase of total energy of the system is referred as Stokes transition, whereas the process of an opposite outcome is referred as anti-Stokes one, additionally the number of created or annihilated phonons gives the order of transition. In thermodynamic equilibrium at low and intermediate temperatures the exited vibrational states are less populated ($\sim$0.7%) than the ground state, so the transition from exited to ground state (anti-Stokes) is of much weaker probability than the opposite Stokes transition. Besides Raman scattering is said to be non-resonant if the system is excited by the incident photon to a virtual (non-stationary state), otherwise it is called resonant.

A.3 Common Nano-fabrication Techniques

In this section conventional micro- and nano-fabrication processes, used in this work are presented.

A.3.1 Microlithography Principle

Lithography is a technique used in micro- and nano-fabrication for transferring patterns onto substrate. Patterns are first transferred to polymer film, commonly referred as *resist*, that will play a role of a mask in the following step, during which the desired process is performed (thin film deposition, chemical or plasma etching, ion implantation etc.) and finally the polymer film as well as eventual excess materials are removed.

Resist is a material, that is sensitive to light of certain wavelength interval or to electron beam, i.e. when exposed to it the resist becomes soluble in a special solution called *developer* (in analogy with photographic developer, the procedure is hence called *development*) and is removed, whereas unexposed portion of the resist remains insoluble. In this case the resist is called positive. If on the contrary, it is the unexposed portion that is removed by developer and the exposed one remains on the substrate, the resist is called negative.

In order, the wafer surface is first cleaned and dehydrated. Next, it is coated with the resist by high speed rotation of the wafer with a small amount of liquid resist, spread over its surface by centrifugal force (spin-coating process) and baked to evaporate the resist solvent. The desired pattern is then exposed on the resist and the resist is developed. As a result one obtains a mask that covers the wafer surface and will protect it during the following process. For instance, during etching such a mask will protect underlying film from etchant action, so only the desired pattern will be removed from substrate surface. Just as during a thin film

deposition the mask will protect the substrate from the film sticking on its surface separating it from the film so that the resist removal will also result in removal of the film on its top (a process called *lift-off*) and only the desired pattern of thin film will remain on the substrate. Of cause, the resist mask must be much thicker than the thin film for a correct result. The resist is usually removed at the end rather easily in a solvent.

A.3.2 Optical and E-Beam lithography

Optical or UV (ultraviolet) lithography as well as electron beam (e-beam) lithography were both used in present work for samples fabrication.

UV lithography is widely used in laboratories and for industrial processes. This is a stencil technique, it consist of illuminating the UV-sensible resist through an optical mask that corresponds to a desired pattern. The resolution of the UV lithography (in terms of the minimum feature size) is limited by the wavelength of the used light as well as by the process-related factors and is typically under 1 µm, the most advanced tools claiming minimum feature size down to 50 nm. Exposure systems also allow to align the mask with the wafer to precisely place the pattern. The advantage of this technique is its throughput and relative ease of operation, it is extremely handy for transferring the same pattern several times. However its minimal resolution and alignment precision can be a limitation in certain cases and it is absolutely not suitable if one needs to modify the pattern from one exposure to another, for a new mask has to be manufactured each time.

E-beam lithography allows a much lower resolution than optical one and has a higher alignment precision. Moreover it does not require any physical mask and is hence suitable for tasks with often pattern modification. Yet its throughput is very low as compared to optical lithography, that also makes it vulnerable to beam drift or instabilities during wide area exposures which usually take a long time. The electron beam is produced by field electron emission from a heated filament and focused on sample by several magnetic and electrostatic lenses, while the stage, controlled by a special software, is displacing the sample to produce a desired pattern. Even though the beam width of such a system is mostly limited by the electron optics abilities, the pattern resolution is limited by incident electrons scattering in the resist, that will enlarge the effect of the beam on the resist, whereas the minimal distance between two features is limited by so called proximity effect. This effect is due to the secondary electrons created by inelastic scattering of the incident electrons. Secondary electrons can propagate far from the irradiated area in any direction, thus the effect of secondary electrons from two neighbouring areas can be sufficient to affect the resist separating them. This effect can be important depending on resists and on incident electrons energy on the distances between 30 nm and 100 nm. So one should beware of this effect while designing

dense patterns.

A.3.3 Thin Films Deposition

In present work only metallic thin films deposition was required and Physical Vapour Deposition (PVD) technique was used for this purpose. The principle of this technique, which involves purely physical processes, is that the source material (target) is evaporated at high temperature and in high vacuum conditions and subsequently condensed on the desired surface. Various methods are possible for transforming the target material into the gaseous phase, including laser pulse (ablation) or plasma discharge (sputtering). In our case Joule heating and electron beam methods were used. In the former case, the target is heated by passing a high current through a resistive crucible, in which it is contained, whereas in the latter the target material is heated by electron bombardment, that allows deposition at very low (as low as 1 nm/min) and much better controlled deposition rates.

Besides, not all materials stick enough well to the substrate surface, so in order to reinforce the adhesion an intermediate thin layer is used. For instance, for gold deposition on $Si\backslash SiO_2$ substrate titanium or chromium adhesion layer is commonly used.

Appendix B

Measurement System

B.1 Cryogenic Inset

In our experiment, the device, as well as a part of the measurement system are situated inside the *Variable Temperature Inset*, placed in He^4 bath, provided thanks to *Oxford* dewar, which is also equipped by a magnet allowing to obtain magnetic fields up to $\simeq 7.5\,T$. Inside the inset vacuum can be attained or exchange gas (He^4) can be used to accelerate the thermal exchange with the bath while cooling or with the room atmosphere, while returning to the room temperature. In addition, the inset has a 1 K pot that can cool the device down to $\approx 1.5\,K$ (not used in this work). Another important elements of the inset are:

- 4 K thermalization board, thanks to which most of the cryogenic coaxial cables (manufacturer *Lakeshore*) are thermalized. The cryogenic amplifiers outputs are connected to the room temperature through the stainless sill rigid coaxial cables.
- Separate thermalization board on which the amplifiers are placed
- Low temperature stage, connected directly to the 1 K pot, on which the sample holder with the device is placed.
- Two thermometers (*Cernox* resistors, temperature range: from 1.4 K to 420 K.

B.2 Data Acquisition Module

The data acquisition module is based on two channels *Spectrum M2i.3011-exp* analog-to-digital conversion board and allows to perform the phase sensitive



Figure B.1: Design of the cryogenic inset.

Table B.1: Technical characteristics of the *Spectrum M2i.3011-exp* board.

Resolution	12 bit
Number of Channels	2
Maximum Sampling Rate	40 MSamples/s
Input impedance	$50\,\Omega/1\,\mathrm{M}\Omega$ [1]
On-board Memory	1024 Mbytes
Min/Max Input Ranges	$\pm 0.1\,\mathrm{V}/\pm 1\,\mathrm{V}$

detection (with an external AC source) as well as the noise power spectral density measurement (auto- and crosscorrelation). The main technical characteristics of the board are given on table B.1.

The graphic user interface, realized in the *LabView* environment, allows to configure the acquisition parameters, such as the number of operating channels, sampling rate, number of samples per block, input range or impedance. All other instruments, used in the experiment, are also controlled through this interface. The board configuration, data acquisition and transfer to the PC memory are all done by the external DLL[2]. For the noise power spectral density measurement this DLL was specially modified and the auto-/crosscorrelation calculation based on the FFTW package as well as the running spectra averaging were added to optimize the measurement speed.

Phase Sensistive Detection with the A/D Board. Excitation signal is generated by an external source and is detected by the A/D board directly at the source output (reference signal). Simultaneously, the response of the circuit containing the sample to the excitation driven through it is detected by the remaining channel of the A/D board (response signal).

We note reference signal as $V_{\mathrm{R}}\cos(\omega t)$ (zero phase is thus defined), response signals as $V_{\mathrm{M}}\cos(\omega t + \delta\phi)$, $\delta\phi$ being the phase shift, introduced by the circuit. In addition, the response signal is eventually accompanied by the noise δV (often much stronger than the former).

[1] Can be selected via the software

[2] Dynamic Link Library

Following time averages are calculated:

$$A_0 = \left\langle (V_{\mathrm{R}} \cos(\omega t))^2 \right\rangle = \frac{V_{\mathrm{R}}^2}{2} \left\langle 1 + \cos(\omega t) \right\rangle \tag{B.1}$$

$$\begin{aligned} A_1 =& \left\langle V_{\mathrm{R}} \cos(\omega t) \times (V_{\mathrm{M}} \cos(\omega t + \delta\phi) + \delta V) \right\rangle \\ =& \frac{V_{\mathrm{R}} V_{\mathrm{M}}}{2} \left\langle (\cos\delta\phi + \cos(2\omega t + \delta\phi)) \right\rangle + \langle V_{\mathrm{R}} \cos(\omega t) \delta V \rangle \end{aligned} \tag{B.2}$$

$$\begin{aligned} A_2 =& \left\langle V_{\mathrm{R}} \cos(\omega t + \frac{\pi}{2}) \times (V_{\mathrm{M}} \cos(\omega t + \delta\phi) + \delta V) \right\rangle \\ =& \frac{V_{\mathrm{R}} V_{\mathrm{M}}}{2} \left\langle (\sin\delta\phi + \sin(2\omega t + \delta\phi)) \right\rangle + \langle V_{\mathrm{R}} \sin(\omega t) \delta V \rangle \end{aligned} \tag{B.3}$$

($\frac{\pi}{2}$ phase shift is done numerically). It is clear that the oscillating terms as well as the noise terms average out and only constant terms remain. From A_0 the reference signal amplitude can be found (or confirmed), while two other averages yield

$$\delta\phi = \arctan\left(\frac{A_2}{A_1}\right) \tag{B.4}$$

that also allows to determine V_{M} from above relations.

Noise Spectral Density Calculation. The measured fluctuations δV_0 and δV_1 are detected by the two channels of the A/D board and are sampled by it at the sampling rate f_{s} into two blocks of N samples each. The FFT of each block $\delta\tilde{V}_0$ and $\delta\tilde{V}_1$ is computed using the FFTW package. The autocorrelation of each signal is then calculated as

$$S_{00} = 2|\delta\tilde{V}_0|^2/(N f_{\mathrm{s}}) \quad \text{and} \quad S_{11} = 2|\delta\tilde{V}_1|^2/(N f_{\mathrm{s}}) \tag{B.5}$$

as well as the crosscorrelation (which eventually can contain also a non-zero imaginary part):

$$S_{01} = 2(\delta\tilde{V}_0^* \delta\tilde{V}_1)/(N f_{\mathrm{s}}) \tag{B.6}$$

The data blocks are thus processed one after another and the running average of S_{00}, S_{11} and S_{01} are calculated until the required precision is reached.

B.3 RLC-Filter Pass-Band Calculation

Let us fist examine the problem of the inductor series resistance. Despite the skin effect this resistance is usually still very weak even at high frequencies of the order of several tens of ohms. Consider two circuits presented on fig. B.2. Our

goal is to find the value of R at which the impedances of both circuits are equal. We write

$$\frac{R\imath\omega L}{R\imath\omega L} = \imath\omega L + r \tag{B.7}$$

We equalize the real and the imaginary parts separately

$$r = \frac{R\omega^2 L^2}{R^2 + \omega^2 L^2}, \qquad \frac{R^2}{R^2 + \omega^2 L^2} = 1 \tag{B.8}$$

The second equation can only be satisfied if $R^2 \gg \omega^2 L^2$ or in other terms $\omega^2 L^2 \gg r^2$, which is indeed the case for a 22 µF inductor at 3 MHz (impedance of 200 Ω) with typical series resistance $r = 10\,\Omega$.

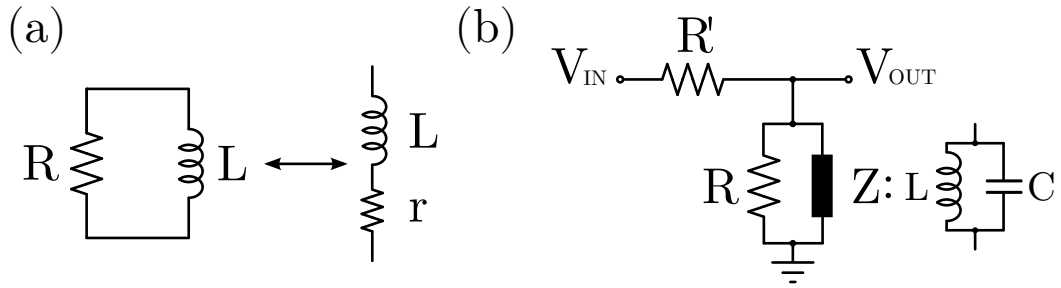

Figure B.2: (a) Original series circuit (right) and equivalent parallel circuit (left) of the same impedance for derivation of the equivalent resistance R. (b) Equivalent circuit for RLC filter response calculation, impedance Z stands for parallel inductor and capacitor.

In the following we calculate the response of a RLC filter, presented on **??**. First, obviously the following relations hold

$$\frac{V_{\text{OUT}}}{V_{\text{IN}}} = \frac{RZ}{R'(R+Z) + RZ}, \qquad Z = \frac{\imath\omega L}{1 - \omega^2 LC} \tag{B.9}$$

These relations yield

$$\begin{aligned} \frac{V_{\text{OUT}}}{V_{\text{IN}}} =& \frac{R}{R+R'} \frac{1}{1 - \imath\frac{RR'}{R+R'}C\left(1/(LC) - \omega^2\right)/\omega} \\ =& A \frac{1}{1 + \imath(\omega^2 - \omega_0^2)/(\omega\Gamma)} \end{aligned} \tag{B.10}$$

with

$$A = \frac{R}{R+R'}, \quad \Gamma = \frac{R+R'}{RR'C}, \quad \text{and} \quad \omega_0 = 1/\sqrt{LC} \tag{B.11}$$

if we go back to the notation used in Chapter 9. When squared, this leads to

$$\frac{V_{\text{OUT}}}{V_{\text{IN}}} = \frac{A^2}{1 + \left(\omega^2 - \omega_0^2\right)^2 / (\omega\Gamma)^2} \tag{B.12}$$

Now if the cross-correlation of two signals V^1_{OUT} and V^2_{OUT} after two filters with different parameters ω_1, Γ_1 and ω_2, Γ_2 is calculated, we have to take (asterisk stands for the complex conjugate):

$$\begin{aligned}\left|\frac{V^1_{\text{OUT}}}{V^1_{\text{IN}}}\left(\frac{V^2_{\text{OUT}}}{V^2_{\text{IN}}}\right)^*\right| &= \left|\frac{A_1}{1 + \imath(\omega^2 - \omega_1^2)/(\omega\Gamma_1)}\frac{A_2}{1 + \imath(\omega^2 - \omega_2^2)/(\omega\Gamma_2)}\right| \\ &= \frac{A_1 A_2}{1 + \frac{\Gamma_2^2(\omega^2-\omega_1^2)^2 + \Gamma_1^2(\omega^2-\omega_2^2)^2}{\omega^2\Gamma_1^2\Gamma_2^2} + \frac{(\omega^2-\omega_1^2)^2(\omega^2-\omega_2^2)^2}{\omega^4\Gamma_1^2\Gamma_2^2}}.\end{aligned} \tag{B.13}$$

Bibliography

[1] D. A. Abanin and L S Levitov. Quantized Transport in Graphene p-n Junctions in a Magnetic Field. Science (New York, N.Y.), 317(5838): 641–3, August 2007. ISSN 1095-9203. doi: 10.1126/science.1144672. URL http://www.ncbi.nlm.nih.gov/pubmed/17600182.

[2] Shaffique Adam, E H Hwang, V M Galitski, and S. Das Sarma. A self-consistent theory for graphene transport. Proceedings of the National Academy of Sciences of the United States of America, 104(47):18392–7, November 2007. ISSN 1091-6490. doi: 10.1073/pnas.0704772104. URL http://www.pubmedcentral.nih.gov/articlerender.fcgi?artid=2141788&tool=pmcentrez&rendertype=abstracthttp://www.pnas.org/content/104/47/18392.abstract.

[3] B. L. Al'tshuler, A. G. Aronov, and B. Z. Spivak. The Aaronov-Bohm effect in disordered conductors. JETP Letters, 33(2):94–97, 1981.

[4] Shaahin Amini, Javier Garay, Guanxiong Liu, Alexander a. Balandin, and Reza Abbaschian. Growth of large-area graphene films from metal-carbon melts. Journal of Applied Physics, 108(9):094321, 2010. ISSN 00218979. doi: 10.1063/1.3498815. URL http://link.aip.org/link/JAPIAU/v108/i9/p094321/s1&Agg=doi.

[5] a.N. Obraztsov, E.a. Obraztsova, a.V. Tyurnina, and a.a. Zolotukhin. Chemical vapor deposition of thin graphite films of nanometer thickness. Carbon, 45(10):2017–2021, September 2007. ISSN 00086223. doi: 10.1016/j.carbon.2007.05.028. URL http://linkinghub.elsevier.com/retrieve/pii/S0008622307002965.

[6] C D Anderson. THE APPARENT EXISTENCE OF EASILY DEFLECTABLE POSITIVES. Science (New York, N.Y.), 76(1967):238–9, September 1932. ISSN 0036-8075. doi: 10.1126/science.76.1967.238. URL http://www.sciencemag.org/content/76/1967/238.

[7] C. W. J. Beenakker and H. van Houten. Quantum Transport in Semiconductor Nanostructures. Solid State Physics, 44:1–228, December 1991. URL http://arxiv.org/abs/cond-mat/0412664.

[8] K. Bennaceur. Transport électronique dans le graphène. PhD thesis, 2011.

[9] K. Bennaceur, P. Jacques, F. Portier, P. Roche, and D. C. Glattli. Unveiling quantum Hall transport by Efros-Shklovskii to Mott variable-range hopping transition in graphene. Physical Review B, 86(8):085433, August 2012. ISSN 1098-0121. doi: 10.1103/PhysRevB.86.085433. URL http://link.aps.org/doi/10.1103/PhysRevB.86.085433.

[10] J Berezovsky, M F Borunda, E J Heller, and R M Westervelt. Imaging coherent transport in graphene. Part I: mapping universal conductance fluctuations. Nanotechnology, 21(27):274013, July 2010. ISSN 1361-6528. doi: 10.1088/0957-4484/21/27/274013. URL http://www.ncbi.nlm.nih.gov/pubmed/20571200.

[11] Claire Berger, Zhimin Song, Tianbo Li, Xuebin Li, Asmerom Y Ogbazghi, Rui Feng, Zhenting Dai, Alexei N Marchenkov, Edward H Conrad, Phillip N First, and Walt A. de Heer. Ultrathin Epitaxial Graphite: 2D Electron Gas Properties and a Route toward Graphene-based Nanoelectronics. The Journal of Physical Chemistry B, 108(52):19912–19916, December 2004. ISSN 1520-6106. doi: 10.1021/jp040650f. URL http://pubs.acs.org/doi/abs/10.1021/jp040650f.

[12] M. V. Berry and R. J. Mondragon. Neutrino Billiards: Time-Reversal Symmetry-Breaking Without Magnetic Fields. Proceedings of the Royal Society of London. Series A, Mathematical and Physical Sciences (1934-1990), 412(1842):53–74, 1987. ISSN 0080-4630. doi: 10.1098/rspa.1987.0080. URL http://rspa.royalsocietypublishing.org/cgi/doi/10.1098/rspa.1987.0080.

[13] P. Blake, E. W. Hill, A. H. Castro Neto, K. S. Novoselov, D. Jiang, R. Yang, T. J. Booth, and A. K. Geim. Making graphene visible. Applied Physics Letters, 91(6):063124, 2007. ISSN 00036951. doi: 10.1063/1.2768624. URL http://link.aip.org/link/APPLAB/v91/i6/p063124/s1&Agg=doi.

[14] Ya. M. Blanter and M. Büttiker. Shot Noise in Mesoscopic Conductors. Physics Reports, 336(1-2):1–166, October 1999. ISSN 03701573. doi: 10.1016/S0370-1573(99)00123-4. URL http://arxiv.org/abs/cond-mat/9910158.

[15] K.I. Bolotin, K.J. Sikes, Z. Jiang, M. Klima, G. Fudenberg, J. Hone, P. Kim, and H.L. Stormer. Ultrahigh electron mobility in suspended graphene. Solid State Communications, 146(9-10):351–355, June 2008. ISSN 00381098. doi: 10.1016/j.ssc.2008.02.024. URL http://linkinghub.elsevier.com/retrieve/pii/S0038109808001178.

[16] M. Büttiker. Four-Terminal Phase-Coherent Conductance. Physical Review Letters, 57(14):1761–1764, October 1986. ISSN 0031-9007. doi: 10.1103/PhysRevLett.57.1761. URL http://link.aps.org/doi/10.1103/PhysRevLett.57.1761.

[17] M. Büttiker. Absence of backscattering in the quantum Hall effect in multiprobe conductors. Physical Review B, 38(14):9375–9389, November 1988. ISSN 0163-1829. doi: 10.1103/PhysRevB.38.9375. URL http://link.aps.org/doi/10.1103/PhysRevB.38.9375.

[18] M. Büttiker. Scattering theory of current and intensity noise correlations in conductors and wave guides. Physical Review B, 46(19):12485–12507, November 1992. ISSN 0163-1829. doi: 10.1103/PhysRevB.46.12485. URL http://link.aps.org/doi/10.1103/PhysRevB.46.12485.

[19] M. Büttiker, Y. Imry, and R. Landauer. Josephson behavior in small normal one-dimensional rings. Physics Letters A, 96(7):365–367, 1983. URL http://www.sciencedirect.com/science/article/pii/0375960183900117.

[20] M. Büttiker, Y. Imry, R. Landauer, and S. Pinhas. Generalized many-channel conductance formula with application to small rings. Physical Review B, 31 (10):6207–6215, May 1985. ISSN 0163-1829. doi: 10.1103/PhysRevB.31.6207. URL http://link.aps.org/doi/10.1103/PhysRevB.31.6207.

[21] V E Calado, Shou-en Zhu, S Goswami, Q Xu, K Watanabe, T Taniguchi, and G C A M Janssen. Ballistic transport in graphene grown by chemical vapor deposition. Applied Physics Letters, 104(2), 2014. doi: 10.1063/1.4861627.

[22] F. Camino, Wei Zhou, and V. Goldman. Quantum transport in electron Fabry-Perot interferometers. Physical Review B, 76(15):155305, October 2007. ISSN 1098-0121. doi: 10.1103/PhysRevB.76.155305. URL http://link.aps.org/doi/10.1103/PhysRevB.76.155305.

[23] L G Cançado, a Jorio, E H Martins Ferreira, F Stavale, C a Achete, R B Capaz, M V O Moutinho, a Lombardo, T S Kulmala, and a C Ferrari. Quantifying defects in graphene via Raman spectroscopy at different excitation energies. Nano letters, 11(8):3190–6, August 2011. ISSN 1530-6992. doi: 10.1021/nl201432g. URL http://www.ncbi.nlm.nih.gov/pubmed/21696186.

[24] C. Casiraghi, S. Pisana, K. S. Novoselov, a. K. Geim, and a. C. Ferrari. Raman fingerprint of charged impurities in graphene. Applied Physics Letters, 91(23):233108, 2007. ISSN 00036951. doi: 10.1063/1.2818692. URL http://link.aip.org/link/APPLAB/v91/i23/p233108/s1&Agg=doi.

[25] C Casiraghi, a Hartschuh, H Qian, S Piscanec, C Georgi, a Fasoli, K S Novoselov, D M Basko, and a C Ferrari. Raman spectroscopy of graphene edges. Nano letters, 9(4):1433–41, April 2009. ISSN 1530-6992. doi: 10.1021/nl8032697. URL http://www.ncbi.nlm.nih.gov/pubmed/19290608.

[26] A. H. Castro Neto, F. Guinea, N. M R Peres, K. S. Novoselov, and A. K. Geim. The electronic properties of graphene. Reviews of Modern Physics, 81(1):109–162, January 2009. ISSN 0034-6861. doi: 10.1103/RevModPhys.81.109. URL http://link.aps.org/doi/10.1103/RevModPhys.81.109.

[27] J.-H. Chen, C. Jang, S. Adam, M. S. Fuhrer, E. D. Williams, and M. Ishigami. Charged-impurity scattering in graphene. Nature Physics, 4(5):377–381, April 2008. ISSN 1745-2473. doi: 10.1038/nphys935. URL http://dx.doi.org/10.1038/nphys935.

[28] Wei Chen and Aashish a. Clerk. Electron-phonon mediated heat flow in disordered graphene. Physical Review B, 86(12):125443, September 2012. ISSN 1098-0121. doi: 10.1103/PhysRevB.86.125443. URL http://link.aps.org/doi/10.1103/PhysRevB.86.125443.

[29] Yung-Fu Chen, Myung-Ho Bae, Cesar Chialvo, Travis Dirks, Alexey Bezryadin, and Nadya Mason. Magnetoresistance in single-layer graphene: weak localization and universal conductance fluctuation studies. Journal of physics. Condensed matter : an Institute of Physics journal, 22(20):205301, May 2010. ISSN 1361-648X. doi: 10.1088/0953-8984/22/20/205301. URL http://www.ncbi.nlm.nih.gov/pubmed/21393703.

[30] B. Chenaud, C. Chaubet, B. Jouault, L. Saminadayar, D. Mailly, G. Faini, and A. Cavanna. Edge states interferometer: an electronic Fabry–Perot. Physica B: Condensed Matter, 346:488–492, 2004. URL http://www.sciencedirect.com/science/article/pii/S0921452604001383.

[31] Rui Cheng, Jingwei Bai, Lei Liao, Hailong Zhou, Yu Chen, Lixin Liu, Yung-Chen Lin, Shan Jiang, Yu Huang, and Xiangfeng Duan. High-frequency self-aligned graphene transistors with transferred gate stacks. Proceedings of the National Academy of Sciences of the United States of America, 109 (29):11588–92, July 2012. ISSN 1091-6490. doi: 10.1073/pnas.1205696109. URL http://www.pubmedcentral.nih.gov/articlerender.fcgi?artid=

3406869&tool=pmcentrez&rendertype=abstracthttp://www.pnas.org/cgi/content/long/1205696109v1.

[32] Artur Ciesielski and Paolo Samorì. Graphene via sonication assisted liquid-phase exfoliation. Chemical Society reviews, 43(1):381–98, January 2014. ISSN 1460-4744. doi: 10.1039/c3cs60217f. URL http://pubs.rsc.org/en/content/articlehtml/2013/cs/c3cs60217f.

[33] Chunxiao Cong, Ting Yu, and Haomin Wang. Raman study on the g mode of graphene for determination of edge orientation. ACS nano, 4(6):3175–80, June 2010. ISSN 1936-086X. doi: 10.1021/nn100705n. URL http://www.ncbi.nlm.nih.gov/pubmed/20446715.

[34] Johann Coraux, Alpha T N'Diaye, Carsten Busse, and Thomas Michely. Structural coherency of graphene on Ir(111). Nano letters, 8(2):565–70, February 2008. ISSN 1530-6984. doi: 10.1021/nl0728874. URL http://www.ncbi.nlm.nih.gov/pubmed/18189442.

[35] R. Danneau, M. F. Craciun, S. Russo, M. Y Tomi, J. Salmilehto, A. F. Morpurgo, P. J Hakonen, and F. Wu. Shot Noise in Ballistic Graphene. Physical Review Letters, 100(19), May 2008. ISSN 0031-9007. doi: 10.1103/PhysRevLett.100.196802. URL http://prl.aps.org/abstract/PRL/v100/i19/e196802http://arxiv.org/abs/0711.4306v2.

[36] a Das, S Pisana, B Chakraborty, S Piscanec, S K Saha, U V Waghmare, K S Novoselov, H R Krishnamurthy, a K Geim, a C Ferrari, and a K Sood. Monitoring dopants by Raman scattering in an electrochemically top-gated graphene transistor. Nature nanotechnology, 3(4):210–5, April 2008. ISSN 1748-3395. doi: 10.1038/nnano.2008.67. URL http://www.ncbi.nlm.nih.gov/pubmed/18654505.

[37] S. Das Sarma, Shaffique Adam, E. H. Hwang, and Enrico Rossi. Electronic transport in two-dimensional graphene. Reviews of Modern Physics, 83(2):407–470, May 2011. ISSN 0034-6861. doi: 10.1103/RevModPhys.83.407. URL http://link.aps.org/doi/10.1103/RevModPhys.83.407.

[38] M. de Jong and C. Beenakker. Mesoscopic fluctuations in the shot-noise power of metals. Physical Review B, 46(20):13400–13406, November 1992. ISSN 0163-1829. doi: 10.1103/PhysRevB.46.13400. URL http://link.aps.org/doi/10.1103/PhysRevB.46.13400.

[39] R. Deacon, K.-C. Chuang, R. Nicholas, K. S. Novoselov, and A. Geim. Cyclotron resonance study of the electron and hole velocity in graphene monolayers. Physical Review B, 76(8):081406, August 2007. ISSN 1098-0121. doi:

10.1103/PhysRevB.76.081406. URL http://link.aps.org/doi/10.1103/PhysRevB.76.081406.

[40] C. R. Dean, A. F. Young, I Meric, C Lee, L Wang, S Sorgenfrei, K Watanabe, T Taniguchi, P Kim, K L Shepard, and J Hone. Boron nitride substrates for high-quality graphene electronics. Nature nanotechnology, 5(10):722–6, October 2010. ISSN 1748-3395. doi: 10.1038/nnano.2010.172. URL http://www.ncbi.nlm.nih.gov/pubmed/20729834.

[41] C. R. Dean, A. F. Young, P. Cadden-Zimansky, L. Wang, H. Ren, K. Watanabe, T. Taniguchi, P. Kim, J. Hone, and K. L. Shepard. Multicomponent fractional quantum Hall effect in graphene. Nature Physics, 7(9):693–696, May 2011. ISSN 1745-2473. doi: 10.1038/nphys2007. URL http://www.nature.com/doifinder/10.1038/nphys2007.

[42] L. DiCarlo, J. R. Williams, Yiming Zhang, D. T McClure, and C. M Marcus. Shot Noise in Graphene. Physical Review Letters, 100(15):2–5, April 2008. ISSN 0031-9007. doi: 10.1103/PhysRevLett.100.156801. URL http://link.aps.org/doi/10.1103/PhysRevLett.100.156801http://arxiv.org/abs/0711.3206v3.

[43] P. A. M. Dirac. The Quantum Theory of the Electron. Proceedings of the Royal Society of London. Series A, 117(778):610–624, February 1928. ISSN 1364-5021. doi: 10.1098/rspa.1928.0023. URL http://rspa.royalsocietypublishing.org/cgi/doi/10.1098/rspa.1928.0023http://rspa.royalsocietypublishing.org/content/117/778/610.short.

[44] ON Dorokhov. On the coexistence of localized and extended electronic states in the metallic phase. Solid state communications, 51(6):381–384, 1984. URL http://www.sciencedirect.com/science/article/pii/0038109884901170.

[45] Xu Du, Ivan Skachko, Anthony Barker, and Eva Y Andrei. Approaching ballistic transport in suspended graphene. Nature nanotechnology, 3(8):491–5, August 2008. ISSN 1748-3395. doi: 10.1038/nnano.2008.199. URL http://dx.doi.org/10.1038/nnano.2008.199.

[46] T J Echtermeyer, L Britnell, P K Jasnos, A Lombardo, R V Gorbachev, A N Grigorenko, A K Geim, A. C Ferrari, and K. S. Novoselov. Strong plasmonic enhancement of photovoltage in graphene. Nature communications, 2:458, January 2011. ISSN 2041-1723. doi: 10.1038/ncomms1464. URL http://www.nature.com/ncomms/journal/v2/n8/pdf/ncomms1464.pdf?WT.ec_id=NCOMMS-201108.

[47] V. Eless, T. Yager, S. Spasov, S. Lara-Avila, R. Yakimova, S. Kubatkin, T. J. B. M. Janssen, a. Tzalenchuk, and V. Antonov. Phase coherence and energy relaxation in epitaxial graphene under microwave radiation. Applied Physics Letters, 103(9):093103, 2013. ISSN 00036951. doi: 10.1063/1.4819726. URL http://link.aip.org/link/APPLAB/v103/i9/p093103/s1&Agg=doi.

[48] Konstantin V Emtsev, Aaron Bostwick, Karsten Horn, Johannes Jobst, Gary L Kellogg, Lothar Ley, Jessica L McChesney, Taisuke Ohta, Sergey a Reshanov, Jonas Röhrl, Eli Rotenberg, Andreas K Schmid, Daniel Waldmann, Heiko B Weber, and Thomas Seyller. Towards wafer-size graphene layers by atmospheric pressure graphitization of silicon carbide. Nature materials, 8(3):203–7, March 2009. ISSN 1476-1122. doi: 10.1038/nmat2382. URL http://www.ncbi.nlm.nih.gov/pubmed/19202545.

[49] Daejin Eom, Deborah Prezzi, Kwang Taeg Rim, Hui Zhou, Michael Lefenfeld, Shengxiong Xiao, Colin Nuckolls, Mark S Hybertsen, Tony F Heinz, and George W Flynn. Structure and electronic properties of graphene nanoislands on Co(0001). Nano letters, 9(8):2844–8, August 2009. ISSN 1530-6992. doi: 10.1021/nl900927f. URL http://www.ncbi.nlm.nih.gov/pubmed/19630380.

[50] Benjamin E. Feldman, Benjamin Krauss, Jurgen H Smet, and Amir Yacoby. Unconventional sequence of fractional quantum Hall states in suspended graphene. Science (New York, N.Y.), 337(6099):1196–9, September 2012. ISSN 1095-9203. doi: 10.1126/science.1224784. URL http://www.sciencemag.org/content/337/6099/1196.

[51] A. C Ferrari, J. C Meyer, V. Scardaci, C. Casiraghi, M. Lazzeri, F. Mauri, S. Piscanec, D. Jiang, K. S. Novoselov, S. Roth, and A. K. Geim. Raman Spectrum of Graphene and Graphene Layers. Physical Review Letters, 97(18):1–4, October 2006. ISSN 0031-9007. doi: 10.1103/PhysRevLett.97.187401. URL http://link.aps.org/doi/10.1103/PhysRevLett.97.187401http://prl.aps.org/abstract/PRL/v97/i18/e187401.

[52] Andrea C. Ferrari. Raman spectroscopy of graphene and graphite: Disorder, electron–phonon coupling, doping and nonadiabatic effects. Solid State Communications, 143(1-2):47–57, July 2007. ISSN 00381098. doi: 10.1016/j.ssc.2007.03.052. URL http://linkinghub.elsevier.com/retrieve/pii/S0038109807002967.

[53] Andrea C Ferrari and Denis M Basko. Raman spectroscopy as a versatile tool for studying the properties of graphene. Nature nanotechnology, 8(4):

235–46, April 2013. ISSN 1748-3395. doi: 10.1038/nnano.2013.46. URL http://www.ncbi.nlm.nih.gov/pubmed/23552117.

[54] Andrea C Ferrari and Denis M Basko. Supplementary information for "Raman spectroscopy as a versatile tool for studying the properties of graphene". Nature nanotechnology, 8(4):235–46, April 2013. ISSN 1748-3395. doi: 10.1038/nnano.2013.46. URL http://www.ncbi.nlm.nih.gov/pubmed/23552117.

[55] Kin Chung Fong, Emma E. Wollman, Harish Ravi, Wei Chen, Aashish a. Clerk, M. D. Shaw, H. G. Leduc, and K. C. Schwab. Measurement of the Electronic Thermal Conductance Channels and Heat Capacity of Graphene at Low Temperature. Physical Review X, 3(4):041008, October 2013. ISSN 2160-3308. doi: 10.1103/PhysRevX.3.041008. URL http://link.aps.org/doi/10.1103/PhysRevX.3.041008.

[56] Slaven Garaj, William Hubbard, and J a Golovchenko. Graphene synthesis by ion implantation. Applied physics letters, 97(18): 183103, November 2010. ISSN 0003-6951. doi: 10.1063/1.3507287. URL http://www.pubmedcentral.nih.gov/articlerender.fcgi?artid=2994927&tool=pmcentrez&rendertype=abstract.

[57] Jorge M. Garcia, Ulrich Wurstbauer, Antonio Levy, Loren N. Pfeiffer, Aron Pinczuk, Annette S. Plaut, Lei Wang, Cory R. Dean, Roberto Buizza, Arend M. Van Der Zande, James Hone, Kenji Watanabe, and Takashi Taniguchi. Graphene growth on h-BN by molecular beam epitaxy. Solid State Communications, 152(12):975–978, June 2012. ISSN 00381098. doi: 10.1016/j.ssc.2012.04.005. URL http://linkinghub.elsevier.com/retrieve/pii/S0038109812002013.

[58] a K Geim and K S Novoselov. The rise of graphene. Nature materials, 6 (3):183–91, March 2007. ISSN 1476-1122. doi: 10.1038/nmat1849. URL http://www.ncbi.nlm.nih.gov/pubmed/17330084.

[59] S. M. Girvin. The Quantum Hall Effect: Novel Excitations and Broken Symmetries. Number July 1998. July 1998. URL http://arxiv.org/abs/cond-mat/9907002.

[60] D. C. Glattli. Quantum shot noise of conductors and general noise measurement methods. The European Physical Journal Special Topics, 172(1):163–179, June 2009. ISSN 1951-6355. doi: 10.1140/epjst/e2009-01049-y. URL http://www.springerlink.com/index/10.1140/epjst/e2009-01049-y.

[61] M. O. Goerbig. Quantum Hall Effects. 2009.

[62] D. Graf, F. Molitor, T. Ihn, and K. Ensslin. Phase-coherent transport measured in a side-gated mesoscopic graphite wire. Physical Review B, 75(24): 245429, June 2007. ISSN 1098-0121. doi: 10.1103/PhysRevB.75.245429. URL http://link.aps.org/doi/10.1103/PhysRevB.75.245429.

[63] Awnish K Gupta, Timothy J Russin, Humberto R Gutiérrez, and Peter C Eklund. Probing graphene edges via Raman scattering. ACS nano, 3(1): 45–52, January 2009. ISSN 1936-086X. doi: 10.1021/nn8003636. URL http://www.ncbi.nlm.nih.gov/pubmed/19206247.

[64] B. Halperin. Quantized Hall conductance, current-carrying edge states, and the existence of extended states in a two-dimensional disordered potential. Physical Review B, 25(4):2185–2190, February 1982. ISSN 0163-1829. doi: 10.1103/PhysRevB.25.2185. URL http://link.aps.org/doi/10.1103/PhysRevB.25.2185.

[65] J. Hass, R. Feng, T. Li, X. Li, Z. Zong, W. a. de Heer, P. N. First, E. H. Conrad, C. a. Jeffrey, and C. Berger. Highly ordered graphene for two dimensional electronics. Applied Physics Letters, 89(14):143106, 2006. ISSN 00036951. doi: 10.1063/1.2358299. URL http://link.aip.org/link/APPLAB/v89/i14/p143106/s1&Agg=doi.

[66] J. Hass, F. Varchon, J. Millán-Otoya, M. Sprinkle, N. Sharma, W. de Heer, C. Berger, P. First, L. Magaud, and E. Conrad. Why Multilayer Graphene on 4H-SiC(0001^{-}) Behaves Like a Single Sheet of Graphene. Physical Review Letters, 100(12):125504, March 2008. ISSN 0031-9007. doi: 10.1103/PhysRevLett.100.125504. URL http://link.aps.org/doi/10.1103/PhysRevLett.100.125504.

[67] R. Haug, A. MacDonald, P. Streda, and K. von Klitzing. Quantized Multichannel Magnetotransport through a Barrier in Two Dimensions. Physical Review Letters, 61(24):2797–2800, December 1988. ISSN 0031-9007. doi: 10.1103/PhysRevLett.61.2797. URL http://link.aps.org/doi/10.1103/PhysRevLett.61.2797.

[68] Ranjit Hawaldar, P Merino, M R Correia, Igor Bdikin, José Grácio, J Méndez, J a Martín-Gago, and Manoj Kumar Singh. Large-area high-throughput synthesis of monolayer graphene sheet by Hot Filament Thermal Chemical Vapor Deposition. Scientific reports, 2: 682, January 2012. ISSN 2045-2322. doi: 10.1038/srep00682.

URL http://www.pubmedcentral.nih.gov/articlerender.fcgi?artid=3448070&tool=pmcentrez&rendertype=abstract.

[69] J. Hone. Graphene nanoelectromechanical systems. Proceedings of the IEEE, 101(7):1766–1779, July 2013. ISSN 0018-9219. doi: 10.1109/JPROC.2013.2253291. URL http://ieeexplore.ieee.org/lpdocs/epic03/wrapper.htm?arnumber=6523077.

[70] B. Huard, J. Sulpizio, N. Stander, K. Todd, B. Yang, and D. Goldhaber-Gordon. Transport Measurements Across a Tunable Potential Barrier in Graphene. Physical Review Letters, 98(23):236803, June 2007. ISSN 0031-9007. doi: 10.1103/PhysRevLett.98.236803. URL http://link.aps.org/doi/10.1103/PhysRevLett.98.236803.

[71] E. Hwang and S. Das Sarma. Acoustic phonon scattering limited carrier mobility in two-dimensional extrinsic graphene. Physical Review B, 77(11):115449, March 2008. ISSN 1098-0121. doi: 10.1103/PhysRevB.77.115449. URL http://link.aps.org/doi/10.1103/PhysRevB.77.115449.

[72] Y Imry. The Quantized Hall Effect and Other Macroscopic Quantum Phenomena. In Yosuke Nagaoka and Hidetoshi Fukuyama, editors, Anderson Localization SE - 20, volume 39 of Springer Series in Solid-State Sciences, pages 198–206. Springer Berlin Heidelberg, 1982. ISBN 978-3-642-81843-1. doi: 10.1007/978-3-642-81841-7_20. URL http://dx.doi.org/10.1007/978-3-642-81841-7_20.

[73] Y Imry. Active Transmission Channels and Universal Conductance Fluctuations. Europhysics Letters (EPL), 1(5):249–256, March 1986. ISSN 0295-5075. doi: 10.1209/0295-5075/1/5/008. URL http://iopscience.iop.org/0295-5075/1/5/008.

[74] Yoseph Imryt. Quantum interference effects in submicron systems. Philosophical Magazine Part B, 56(6):969–970, December 1987. ISSN 1364-2812. doi: 10.1080/13642818708215333. URL http://dx.doi.org/10.1080/13642818708215333http://www.tandfonline.com/doi/abs/10.1080/13642818708215333.

[75] Masa Ishigami, J H Chen, W G Cullen, M S Fuhrer, and E D Williams. Atomic structure of graphene on SiO2. Nano letters, 7(6):1643–8, June 2007. ISSN 1530-6984. doi: 10.1021/nl070613a. URL http://www.ncbi.nlm.nih.gov/pubmed/17497819.

[76] Yang Ji, Yunchul Chung, D Sprinzak, M Heiblum, and D Mahalu. An electronic Mach – Zehnder interferometer. Letters to Nature, 422(8):415–418, 2003. doi: 10.1038/nature01492.1.

[77] Yongsung Ji, Minhyeok Choe, Byungjin Cho, Sunghoon Song, Jongwon Yoon, Heung Cho Ko, and Takhee Lee. Organic nonvolatile memory devices with charge trapping multilayer graphene film. Nanotechnology, 23 (10):105202, March 2012. ISSN 1361-6528. doi: 10.1088/0957-4484/23/10/105202. URL http://iopscience.iop.org/0957-4484/23/10/105202/article/.

[78] Robin John, a Ashokreddy, C Vijayan, and T Pradeep. Single- and few-layer graphene growth on stainless steel substrates by direct thermal chemical vapor deposition. Nanotechnology, 22(16):165701, April 2011. ISSN 1361-6528. doi: 10.1088/0957-4484/22/16/165701. URL http://www.ncbi.nlm.nih.gov/pubmed/21393813.

[79] Long Ju, Baisong Geng, Jason Horng, Caglar Girit, Michael Martin, Zhao Hao, Hans a Bechtel, Xiaogan Liang, Alex Zettl, Y Ron Shen, and Feng Wang. Graphene plasmonics for tunable terahertz metamaterials. Nature nanotechnology, 6(10):630–4, October 2011. ISSN 1748-3395. doi: 10.1038/nnano.2011.146. URL http://www.ncbi.nlm.nih.gov/pubmed/21892164http://dx.doi.org/10.1038/nnano.2011.146.

[80] Thibaut Jullien. MESOSCOPIC FEW ELECTRONS VOLTAGE PULSE SOURC. PhD thesis, Paris Sud XI, 2014.

[81] M I Katsnelson. Zitterbewegung, chirality, and minimal conductivity in graphene. The European Physical Journal B, 51(2):157–160, May 2006. ISSN 1434-6028. doi: 10.1140/epjb/e2006-00203-1. URL http://www.springerlink.com/index/10.1140/epjb/e2006-00203-1.

[82] M. I. Katsnelson, K. S. Novoselov, and A K Geim. Chiral tunnelling and the Klein paradox in graphene. Nature Physics, 2(9):620–625, August 2006. ISSN 1745-2473. doi: 10.1038/nphys384. URL http://www.nature.com/doifinder/10.1038/nphys384.

[83] Jakub Kedzierski, Pei-Lan Hsu, Paul Healey, Peter W. Wyatt, Craig L. Keast, Mike Sprinkle, Claire Berger, and Walt a. de Heer. Epitaxial Graphene Transistors on SiC Substrates. IEEE Transactions on Electron Devices, 55(8):2078–2085, August 2008. ISSN 0018-9383. doi: 10.1109/TED.2008.926593. URL http://ieeexplore.ieee.org/lpdocs/epic03/wrapper.htm?arnumber=4578855.

[84] C Kittel. Introduction to Solid State Physics. Wiley, 2004. ISBN 9780471415268. URL http://books.google.fr/books?id=kym4QgAACAAJ.

[85] U Klass, W Dietsche, K Von Klitzing, and K Ploog. Imaging of the dissipation in quantum-Hall-effect experiments. Zeitschrift für Physik B ..., 354:351–354, 1991. URL http://link.springer.com/article/10.1007/BF01357178.

[86] O. Klein. Die Reflexion von Elektronen an einem Potentialsprung nach der relativistischen Dynamik von Dirac. Zeitschrift für Physik, 53(3-4):157–165, March 1929. ISSN 1434-6001. doi: 10.1007/BF01339716. URL http://link.springer.com/10.1007/BF01339716.

[87] K. Klitzing, G. Dorda, and M. Pepper. New Method for High-Accuracy Determination of the Fine-Structure Constant Based on Quantized Hall Resistance. Physical Review Letters, 45(6):494–497, August 1980. ISSN 0031-9007. doi: 10.1103/PhysRevLett.45.494. URL http://link.aps.org/doi/10.1103/PhysRevLett.45.494.

[88] Klaus Von Klitzing. 25 Years of Quantum Hall Effect. A Personal View on the Discovery , Physics and Applications of this Quantum Effect. In Seminaire Poincare, volume 2, pages 1–16, 2004.

[89] Katsuyoshi Komatsu, Chuan Li, S. Autier-Laurent, H. Bouchiat, and S. Guéron. Superconducting proximity effect in long superconductor/graphene/superconductor junctions: From specular Andreev reflection at zero field to the quantum Hall regime. Physical Review B, 86(11):115412, September 2012. ISSN 1098-0121. doi: 10.1103/PhysRevB.86.115412. URL http://link.aps.org/doi/10.1103/PhysRevB.86.115412.

[90] S. Kubakaddi. Interaction of massless Dirac electrons with acoustic phonons in graphene at low temperatures. Physical Review B, 79(7):075417, February 2009. ISSN 1098-0121. doi: 10.1103/PhysRevB.79.075417. URL http://link.aps.org/doi/10.1103/PhysRevB.79.075417.

[91] R. Landauer. Spatial Variation of Currents and Fields Due to Localized Scatterers in Metallic Conduction. IBM Journal of Research and Development, 1(3):223–231, July 1957. ISSN 0018-8646. doi: 10.1147/rd.13.0223. URL http://ieeexplore.ieee.org/lpdocs/epic03/wrapper.htm?arnumber=5392683.

[92] R. Landauer and M. Büttiker. Resistance of Small Metallic Loops. Physical Review Letters, 54(18):2049–2052, May 1985. ISSN 0031-9007. doi:

10.1103/PhysRevLett.54.2049. URL http://link.aps.org/doi/10.1103/PhysRevLett.54.2049.

[93] Rolf Landauer. Electrical resistance of disordered one-dimensional lattices. Philosophical Magazine, 21(172):863–867, April 1970. ISSN 1478-6435. doi: 10.1080/14786437008238472. URL http://www.informaworld.com/openurl?genre=article&doi=10.1080/14786437008238472&magic=crossref||D404A21C5BB053405B1A640AFFD44AE3.

[94] Rolf Landauer. Can a length of perfect conductor have a resistance? Physics Letters A, 85(2):91–93, 1981. URL http://www.sciencedirect.com/science/article/pii/0375960181902309.

[95] G. S. Landsberg and L. I. Mandelstam. Eine neue Erscheinung bei der Lichtzerstreuung in Krystallen. Die Naturwissenschaften, 16(28):557–558, July 1928. ISSN 0028-1042. doi: 10.1007/BF01506807. URL http://link.springer.com/10.1007/BF01506807.

[96] C. Lewenkopf, E. Mucciolo, and A. Castro Neto. Numerical studies of conductivity and Fano factor in disordered graphene. Physical Review B, 77(8):081410, February 2008. ISSN 1098-0121. doi: 10.1103/PhysRevB.77.081410. URL http://prb.aps.org/abstract/PRB/v77/i8/e081410http://link.aps.org/doi/10.1103/PhysRevB.77.081410.

[97] Qiuzi Li and S. Das Sarma. Finite temperature inelastic mean free path and quasiparticle lifetime in graphene. Physical Review B, 87(8):085406, February 2013. ISSN 1098-0121. doi: 10.1103/PhysRevB.87.085406. URL http://link.aps.org/doi/10.1103/PhysRevB.87.085406.

[98] Guanxiong Liu, Sonia Ahsan, Alexander G. Khitun, Roger K. Lake, and Alexander A. Balandin. Graphene-based non-Boolean logic circuits. Journal of Applied Physics, 114(15):154310, 2013. ISSN 00218979. doi: 10.1063/1.4824828. URL http://link.aip.org/link/JAPIAU/v114/i15/p154310/s1&Agg=doi.

[99] Demetrio Logoteta, Paolo Marconcini, and Massimo Macucci. Numerical simulation of shot noise in disordered graphene. 2013 22nd International Conference on Noise and Fluctuations (ICNF), 6578889(June):1–4, June 2013. doi: 10.1109/ICNF.2013.6578889. URL http://ieeexplore.ieee.org/lpdocs/epic03/wrapper.htm?arnumber=6578889.

[100] Vorrada Loryuenyong, Krit Totepvimarn, Passakorn Eimburanapravat, Wanchai Boonchompoo, and Achanai Buasri. Preparation and Characterization of Reduced Graphene Oxide Sheets via Water-Based Exfoliation

and Reduction Methods. Advances in Materials Science and Engineering, 2013:1–5, 2013. ISSN 1687-8434. doi: 10.1155/2013/923403. URL http://www.hindawi.com/journals/amse/2013/923403/.

[101] L.M. Malard, M.a. Pimenta, G. Dresselhaus, and M.S. Dresselhaus. Raman spectroscopy in graphene. Physics Reports, 473(5-6):51–87, April 2009. ISSN 03701573. doi: 10.1016/j.physrep.2009.02.003. URL http://linkinghub.elsevier.com/retrieve/pii/S0370157309000520.

[102] Alexander Malesevic, Roumen Vitchev, Koen Schouteden, Alexander Volodin, Liang Zhang, Gustaaf Van Tendeloo, Annick Vanhulsel, and Chris Van Haesendonck. Synthesis of few-layer graphene via microwave plasma-enhanced chemical vapour deposition. Nanotechnology, 19(30): 305604, July 2008. ISSN 0957-4484. doi: 10.1088/0957-4484/19/30/305604. URL http://www.ncbi.nlm.nih.gov/pubmed/21828766.

[103] P. Marconcini, D. Logoteta, M. Fagotti, and M. Macucci. Numerical solution of the Dirac equation for an armchair graphene nanoribbon in the presence of a transversally variable potential. In 2010 14th International Workshop on Computational Electronics, pages 1–4. IEEE, October 2010. ISBN 978-1-4244-9383-8. doi: 10.1109/IWCE.2010.5677938. URL http://ieeexplore.ieee.org/lpdocs/epic03/wrapper.htm?arnumber=5677938.

[104] J Martin, N Akerman, G Ulbricht, T Lohmann, J H Smet, K. von Klitzing, and A Yacoby. Observation of electron–hole puddles in graphene using a scanning single-electron transistor. Nature Physics, 4(2):144–148, November 2007. ISSN 1745-2473. doi: 10.1038/nphys781. URL http://www.nature.com/doifinder/10.1038/nphys781.

[105] J. Martin, N. Akerman, G. Ulbricht, T. Lohmann, K. von Klitzing, J. H. Smet, and A. Yacoby. The nature of localization in graphene under quantum Hall conditions. Nature Physics, 5(9):669–674, July 2009. ISSN 1745-2473. doi: 10.1038/nphys1344. URL http://www.nature.com/doifinder/10.1038/nphys1344http://dx.doi.org/10.1038/nphys1344.

[106] Cecilia Mattevi, Hokwon Kim, and Manish Chhowalla. A review of chemical vapour deposition of graphene on copper. Journal of Materials Chemistry, 21(10):3324, 2011. ISSN 0959-9428. doi: 10.1039/c0jm02126a. URL http://xlink.rsc.org/?DOI=c0jm02126a.

[107] Inanc Meric, Melinda Y Han, A. F. Young, Barbaros Ozyilmaz, Philip Kim, and Kenneth L Shepard. Current saturation in zero-bandgap, top-gated graphene field-effect transistors. Nature nanotechnology, 3(11):

654–9, November 2008. ISSN 1748-3395. doi: 10.1038/nnano.2008.268. URL http://www.ncbi.nlm.nih.gov/pubmed/18989330http://www.nature.com/nnano/journal/v3/n11/abs/nnano.2008.268.html.

[108] F Miao, S Wijeratne, Y Zhang, U C Coskun, W Bao, and C N Lau. Phase-coherent transport in graphene quantum billiards. Science (New York, N.Y.), 317(5844):1530–3, September 2007. ISSN 1095-9203. doi: 10.1126/science.1144359. URL http://www.ncbi.nlm.nih.gov/pubmed/17872440.

[109] S. Minke, J. Bundesmann, D. Weiss, and J. Eroms. Phase coherent transport in graphene nanoribbons and graphene nanoribbon arrays. Physical Review B, 86(15):155403, October 2012. ISSN 1098-0121. doi: 10.1103/PhysRevB.86.155403. URL http://link.aps.org/doi/10.1103/PhysRevB.86.155403.

[110] E. Moreau, F. J. Ferrer, D. Vignaud, S. Godey, and X. Wallart. Graphene growth by molecular beam epitaxy using a solid carbon source. Physica Status Solidi (a), 207(2):300–303, February 2010. ISSN 18626300. doi: 10.1002/pssa.200982412. URL http://doi.wiley.com/10.1002/pssa.200982412.

[111] S. V. Morozov, K. S. Novoselov, M. I. Katsnelson, F. Schedin, L. Ponomarenko, D. Jiang, and A. Geim. Strong Suppression of Weak Localization in Graphene. Physical Review Letters, 97(1), March 2006. ISSN 0031-9007. doi: 10.1103/PhysRevLett.97.016801. URL http://arxiv.org/abs/cond-mat/0603826.

[112] K. Nagashio, T. Yamashita, T. Nishimura, K. Kita, and a. Toriumi. Electrical transport properties of graphene on SiO2 with specific surface structures. Journal of Applied Physics, 110(2):024513, 2011. ISSN 00218979. doi: 10.1063/1.3611394. URL http://link.aip.org/link/JAPIAU/v110/i2/p024513/s1&Agg=doi.

[113] R R Nair, H A Wu, P N Jayaram, I V Grigorieva, and A K Geim. Unimpeded permeation of water through helium-leak-tight graphene-based membranes. Science (New York, N.Y.), 335(6067):442–444, January 2012. ISSN 1095-9203. doi: 10.1126/science.1211694. URL http://www.sciencemag.org/content/335/6067/442.

[114] K. S. Novoselov, A K Geim, S. V. Morozov, D Jiang, Y Zhang, S V Dubonos, I V Grigorieva, and A A Firsov. Electric field effect in atomically thin carbon films. Science (New York, N.Y.), 306(5696):666–9, October 2004. ISSN 1095-9203. doi: 10.1126/science.1102896. URL http://www.sciencemag.org/content/306/5696/666.abstract.

[115] K. S. Novoselov, A K Geim, S. V. Morozov, D Jiang, I. V. Grigorieva, S V Dubonos, and A A Firsov. Two-dimensional gas of massless Dirac fermions in graphene. Nature, 438(7065):197–200, 2005.

[116] K. S. Novoselov, Z Jiang, Y Zhang, S. V. Morozov, H L Stormer, U Zeitler, J C Maan, G S Boebinger, P Kim, and A K Geim. Room-temperature quantum Hall effect in graphene. Science (New York, N.Y.), 315(5817): 1379, March 2007. ISSN 1095-9203. doi: 10.1126/science.1137201. URL http://www.sciencemag.org/content/315/5817/1379.abstract.

[117] KS Novoselov, AK Geim, SV Morozov, D. Jiang, M.I.K.I.V. Grigorieva, SV Dubonos, and AA Firsov. Two-dimensional gas of massless Dirac fermions in graphene. Arxiv preprint cond-mat/0509330, 438:197–200, 2005. URL http://arxiv.org/abs/cond-mat/0509330.

[118] Landon Oakes, Andrew Westover, Jeremy W Mares, Shahana Chatterjee, William R Erwin, Rizia Bardhan, Sharon M Weiss, and Cary L Pint. Surface engineered porous silicon for stable, high performance electrochemical supercapacitors. Scientific reports, 3:3020, January 2013. ISSN 2045-2322. doi: 10.1038/srep03020. URL http://www.nature.com/srep/2013/131022/srep03020/full/srep03020.html#affil-auth.

[119] Barbaros Özyilmaz, Pablo Jarillo-Herrero, Dmitri Efetov, D. A. Abanin, Leonid Levitov, and Philip Kim. Electronic Transport and Quantum Hall Effect in Bipolar Graphene p-n-p Junctions. Physical Review Letters, 99 (16):166804, October 2007. ISSN 0031-9007. doi: 10.1103/PhysRevLett.99.166804. URL http://link.aps.org/doi/10.1103/PhysRevLett.99.166804.

[120] Sungjin Park and Rodney S Ruoff. Chemical methods for the production of graphenes. Nature nanotechnology, 4(4):217–24, April 2009. ISSN 1748-3395. doi: 10.1038/nnano.2009.58. URL http://www.ncbi.nlm.nih.gov/pubmed/19350030.

[121] I Pócsik, Martin Hundhausen, M Koós, and Lothar Ley. Origin of the D peak in the Raman spectrum of microcrystalline graphite. Journal of Non-Crystalline Solids, pages 1083–1086, 1998. URL http://www.sciencedirect.com/science/article/pii/S0022309398003494.

[122] L a Ponomarenko, F Schedin, M. I. Katsnelson, R Yang, E W Hill, K. S. Novoselov, and a K Geim. Chaotic Dirac billiard in graphene quantum dots. Science (New York, N.Y.), 320(5874):356–8, April 2008. ISSN 1095-9203. doi: 10.1126/science.1154663. URL http://www.ncbi.nlm.nih.gov/pubmed/18420930.

[123] a. Preobrajenski, May Ng, a. Vinogradov, and N. Må rtensson. Controlling graphene corrugation on lattice-mismatched substrates. Physical Review B, 78(7):073401, August 2008. ISSN 1098-0121. doi: 10.1103/PhysRevB.78.073401. URL http://link.aps.org/doi/10.1103/PhysRevB.78.073401.

[124] Wen Qian, Rui Hao, Yanglong Hou, Yuan Tian, Chengmin Shen, Hongjun Gao, and Xuelei Liang. Solvothermal-assisted exfoliation process to produce graphene with high yield and high quality. Nano Research, 2(9):706–712, September 2009. ISSN 1998-0124. doi: 10.1007/s12274-009-9074-z. URL http://link.springer.com/10.1007/s12274-009-9074-z.

[125] C V Raman. A new radiation. Indian Journal of Physics, 2(387-398), 1928.

[126] S. Reich, J. Maultzsch, C. Thomsen, and P. Ordejón. Tight-binding description of graphene. Physical Review B, 66(3):035412, July 2002. ISSN 0163-1829. doi: 10.1103/PhysRevB.66.035412. URL http://link.aps.org/doi/10.1103/PhysRevB.66.035412.

[127] Joshua a Robinson, Maxwell Wetherington, Joseph L Tedesco, Paul M Campbell, Xiaojun Weng, Joseph Stitt, Mark a Fanton, Eric Frantz, David Snyder, Brenda L VanMil, Glenn G Jernigan, Rachael L Myers-Ward, Charles R Eddy, and D Kurt Gaskill. Correlating Raman spectral signatures with carrier mobility in epitaxial graphene: a guide to achieving high mobility on the wafer scale. Nano letters, 9(8):2873–6, August 2009. ISSN 1530-6992. doi: 10.1021/nl901073g. URL http://www.ncbi.nlm.nih.gov/pubmed/19719106.

[128] Preden Roulleau, F. Portier, D. Glattli, P. Roche, A. Cavanna, G. Faini, U. Gennser, and D. Mailly. Finite bias visibility of the electronic Mach-Zehnder interferometer. Physical Review B, 76(16):161309, October 2007. ISSN 1098-0121. doi: 10.1103/PhysRevB.76.161309. URL http://link.aps.org/doi/10.1103/PhysRevB.76.161309.

[129] Sunmin Ryu, Janina Maultzsch, Melinda Y Han, Philip Kim, and Louis E Brus. Raman spectroscopy of lithographically patterned graphene nanoribbons. ACS nano, 5(5):4123–30, May 2011. ISSN 1936-086X. doi: 10.1021/nn200799y. URL http://www.ncbi.nlm.nih.gov/pubmed/21452879.

[130] M. L. Sadowski, G. Martinez, and M. Potemski. Landau Level Spectroscopy of Ultrathin Graphite Layers. Physical Review Letters, 97(26):266405, December 2006. ISSN 0031-9007. doi: 10.1103/PhysRevLett.97.266405. URL http://link.aps.org/doi/10.1103/PhysRevLett.97.266405.

[131] Lauren Saminadayar. Fluctuations Temporelles Quantiques du Courant dans des Nanostr PhD thesis, 1997.

[132] Pablo San-Jose, Elsa Prada, and Dmitry Golubev. Universal scaling of current fluctuations in disordered graphene. Physical Review B, 76(19):195445, November 2007. ISSN 1098-0121. doi: 10.1103/PhysRevB.76.195445. URL http://link.aps.org/doi/10.1103/PhysRevB.76.195445.

[133] E Schrödinger. Über die kräftefreie bewegung in der relativistischen quantenmechanik. Akademie der wissenschaften in kommission bei W. de Gruyter u. Company, 1930. URL http://books.google.fr/books?id=QhMXAQAAMAAJ.

[134] Yuyan Shao, Jun Wang, Hong Wu, Jun Liu, Ilhan A. Aksay, and Yuehe Lin. Graphene Based Electrochemical Sensors and Biosensors: A Review. Electroanalysis, 22(10):1027–1036, May 2010. ISSN 10400397. doi: 10.1002/elan.200900571. URL http://doi.wiley.com/10.1002/elan.200900571.

[135] D. Yu. Sharvin and Yu. V. Sharvin. Magnetic-flux quantization in cylindrical film of a normal metal. JETP Letters, 34(5):272–275, 1981.

[136] VMF Soler and J Badia-Canal. Hot-Wire Chemical Vapor Deposition of Few-Layer Graphene on Copper Substrates. Japanese Journal of ..., 52:1–6, 2013. URL http://adsabs.harvard.edu/abs/2013JaJAP..52aAK02S.

[137] M. Sprinkle, D. Siegel, Y. Hu, J. Hicks, a. Tejeda, a. Taleb-Ibrahimi, P. Le Fèvre, F. Bertran, S. Vizzini, H. Enriquez, S. Chiang, P. Soukiassian, C. Berger, W. a. de Heer, a. Lanzara, and E. H. Conrad. First Direct Observation of a Nearly Ideal Graphene Band Structure. Physical Review Letters, 103(22):226803, November 2009. ISSN 0031-9007. doi: 10.1103/PhysRevLett.103.226803. URL http://link.aps.org/doi/10.1103/PhysRevLett.103.226803.

[138] N Srivastava, Guowei He, P C Mende, R M Feenstra, and Yugang Sun. Graphene formed on SiC under various environments: comparison of Si-face and C-face. Journal of Physics D: Applied Physics, 45(15):154001, April 2012. ISSN 0022-3727. doi: 10.1088/0022-3727/45/15/154001. URL http://stacks.iop.org/0022-3727/45/i=15/a=154001?key=crossref.27af4213284642fcf3e0375bab092ca9.

[139] N. Stander, B. Huard, and D. Goldhaber-Gordon. Evidence for Klein Tunneling in Graphene p-n Junctions. Physical Review Letters, 102(2):026807, January 2009. ISSN 0031-9007. doi: 10.1103/PhysRevLett.102.026807. URL http://link.aps.org/doi/10.1103/PhysRevLett.102.026807.

[140] Elena Stolyarova, Kwang Taeg Rim, Sunmin Ryu, Janina Maultzsch, Philip Kim, Louis E Brus, Tony F Heinz, Mark S Hybertsen, and George W Flynn. High-resolution scanning tunneling microscopy imaging of mesoscopic graphene sheets on an insulating surface. Proceedings of the National Academy of Sciences of the United States of America, 104(22): 9209–12, May 2007. ISSN 0027-8424. doi: 10.1073/pnas.0703337104. URL http://www.pubmedcentral.nih.gov/articlerender.fcgi?artid=1874226&tool=pmcentrez&rendertype=abstract.

[141] A. Stone and Y. Imry. Periodicity of the Aharonov-Bohm effect in normal-metal rings. Physical Review Letters, 56(2):189–192, January 1986. ISSN 0031-9007. doi: 10.1103/PhysRevLett.56.189. URL http://link.aps.org/doi/10.1103/PhysRevLett.56.189.

[142] Peter Sutter, Jerzy T. Sadowski, and Eli Sutter. Graphene on Pt(111): Growth and substrate interaction. Physical Review B, 80(24):245411, December 2009. ISSN 1098-0121. doi: 10.1103/PhysRevB.80.245411. URL http://link.aps.org/doi/10.1103/PhysRevB.80.245411.

[143] Peter W Sutter, Jan-Ingo Flege, and Eli a Sutter. Epitaxial graphene on ruthenium. Nature materials, 7(5):406–11, May 2008. ISSN 1476-1122. doi: 10.1038/nmat2166. URL http://www.ncbi.nlm.nih.gov/pubmed/18391956.

[144] Y.-W. Tan, Y. Zhang, K. Bolotin, Y. Zhao, S. Adam, E. H. Hwang, S. Das Sarma, H. L. Stormer, and P. Kim. Measurement of Scattering Rate and Minimum Conductivity in Graphene. Physical Review Letters, 99(24):246803, December 2007. ISSN 0031-9007. doi: 10.1103/PhysRevLett.99.246803. URL http://link.aps.org/doi/10.1103/PhysRevLett.99.246803.

[145] Zhenbing Tan, Changling Tan, Li Ma, G. T. Liu, L. Lu, and C. L. Yang. Shubnikov-de Haas oscillations of a single layer graphene under dc current bias. Physical Review B, 84(11):115429, September 2011. ISSN 1098-0121. doi: 10.1103/PhysRevB.84.115429. URL http://link.aps.org/doi/10.1103/PhysRevB.84.115429.

[146] K. J. Tielrooij, J. C. W. Song, S. A. Jensen, A. Centeno, A. Pesquera, A. Zurutuza Elorza, M. Bonn, L. S. Levitov, and F. H. L. Koppens. Photoexcitation cascade and multiple hot-carrier generation in graphene. Nature Physics, 9(4):248–252, February 2013. ISSN 1745-2473. doi: 10.1038/nphys2564. URL http://dx.doi.org/10.1038/nphys2564.

[147] F. Tikhonenko, A. Kozikov, A. Savchenko, and R. Gorbachev. Transition between Electron Localization and Antilocalization in Graphene. Physical Review Letters, 103(22):226801, November 2009. ISSN 0031-9007. doi: 10.1103/PhysRevLett.103.226801. URL http://link.aps.org/doi/10.1103/PhysRevLett.103.226801.

[148] J. Tworzydlo, B Trauzettel, M Titov, A Rycerz, and C. W. J. Beenakker. Quantum-limited shot noise in graphene. Physical Review Letters, 96 (24):246802, March 2006. ISSN 0031-9007. doi: 10.1103/PhysRevLett.96.246802. URL http://arxiv.org/abs/cond-mat/0603315v3http://arxiv.org/abs/cond-mat/0603315.

[149] J. Tworzydlo, B Trauzettel, M Titov, A Rycerz, and C. W. J. Beenakker. Quantum-limited shot noise in graphene. arXiv, cond-mat.m, January 2006. doi: 10.1103/PhysRevLett.96.246802. URL http://arxiv.org/abs/cond-mat/0603315v3.

[150] D. Usachov, a. Dobrotvorskii, a. Varykhalov, O. Rader, W. Gudat, a. Shikin, and V. Adamchuk. Experimental and theoretical study of the morphology of commensurate and incommensurate graphene layers on Ni single-crystal surfaces. Physical Review B, 78(8):085403, August 2008. ISSN 1098-0121. doi: 10.1103/PhysRevB.78.085403. URL http://link.aps.org/doi/10.1103/PhysRevB.78.085403.

[151] H. van Houten, B. J. van Wees, M. G. J. Heijman, and J. P. Andre. Submicron conducting channels defined by shallow mesa etch in GaAs-AlGaAs heterojunctions. Applied Physics Letters, 49(26):1781, 1986. ISSN 00036951. doi: 10.1063/1.97243. URL http://link.aip.org/link/APPLAB/v49/i26/p1781/s1&Agg=doi.

[152] B. van Wees, H. van Houten, C. W. J. Beenakker, J. Williamson, L. Kouwenhoven, D. van der Marel, and C. Foxon. Quantized conductance of point contacts in a two-dimensional electron gas. Physical Review Letters, 60(9): 848–850, February 1988. ISSN 0031-9007. doi: 10.1103/PhysRevLett.60.848. URL http://link.aps.org/doi/10.1103/PhysRevLett.60.848.

[153] a. Varykhalov, J. Sánchez-Barriga, a. Shikin, C. Biswas, E. Vescovo, a. Rybkin, D. Marchenko, and O. Rader. Electronic and Magnetic Properties of Quasifreestanding Graphene on Ni. Physical Review Letters, 101(15):157601, October 2008. ISSN 0031-9007. doi: 10.1103/PhysRevLett.101.157601. URL http://link.aps.org/doi/10.1103/PhysRevLett.101.157601.

[154] L Vicarelli, M S Vitiello, D Coquillat, A Lombardo, A. C Ferrari, W Knap, M Polini, V Pellegrini, and A Tredicucci. Graphene field-effect transistors as room-temperature terahertz detectors. Nature materials, 11(10):865–71, October 2012. ISSN 1476-1122. doi: 10.1038/nmat3417. URL http://dx.doi.org/10.1038/nmat3417.

[155] Lisa M. Viculis, Julia J. Mack, Oren M. Mayer, H. Thomas Hahn, and Richard B. Kaner. Intercalation and exfoliation routes to graphite nanoplatelets. Journal of Materials Chemistry, 15(9):974, February 2005. ISSN 0959-9428. doi: 10.1039/b413029d. URL http://pubs.rsc.org/en/content/articlehtml/2005/jm/b413029d.

[156] J. K. Viljas and T. T. Heikkilä. Electron-phonon heat transfer in monolayer and bilayer graphene. Physical Review B, 81(24):245404, June 2010. ISSN 1098-0121. doi: 10.1103/PhysRevB.81.245404. URL http://link.aps.org/doi/10.1103/PhysRevB.81.245404.

[157] D A Wharam, T J Thornton, R Newbury, M Pepper, H Ahmed, J E F Frost, D G Hasko, D C Peacock, D A Ritchie, and G A C Jones. One-dimensional transport and the quantisation of the ballistic resistance. Journal of Physics C: Solid State Physics, 21(8):L209–L214, March 1988. ISSN 0022-3719. doi: 10.1088/0022-3719/21/8/002. URL http://iopscience.iop.org/0022-3719/21/8/002.

[158] J. R. Williams. Electronic Transport in Graphene : p-n Junctions , Shot Noise , and Nanoribbon PhD thesis, Harvard University Cambridge, Massachusetts, 2009.

[159] J. R. Williams, L. DiCarlo, and C M Marcus. Quantum Hall effect in a gate-controlled p-n junction of graphene. Science (New York, N.Y.), 317(5838):638–41, August 2007. ISSN 1095-9203. doi: 10.1126/science.1144657. URL http://www.sciencemag.org/content/317/5838/638.short.

[160] J R Williams, L. DiCarlo, and C M Marcus. Quantum Hall Effect in a Graphene p-n Junction. (2):1–4, April 2007. URL http://arxiv.org/abs/0704.3487.

[161] Xiaosong Wu, Xuebin Li, Zhimin Song, Claire Berger, and Walt de Heer. Weak Antilocalization in Epitaxial Graphene: Evidence for Chiral Electrons. Physical Review Letters, 98(13):5, November 2007. ISSN 0031-9007. doi: 10.1103/PhysRevLett.98.136801. URL http://arxiv.org/abs/cond-mat/0611339.

[162] Jilin Xia, Fang Chen, Jinghong Li, and Nongjian Tao. Measurement of the quantum capacitance of graphene. Nature nanotechnology, 4(8):505–9,

August 2009. ISSN 1748-3395. doi: 10.1038/nnano.2009.177. URL http://www.ncbi.nlm.nih.gov/pubmed/19662012.

[163] A. Yacoby, M. Heiblum, V. Umansky, H. Shtrikman, and D. Mahalu. Unexpected Periodicity in an Electronic Double Slit Interference Experiment. Physical Review Letters, 73(23):3149–3152, December 1994. ISSN 0031-9007. doi: 10.1103/PhysRevLett.73.3149. URL http://link.aps.org/doi/10.1103/PhysRevLett.73.3149.

[164] Jai Seung Yoo, Yung Woo Park, Viera Skakalova, and Siegmar Roth. Shubnikov–de Haas and Aharonov Bohm effects in a graphene nanoring structure. Applied Physics Letters, 96(14):143112, April 2010. ISSN 00036951. doi: 10.1063/1.3380616. URL http://link.aip.org/link/APPLAB/v96/i14/p143112/s1&Agg=doihttp://scitation.aip.org/content/aip/journal/apl/96/14/10.1063/1.3380616.

[165] YuMeng You, ZhenHua Ni, Ting Yu, and ZeXiang Shen. Edge chirality determination of graphene by Raman spectroscopy. Applied Physics Letters, 93(16):163112, 2008. ISSN 00036951. doi: 10.1063/1.3005599. URL http://link.aip.org/link/APPLAB/v93/i16/p163112/s1&Agg=doi.

[166] A. F. Young, C. R. Dean, L. Wang, H. Ren, P. Cadden-Zimansky, K. Watanabe, T. Taniguchi, J. Hone, K. L. Shepard, and P. Kim. Spin and valley quantum Hall ferromagnetism in graphene. Nature Physics, 8(7):550–556, May 2012. ISSN 1745-2473. doi: 10.1038/nphys2307. URL http://www.nature.com/nphys/journal/v8/n7/full/nphys2307.html?WT.ec_id=NPHYS-201207.

[167] Andrea F. Young and Philip Kim. Quantum interference and Klein tunnelling in graphene heterojunctions. Nature Physics, 5(3):222–226, February 2009. ISSN 1745-2473. doi: 10.1038/nphys1198. URL http://dx.doi.org/10.1038/nphys1198.

[168] Guihua Yu, Liangbing Hu, Nian Liu, Huiliang Wang, Michael Vosgueritchian, Yuan Yang, Yi Cui, and Zhenan Bao. Enhancing the supercapacitor performance of graphene/MnO2 nanostructured electrodes by conductive wrapping. Nano letters, 11(10):4438–42, October 2011. ISSN 1530-6992. doi: 10.1021/nl2026635. URL http://dx.doi.org/10.1021/nl2026635.

[169] G.D. Yuan, W.J. Zhang, Y. Yang, Y.B. Tang, Y.Q. Li, J.X. Wang, X.M. Meng, Z.B. He, C.M.L. Wu, I. Bello, C.S. Lee, and S.T. Lee. Graphene sheets via microwave chemical vapor deposition. Chemical Physics Letters, 467(4-6):361–364, January 2009. ISSN 00092614. doi: 10.1016/

j.cplett.2008.11.059. URL http://linkinghub.elsevier.com/retrieve/pii/S0009261408015753.

[170] L. Zhang, J. Camacho, H. Cao, Y. P. Chen, M. Khodas, D. E. Kharzeev, A. M. Tsvelik, T. Valla, and I. A. Zaliznyak. Breakdown of the N=0 quantum Hall state in graphene: Two insulating regimes. Physical Review B, 80(24): 241412–, December 2009. doi: 10.1103/PhysRevB.80.241412. URL http://link.aps.org/doi/10.1103/PhysRevB.80.241412.

[171] Y. Zhang, Z. Jiang, J. P. Small, M. S. Purewal, Y.-W. Tan, M. Fazlollahi, J. D. Chudow, J. A. Jaszczak, H. L. Stormer, and P. Kim. Landau-Level Splitting in Graphene in High Magnetic Fields. Physical Review Letters, 96(13):136806, April 2006. ISSN 0031-9007. doi: 10.1103/PhysRevLett.96.136806. URL http://link.aps.org/doi/10.1103/PhysRevLett.96.136806.

[172] Yi Zhang, Luyao Zhang, and Chongwu Zhou. Review of chemical vapor deposition of graphene and related applications. Accounts of chemical research, 46(10):2329–39, October 2013. ISSN 1520-4898. doi: 10.1021/ar300203n. URL http://www.ncbi.nlm.nih.gov/pubmed/23480816.

[173] Yuanbo Zhang, Y.-W. Tan, Horst L Stormer, and Philip Kim. Experimental observation of the quantum Hall effect and Berry's phase in graphene. Nature, 438(7065):201–4, November 2005. ISSN 1476-4687. doi: 10.1038/nature04235. URL http://www.ncbi.nlm.nih.gov/pubmed/16281031.

[174] Jiaxin Zheng, Lu Wang, Ruge Quhe, Qihang Liu, Hong Li, Dapeng Yu, Wai-Ning Mei, Junjie Shi, Zhengxiang Gao, and Jing Lu. Sub-10 nm gate length graphene transistors: operating at terahertz frequencies with current saturation. Scientific reports, 3:1314, January 2013. ISSN 2045-2322. doi: 10.1038/srep01314. URL http://www.pubmedcentral.nih.gov/articlerender.fcgi?artid=3575621&tool=pmcentrez&rendertype=abstract.

[175] Mi Zhou, Frank L Pasquale, Peter a Dowben, Alex Boosalis, Mathias Schubert, Vanya Darakchieva, Rositza Yakimova, Lingmei Kong, and Jeffry a Kelber. Direct graphene growth on Co3O4(111) by molecular beam epitaxy. Journal of physics. Condensed matter : an Institute of Physics journal, 24 (7):072201, February 2012. ISSN 1361-648X. doi: 10.1088/0953-8984/24/7/072201. URL http://www.ncbi.nlm.nih.gov/pubmed/22223630.